

Annals of the ICRP

ICRP PUBLICATION XXX

Adult Mesh-type Reference Computational Phantoms

Editor-in-Chief
C.H. CLEMENT

Associate Editor
H. FUJITA

Authors on behalf of ICRP
C.H. Kim,

PUBLISHED FOR
The International Commission on Radiological Protection

by

[SAGE logo]

Please cite this issue as 'ICRP, 20YY. Title of the annals. ICRP Publication XXX,
Ann. ICRP 00 (0).'

CONTENTS

Abstract	1
PREFACE	3
MAIN POINTS	4
GLOSSARY	5
1. INTRODUCTION	12
2. IMPROVEMENTS OF THE ADULT MESH-TYPE REFERENCE PHANTOMS OVER THE ADULT VOXEL-TYPE REFERENCE PHANTOMS	16
3. CONVERSION OF THE ADULT VOXEL-TYPE REFERENCE PHANTOMS TO MESH FORMAT	19
3.1. Simple organs and tissues	19
3.2. Skeletal system.....	21
3.3. Small intestine.....	22
3.4. Lymphatic nodes.....	22
3.5. Eyes.....	24
3.6. Blood in large vessels	24
3.7. Muscle.....	25
4. INCLUSION OF BLOOD TO ORGANS AND TISSUES.....	27
4.1. Calculation of mass, density, and elemental composition of organs and tissues inclusive of blood content.....	27
4.2. Phantom adjustment for blood inclusion	30
4.3. Definition of residual soft tissue (RST).....	33
5. INCLUSION OF THIN TARGET AND SOURCE REGIONS.....	34
5.1. Skin	34
5.2. Alimentary tract system	34
5.3. Respiratory tract system.....	35
5.4. Urinary bladder	37
6. DESCRIPTION OF THE ADULT MESH-TYPE REFERENCE PHANTOMS.....	39
6.1. General phantom characteristics	39
6.2. Geometric similarity comparison with the adult voxel-type reference phantoms	43
6.3. Compatibility with Monte Carlo codes.....	44
6.3.1. Monte Carlo codes	44
6.3.2. Computation time and memory usage	45
7. DOSIMETRIC IMPACT OF THE ADULT MESH-TYPE REFERENCE PHANTOMS	46
8. APPLICATION: CALCULATION OF DOSE COEFFICIENTS FOR INDUSTRIAL RADIOGRAPHY SOURCES	49
REFERENCES	53
ANNEX A. LIST OF ORGAN ID, MEDIUM, DENSITY AND MASS OF EACH ORGAN/TISSUE.....	57
ANNEX B. LIST OF MEDIA AND THEIR ELEMENTAL COMPOSITION	63
ANNEX C. LIST OF ANATOMICAL SOURCE REGIONS, ACRONYMS and ID NUMBERS	67
ANNEX D. LIST OF ANATOMICAL TARGET REGIONS, ACRONYMS AND ID NUMBERS	70
ANNEX E. ORGAN DEPTH DISTRIBUTIONS OF SELECTED ORGANS/TISSUES.....	72
ANNEX F. CHORD-LENGTH DISTRIBUTIONS BETWEEN SELECTED ORGAN PAIRS (SOURCE/TARGET TISSUES).....	86

ANNEX G.	CROSS-SECTIONAL IMAGES	92
G.1.	Images of the adult mesh-type reference computation phantom for male.....	92
G.1.1.	Transverse (axial) images	92
G.1.2.	Coronal and sagittal images	94
G.2.	Images of the adult mesh-type reference computational phantom for female.....	95
G.2.1.	Transverse (axial) images	95
G.2.2.	Coronal and sagittal images	97
ANNEX H.	COMPARISON OF DOSE COEFFICIENTS FOR EXTERNAL EXPOSURE	98
H.1.	Uncharged particles	98
H.2.	Charged particles	104
ANNEX I.	COMPARISON OF SPECIFIC ABSORBED FRACTIONS.....	110
ANNEX J.	DOSE COEFFICIENTS FOR INDUSTRIAL RADIOGRAPHY SOURCES	120
ANNEX K.	DESCRIPTION OF ELECTRONIC FILES	138

ADULT MESH-TYPE REFERENCE COMPUTATIONAL PHANTOMS

ICRP Publication XXX

Approved by the Commission in October 20YY

Abstract- Following the issuance of new radiological protection recommendations in *Publication 103* (ICRP, 2007), the Commission released, in *Publication 110* (ICRP, 2009), the adult male and female voxel-type reference computational phantoms to be used for the calculation of the reference dose coefficients for both external and internal exposures. While providing more anatomically realistic representations of internal anatomy than the older stylised phantoms, the voxel phantoms have their limitations, mainly due to voxel resolution, especially with respect to small tissue structures (e.g. lens of the eye) and very thin tissue layers (e.g. stem cell layers in the stomach wall mucosa and intestinal epithelium).

This report describes the construction of the adult mesh-type reference computational phantoms (MRCPs) that are the modelling counterparts of the *Publication 110* voxel-type reference computational phantoms. The MRCPs include all source and target regions needed for estimating effective dose, even the μm -thick target regions in the respiratory and alimentary tract, skin, and urinary bladder, thereby obviating the need for supplemental stylised models. The MRCPs can be directly implemented into Monte Carlo particle transport codes for dose calculations, i.e. without voxelisation, fully maintaining the advantages of the mesh geometry. Dose coefficients (DCs) of organ dose and effective dose and specific absorbed fractions (SAFs) calculated with the MRCPs for some external and internal exposures show that – while some differences were observed for small tissue structures and for weakly penetrating radiation – the MRCPs provide the same or very similar values as the previously published reference DCs and SAFs for most tissues and penetrating radiations; consequently, the DCs for effective dose, i.e. the fundamental protection quantity, were found not to be different. The DCs of *Publications 116* (ICRP, 2010) and the SAFs of *Publication 133* (ICRP, 2016) thus remain valid.

To demonstrate deformability of the MRCPs in this report, the phantoms were transformed to construct phantoms that represent the 10th and 90th percentiles of body height and weight for the Caucasian population. The constructed non-reference phantoms were then used to calculate DCs for industrial radiography sources near the body, which can be used to estimate organ doses of workers accidentally exposed by these sources, and which reflect the stature of the exposed worker. The MRCPs of this report were also transformed to phantoms that represent different postures (walking, sitting, bending, kneeling, and squatting), which were then used to evaluate variations in the DCs from the traditional up-right standing position.



42
43
44
45
46
47
48
49
50

© 20YY ICRP. Published by SAGE.

Keywords: Phantoms; polygon mesh; tetrahedral mesh; dose coefficients; internal and external exposures

AUTHORS ON BEHALF OF ICRP
C.H. KIM,

51

52

PREFACE

53

54 The membership of Task Group 103 on Mesh-type Reference Computational Phantoms
55 (MRCP) at the time of completion of this publication was:

56

C.H. Kim (Chair)	C. Lee	Y.S. Yeom
W. Bolch	N. Petoussi-Henss	M. Zankl

57

58 Corresponding members were:

59

C. Choi	M.C. Han	R. Qiu
B.S. Chung	H.S. Kim	
K. Eckerman	T.T. Nguyen	

60

61 The membership of Committee 2 during the period of preparation of this report was:

62

63 *(2013-2017)*

J.D. Harrison (Chair)	M. Degteva (~2016)	M.A. Lopez (2017~)
F. Paquet (Vice-Chair)	A. Endo (~2016)	J. Ma (~2016)
M.R. Bailey (~2016)	A. Giussani (2017~)	D. Nosske (~2016)
V. Berkovskyy	J.G. Hunt (~2016)	N. Petoussi-Henss
L. Bertelli	D. Jokisch (2017~)	T. Smith (2017~)
E. Blanchardon (2017~)	C.H. Kim	A. Ulanowski (2017~)
W.E. Bolch (Secretary)	R. Leggett	F. Wissmann
D. Chambers (~2016)	J. Li (2017~)	

72

73

74

MAIN POINTS

- 75 • This document presents mesh-type reference computational phantoms (MRCPs)
76 representing the Reference Adult Male and Reference Adult Female, which are the
77 counterparts of the voxel-type reference computational phantoms of *Publication 110*
78 (ICRP, 2009) developed from segmented computed tomographic data of real persons.
- 79 • The adult MRCPs were constructed by converting the voxel-type *Publication 110*
80 reference phantoms to a high-quality mesh format and adding those tissue layers that
81 are considered to contain the cells at radiogenic cancer risk, which were below the
82 image resolution of the voxel phantoms and could therefore not be represented
83 previously.
- 84 • The MRCPs include all the source and target organs/tissues required for the
85 calculation of effective dose, including the μm -thick target layers of the alimentary
86 and respiratory tract organs, skin and urinary bladder, thereby obviating the need
87 for supplemental stylised models (e.g. respiratory airways, alimentary tract organ
88 walls and stem cell layers, lens of the eye and skin basal layer).
- 89 • The organ/tissue masses of the MRCPs are in agreement with *Publications 89* (ICRP,
90 2002) and are given as *in situ* values i.e. organ/tissue with blood content. Small
91 differences exist between the organ/tissue masses of the voxel-type reference
92 phantoms (given in Annex A of *Publication 110*) and those of the MRCPs described
93 in this report, as the latter now include the in-situ blood content of each organ/tissue.
- 94 • To investigate the impact of the MRCPs, the dose coefficients (DCs) of organ dose
95 and effective dose and specific absorbed fractions (SAFs) for some selected external
96 and internal exposures were calculated and compared with the reference values of
97 *Publications 116* and *133* (ICRP, 2010, 2016) calculated using the *Publication 110*
98 phantoms and supplemental stylised models (ICRP, 1994a, 2006, 2016). While some
99 differences in the DCs and SAFs were observed for small tissue structures and weakly
100 penetrating radiations, the values of the effective dose, the quantity of most relevance
101 in radiation protection, and the DCs and SAFs of most of the organs considered in
102 the computation of the effective dose, were found not to be different. Therefore, the
103 DCs of *Publications 116* (ICRP, 2010) and the SAFs of *Publication 133* (ICRP, 2016)
104 remain valid.
- 105 • The MRCPs were modified to construct additional (standing) phantoms representing
106 individuals of the 10th and 90th body height/weight percentile of Caucasian adult
107 males and adult females. In addition, non-standing phantoms (i.e. with different
108 postures of the reference size) were created. These modified phantoms were used to
109 calculate DCs for exposures to industrial radiography sources, reflecting different
110 statures or postures, which can be used to estimate the organ/tissue doses of a worker
111 accidentally exposed to these radiation sources.
- 112 • The phantom data in the PM and TM formats, as well as examples of input files for
113 the Monte Carlo codes (Geant4, MCNP6 and PHITS), are included in the
114 supplementary electronic data that accompany the printed document.

115

116

GLOSSARY

117

118

119 Absorbed dose, D

120 The absorbed dose is given by:

121
$$D = \frac{d\bar{\epsilon}}{dm}$$

122 where $d\bar{\epsilon}$ is the mean energy imparted by ionising radiation to matter of mass dm . The
 123 SI unit of absorbed dose is joule per kilogramme (J kg^{-1}), and its special name is gray
 124 (Gy).

125 Absorbed fraction, AF, $\phi(r_T \leftarrow r_S, E_{R,i})$

126 Fraction of energy $E_{R,i}$ of the i^{th} radiation of type R emitted within the source region r_S
 127 that is absorbed in the target region r_T . These target regions may be tissues (e.g. liver)
 128 or may be cell layers within organs (e.g. stem cells of the stomach wall) (see definitions
 129 for ‘Target region’ and ‘Target tissue’).

130 Active (bone) marrow

131 Active marrow is haematopoietically active and gets its red colour from the large
 132 numbers of erythrocytes (red blood cells) being produced. Active bone marrow serves
 133 as a target region for radiogenic risk of leukaemia.

134 Activity

135 The number of nuclear transformations of a radioactive material during an infinitesimal
 136 time interval, divided by its duration (s). The SI unit of activity is s^{-1} and its special
 137 name is becquerel (Bq).

138 Bone marrow [see also ‘Active (bone) marrow’ and ‘Inactive (bone) marrow’]

139 Bone marrow is a soft, highly cellular tissue that occupies the cylindrical cavities of
 140 long bones and the cavities defined by the bone trabeculae of the axial and appendicular
 141 skeleton. Total bone marrow consists of a sponge-like, reticular, connective tissue
 142 framework called ‘stroma’, myeloid (blood-cell-forming) tissue, fat cells (adipocytes),
 143 small accumulations of lymphatic tissue and numerous blood vessels and sinusoids.
 144 There are two types of bone marrow: active (red) and inactive (yellow), where these
 145 adjectives refer to the marrow’s potential for the production of blood cell elements
 146 (haematopoiesis).

147 Charged-particle equilibrium

148 Charged-particle equilibrium in a volume of interest means that the energies, numbers,
 149 and directions of the charged particles are constant throughout this volume. This is
 150 equivalent to saying that the distribution of charged-particle energy radiance does not
 151 vary within the volume. In particular, it follows that the sums of the energies (excluding
 152 rest energies) of the charged particles entering and leaving the volume are equal.

153 Cortical (bone) marrow

154 The marrow contained in the medullary cavities in the shafts of the long bones.

155 Cross section, σ

156 The cross section of a target entity, for a particular interaction produced by incident
157 charged or uncharged particles of a given type and energy, is given by:

158
$$\sigma = \frac{N}{\Phi}$$

159 where N is the mean number of such interactions per target entity subjected to the
160 particle fluence, Φ . The unit of cross section is m^2 . A special unit often used for the
161 cross section is the barn, where 1 barn (b) = 10^{-28}m^2 . A full description of an interaction
162 process requires, ‘inter alia’, knowledge of the distributions of cross sections in terms
163 of energy and direction of all emergent particles from the interaction. Such
164 distributions, sometimes called ‘differential cross sections’, are obtained by
165 differentiations of r with respect to energy and solid angle.

166 Dose coefficient

167 A coefficient relates a dose quantity to a physical quantity, both for internal and external
168 radiation exposure. For external exposure, the physical quantity ‘fluence’ or ‘air kerma’
169 is chosen. In internal dosimetry, a dose coefficient is defined as either the committed
170 equivalent dose in tissue T per activity intake, $h_T(50)$, or the committed effective dose
171 per activity intake, $e(50)$, where 50 is the dose-commitment period in years over which
172 the dose is calculated. Note that elsewhere, the term ‘dose per intake coefficient’ is
173 sometimes used for dose coefficient.

174 Dose equivalent, H

175 The product of D and Q at a point in tissue, where D is the absorbed dose and Q is the
176 quality factor for the specific radiation at this point, thus:

177
$$H = DQ$$

178 The unit of dose equivalent is joule per kilogramme (J kg^{-1}), and its special name is
179 sievert (Sv).

180 Dose–response function (DRF)

181 A particular function used in this publication to represent the absorbed dose in a target
182 region per particle fluence in that region, derived using models of the microscopic
183 structure of the target region geometry and the transport of the secondary ionising
184 radiations in those regions.

185 Effective dose, E

186 The tissue-weighted sum of equivalent doses in all specified organs and tissues of the
187 body, given by the expression:

188
$$E = \sum_{\text{T}} w_{\text{T}} \sum_{\text{R}} w_{\text{R}} D_{\text{T,R}} = \sum_{\text{T}} w_{\text{T}} H_{\text{T}}$$

189 where H_{T} is the equivalent dose in an organ or tissue T , $D_{\text{T,R}}$ is the mean absorbed dose
190 in an organ or tissue T from radiation of type R , and w_{T} is the tissue weighting factor.

191 The sum is performed over organs and tissues considered to be sensitive to the
 192 induction of stochastic effects. The unit of effective dose is joule per kilogramme (J kg⁻¹), and its special name is sievert (Sv).
 193

194 Endosteum (or endosteal layer)

195 A 50-µm-thick layer covering the surfaces of the bone trabeculae in regions of
 196 trabecular spongiosa and those of the cortical surfaces of the medullary cavities within
 197 the shafts of all long bones. It is assumed to be the target tissue for radiogenic bone
 198 cancer. This target region replaces that previously introduced in ICRP *Publications 26*
 199 and *30* (ICRP, 1977, 1979) – the bone surfaces – which had been defined as a single-
 200 cell layer, 10 µm in thickness, covering the surfaces of both the bone trabeculae and
 201 the Haversian canals of cortical bone.

202 Equivalent dose, H_T

203 The equivalent dose in an organ or tissue T is given by:

204
$$H_T = \sum_R w_R D_{T,R}$$

205 where $D_{T,R}$ is the mean absorbed dose from radiation of type R in the specified organ
 206 or tissue T, and w_R is the radiation weighting factor. The unit of equivalent dose is joule
 207 per kilogramme (J kg⁻¹), and its special name is sievert (Sv).

208 Fluence, Φ

209 The quotient of dN by da , where dN is the number of particles incident on a sphere of
 210 cross-sectional area da , thus:

211
$$\Phi = \frac{dN}{da}$$

212 The unit of fluence is m⁻².

213 Identification (ID) number

214 Number assigned unequivocally to each individually segmented organ/tissue.

215 Inactive (bone) marrow

216 In contrast to the active marrow, the inactive marrow is haematopoietically inactive,
 217 i.e. does not directly support haematopoiesis. It gets its yellow colour from fat cells,
 218 which occupy most of the space of the yellow bone marrow framework.

219 Intake, I

220 Activity that enters the body through the respiratory tract or the gastrointestinal tract or
 221 the skin.

222 – Acute intake

223 A single intake by inhalation or ingestion, taken to occur instantaneously.

224 – Chronic intake

225 An intake over a specified period of time.

226 LET

227 See ‘Linear energy transfer’.

228 Linear energy transfer/unrestricted linear energy transfer, L or LET

229 The quotient of dE by dl , where dE is the mean energy lost by the charged particle due
230 to electronic interactions in traversing a distance dl , thus:

231
$$L = \frac{dE}{dl}$$

232 The unit of linear energy transfer is joule per metre ($J m^{-1}$), often given in $keV/\mu m$.

233 Mean absorbed dose in an organ or tissue, D_T

234 The mean absorbed dose in a specified organ or tissue T , is given by:

235
$$D_T = \frac{1}{m_T} \int_{m_T} D dm$$

236 where m_T is the mass of the organ or tissue, and D is the absorbed dose in the mass
237 element dm . The unit of mean absorbed dose is joule per kilogramme ($J kg^{-1}$), and its
238 special name is gray (Gy). The mean absorbed dose in an organ is sometimes termed
239 ‘organ dose’.

240 Mesh phantom

241 Computational anthropomorphic phantom whose anatomy is represented by either the
242 polygon mesh format or the tetrahedral mesh format.

243 NURBS

244 NURBS, Non-Uniform Rational B-Spline, represents 3D surface geometry by
245 mathematical curves defined by four parameters: degree, control points, knots and an
246 evaluation rule. NURBS-based models are widely used in computer-aided design
247 (CAD), manufacturing (CAM) and engineering (CAE) and other various 3D modelling
248 and animation applications.

249 Organ absorbed dose or organ dose

250 Short phrase for ‘mean absorbed dose in an organ or tissue’.

251 Polygon mesh

252 Polygon mesh represents 3D surface geometry composed of polygonal facets (such as
253 triangles), and is one of the geometry formats of a mesh phantom (see ‘Mesh
254 phantom’).

255 Radiation weighting factor, w_R

256 A dimensionless factor by which the organ or tissue absorbed dose is multiplied to
257 reflect the higher biological effectiveness of high-LET radiation compared with low-
258 LET radiation. It is used to derive the equivalent dose from the absorbed dose averaged
259 over a tissue or organ.

- 260 Red (bone) marrow
261 See 'Active (bone) marrow'.
- 262 Reference Male and Reference Female
263 Reference males and females are defined as either adults or children of ages 0, 1, 5, 10
264 and 15 years.
- 265 Reference Person
266 An idealised person for whom the equivalent doses to organs and tissues are calculated
267 by averaging the corresponding organ doses in the Reference Male and Reference
268 Female. The equivalent doses of Reference Person are used for the calculation of
269 effective dose.
- 270 Reference phantom
271 The computational phantom of the human body (male or female voxel phantom based
272 on medical imaging data), defined in *Publication 110* (ICRP, 2009), with the
273 anatomical and physiological characteristics of the Reference Male and Reference
274 Female defined in *Publication 89* (ICRP, 2002).
- 275 Reference value
276 Value of a quantity recommended by ICRP for use in dosimetric applications or
277 biokinetic models. Reference values are fixed and specified with no uncertainty,
278 independent of the fact that the basis of these values includes many uncertainties.
- 279 Sievert (Sv)
280 The special name for the SI unit of equivalent dose, effective dose and operational dose
281 quantities. The unit is joule per kilogramme (J kg^{-1}).
- 282 Source
283 An entity for which radiological protection can be optimised as an integral whole, such
284 as the x-ray equipment in a hospital, or the release of radioactive material from an
285 installation. Sources of radiation, such as radiation generators and sealed radioactive
286 materials, and, more generally, the cause of exposure to radiation or to radionuclides.
- 287 Source region, S_i
288 An anatomical region within the reference phantom body which contains the
289 radionuclide following its intake. The region may be an organ, a tissue, the contents of
290 the gastrointestinal tract or urinary bladder, or the surfaces of tissues as in the skeleton,
291 the alimentary tract and the respiratory tract.
- 292 Specific absorbed fraction (*SAF*)
293 The fraction of energy of that emitted as a specified radiation type in a source region,
294 S , that is absorbed per mass of target tissue, T (kg^{-1}).
- 295 Spongiosa

296 Term referring to the combined tissues of the bone trabeculae and marrow tissues (both
 297 active and inactive) located within cortical bone cortices across regions of the axial and
 298 appendicular skeleton. Spongiosa is one of three bone regions defined in the ICRP
 299 *Publication 110* reference phantoms (ICRP, 2009), the other two being cortical bone
 300 and medullary marrow of the long bone shafts. As the relative proportions of trabecular
 301 bone, active marrow and inactive marrow vary with skeletal site, the homogeneous
 302 elemental composition and mass density of spongiosa are not constant but varies with
 303 skeletal site [see Annex B of ICRP *Publication 110* (ICRP, 2009)].

304 Stem cell

305 Non-differentiated, pluripotent cell, capable of unlimited cell division.

306 Stochastic effects of radiation

307 Malignant disease and heritable effects for which the probability of an effect occurring,
 308 but not its severity, is regarded as a function of dose without threshold.

309 Target region, r_T

310 A tissue region of the body in which a radiation absorbed dose or equivalent dose is
 311 received.

312 Target tissue, T

313 Organ or tissue in the body for which tissue weighting factors are assigned in the
 314 effective dose (ICRP, 1991a, 2007). In many cases, each target tissue T corresponds to
 315 a single target region r_T . In the case of the extrathoracic region, lungs, colon and
 316 lymphatic nodes, however, a fractional weighting of more than one target region r_T
 317 defines the target tissue T (ICRP, 1991a, 2007).

318 Tetrahedral mesh

319 Tetrahedral mesh represents 3D geometry composed of tetrahedrons, which is one of
 320 the geometry formats of a mesh phantom (see ‘Mesh phantom’). Tetrahedral mesh can
 321 be generated by subdividing polygon mesh (see ‘Polygon mesh’) with tetrahedrons.

322 Tissue reaction

323 Injury in populations of cells, characterised by a threshold dose and an increase in the
 324 severity of the reaction as the dose is increased further. Also termed ‘deterministic
 325 effect’. In some cases, these effects are modifiable by postirradiation procedures
 326 including biological response modifiers.

327 Tissue weighting factor, w_T

328 The factor by which the equivalent dose in an organ or tissue T is weighted to represent
 329 the relative contribution of that organ or tissue to overall radiation detriment from
 330 stochastic effects (ICRP, 1991a, 2007). It is defined such that:

331
$$\sum_T w_T = 1 .$$

332 Trabecular (bone) marrow

333 The marrow contained in the spongiosa regions of all bones.

334 Voxel phantom

335 Computational anthropomorphic phantom based on medical tomographic images or
336 photographic images of a cadaver in which the anatomy is described by small three-
337 dimensional volume elements (voxels) specifying the organ or tissue to which they
338 belong.

339 Yellow (bone) marrow

340 See 'Inactive (bone) marrow'.

341

342

1. INTRODUCTION

343 (1) Implementing a system of radiological protection requires the assessment of doses from
344 radiation exposures of individuals, including workers and members of the general public. The
345 protection quantities are used in the control of radiation exposures, to ensure that the occurrence
346 of stochastic health effects is kept below acceptable levels and that tissue reactions are avoided.

347 (2) The effective dose (E), in units of sievert (Sv), is accepted internationally as the central
348 radiological protection quantity, providing a risk-adjusted measure of dose delivered to the
349 human body from both external and internal radiation sources. E has proved to be a valuable
350 and robust quantity for use in the optimisation of protection, for the setting of control criteria
351 (limits, constraints and reference levels), and for the demonstration of regulatory compliance.
352 E is calculated for sex-averaged Reference Persons of specified ages, by estimating their organ
353 absorbed doses and applying both radiation and tissue weighting factors (ICRP, 2007).

354 (3) Absorbed dose (D), in units of gray (Gy), averaged over a specified organ and tissue is
355 the physical quantity from which E is calculated. Equivalent dose (H) to organs and tissues is
356 obtained by multiplying the absorbed dose by radiation weighting factors (w_R) to account for
357 the relative effectiveness of different radiation types in causing stochastic effects at low levels
358 of exposure. Nominal stochastic risk coefficients and corresponding detriment values, to which
359 E relates, are calculated as averages from sex-, age-, and population-specific values, to provide
360 internationally applicable values for all workers (18–65y) and for the whole population (all
361 ages). Tissue-weighting factors (w_T) used in the calculation of effective dose are a simplified
362 representation of relative detriment values, relating to detriment for the whole population (sex,
363 age and population averaged).

364 (4) The estimation of organ absorbed doses requires, among other tools, computational
365 anatomical phantoms (or models). A computational anatomical phantom is a 3D computerised
366 representation of the human anatomy, with definitions of both internal organs and outer body
367 surfaces.

368 (5) Until the mid-2000s, the ICRP relied on the use of so-called stylised or mathematical
369 models of organ anatomy, such as those developed at the Oak Ridge National Laboratory
370 (ORNL) (Snyder et al., 1969, 1978; Cristy, 1980; Cristy and Eckerman, 1987) and by the
371 Medical Internal Radiation Dose (MIRD) Committee of the Society of Nuclear Medicine. Body
372 and organ surfaces are defined in these stylised phantoms using geometrical 3D surface
373 equations such as spheres, cones, ellipsoids, and toroids. These models are generally
374 hermaphrodites with both male and female sex organs included. As an improvement to these
375 early stylised models, “Adam” and “Eva”, separate male and female adult mathematical
376 phantoms, were introduced (Kramer et al., 1982). Subsequently, four models representing the
377 non-pregnant adult female and the pregnant female at 3 stages of pregnancy were developed
378 by Stabin et al. (1995). All of the above phantoms were employed for the estimation of
379 reference dose coefficients (DCs) and specific absorbed fractions (SAFs) issued by ICRP for
380 internal and external exposures, as given in *Publications 30, 53, 56, 60, 61, 66, 67, 68, 69, 71,*
381 *72, 74, 80 and 100* (ICRP, 1979, 1988, 1990, 1991a, 1991b, 1994a, 1993, 1994b, 1995a, b,
382 1996a, b, 1998, 2006).

383 (6) The most recent recommendations by ICRP were published in 2007 in *Publication 103*
384 (ICRP, 2007). In that document, the Commission includes the specifications of separate
385 reference male and female anatomical models to be used together with radiation transport codes
386 that simulate the radiation transport and energy deposition for the assessment of the mean

387 absorbed dose, D_T , in specified target organs or tissues T , from which equivalent doses and the
388 effective dose can be successively calculated.

389 (7) Consequently, the Commission released new computational phantoms of ICRP reference
390 adult male and reference adult female in *Publication 110* (ICRP, 2009). These reference
391 computational phantoms are based on human computed tomographic data. They are consistent
392 with the information given in *Publication 89* (ICRP, 2002) on the reference anatomical
393 parameters for both the reference adult male and female.

394 (8) The reference computational phantoms (or models) were constructed by modifying the
395 voxel models (Zankl and Wittmann, 2001; Zankl et al., 2005) of two individuals (Golem and
396 Laura) whose body height and mass closely resembled the reference data. The organ masses of
397 both phantoms were adjusted to the ICRP data without significantly altering their realistic
398 anatomy. The phantoms contain all target regions relevant to the assessment of human exposure
399 to ionising radiation for radiological protection purposes (ICRP, 2007), with the exception of
400 certain very thin target tissues located within the alimentary and respiratory tracts. Each
401 phantom is represented in the form of a 3D array of cuboidal voxels. Each voxel is a volume
402 element, and the voxels are arranged in columns, rows, and slices. Each entry in the array
403 identifies the organ or tissue to which the corresponding voxel belongs. The male reference
404 computational phantom consists of approximately 1.95 million tissue voxels (excluding voxels
405 representing the surrounding vacuum), each with a slice thickness (corresponding to the voxel
406 height) of 8.0 mm and an in-plane resolution (i.e. voxel width and depth) of 2.137 mm,
407 corresponding to a voxel volume of 36.54 mm³. The number of slices is 220, resulting in a
408 body height of 1.76 m; the body mass is 73 kg. The female reference computational phantom
409 consists of approximately 3.89 million tissue voxels, each with a slice thickness of 4.84 mm
410 and an in-plane resolution of 1.775 mm, corresponding to a voxel volume of 15.25 mm³. The
411 number of slices is 346, and the body height is 1.63 m; the body mass is 60 kg. The number of
412 individually segmented structures is 136 in each phantom, to which 53 different tissue
413 compositions have been assigned. The various tissue compositions reflect both the elemental
414 composition of the tissue parenchyma (ICRU, 1992) and each organ's blood content (ICRP,
415 2002) (i.e. organ composition inclusive of blood).

416 (9) While providing more anatomically realistic representations of internal anatomy than the
417 older stylised phantoms, voxel phantoms have their limitations mainly due to image resolution,
418 especially with respect to small tissue structures (e.g. lens of the eye) and very thin tissue layers
419 (e.g. stem cell layers in the stomach wall mucosa and intestinal epithelium). The in-plane
420 resolution of modern CT scanners is generally 0.5 mm or better. However, the Z dimension of
421 the phantom voxels corresponding to the image slice thickness can be a few to several mm for
422 typical clinical protocols (Bolch et al., 2010). Images with higher in-plane resolution would be
423 difficult to obtain, since significant absorbed doses would be given to the patient or volunteer.

424 (10) The voxel-based reference computational phantoms have been used to estimate the
425 reference DCs for external radiation exposures of *Publication 116* (ICRP, 2010), the SAFs of
426 *Publication 133* (ICRP, 2016) and for the series of reports on occupational intakes of
427 radionuclides (ICRP, 2015, 2017a, b). Calculations for DCs due to ingestion and inhalation
428 from members of the public are in progress. For these calculations, supplemental organ-specific
429 stylised models were employed for estimating internal electron and alpha particle SAFs for thin
430 tissue layers to replace those computed directly in the computational reference voxel phantoms.
431 Similarly, for some selected external exposures, separate simulations were made to determine
432 the absorbed dose to the eye lens and to local regions of the skin (ICRP, 2010).

433 (11) In order to overcome the limitations of the voxel-type ICRP reference phantoms related
434 to their resolution, to avoid the use of supplementary phantoms, and to provide all-in-one
435 anatomical computational phantoms, ICRP formed the Task Group 103 - Mesh-type Reference
436 Computational Phantoms. The aim of this Task Group was to provide a new generation of
437 ICRP reference computational phantoms, constructed by converting the voxel-type ICRP
438 reference phantoms to a high-quality mesh format to include thin target and source regions,
439 even the 8–40- μm -thick target layers of the alimentary and respiratory tract.

440 (12) It is noted that these mesh-type computational phantoms, represented by either polygon
441 mesh (PM) or tetrahedral mesh (TM) geometry as necessary, are considered presently as the
442 most advanced type of computational phantoms, in that they can be directly implemented into
443 Monte Carlo codes, i.e. without the conventionally used ‘voxelisation’ process, thus fully
444 maintaining the advantages of the mesh geometry in Monte Carlo dose calculations (Kim et
445 al., 2011; Yeom et al., 2013, 2014; Han et al., 2015). Note that the tetrahedral mesh (TM)
446 geometry is available in Geant4 and MCNP since 2013 and in PHITS since 2015.

447 (13) This report describes (1) the conversion of the voxelised ICRP adult reference
448 computational phantoms to their mesh-format counterparts; (2) the simulation of several
449 additional tissues such as target cell layers defined by ICRP for the respiratory and alimentary
450 tract, urinary bladder, skin, eye and lymph nodes, and their inclusion in the phantoms; (3)
451 investigates the impact of the newly developed phantoms for the determination of DCs within
452 the ICRP system; and (4) discusses further applications.

453 (14) The new mesh-type ICRP reference phantoms preserve the original topology of the voxel-
454 type ICRP reference phantoms, present substantial improvements in the anatomy of small
455 tissues, and include all of the necessary source and target tissues defined by the Commission,
456 thereby obviating the need for supplemental stylised models such as those defined for
457 respiratory tract airways, the alimentary tract organ walls and stem cell layers, the lens of the
458 eye and the skin basal layer. In the mesh phantoms, the skeletal target tissues (red bone marrow
459 and endosteum) are not explicitly represented, but implicitly included in the spongiosa and
460 medullary cavity in the same manner as provided in the *Publication 110* phantoms). Doses to
461 these skeletal tissues can be estimated by using dedicated skeletal-dose-calculation methods
462 (e.g. fluence-to-dose response functions) such as those given in Annex E and F of in
463 *Publication 116* (ICRP, 2010).

464 (15) In general, it can be stated that the mesh-type reference phantoms provide effective dose
465 DCs very similar to those of the voxel-type ICRP reference phantoms for penetrating radiations
466 and, at the same time, more accurate DCs for weakly penetrating radiations.

467 (16) In addition to the greater anatomical accuracy of the mesh-type phantoms, they are
468 deformable and, as such, can serve as a starting point to create phantoms of various statures
469 and postures for use, for example, in retrospective emergency or accidental dose reconstruction
470 calculations. These non-reference versions may be useful to calculate organ doses for purposes
471 other than calculating effective dose. To demonstrate this feature, the MRCPs in this report
472 were modified via various scaling/deforming procedures to construct (standing) phantoms
473 which represent the 10th and 90th body height/weight percentiles of the adult male and female
474 Caucasian populations. Furthermore, they were also used to create non-standing phantoms (i.e.
475 with different postures of the reference size). The constructed phantoms were then used to
476 calculate DCs for exposures to industrial radiography sources near the body, reflecting different
477 statures or postures, which can be used to estimate the organ/tissue doses to workers
478 accidentally exposed to these radionuclide sources.

479 (17)The new phantoms have applications beyond the calculation of reference DCs. For
480 example, the deformation capability of the phantoms can facilitate the virtual calibration of
481 whole body counters to account for the stature of radiation workers in efficiency calibration.
482 The new phantoms are in mesh format and therefore can be directly used to produce physical
483 phantoms, as necessary, with 3D printing technology. It is relatively easy to model detailed
484 structures in the phantoms and, therefore, the new phantoms could find applications in
485 medicine and other areas requiring sophisticated organ models. One of the aims of this report
486 is to assist those who wish to implement the phantoms for their own applications; therefore,
487 the detailed data on the phantoms in both polygonal mesh and tetrahedral mesh formats are
488 provided in the supplementary electronic data that accompany the printed publication, together
489 with some input examples of the Monte Carlo codes.

490 (18)Chapter 1 explains the main motives for the construction of the adult mesh-type reference
491 computational phantoms. Chapter 2 focuses on those tissues of the reference computational
492 phantoms of *Publication 110* for which the anatomical description has been significantly
493 improved in the mesh-type formats. Chapter 3 describes the general procedure for the
494 conversion of the *Publication 110* phantoms to the mesh format. Chapter 4 describes the
495 adjustment of the converted MRCPs to the reference values for the mass, density and elemental
496 composition of organs and tissues inclusive of blood content. Chapter 5 describes the inclusion
497 of the thin target and source regions of the skin, alimentary tract system, respiratory tract
498 system, and the urinary bladder in the MRCPs. Chapter 6 describes the general characteristics
499 of the resulting mesh-type reference computational phantoms. Chapter 7 investigates the
500 impact of the improved internal morphology of the MRCPs on the calculation of DCs for
501 external and internal exposures. Finally, Chapter 8 describes an application to the calculation
502 of DCs for industrial radiography exposures in order to demonstrate the capability of the
503 MRCPs in calculation of DCs for accidental or emergency exposure scenarios.

504 (19)A detailed description of the MRCPs is given in Annexes A–F. Annex A presents a list
505 of the individual organs/structures (identification list), together with the assigned media,
506 densities and masses. Annex B presents a list of the phantom media and their elemental
507 compositions. Annexes C and D list the source and target regions, respectively, together with
508 their acronyms and identification numbers. Annex E provides depth distributions for selected
509 organs from the front, back, left, right, top and bottom, along with the respective data of the
510 *Publication 110* phantoms. Annex F provides chord-length distributions between selected pairs
511 of source and target organs, along with the data of the *Publication 110* phantoms.

512 (20)Annex G presents selected transverse, sagittal, and coronal slice images of the mesh-type
513 reference phantoms.

514 (21)In Annexes H and I, the DCs and SAFs calculated with the MRCPs for some selected
515 idealised external and internal exposure cases are compared with the reference values of
516 *Publications 116* and *133* (ICRP, 2010, 2016). Annex H shows comparisons of the organ and
517 effective dose DCs, calculated for external exposure to photons, neutrons, electrons and helium
518 ions, with the *Publication 116* values. Annex I compares the SAFs for photons and electrons
519 with the *Publication 133* values.

520 (22)Annex J presents the DCs for industrial radiography sources calculated with the MRCPs
521 as well as the stature-specific phantoms that were constructed by modifying the MRCPs.

522 (23)Annex K describes the contents of the supplementary electronic data that accompanies
523 the printed publication including the detailed phantom data and the input examples of some
524 Monte Carlo codes.

525

526 **2. IMPROVEMENTS OF THE ADULT MESH-TYPE REFERENCE**
527 **PHANTOMS OVER THE ADULT VOXEL-TYPE REFERENCE**
528 **PHANTOMS**

529 (24)The adult voxel-type reference computational phantoms described in *Publication 110*
530 (ICRP, 2009) were adopted by ICRP and the International Commission on Radiation Units and
531 Measurements (ICRU) as the phantoms for computation of the ICRP/ICRU reference dose
532 coefficients (DCs) for radiological protection purposes. These computational phantoms are
533 digital 3D representations of the human anatomy, constructed using computed tomographic
534 (CT) images of real persons. The phantoms are consistent with the information given in
535 *Publication 89* (ICRP, 2002) on the reference anatomical parameters of the Reference Adult
536 Male and Reference Adult Female. The *Publication 110* phantoms are shown below in Fig.
537 2.1.

538 (25)While providing more anatomically realistic representations of internal anatomy than the
539 older type of stylised phantoms, the adult voxel-type reference phantoms have limitations due
540 to their voxel resolution, and hence some organs and tissues could not be explicitly represented
541 or could not be adjusted to their reference mass due to their small dimensions or complex
542 anatomic structure. This fact was already discussed in *Publication 110* (ICRP, 2009). In an
543 attempt to address the limitations of the voxel-type reference phantoms related to the image
544 resolution, further improvements in representing those organs and tissues were made in the
545 adult mesh-type reference computational phantoms (MRCPs) described in the present
546 publication. These improvements are summarised in the following paragraphs.

547 (26) The skin of the voxel-type reference phantoms is represented by a single voxel layer,
548 considering only transverse directions, resulting in the skin being discontinuous between
549 individual transverse slices, while at the same time the total skin mass of the phantoms is 13 %
550 and 18 % higher than the reference values for the adult male and female, respectively. Through
551 the discontinuous parts of the skin, radiation incident at non-zero angles of incidence relative
552 to the transverse slices can directly reach internal organs or tissues (e.g. breasts, testes and
553 salivary glands) without first penetrating the skin layer. This might lead to an overestimation
554 of DCs for weakly penetrating radiations incident at angles that are not perpendicular to the
555 body length axis. The mesh-type reference phantoms, in contrast, are fully wrapped by the skin
556 whose total mass is in accordance with the reference value. Note that also other organs and
557 tissues having thin tissue structures (such as gastrointestinal (GI) tract organs and cortical bone)
558 are discontinuous in the voxel-type reference phantoms, an issue which is fully resolved within
559 the mesh-type reference phantoms.

560 (27)The small intestine of the voxel-type reference phantoms, in addition to showing
561 discontinuous parts, does not precisely represent its complex tubular structure. Therefore, high-
562 quality small-intestine models were incorporated into the mesh-type reference phantoms,
563 whereby models were generated by using a dedicated procedure based on a Monte Carlo
564 sampling approach (Yeom et al., 2016a). Similarly, high-quality detailed models of the spine
565 (cervical, thoracic and lumbar) and hand and foot bones were incorporated into the mesh-type
566 reference phantoms (Yeom et al., 2016b).

567 (28)The lymphatic nodes of the voxel-type reference phantoms were manually drawn at
568 locations specified in anatomical textbooks (Brash and Jamieson, 1943; Möller and Reif, 1993,
569 1997; GEO kompakt, 2005), because they could not be identified on the original CT images.
570 Although the higher concentration at specific locations (e.g. groin, axillae, the hollows of the
571 knees, crooks of the arms) described in the textbooks was correctly incorporated into the

572 *Publication 110* phantoms, site-specific numbers of the lymphatic nodes presented in
573 *Publication 89* (ICRP, 2002) were not considered. In the mesh-type reference phantoms,
574 lymphatic nodes were regenerated by a modelling approach used for the UF/NCI family of
575 phantoms (Lee et al., 2013) based on the lymphatic node data derived from the data of
576 *Publications 23, 66 and 89* (ICRP, 1975, 1994a, 2002) (see Chapter 3.4).

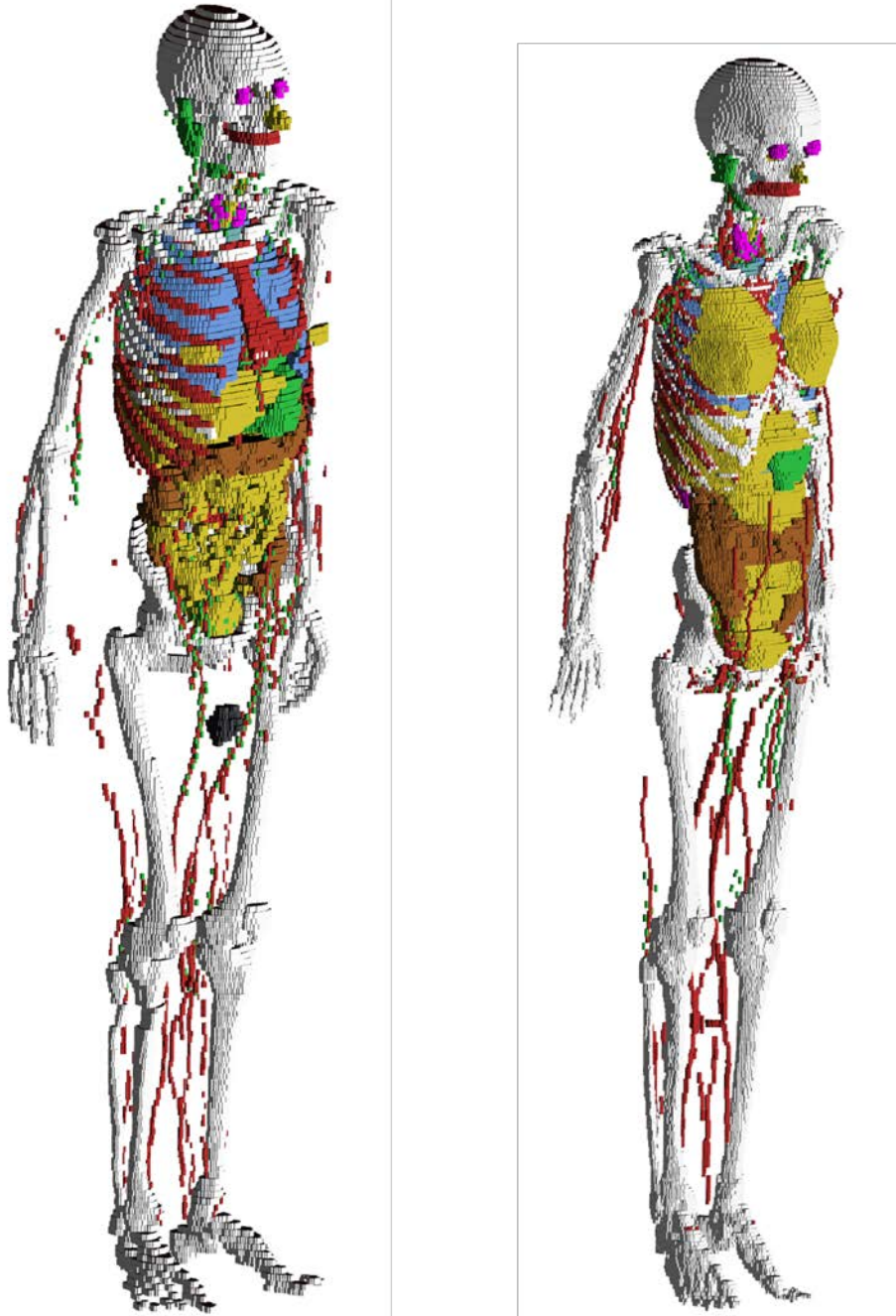
577 (29) The complex structure of the eye also could not be precisely represented in the voxel-
578 type reference phantoms due to the image resolution. Therefore, the detailed eye model of
579 Behrens et al. (2009) was adopted in *Publication 116* (ICRP, 2010), and the *Publication 116*
580 lens DCs were calculated using either the voxel-type reference phantoms or the adopted eye
581 model, depending on radiation type, energy, and irradiation geometry. In order to be able to
582 compute the absorbed dose to the eye lens using only one anthropomorphic phantom for each
583 sex, the detailed eye model of Behrens et al. (2009) was directly incorporated into the mesh-
584 type reference phantoms (Nguyen et al., 2015).

585 (30) The Commission recommended that a range from 50–100 μm below the skin surface
586 should be considered as an appropriate depth for the basal cell layer of most body regions of
587 the skin (ICRP, 1977, 2010, 2015). The 50- μm -thick radiosensitive skin layer, however, cannot
588 be represented in the voxel-type reference phantoms, due to their limited voxel resolution. The
589 skin DCs of *Publication 116* (ICRP, 2010) for external exposures were thus calculated by
590 averaging the absorbed dose over the entire skin of the phantoms. This approximation is
591 acceptable for the calculation of effective doses for penetrating radiations, considering the
592 small tissue weighting factor of the skin ($w_T = 0.01$). However, for weakly penetrating
593 radiations, such as alpha and beta particles, this approximation leads to underestimations or
594 overestimations in skin target cell layer doses. In the skin of the mesh-type reference phantoms,
595 the 50- μm -thick radiosensitive target layer was defined explicitly.

596 (31) Similarly, the micrometre scales of radiosensitive tissues and source regions for
597 radionuclide retention of the respiratory and alimentary tract systems, as described in
598 *Publications 66 and 100* (ICRP, 1994a, 2006), could not be represented in the voxel-type
599 reference phantoms. Separate stylised models, describing the respiratory and alimentary tract
600 organs as mathematical shapes (e.g. a sphere or a right circular cylinder), were used for the
601 calculation of specific absorbed fractions (SAFs) for charged particles (ICRP, 1994a, 2006,
602 2016). In the mesh-type reference phantoms, the micrometre-thick target and source regions in
603 the alimentary and respiratory tract systems as described in *Publications 66 and 100* (ICRP,
604 1994a, 2006) were included (Kim et al., 2017). Realistic lung airway models that represent the
605 bronchial (BB) and bronchiolar (bb) regions were also developed and incorporated into the
606 mesh-type reference phantoms, whereas in the voxel-type reference phantoms the bronchi
607 could not be followed down to more than the very first generations of airway branching.
608 Furthermore, the bronchioles are too small to be represented in a voxel basis (ICRP, 2009).

609 (32) Previously, the organ and tissue masses of computational anthropomorphic phantoms
610 (Lee et al., 2007; ICRP, 2009; Yeom et al., 2013), were commonly adjusted to the reference
611 values listed in Table 2.8 of *Publication 89* (ICRP, 2002). However, these masses correspond
612 to the masses of organ/tissue parenchyma only, while the optimal phantom design would
613 provide organ volumes consistent with both the organ parenchyma and included blood
614 vasculature. In a living person, on the other hand, a large proportion of blood is distributed in
615 small vessels and capillaries within the organs and tissues, thus increasing slightly the organ
616 and tissue masses within the phantom body. In recognition of this circumstance, target
617 tissue/organ masses inclusive of blood were used to calculate the self-irradiation SAFs of
618 *Publication 133* (ICRP, 2016). To reflect this also in the new mesh-type reference phantoms,

619 the organ and tissue masses and tissue compositions of these phantoms were adjusted such as
 620 to include their organ blood content. The blood distribution among the organs and tissues was
 621 derived from the reference regional blood volume fractions given in *Publication 89* (ICRP,
 622 2002) using an approach similar to that outlined in *Publication 133* (ICRP, 2016).



623
 624 Fig. 2.1. The voxel-type reference phantoms of adult reference male (left) and adult reference female
 625 (right). The skin, muscle and adipose tissue are not displayed in this figure.

626
 627
 628
 629

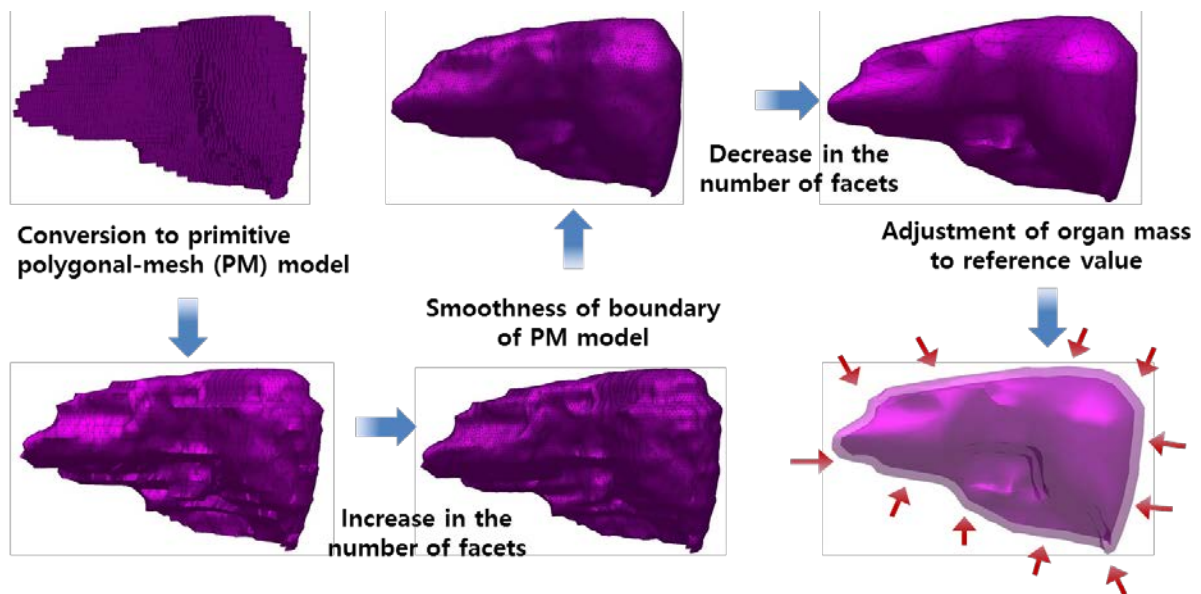
630
631

3. CONVERSION OF THE ADULT VOXEL-TYPE REFERENCE PHANTOMS TO MESH FORMAT

3.1. Simple organs and tissues

633 (33) Most of the organs and tissues in the mesh phantoms were constructed by directly
 634 converting the adult voxel-type reference phantoms to the polygon-mesh (PM) format via 3D
 635 surface rendering and subsequent refinement procedures. Figure 3.1 schematically describes
 636 the procedure. The voxel data of the phantoms were imported into *3D-DOCTOR™* (Able
 637 Software Corp., Lexington MA). The organs and tissues were then contoured using the
 638 *Interactive Segmentation* command of the software. The contoured lines were converted to
 639 primitive PM models using the *Surface Rendering* command. These primitive PM models,
 640 generally showing some stair-stepped surfaces with holes and defects, were refined into high-
 641 quality PM models by using the *Rapidform™* software (INUS Technology Inc., Korea). In
 642 order to minimise the distortion of the original shape during the refinement process, the number
 643 of facets was increased using the *Subdivide* command of *Rapidform™* software. The PM
 644 models were smoothed with the *Smooth* command and, at the same time, their holes and
 645 defects were eliminated using the *Fill Holes* and *Healing Wizard* commands. Subsequently,
 646 the number of polygonal facets was reduced to a reasonable number by repeatedly applying the
 647 *Decimate* command. Finally, the refined PM models were adjusted to match their target mass
 648 using the *Deform* command. Reference target organ masses (inclusive of blood content) are
 649 given in Annex A of this Report. For the organs and tissues including inner structures such as
 650 hollow organs, the refined PM models were replicated to produce separate models to define
 651 inner structures. The sizes of the inner-structure models were then reduced by adjusting their
 652 volumes to match the target mass using the *Offset* and *Deform* commands. For some complex
 653 organs such as the colon, the voxels were first converted to NURBS (Non Uniform Rational
 654 B-Spline) models and then to PM models.

655



656
657
658

Fig. 3.1. Conversion procedure applied for most organs and tissues.

659 (34) Note that the reference value for the oesophageal contents is not given in *Publication 89*
660 (ICRP, 2002); thus, the *Publication 110* phantoms do not include the oesophageal contents,
661 which makes it impossible to calculate SAFs for the oesophagus for radiations emitted by
662 ingested radioactive material during passage through the oesophagus. In the mesh phantoms,
663 therefore, the oesophageal contents were added as part of the oesophagus, having the same
664 volume as the *Publication 100* (ICRP, 2006) stylised models (male: 22.0 cm³ and female: 20.4
665 cm³). For this change, both the length and diameter of the original voxel-type oesophagus had
666 to be increased by ~0.3 cm. Resultantly, the mass of the residual soft tissue (RST) was
667 decreased in order to keep the body mass unchanged. The RST will be discussed in detail later
668 in Section 4.3.

669 (35) During the inclusion of the oesophageal contents, it was found that in the *Publication 110*
670 phantoms, the oesophagus contacts the thyroid for both the male and female phantoms and the
671 thyroid contacts the thymus for the male phantom, which are anatomically incorrect. These
672 organs were separated in the mesh phantoms.

673 (36) Due to the limited voxel resolution of the original voxel-type reference computational
674 phantoms, it was impossible to properly segment the blood in the lungs of the *Publication 110*
675 phantoms. Consequently, the blood mass (male: 150 g and female: 101 g) is significantly
676 smaller than the reference value (male: 700 g and female: 530 g) and the unsegmented blood
677 is implicitly included in the lung tissue (ICRP, 2009). In the PM model of the lungs, the
678 segmented blood was included in the lung tissue by recalculating the density and elemental
679 composition of the lung tissue. This approach slightly increased the lung density by 8.6%
680 (male) and 7.3% (female). These changes will not significantly affect calculated absorbed
681 doses to the lungs.

682 (37) During the conversion process, the PM models were adjusted to the voxel models,
683 monitoring two indices which show the geometrical similarity between two given objects. The
684 first index used in the process was the Dice index (DI), which simply represents the volume
685 overlap fraction of two objects (Dice, 1945). For confirmation of successful adjustment, it was
686 considered that the DI should be greater than 95% of the maximum achievable Dice index
687 (MADI) for a given organ. Note that the MADI exists for a given organ due to the fundamental
688 difference in the geometry format (i.e. voxel vs. PM), which was estimated by calculating the
689 DI between the PM model under adjustment and its voxelised model with the same voxel
690 resolution as the *Publication 110* phantoms. The second index is the centroid distance (CD),
691 which is the distance between the centroids of the voxel model and the corresponding PM
692 model. It was considered that the CD should be less than 0.5 mm for confirmation of a
693 successful adjustment.

694 (38) The CD values were less than 0.5 mm for all organs and tissues which were directly
695 converted from the *Publication 110* voxel models. The DI values were greater than the target
696 DI (= 95% of MADI) for most of the organs and tissues, but there were some exceptions. For
697 the oesophagus, for example, the DI value was less than the target DI, because the total volume
698 of the oesophagus of the PM models was intentionally increased in order to include the
699 oesophageal contents as discussed above. A few other organs and tissues also showed low DI
700 values, because the finite voxel resolution resulted in disconnections of these organs in the
701 *Publication 110* phantoms. For the PM models, the disconnected organ/tissue was first
702 connected and then adjusted to maximise the DI value. After the completion of conversion, we
703 also calculated an additional geometrical similarity index, the Hausdorff distance (HD)
704 (Hausdorff, 1918), which is defined as follows:

$$\text{HD} = \max(\bar{D}(A \cap B^c, B), \bar{D}(B \cap A^c, A)) \quad (1)$$

$$\bar{D}(A, B) = \frac{1}{N_a} \sum_{a \in A} D(a, B) \quad (2)$$

705

706 where a is a point within an object A and $D(a, B)$ is the minimum distance from point a to the
707 other object B . It was found that the HD values are less than 2.5 mm for all organs and tissues,
708 and for most cases less than 1.2 mm, which additionally indicates the high similarity of the PM
709 models with the original voxel models.

710 3.2. Skeletal system

711 (39) Most of the bones (i.e. upper arm bones (humeri), lower arm bones (ulnae and radii),
712 clavicles, upper leg bones (femora), lower leg bones (tibiae, fibulae and patellae), mandible,
713 pelvis, scapulae, sternum, cranium and ribs) were produced by using the same conversion
714 procedure employed for the single-region organs and tissues as demonstrated above for the
715 liver. For the spine (cervical, thoracic and lumbar) which is a very complicated tissue structure,
716 a set of existing high-quality PM models produced from serially sectioned color-photographic
717 images of cadavers (Park et al., 2005) were taken and adjusted to the voxel models monitoring
718 both the DI and CD. Similarly, for the hands and feet, a set of high-quality PM models produced
719 from micro-CT data of cadavers (<http://dk.kisti.re.kr>) were adopted; these models were not
720 adjusted to the voxel models but simply scaled to match the target masses and then placed at
721 the ends of the arms and legs of the mesh phantoms. Note that the *Publication 110* female
722 phantom, the feet are inclined (because the original subject was imaged under CT in a prone
723 position). In the mesh-type phantom, the feet were reoriented in a flat, standing position such
724 as found in the *Publication 110* male phantom.

725 (40) In the *Publication 110* phantoms, the cartilage was not fully segmented due mainly to
726 low contrast in the original CT data. In the mesh-type phantoms, the costal cartilage and
727 intervertebral disks were additionally modelled following the method used for the construction
728 of the UF/NCI phantoms (Lee et al., 2010). To maintain the reference cartilage mass, the
729 remaining cartilage was simply included in the residual soft tissue (RST), which is discussed
730 later in Section 4.3. Strictly speaking, this approach is equally incorrect as the approach used
731 in the *Publication 110* phantoms in which the non-segmented cartilage was included in the
732 spongiosa regions. However, the present approach is dosimetrically more acceptable,
733 considering that the density and effective atomic number of the cartilage are close to those of
734 soft tissues and that the cartilage is neither a radiation-sensitive tissue nor a frequent source
735 region for internal dosimetry; the exact location or distribution of remaining cartilage is thus
736 not important from the dosimetric point of view.

737 (41) The sacrum of the *Publication 110* female phantom lacks cortical bone, again due to
738 limitations with voxel resolution (ICRP, 2009); therefore, cortical bone was added to the
739 sacrum of the female phantom, assuming the female cortical bone mass fraction is identical to
740 that of the male. To maintain the total cortical bone mass unchanged, the cortical bone of the
741 female lower leg bones was reduced considering that the cortical bone mass fraction of the
742 female lower leg bones (= 19%) was significantly higher than that of the male lower leg bones
743 (= 12%). More detailed information on the skeleton conversion can be found in Yeom et al.
744 (2016b).

745 (42) Note that in the skeletal system, the micron-scale structure of the skeletal target tissues
746 (i.e. active bone marrow and skeletal endosteum) are not modelled and, therefore, the dose to

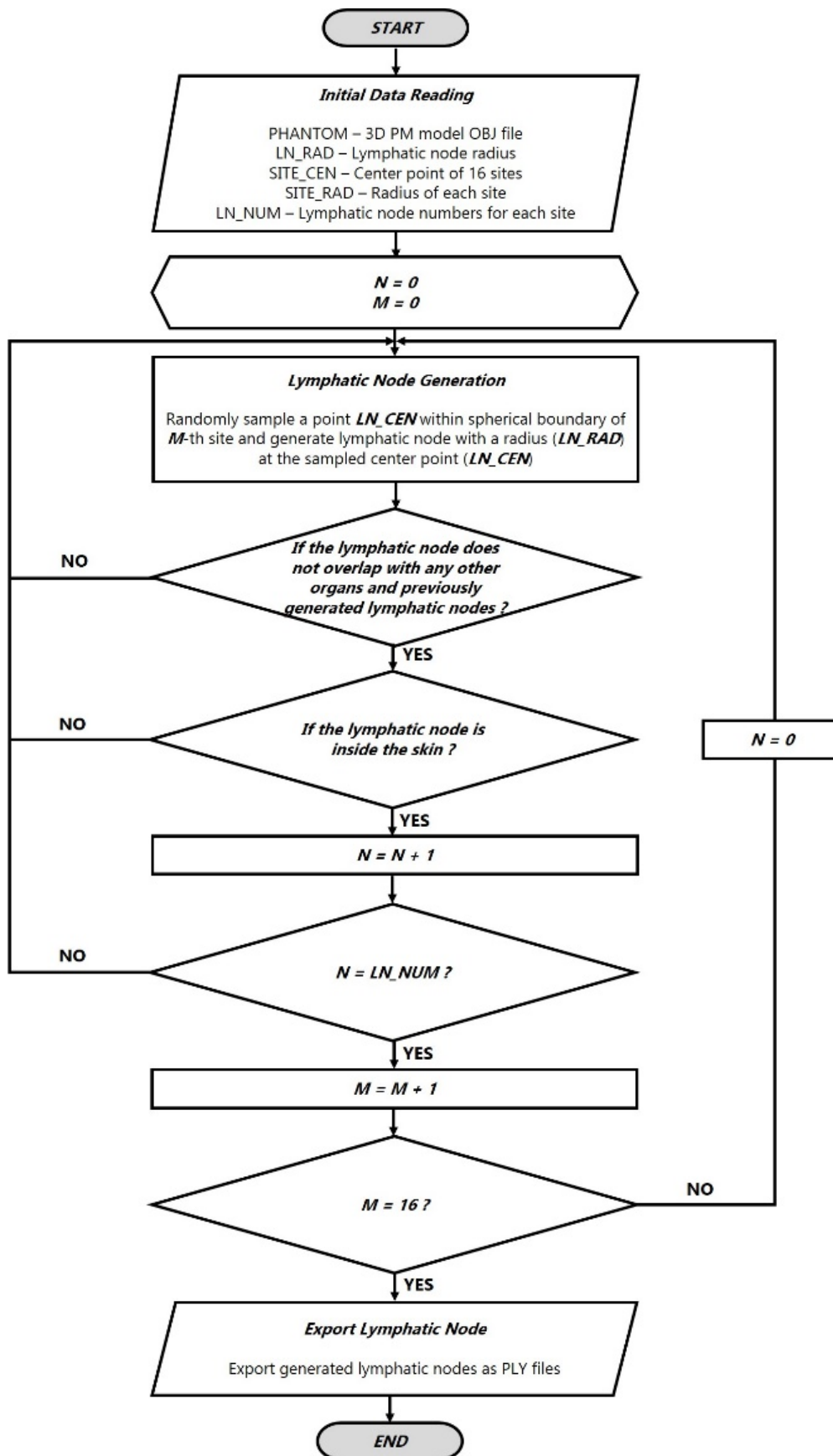
747 these skeletal tissues needs to be calculated by using fluence-to-dose response functions, such
748 as those presented and described in Annexes D and E of *Publication 116* (ICRP, 2010).

749 **3.3. Small intestine**

750 (43) The small intestine was not precisely represented in the *Publication 110* phantoms (ICRP,
751 2009), mainly because its complex tubular structure was not clearly distinguishable in the
752 original cross-sectional CT data and its modelling was limited due to the finite voxel resolution.
753 Accordingly, a dedicated procedure and a computer program were used to generate the small-
754 intestine models in the mesh phantoms (Yeom et al., 2016a). First, a surface frame, entirely
755 enclosing the original small-intestine voxel model, was constructed using the alpha-shape
756 algorithm (Edelsbrunner et al., 1983). Next, a dedicated computer program developed in C++
757 was used to generate a small-intestine passage line using a Monte Carlo sampling approach.
758 Along with the passage line, a PM-format small-intestine model was generated, whose masses
759 of the wall and contents were matched to the reference values given in *Publication 89* (ICRP,
760 2002). The aforementioned procedure was repeated to produce 1000 different small-intestine
761 models, with the best model selected considering both its geometric and dosimetry similarity.
762 More detailed information on the construction of the small-intestine model can be found in
763 Yeom et al. (2016a).

764 **3.4. Lymphatic nodes**

765 (44) The lymphatic nodes of the *Publication 110* phantoms could not be directly converted to
766 the PM format due to their complexity and distributed nature in the body. The lymphatic nodes
767 in the PM format were therefore generated by using a similar modelling approach used to
768 generate lymphatic nodes in the UF/NCI family phantoms (Lee et al., 2013) based on the
769 lymphatic node data (see Table 3.1), which were derived from the data of *Publications 23, 66*
770 *and 89* (ICRP, 1975, 1994a, 2002). Note that the derived lymphatic node data are consistent
771 with the values adopted for the calculations of *Publication 133* (ICRP, 2016). For the
772 generation of the lymphatic nodes, a dedicated computer program was developed following the
773 procedure shown in Fig. 3.2. The program first loads the initial data: (1) the PM phantom data,
774 (2) the single node PM data, (3) the nodal diameter, (4) the coordinates of the lymphatic nodal
775 sites, (5) the diameters of the spherical clusters for the sites and (6) the site-specific nodal
776 numbers. Then, the program randomly generates lymphatic nodes satisfying the following two
777 criteria: (1) a node should be placed within the corresponding cluster sphere and (2) a node
778 should overlap neither with other organs and tissues nor with the previously generated nodes.
779 The procedure is repeated until the number of generated nodes reaches a predefined number.
780



781
782

Fig. 3.2. Flowchart of developed program to generate lymphatic nodes in the PM phantoms.

783 Table 3.1. Lymphatic nodal numbers and masses for the adult male and female derived from the data
 784 of *Publication 23, 66 and 89* (ICRP, 1975, 1994a, 2002), along with reference nodal numbers given in
 785 *Publication 89* (ICRP, 2002).

Lymphatic nodal site	Reference nodal numbers in <i>Publication 89</i>	Derived nodal numbers	Mass (g)	
			Male	Female
Extrathoracic		55	15.0	12.0
Cervical		19	5.2	4.1
Thoracic	50–60	55	15.0	12.0
Breast (left and right)		38	10.4	8.3
Mesentery (left and right)	200–500	350	95.5	76.4
Axillary (left and right)	8–37	23	6.3	5.0
Cubital (left and right)		38	10.4	8.3
Inguinal (left and right)		38	10.4	8.3
Popliteal (left and right)		38	10.4	8.3
Total	600–700	654	178.4	142.7

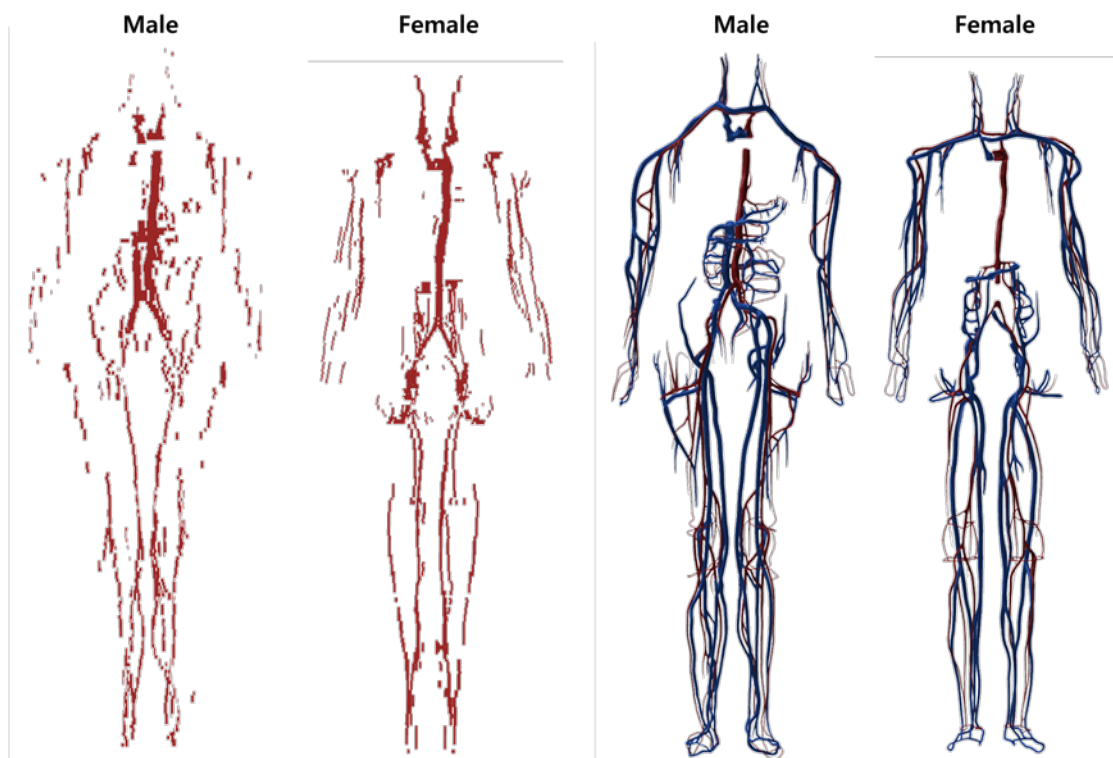
786 **3.5. Eyes**

787 (45)The *Publication 110* phantoms (ICRP, 2009), due to their voxel sizes on the order of a
 788 few millimetres, do not properly represent the detailed structure of the eye. The lens DCs of
 789 *Publication 116* (ICRP, 2010) on idealised external radiation exposures were therefore
 790 calculated using either the *Publication 110* phantoms or the detailed stylised eye model
 791 developed by Behrens et al. (2009), depending on radiation type, energy and irradiation
 792 geometry. To avoid this situation, the detailed eye model of Behrens et al. (2009) was directly
 793 incorporated into the male and female mesh phantoms. First, using the geometrical information
 794 of the Behrens’ detailed eye model, a NURBS-format eye model was produced and then
 795 converted to the PM format. Defects in the converted model were repaired by using the
 796 refinement functions of the *RapidformTM* software (INUS Technology Inc., Korea). Finally, the
 797 PM eye model was placed in the mesh phantoms, matching the centroid of the eye of the
 798 *Publication 110* phantoms. More detailed information on the eye model can be found in
 799 Nguyen et al. (2015).

800 **3.6. Blood in large vessels**

801 (46)Only the blood in the large blood vessels is modelled in the *Publication 110* phantoms,
 802 again due to the limited resolution of the original CT image data (8 and 5 mm slice thicknesses
 803 for the male and female phantoms, respectively). Consequently, the mass of the segmented
 804 blood in the *Publication 110* phantoms (male: 371 g and female: 384 g) is significantly smaller
 805 than their corresponding reference values (male: 1344 g and female: 984 g). This issue was
 806 addressed in the mesh phantoms. For the mesh phantoms, first, the blood of the large blood
 807 vessels was converted to the PM format, whose mass was then matched to the reference value.
 808 For this step, the blood models of the *Publication 110* phantoms were first converted to
 809 primitive PM models using a surface rendering method in 3D-DOCTORTM (Able Software
 810 Corp., Lexington MA). Then, the contour lines were carefully generated along the blood
 811 passages identified in the primitive PM models using the *Section* command of the *Rhinoceros*
 812 software (Robert McNeel & Associates, Seattle, Wash). The generated contour lines were then
 813 used to generate NURBS surfaces using the *Loft* command of the software. Finally, the NURBS

814 surfaces were converted to the PM format using the *Mesh* command. In the mesh phantoms,
 815 the remaining part of the blood in the smaller blood vessels was modelled manually with the
 816 NURBS modelling tools of the *Rhinoceros* software, referring to the high-quality 3D blood
 817 models provided by BioDigital (<https://www.biodigital.com>). The modelled NURBS surfaces
 818 were converted to the PM format and then the converted PM models were connected to the PM
 819 models of the blood in the large vessels by using the *Union* command of the *RapidformTM*
 820 software (INUS Technology Inc., Korea). Finally, the combined PM models were adjusted to
 821 match the reference values using the *Deform* command of the software. Figure 3.3 shows the
 822 developed blood PM models, along with the *Publication 110* blood voxel models. Note that
 823 the intra-organ vasculature is not modelled in the phantoms; that is, the blood in the large
 824 vessels stops at the surface of the organs and the blood within the organs is assumed to be
 825 homogeneously mixed with the parenchyma of the organs.
 826



827
 828 Fig. 3.3. Blood in large vessels of the *Publication 110* phantoms (left) and the MRCPs (right). In the
 829 MRCPs, the red colour indicates the blood in the large arteries and the blue colour indicates the blood
 830 in the large veins.

831 3.7. Muscle

832 (47)The muscle of the PM models was constructed after completion of all internal organs and
 833 tissues. Most of the muscle (i.e. trunk, arms and legs) were constructed by direct conversion
 834 and refinement, whereas the other complex parts (i.e. head, hands and feet) were constructed
 835 by a modelling approach. For the construction, a series of labour-intensive refinement work
 836 was involved to eliminate the defects and overlapping problems with the other organs and
 837 tissues by using the refinement tools of the *RapidformTM* software (INUS Technology Inc.,
 838 Korea). In addition, the rear side of the muscle (back, hip and calf), which had been flattened

839 in the *Publication 110* phantoms due to the lying position of the individual original imaged
840 under CT, was reshaped to produce the muscular shape present in a standing person.
841

842

4. INCLUSION OF BLOOD TO ORGANS AND TISSUES

843 (48)The organ/tissue masses of the mesh phantoms include their intra-organ blood content.
844 This is not the case in the *Publication 110* phantoms, in which the organ/tissue masses are
845 based on reference values listed in Table 2.8 of *Publication 89* (ICRP, 2002) which are the
846 masses of organ/tissue parenchyma, i.e. not including blood content. Note that a large portion
847 of blood situated in the small vessels and capillaries is distributed in the organs and tissues. For
848 the mesh phantoms, therefore, the organ/tissue masses and compositions inclusive of the blood
849 content for adult male and female were calculated based on the reference regional volume
850 fractions given in *Publication 89* (ICRP, 2002) and, accordingly, the mesh phantoms were
851 adjusted in volume to include the blood content in their organs and tissues. Note that
852 *Publication 133* (ICRP, 2016) also considered the target masses inclusive of blood content for
853 the calculation of SAFs for self-irradiation.

854

4.1. Calculation of mass, density, and elemental composition of organs and tissues inclusive of blood content

855

856 (49)Blood-content masses for all the organs and tissues listed in Table 2.8 of *Publication 89*
857 (ICRP, 2002) were calculated by using the reference values of regional blood volume fractions
858 given in Table 2.14 of *Publication 89* (ICRP, 2002), which is replicated in Table 4.1 below.
859 There are organs and tissues whose reference blood fraction is explicitly given (i.e. fat, brain,
860 stomach, oesophagus, small intestine, large intestine, right heart, left heart, coronary tissue,
861 kidneys, liver, pulmonary, bronchial tissue, skeletal muscle, pancreas, active marrow,
862 trabecular bone, cortical bone, other skeleton, skin, spleen, thyroid, lymph nodes, gonads,
863 adrenals and urinary bladder). Their blood-content mass was simply calculated as the product
864 of their reference blood fraction and the reference total body blood mass (adult male: 5600 g
865 and adult female: 4100 g) given in *Publication 89* (ICRP, 2002).

866 (50)The reference blood fraction for the stomach and oesophagus is given as a single value,
867 and thus not given separately as shown in Table 4.1; therefore, their blood mass was assigned
868 in proportion to the organ mass under the assumption that the blood is uniformly distributed
869 over these two organs. The same approach was used to calculate the blood mass of the inactive
870 marrow, cartilage, teeth and miscellaneous skeletal tissue, which are grouped as ‘other
871 skeleton’ in Table 4.1.

872 (51)In Table 2.8 of *Publication 89* (ICRP, 2002), there are organs and tissues whose blood
873 fractions are not explicitly listed in Table 2.14 of *Publication 89* (ICRP, 2002), i.e. Table 4.1
874 (i.e. tongue, salivary glands, gall bladder wall, breasts, eyes, pituitary gland, larynx, trachea,
875 thymus, tonsils, ureters, urethra, epididymis, prostate, fallopian tubes, uterus and ‘remaining
876 4%’ tissues), which are represented by the ‘all other tissues’ in Table 4.1. Note that the
877 ‘remaining 4%’ tissues indicate all of the organs and tissues that are not explicitly listed in
878 Table 2.8 of *Publication 89* (ICRP, 2002), which is about 4% of the body mass, mostly
879 composed of separable connective tissues and certain lymphatic tissues. The blood mass of the
880 ‘all other tissue’ (male: 107.5 g and female: 78.7 g) was distributed to these organs and tissues
881 with proportion to their masses. For this calculation, the mass of the ‘remaining 4%’ tissues
882 was reduced due to the extraction of the lymphatic nodes of which the mass (male: 178.4 g and
883 female: 142.7 g) was adopted in *Publication 133* (ICRP, 2016), considering that the reference
884 blood fraction for the lymphatic nodes is explicitly given as shown in Table 4.1. The reference

885 organ/tissue masses (exclusive of blood content) and the calculated blood content masses are
 886 given in Table 4.2.

887
 888 Table 4.1. Reference values for regional blood volumes in adults given in *Publication 89* (ICRP, 2002).

Organ/tissue	Blood content (% total blood volume)	
	Male	Female
Fat	5.0	8.5
Brain	1.2	1.2
Stomach and oesophagus	1.0	1.0
Small intestine	3.8	3.8
Large intestine	2.2	2.2
Right heart	4.5	4.5
Left heart	4.5	4.5
Coronary tissue	1.0	1.0
Kidneys	2.0	2.0
Liver	10	10
Pulmonary	10.5	10.5
Bronchial tissue	2.0	2.0
Skeletal muscle	14	10.5
Pancreas	0.6	0.6
Skeleton	7.0	7.0
Red marrow	4.0	4.0
Trabecular bone	1.2	1.2
Cortical bone	0.8	0.8
Other skeleton	1.0	1.0
Skin	3.0	3.0
Spleen	1.4	1.4
Thyroid	0.06	0.06
Lymph nodes	0.2	0.2
Gonads	0.04	0.02
Adrenals	0.06	0.06
Urinary bladder	0.02	0.02
All other tissues	1.92	1.92
Aorta and large arteries	6.0	6.0
Large veins	18	18

889

890

891 Table 4.2. Reference masses of organs and tissues for Reference Adult Male and Reference Adult
892 Female.

Organ/tissue	Male		Female	
	Organ/tissue only (g)	Blood content (g)	Organ/tissue only (g)	Blood content (g)
Adipose tissue	14500	280.000	19000	348.500
Adrenals	14	3.360	13	2.460
Tongue	73	2.656	60	1.491
Salivary glands	85	3.093	70	1.739
Oesophagus, wall	40	11.789	35	8.200
Stomach, wall	150	44.211	140	32.800
Stomach, contents	250		230	
Small intestine, wall	650	212.800	600	155.800
Small intestine, contents	350		280	
Right colon, wall	150	49.946	145	36.331
Right colon, contents	150		160	
Left colon, wall	150	49.946	145	36.331
Left colon, contents	75		80	
Rectosigmoid, wall	70	23.308	70	17.539
Rectosigmoid, contents	75		80	
Liver	1800	560.000	1400	410.000
Gallbladder, wall	10	0.364	8	0.199
Gallbladder, contents	58		48	
Pancreas	140	33.600	120	24.600
Brain	1450	67.200	1300	49.200
Breasts, adipose	15	0.546	300	7.454
Breasts, glandular	10	0.364	200	4.969
Blood in heart chambers	510*	510.000	370*	370.000
Heart – tissue only	330	56.000	250	41.000
Total blood	5600	5600.000	4100	4100.000
Eyes	15	0.546	15	0.373
Skin	3300	168.000	2300	123.000
Muscle, skeletal	29000	784.000	17500	430.500
Pituitary gland	0.6	0.022	0.6	0.015
Larynx	28	1.019	19	0.472
Trachea	10	0.364	8	0.199
Blood in lung	700*	700.000	530*	530.000
Lung – tissue only	500		420	
Bone, cortical	4400	44.800	3200	32.800
Bone, trabecular	1100	67.200	800	49.200
Marrow, active	1170	224.000	900	164.000
Marrow, inactive	2480	36.261	1800	25.448
Cartilage	1100	16.084	900	12.724
Teeth	50	0.731	40	0.566
Skeletal miscellaneous	200	2.924	160	2.262
Spleen	150	78.400	130	57.400
Thymus	25	0.910	20	0.497
Thyroid	20	3.360	17	2.460
Tonsils	3	0.109	3	0.074
Kidneys	310	112.000	275	82.000
Ureters	16	0.582	15	0.373
Urinary bladder	50	1.120	40	0.820
Urethra	10	0.364	3	0.074
Testes	35	2.240		
Epididymes	4	0.145		
Prostate	17	0.619		

Ovaries			11	1.640
Fallopian tubes			2.1	0.052
Uterus			80	1.987
Lymphatic nodes	178.4 [†]	11.200	142.7 [‡]	8.200
Blood, arteries		336.000		246.000
Blood, veins		1008.000		738.000
'Remaining 4%' tissues	2633.0 [‡]	89.817	2364.6 [‡]	40.251
Total body (kg)	73000		60000	

893 * The mass of blood in the heart chambers and lungs were included in the total blood and should not be included
 894 in the whole-body summation.

895 [†]The mass of the lymphatic nodes exclusive of blood content was adopted in *Publication 133* (ICRP, 2016).

896 [‡]The mass of the 'remaining 4%' tissues was calculated by subtracting the total mass of all other organs and tissues
 897 from body mass.

898

899 (52) After the calculation of the blood masses, the densities and elemental compositions of the
 900 blood-inclusive organs and tissues were calculated by using the data in *Publication 89* (ICRP,
 901 2002) and *Report 46* (ICRU, 1992), again under the assumption that the blood content is
 902 uniformly distributed over the organs and tissues. The density of the blood-inclusive liver, for
 903 example, was calculated by using the following equation:

904

$$911 \quad \rho_{liver}^{with-blood} = \frac{m_{liver}^{ICRP89} + m_{blood-in-liver}}{\frac{m_{liver}^{ICRP89}}{\rho_{liver}^{ICRU46}} + \frac{m_{blood-in-liver}}{\rho_{blood}^{ICRU46}}} \quad (1)$$

912

905 where $\rho_{liver}^{with-blood}$ is the density of the blood-inclusive liver, ρ_{liver}^{ICRU46} is the density of the liver
 906 parenchyma as given in *Report 46* (ICRU, 1992), ρ_{blood}^{ICRU46} is the density of the blood, m_{liver}^{ICRP89}
 907 is the mass of the liver parenchyma as given in *Publication 89* (ICRP, 2002), and
 908 $m_{blood-in-liver}$ is the mass of the blood in the liver. Regarding the elemental composition, the
 909 mass percentage of hydrogen in the blood-inclusive liver, for example, was calculated by using
 910 the following equation:

913

$$914 \quad (\%H)_{liver}^{with-blood} = \frac{(\%H)_{liver}^{ICRU46} m_{liver}^{ICRP89} + (\%H)_{blood}^{ICRU46} m_{blood-in-liver}}{m_{liver}^{ICRP89} + m_{blood-in-liver}} \quad (2)$$

915

916 where $(\%H)_{liver}^{with-blood}$ is the percentage by mass of hydrogen in the blood-inclusive liver,
 917 $(\%H)_{liver}^{ICRU46}$ is the percentage by mass of hydrogen in the liver parenchyma as given in *Report*
 918 *46* (ICRU, 1992), and $(\%H)_{blood}^{ICRU46}$ is the percentage by mass of hydrogen in the blood. These
 919 calculation methods were used to calculate all of the densities and elemental compositions for
 920 the organs and tissues of the mesh phantoms. The calculated values of the density and elemental
 921 compositions are given in Table B.1 and Table B.2.

922 4.2. Phantom adjustment for blood inclusion

923 (53) The PM models for all organs and tissues were subsequently adjusted to increase their
 924 volumes to allow for the volumetric inclusion of their blood content. The adjustment was
 925 performed again using the *RapidformTM* software (INUS Technology Inc., Korea).
 926 Preferentially the volumes of the organs and tissues were increased to match the blood-
 927 inclusive reference masses by globally enlarging a PM surface in the normal direction of the

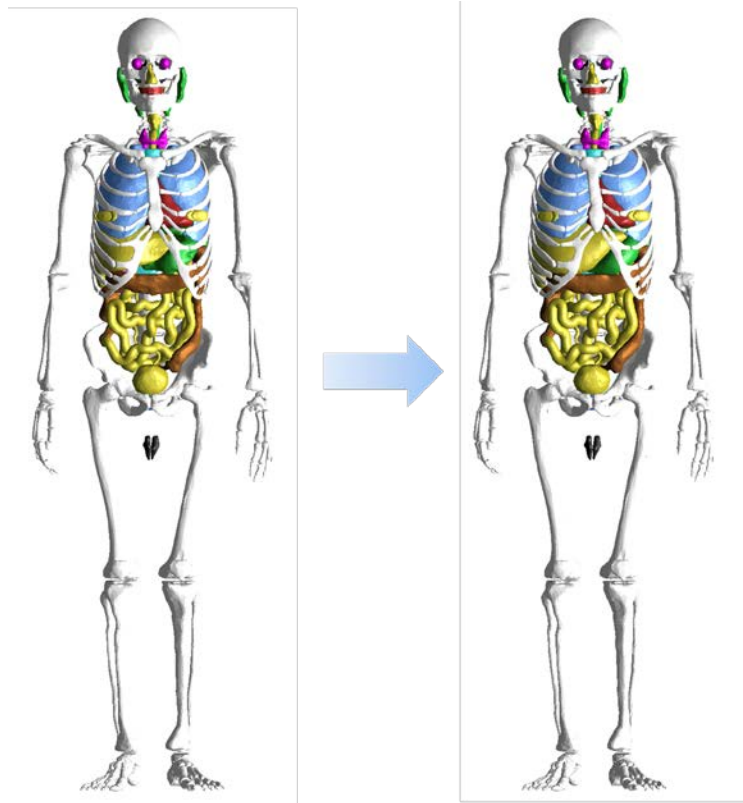
928 facets, which tends to maintain the centroid and original shape of the models. Among the
929 increased organs and tissues, some overlaps were detected and the overlapping regions of the
930 larger organs and tissues were preferentially eliminated rather than the smaller organs and
931 tissues, in order to minimise the distortion of the organ/tissue shapes. The organs and tissues
932 with decreased volumes were then manually adjusted to increase their volumes to match the
933 reference masses, while at the same time monitoring the DI and CD to minimise the
934 deformation of the organ shape from the original shape.

935 (54) If there was insufficient space for the increase of the organ/tissue volumes, the organs
936 and tissues were moved slightly to secure space. For example, the volume of the liver was
937 increased significantly, i.e. more than 30% for both the male and the female, resulting in
938 significant overlap problems with the adjacent organs and tissues, especially for the female
939 mesh phantom. The lungs and ribs, therefore, had to be moved outward in the lateral direction
940 by ~2 mm and ~4 mm for the male and female, respectively, after which the liver and adjacent
941 organs and tissues were again adjusted to match the reference masses without overlapping
942 regions.

943 (55) Figures 4.1–4.2 compare the internal organs and tissues of the mesh phantoms before and
944 after inclusion of blood content for male and female, respectively. It can be seen that in general,
945 the inclusion of the blood content does not significantly change the topology of the phantoms.
946 For detailed investigation to quantify geometric dissimilarity produced by the blood inclusion,
947 three similarity indices (DI, CD and HD) were evaluated between the organs and tissues of the
948 phantoms before and after their volumetric adjustment.

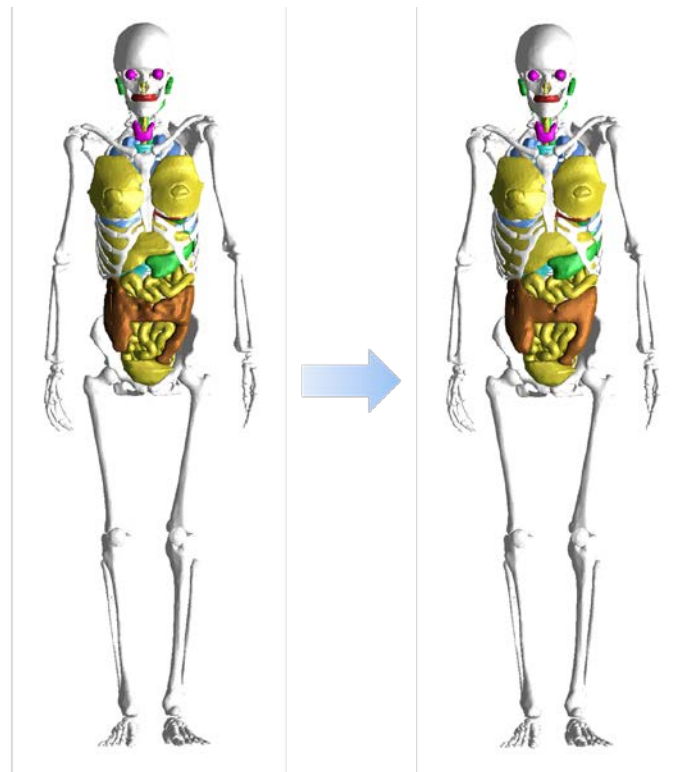
949 (56) It was found that the CD and HD values were less than ~2 mm for most of the organs and
950 tissues. The DI values were greater than 0.95 for most of the organs and tissues. On the other
951 hand, there are some organs and tissues that were significantly changed due to the blood
952 inclusion. For the liver and kidney, for example, the CD and HD values ranged from 3.4 mm
953 to 5.4 mm, and the DI values were within the range of 0.83–0.87; these differences are due to
954 the fact that their mass was significantly increased by the blood inclusion. In addition, some
955 organs and tissues (such as ribs and spleen), located near the liver or kidneys, were significantly
956 changed because they were moved to secure space for blood inclusion.

957



958
959
960
961

Fig. 4.1. Male phantom before (left) and after (right) adjustment for inclusion of blood content into organs and tissues.



962
963
964

Fig. 4.2. Female phantom before (left) and after (right) adjustment for inclusion of blood content into organs and tissues.

965 4.3. Definition of residual soft tissue (RST)

966 (57) Although most of the organs and tissues in Table 4.2 are defined in the mesh phantoms,
967 several organs and tissues (i.e. adipose tissue, larynx, urethra, epididymis and fallopian tubes)
968 are not included explicitly in the phantom anatomical structure. In contrast, several organs and
969 tissues of the phantoms (i.e. main bronchi (= generation 1), spinal cord, urine, oesophageal
970 contents, extrathoracic (ET) and inner air) are not listed in the table, but they can be considered
971 as a part of the ‘remaining 4%’ tissues in Table 4.2. In addition, the mesh phantoms include
972 only costal and intervertebral cartilages, the total masses of which are significantly smaller than
973 the reference values.

974 (58) Despite these inconsistencies, the phantom mass should be consistent with the reference
975 total body mass (male: 73 kg and female: 60 kg). This agreement was reached by defining an
976 imaginary tissue, called ‘residual soft tissue (RST)’, in the mesh phantoms. The RST implicitly
977 includes all of the reference organs and tissues that are not explicitly defined in the phantoms:
978 adipose tissue, larynx, cartilage (excluding costal and intervertebral cartilages defined in the
979 phantoms), urethra, epididymis, fallopian tubes, ‘remaining 4%’ tissue (excluding the organs
980 and tissues defined in the phantoms but not listed in the reference values).

981 (59) This approach has been generally used in the field of phantom development to match the
982 phantom body mass to the reference body mass (ICRP, 2009; Lee et al., 2010; Kim et al., 2011;
983 Yeom et al., 2013). In *Publication 133* (ICRP, 2016), a similar approach was also used to
984 establish the source organ/tissue masses (see Table A.3 of *Publication 133*) for the purpose of
985 use in the latest biokinetic models of the OIR *Publication* series (ICRP, 2015, 2017a, b). The
986 established source organs/tissues do not include some reference organs/tissues, but the total
987 mass of the source organs/tissues was matched to the reference body mass simply by increasing
988 the adipose tissue mass. The increased adipose tissue plays the same role as the RST defined
989 in the mesh phantoms.

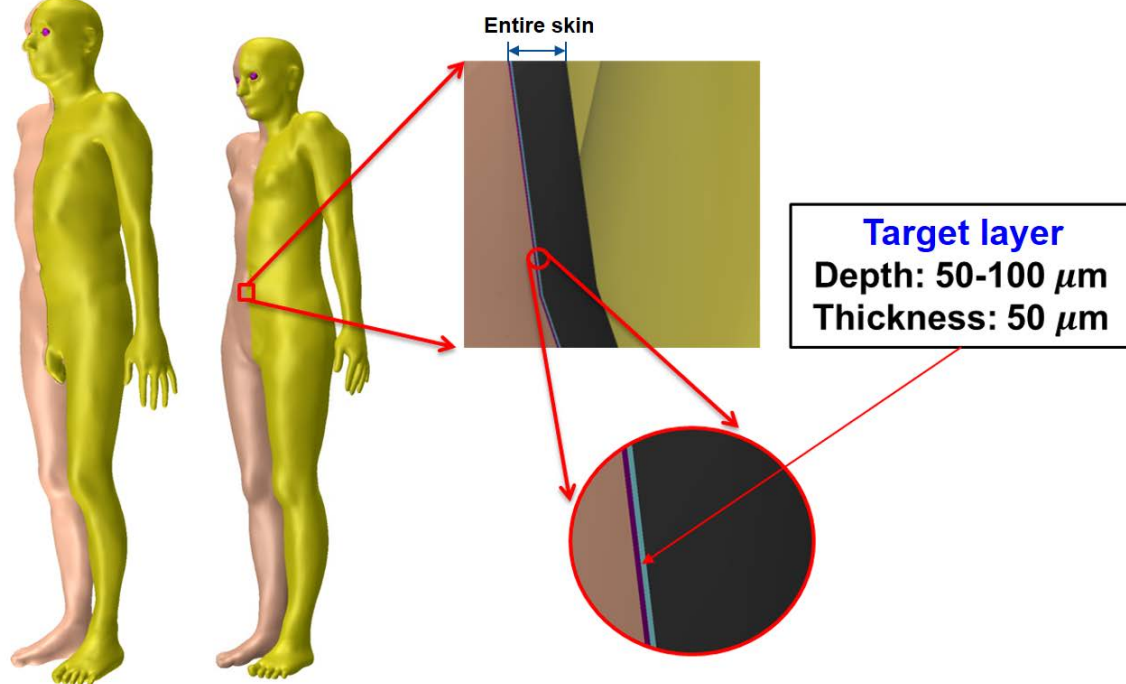
990

991 **5. INCLUSION OF THIN TARGET AND SOURCE REGIONS**

992 **5.1. Skin**

993 (60) The cells at risk in the skin are assumed to be in the tissue layer 50 μm to 100 μm below
 994 the skin surfaces (ICRP, 1977, 2010, 2015). However, the *Publication 110* phantoms, due to
 995 their voxel resolution, do not have this thin target layer and consequently cannot be used for
 996 skin dose calculation for weakly penetrating radiations (ICRP, 2010). In the mesh phantoms,
 997 the 50- μm -thick target layer was explicitly defined within the volume defining the total skin.

998 (61) For this, first, the exterior surface of the skin was imported into the *RapidformTM* software
 999 (INUS Technology Inc., Korea) and then replicated to two additional surfaces. The sizes of the
 1000 two surfaces were reduced to define the target layer within the skin at a depth of 50 μm and
 1001 100 μm from the exterior skin surface, respectively, using the *Offset* command of the software.
 1002 Note that the *Offset* command shrinks or enlarges a PM surface in the normal direction of the
 1003 facets in the model, which allows the creation of surfaces to define the tens-of-micrometre-
 1004 thick layer at a specific depth. Figure 5.1 shows the skin of the mesh phantoms including the
 1005 50- μm -thick target layer.
 1006



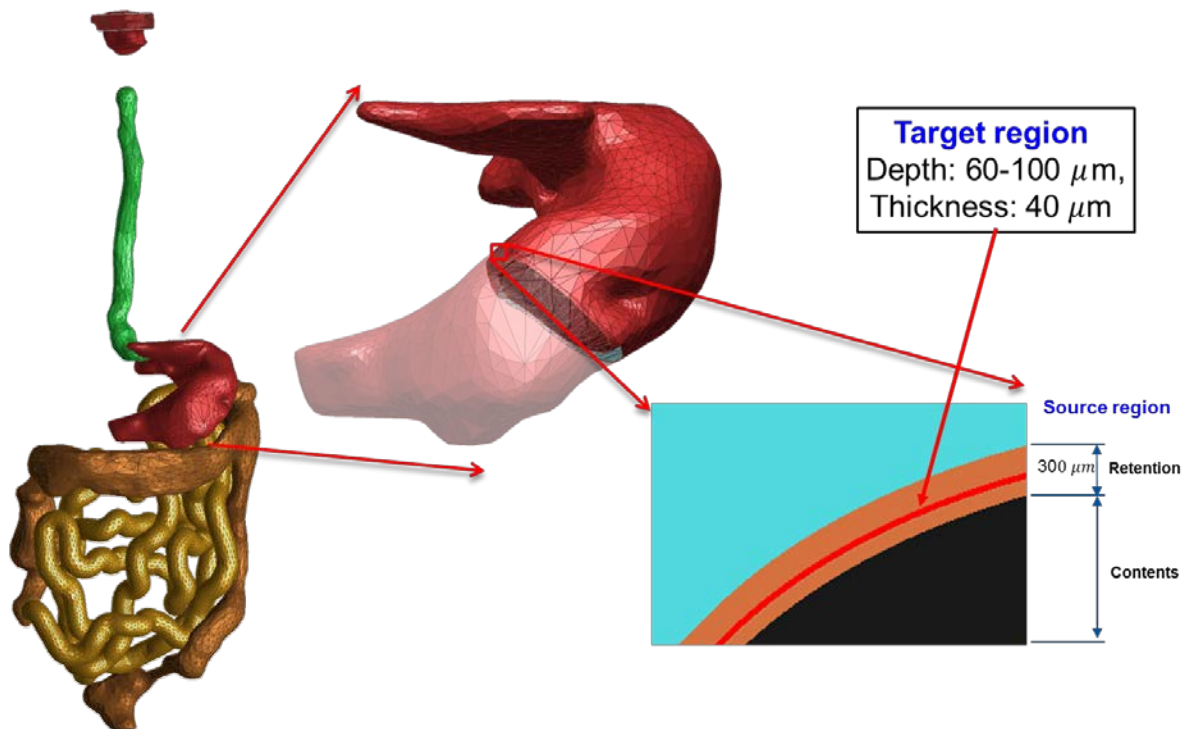
1007
 1008 Fig. 5.1. Skin of the mesh phantoms including the 50- μm -thick target layer: dead layer (purple colour),
 1009 target layer (sky blue colour) and dermis layer (black colour).

1010 **5.2. Alimentary tract system**

1011 (62) The target regions (stem cell layers) and source regions (mucosal layers) of the alimentary
 1012 tract organs (i.e. oral cavity, oesophagus, stomach, small intestine and large intestine) were
 1013 defined in the mesh phantoms according to the depth and thickness data for the target and
 1014 source regions given in *Publication 100* (ICRP, 2006). For all organs except the oral cavity,

1015 the thin target and source regions were simply defined using the *Offset* command of the
 1016 *RapidformTM* software (INUS Technology Inc., Korea) following the same method as used for
 1017 the skin. Figure 5.2 shows, as an example, the stomach of the male phantom including the
 1018 target and source regions.

1019 (63) In the oral cavity, two source regions were defined: source in food and source retained
 1020 on the surface of the teeth. The food source volume ($= 20 \text{ cm}^3$) should be placed on the tongue,
 1021 but in the *Publication 110* phantoms, there was no sufficient space to define the food source
 1022 region; therefore, the tongue was divided into two parts, i.e. upper and lower parts, and the
 1023 upper part was considered to be the food source region for the purpose of SAF calculation. The
 1024 teeth-retained radionuclides were defined by adding a 10- μm layer on the surface of the teeth.
 1025 The target layer in the oral mucosa was defined in three parts: tongue, roof of mouth and lip
 1026 and cheek. More detailed information on the alimentary tract system can be found in Kim et
 1027 al. (2017).
 1028



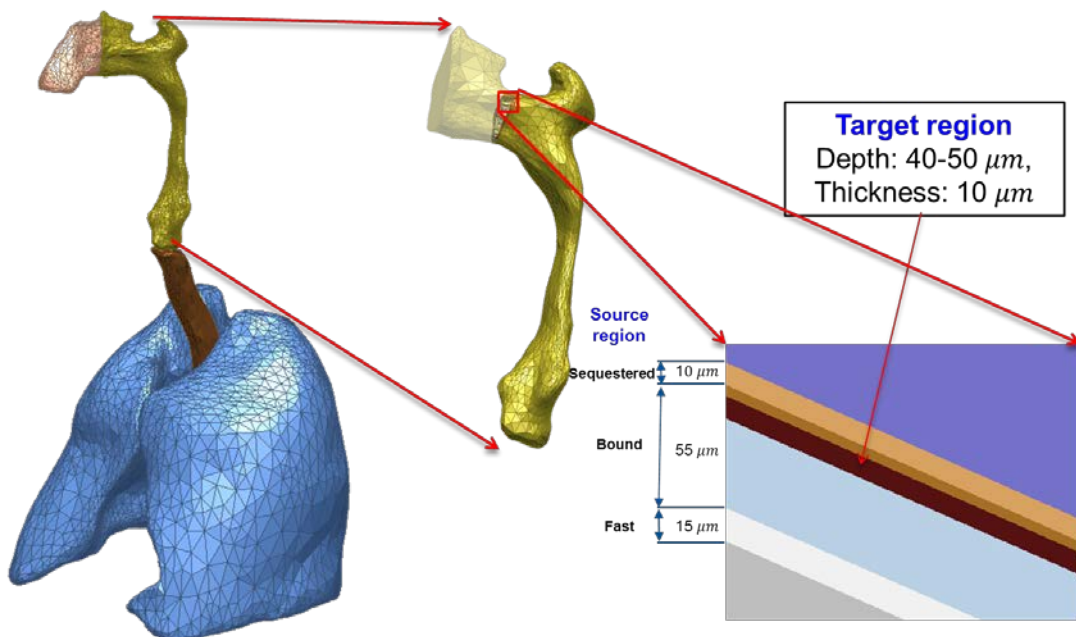
1029 Fig. 5.2. Alimentary tract organs (left) of the male mesh phantom and the enlarged view (right) of the
 1030 stomach including the target and source regions.
 1031

1032 5.3. Respiratory tract system

1033 (64) The target and source regions of the respiratory tract organs were defined in the mesh
 1034 phantoms following the morphometric data given in *Publication 66* (ICRP, 1994a). The
 1035 respiratory tract organs are composed of the extrathoracic regions (i.e. ET₁ and ET₂), bronchi
 1036 (BB), bronchiole (bb) and alveoli-interstitial (AI). The AI was not defined separately but
 1037 simply assumed to be homogeneously distributed within the lung tissue, except for the BB and
 1038 bb regions in the MRCPs, considering the statement of *Publication 66* (ICRP, 1994a): '(313)
 1039 *In the AI region, the interalveolar septa and the walls of blood and lymphatic capillaries are*
 1040 *sufficiently thin to ensure that sensitive target cells are distributed homogeneously throughout*

1041 *the tissue mass. Therefore, it can be assumed that the average dose received by the target cells*
 1042 *is the same as that received by the whole tissue mass?*

1043 (65) For the ET₁ and ET₂ regions, they were directly converted from the *Publication 110* voxel
 1044 models to a PM format, with their target and source regions defined using the *Offset* command
 1045 of the *Rapidform™* software (INUS Technology Inc., Korea) following the same method
 1046 applied for the skin and alimentary tract organs. The same method was also applied to the main
 1047 bronchi (generation 1) that were directly converted from the *Publication 110* voxel models to
 1048 the PM format. Figure 5.3 shows the ET₂ region of the male phantom, as an example, including
 1049 both its *Publication 66* source and target regions.
 1050



1051 Fig. 5.3. Respiratory tract organs (left) of the male mesh phantom and the enlarged view (right) of the
 1052 ET₂ including the target and source regions.
 1053

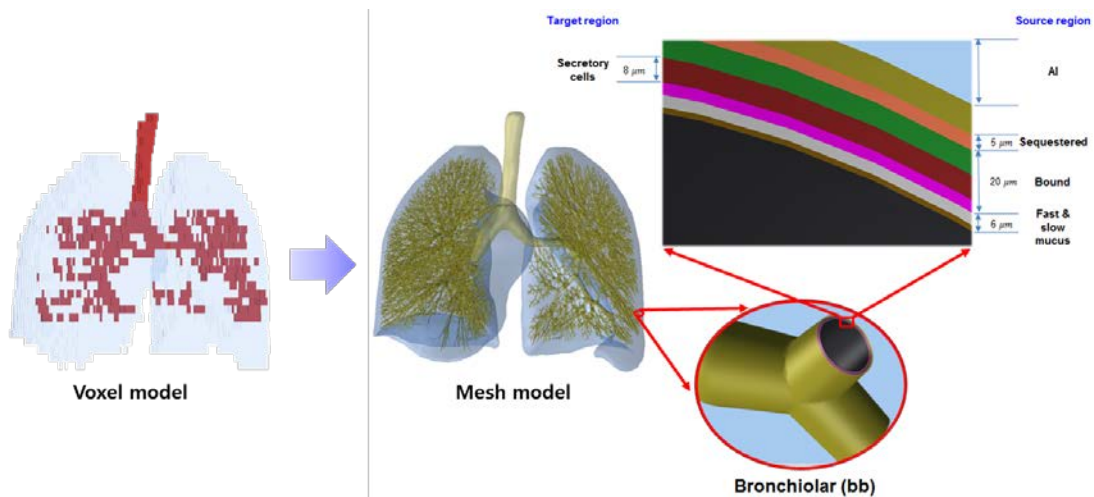
1054

1055 (66) The other generations (i.e. airway generations 2–8) of the bronchi (BB) and all
 1056 subsequent generations of the bronchioles (bb) (i.e. airway generations 9–15) could not be
 1057 converted from the *Publication 110* voxel models; therefore, these airways were modelled
 1058 using a dedicated computer program developed by Kim et al. (2017). The developed computer
 1059 program generated branch-centre lines within the left and right lungs of the mesh phantoms
 1060 based on a branching generation algorithm (Tawhai et al., 2000), following the diameter and
 1061 length for each airway generation as given in *Publication 66* (ICRP, 1994a). The branch-centre
 1062 lines were used to construct airway models in the constructive solid geometry (CSG) format,
 1063 whose models are based on an inverted Y-shape represented as a union geometry of spheres
 1064 and truncated cones. The spheres, the diameters of which correspond to the branch diameters,
 1065 are located at the ends of the branch-centre lines and the truncated cones are located so as to
 1066 be tangent to the mother and daughter spheres. The use of the inverted Y-shape model makes
 1067 it possible to not only precisely connect the surfaces of the neighbouring branches but also to
 1068 define the micrometre-thick source and target layers simply by changing the sphere diameters
 1069 (i.e. branch diameters) (Lázaro, 2011).

1070 (67) Note that the CSG-format airway models needed to be converted to the PM format for
 1071 incorporation into the mesh phantoms. For this step, however, a large number of polygonal
 1072 facets, eventually tetrahedrons, would be necessary to properly represent the airways, requiring

1073 a very large memory allocation (> ~50 GB), which is, at least at the present time, impractical.
 1074 Therefore, a different approach was used for the airways; that is, the MRCPs were overlaid
 1075 with the CSG lung airways in the Geant4 code (Agostinelli et al., 2003) by using the
 1076 *G4VUserParalleWorld* class, which is used for implementation of hierarchically overlapping
 1077 multiple geometries called ‘parallel geometries’ (Apostolakis et al., 2008). This overlaying
 1078 approach is currently available only in Geant4, but enables us to perform dose calculation for
 1079 the detailed CSG lung airways with minimal additional memory usage.

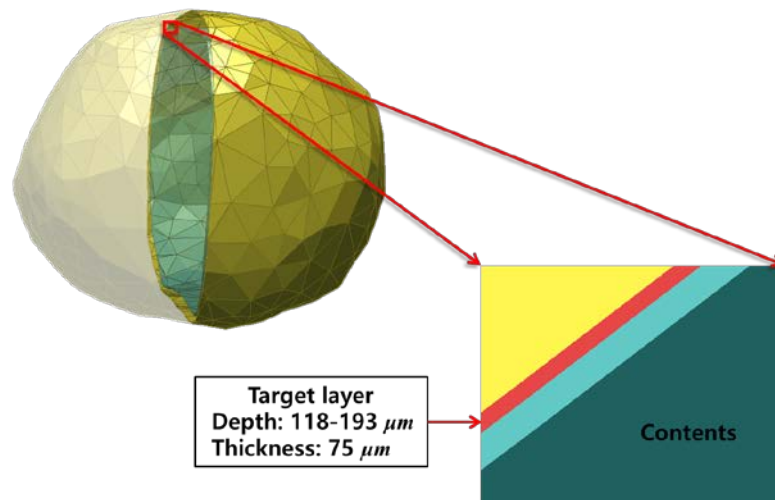
1080 (68)Figure 5.4 shows the airway model produced in the lungs of the male phantom along with
 1081 the original voxel model of the *Publication 110* male phantom. The airway models of the mesh
 1082 phantoms represent a complex tree structure, at the same time representing the thin target and
 1083 source layers. The total lengths of the airway branches for each generation of the lung tree are
 1084 in good agreement with their reference values; that is, the discrepancies are less than 10% for
 1085 all generations. More detailed information on the respiratory tract system can be found in Kim
 1086 et al. (2017).
 1087



1088 Fig. 5.4. Lung voxel model (left) and lung mesh model (right) for the male phantom (Kim et al., 2017).
 1089
 1090

1091 5.4. Urinary bladder

1092 (69)The target layer of the urinary bladder was also defined in the mesh phantoms. In the
 1093 urinary bladder, the basal cells of the epithelium are believed to be the relevant target cells at
 1094 radiogenic risk (Colin et al., 2009), but doses have previously been calculated to the whole wall
 1095 of the bladder (ICRP, 2016). Eckerman and Veinot (2018) derived the depth and thickness of
 1096 the basal cell layer of the urinary bladder as 118 μm and 75 μm, respectively, for the adult male
 1097 and 116 μm and 69 μm, respectively, for the adult female, assuming a constant and reference
 1098 urine volume of 200 cm³ for both phantoms. In the mesh phantoms, these values were adopted
 1099 to define the target layer in the urinary bladder, again by using the *Offset* command of the
 1100 *RapidformTM* software (INUS Technology Inc., Korea). Figure 5.5 shows the urinary bladder
 1101 of the male mesh phantom including the target layer.
 1102



1103
1104
1105

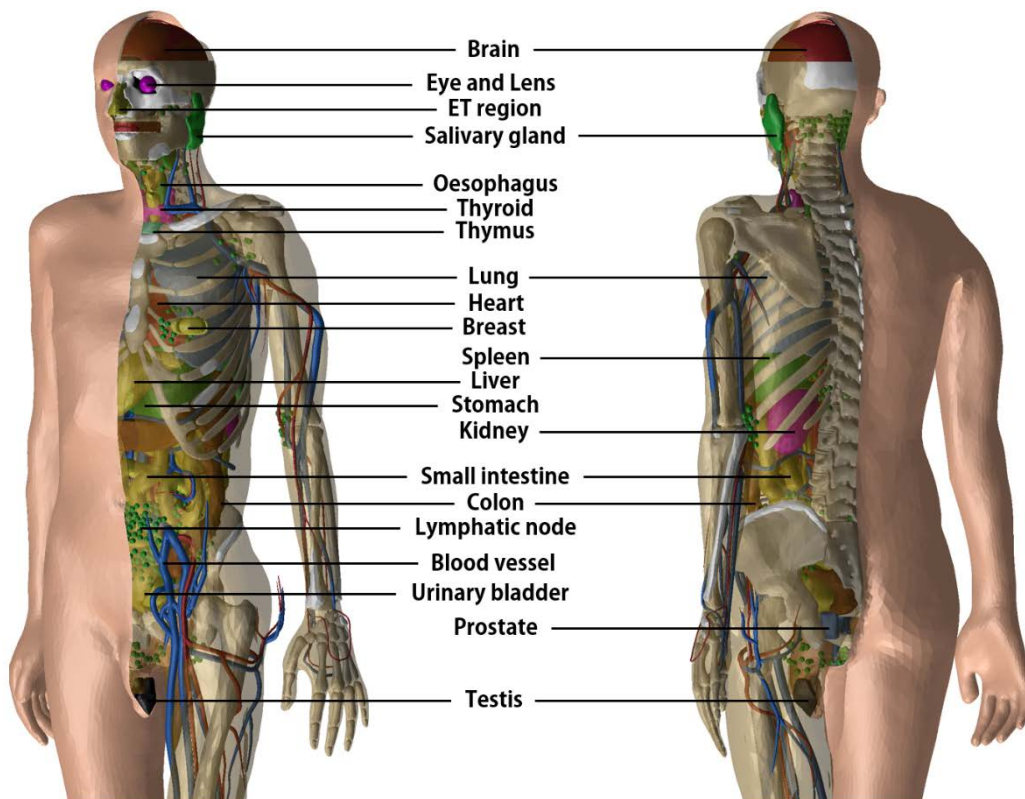
Fig. 5.5. Urinary bladder of the male mesh phantom including the target layer (red).

1106
1107

6. DESCRIPTION OF THE ADULT MESH-TYPE REFERENCE PHANTOMS

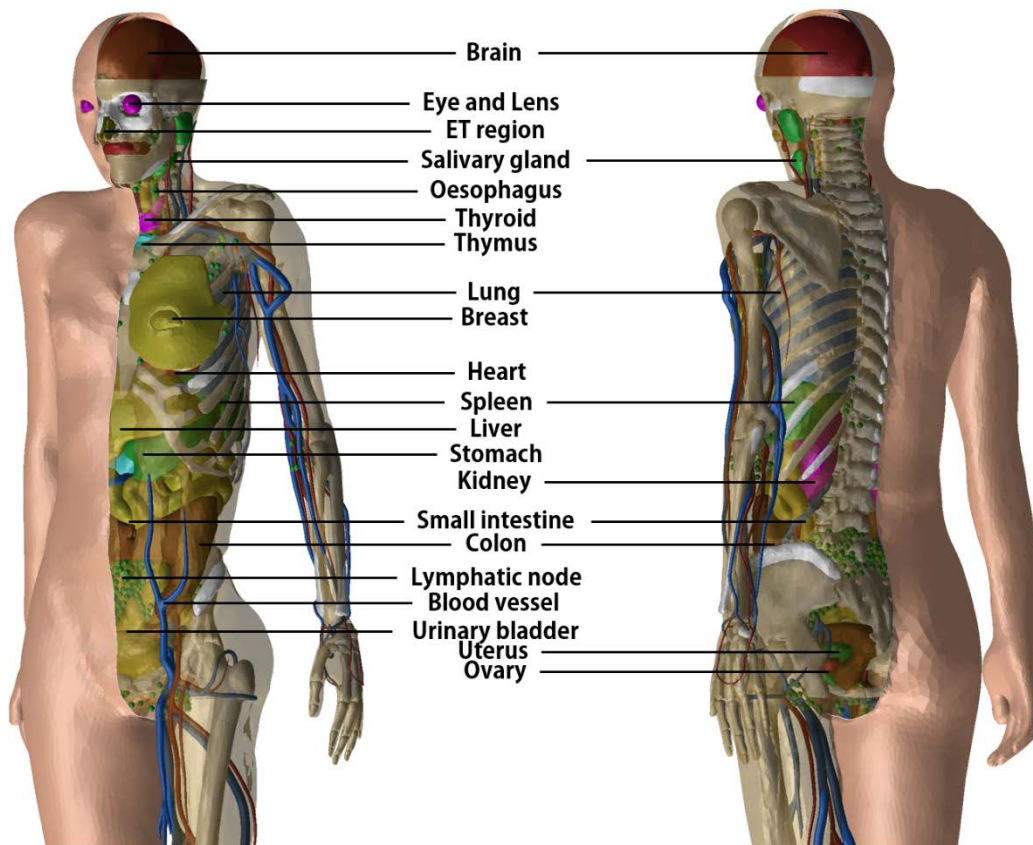
6.1. General phantom characteristics

1109 (70) Figures 6.1 and 6.2 show the adult male and female mesh-type reference computational
 1110 phantoms (MRCPs), respectively. The height and weight of the MRCPs are in accordance with
 1111 the reference values (male: 176 cm and 73 kg; female: 163 cm and 60 kg). The male phantom
 1112 is composed of 2.5 million triangular facets in the polygon mesh (PM) format and 8.2 million
 1113 tetrahedrons in the tetrahedral mesh (TM) format. The female phantom is composed of 2.6
 1114 million triangular facets in the PM format and 8.6 million tetrahedrons in the TM format. Note
 1115 that the TM-version MRCPs were directly converted from the PM-version MRCPs by using
 1116 the TetGen code (Si, 2015). The MRCPs include all the radiosensitive organs and tissues
 1117 relevant to dose assessment for ionising radiation exposure for radiological protection
 1118 purposes. Note that the micron-scale structure of the active bone marrow and skeletal
 1119 endosteum are not modelled in the MRCPs and, therefore, the calculation of the doses to these
 1120 skeletal tissues should involve fluence-to-dose response functions, such as those presented in
 1121 *Publication 116* (ICRP, 2010). The MRCPs include the tens-of-micrometre source and target
 1122 regions of the eye lens, skin, alimentary tract organs, respiratory tract organs and urinary
 1123 bladder. The lung airway models (representing the various branches of both the bronchi and
 1124 bronchioles) produced in the CSG format are incorporated into the MRCPs using the Geant4
 1125 code (Agostinelli et al., 2003) via the parallel-geometry technique (Apostolakis et al., 2008).
 1126



1127
1128
1129
1130

Fig. 6.1. Mesh-type ICRP adult male reference phantom.



1131
1132 Fig. 6.2. Mesh-type ICRP adult female reference phantom.
1133

1134 (71) The masses of the organs and tissues of the MRCs match the reference values inclusive
1135 of blood content (see Table 4.2) within 0.1% deviation. Table A.1 provides the numerical
1136 information of the MRCs including the organ ID numbers, medium, densities and masses for
1137 each organ and tissue. Table B.1 and Table B.2 provide the elemental composition for each
1138 medium for the male and female, respectively. Table C.1 provides the list of source regions,
1139 their acronyms and corresponding organ ID numbers in the phantoms. Table D.1 provides the
1140 list of target regions, their acronyms and corresponding organ ID numbers in the phantoms.

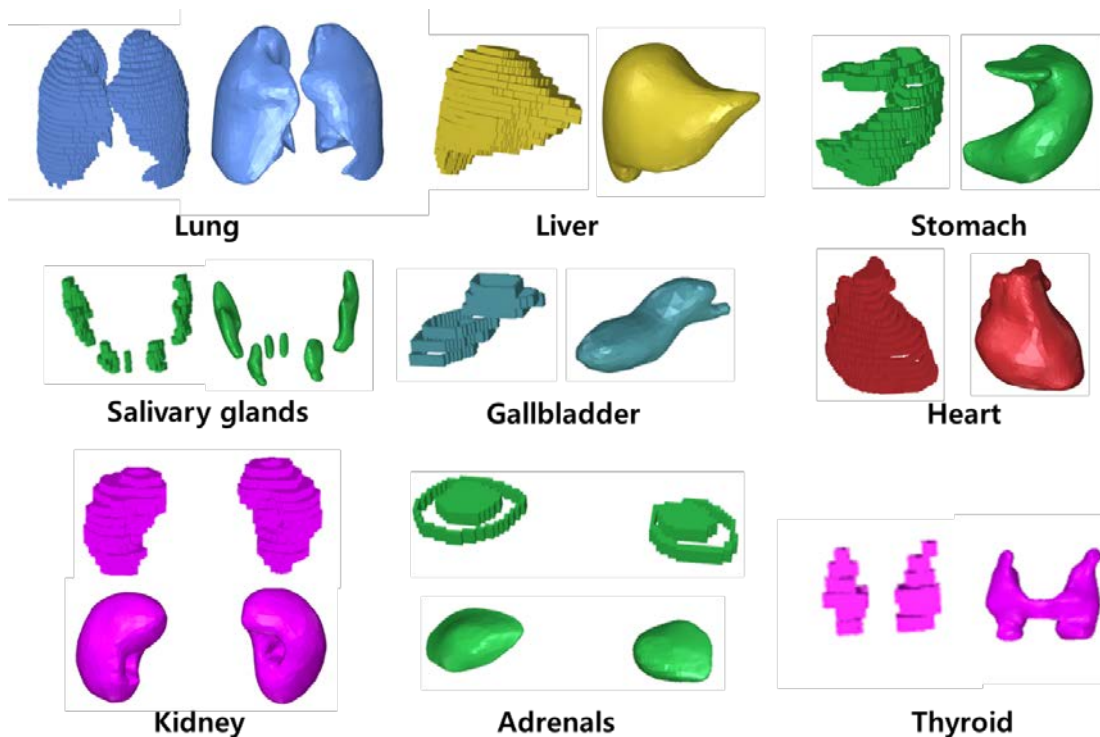
1141 (72) For the alimentary and respiratory tract organs, the dose values of the thin target regions,
1142 due to the tiny volumes, tend to have relatively larger statistical uncertainties when compared
1143 to other organs. For external exposures to penetrating radiation (such as photons and neutrons),
1144 the spatial gradients of the absorbed dose are very small, and thus the absorbed dose averaged
1145 over the thin target region tends to be close to the absorbed dose averaged over the entire region
1146 of the organ. Therefore, for these exposure cases, it is recommended that one use the entire
1147 region of the organ, not the thin target region, for dose calculation so as to save computation
1148 time.

1149 (73) On the other hand, the target region of the skin and eye lens should be used in dose
1150 calculation for all external exposure cases, considering that there will be significant dose
1151 differences between the target region and the entire region even for penetrating uncharged
1152 particles (such as photons and neutrons), because charged-particle equilibrium (CPE) is not
1153 well established in these superficial organs. For the skin dose calculation, computation time is
1154 no longer a problem assuming the entire skin is exposed to the incident radiation field. For the
1155 lens dose calculation, computation time can be significantly reduced by assuming that only the
1156 head of the phantoms is exposed to radiation.

1157 (74)The thin target regions of the alimentary and respiratory tract systems and the urinary
 1158 bladder should be used in dose calculation for the internal exposure cases when subregions of
 1159 these organs (e.g. contents) are considered as source regions. For these calculations,
 1160 computation time is no longer an issue considering the layered geometries of the source and
 1161 target regions.

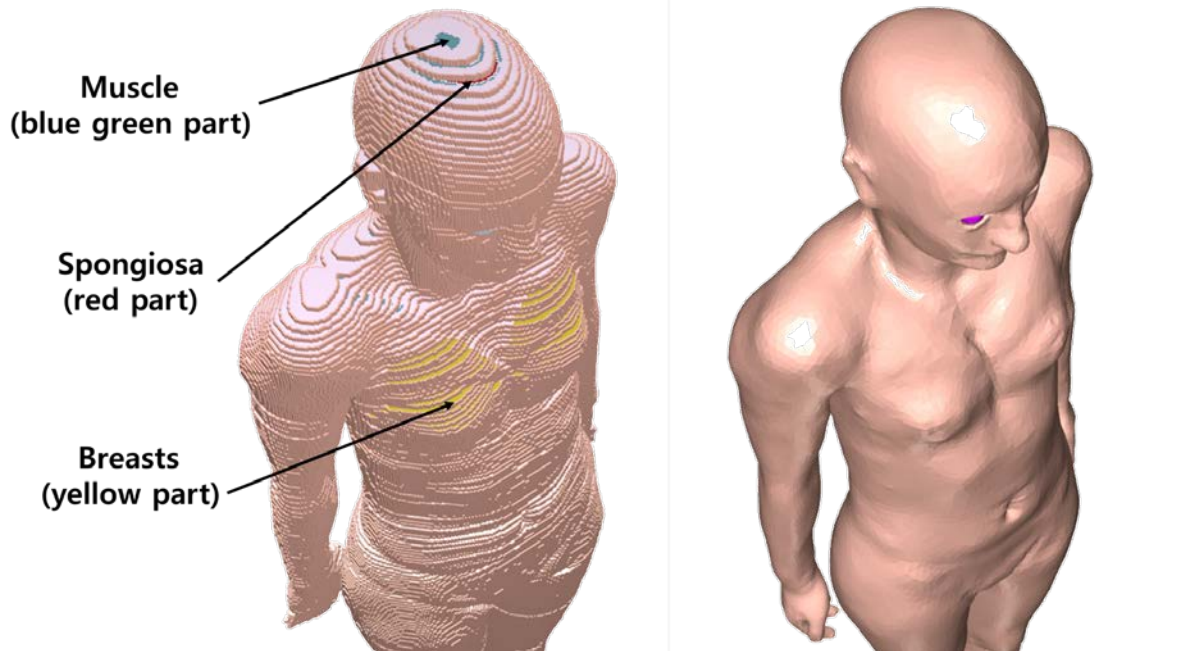
1162 (75)For cross-fire irradiation (e.g. stomach ← liver), it is recommended that one use the entire
 1163 region of the organ, not just the thin target region, for dose calculation, as once again, dose
 1164 gradients are small, and there will be savings in computation time. For electron cross-fire
 1165 irradiation, there could be significant dose discrepancies, depending on the electron energy and
 1166 organ topology, in which case it is recommended to use the thin target region.

1167 (76)The MRCPs have addressed the geometrical limitations of the *Publication 110* phantoms
 1168 due to the limited voxel resolution and the nature of voxel geometry. Figure 6.3 shows some
 1169 internal organs and tissues of the mesh-type male phantom alongside with those of the
 1170 *Publication 110* male phantom. It can be seen that the voxel models show stair-stepped surfaces,
 1171 whereas the mesh models show smooth surfaces in their 3D viewing. In addition, the
 1172 discontinuous structure of the hollow organs of the *Publication 110* phantoms is fully addressed
 1173 in the MRCPs. Figure 6.4 shows the mesh-type female phantom and the *Publication 110*
 1174 female phantom viewed in the superior-inferior direction. It can be seen that the *Publication 110*
 1175 phantoms are not fully enclosed by the skin, showing many holes and several radiosensitive
 1176 organs and tissues (such as breasts and muscle) directly exposed to the air. On the other hand,
 1177 the MRCPs are fully enclosed by the skin without any holes; this improvement will prevent
 1178 significant overestimates in DCs for these organs and tissues for specific situations of external
 1179 exposure to weakly penetrating radiation. Similarly, the spongiosa and medullary cavity of the
 1180 *Publication 110* phantoms are not fully enclosed by the cortical bone; this limitation is also
 1181 addressed in the MRCPs, as shown in Fig. 6.5.
 1182



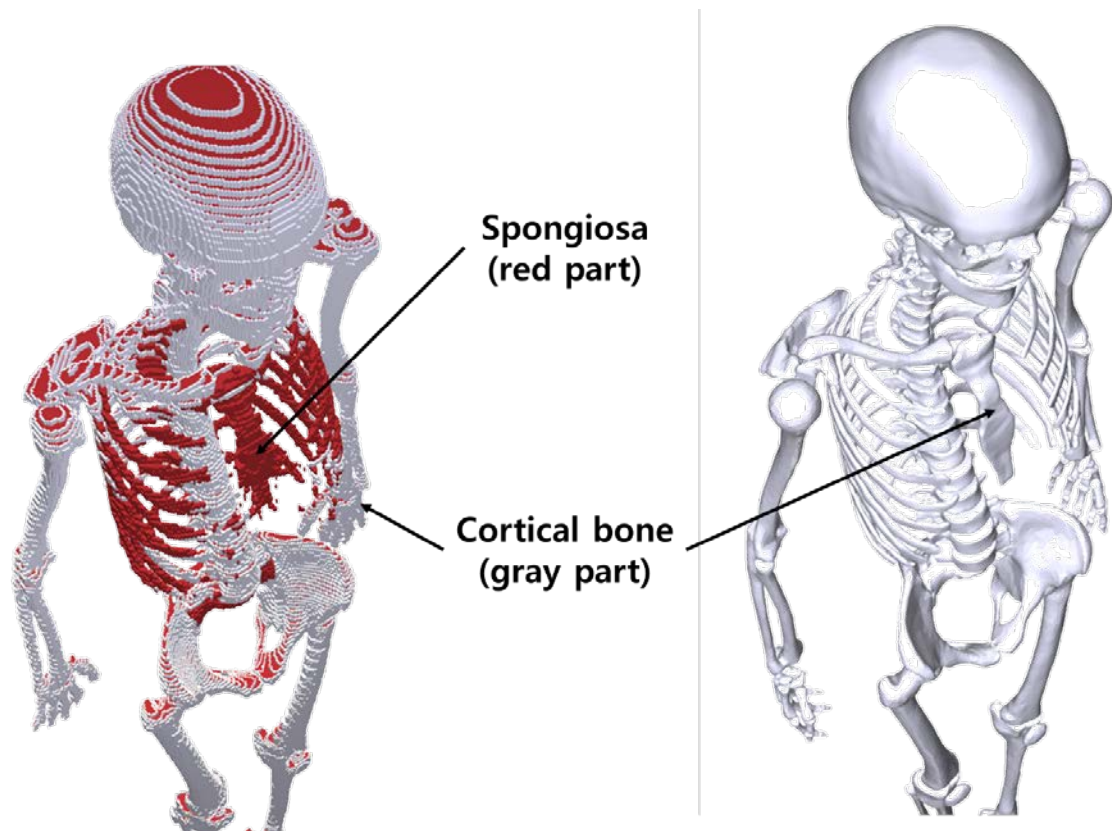
1183 Fig. 6.3. Comparison of organs and tissues of the mesh-type male phantom with those of the *Publication*
 1184 *110* male phantom.
 1185

1186



1187
1188
1189
1190

Fig. 6.4. ICRP-110 female phantom (left) and mesh-type female phantom (right); muscle (blue green part), spongiosa (red part) and breasts (yellow part) in ICRP-110 female phantom.



1191
1192
1193
1194

Fig. 6.5. Skeletal system of *Publication 110* female phantom (left) and mesh-type female phantom (right); spongiosa (red part) and cortical bone (gray part). The mesh phantom shows only cortical bone (gray part), which fully encloses inner structures (spongiosa and also medullary cavity).

1195 **6.2. Geometric similarity comparison with the adult voxel-type reference**
 1196 **phantoms**

1197 (77) In order to determine the geometric similarity between the MRCPs and the adult voxel-
 1198 type reference phantoms, the Dice Index (DI), Centroid Distance (CD) and Hausdorff Distance
 1199 (HD) for the organs and tissues between these phantoms were evaluated as shown in Table 6.1.
 1200 It can be seen that for most of the organs and tissues, the DI values were greater than 0.95, and
 1201 that the CD and HD values were less than 2 mm. These results demonstrate good geometrical
 1202 similarity between the MRCPs and the *Publication 110* phantoms in general.

1203 (78) There were, however, relatively large dissimilarities for some organs and tissues. For
 1204 example, the female hand bone showed the largest dissimilarity; the DI, CD and HD values
 1205 were 0.13, 27.8 mm and 15.6 mm, respectively. Such large dissimilarities are due mainly to
 1206 two reasons: (1) the organs and tissues such as spine, hands, feet and small intestine could not
 1207 be directly converted from the voxel models, and therefore were constructed with modelling
 1208 approaches, and (2) the organs and tissues such as ribs, liver, spleen and kidneys were more
 1209 significantly adjusted to include the blood content, even though these organs were mostly
 1210 constructed by using the direct conversion method.

1211 (79) The organ depth distributions (ODDs) and the chord length distributions (CLDs) of the
 1212 MRCPs were also compared with those of the *Publication 110* phantoms, as shown in Annexes
 1213 E and F. The ODDs represent the organ depth below the body surface, which mainly influences
 1214 external dose calculation, and the CLDs represent the distance between the target and source
 1215 organs/tissues, which mainly influences internal dose calculation. The comparison results
 1216 showed that the ODDs and CLDs of the MRCPs were generally in good agreement with those
 1217 of the *Publication 110* phantoms for most of the organs and tissues, even though the MRCPs
 1218 were adjusted for the blood inclusion.

1219 (80) The results of the geometric similarity comparison indicate that overall, the MRCPs
 1220 faithfully preserve the original shape and location of the organs and tissues in the *Publication*
 1221 *110* phantoms, and that therefore, they can be expected to provide similar dose values for
 1222 penetrating radiation in both external and internal exposures.

1223
 1224 Table 6.1. Dice index (DI), centroid distance (CD) and Hausdorff distance (HD) comparing the adult
 1225 mesh-type reference phantoms (MRCPs) and the adult voxel-type reference phantoms.

Organs	Male			Female		
	DI	CD (mm)	HD (mm)	DI	CD (mm)	HD (mm)
Humeri	0.88	0.8	1.5	0.92	0.6	0.7
Ulnae and radii	0.89	0.5	0.8	0.90	0.7	0.9
Wrists and hand bones	0.24	17.8	12.7	0.13	27.8	15.6
Clavicles	0.83	0.4	0.8	0.84	1.1	0.8
Cranium	0.76	3.3	1.6	0.83	1.6	1.0
Femora	0.89	0.4	1.8	0.94	1.1	0.9
Tibiae, fibulae and patellae	0.90	0.5	1.1	0.91	0.4	1.1
Ankles and foot bones	0.56	8.0	4.3	0.32	4.1	11.8
Mandible	0.85	0.5	0.9	0.84	1.4	2.0
Pelvis	0.89	0.3	1.0	0.93	0.4	0.6
Ribs	0.56	4.9	2.0	0.32	2.1	2.7
Scapulae	0.82	1.4	1.0	0.86	0.4	0.7
Cervical spine	0.57	4.2	2.8	0.60	4.5	2.0
Thoracic spine	0.67	6.6	2.6	0.70	6.0	2.5

Lumbar spine	0.70	5.1	2.0	0.63	9.3	2.5
Sacrum	0.86	1.3	1.0	0.80	0.8	1.0
Sternum	0.79	5.1	1.3	0.31	9.3	5.9
Teeth	0.92	0.8	0.3	0.87	1.2	0.5
Tongue	0.90	1.3	1.1	0.94	0.9	0.6
Oesophagus	0.68	1.8	1.3	0.67	4.3	1.5
Stomach	0.87	4.5	2.0	0.92	2.7	1.3
Small intestine	0.40	23.3	6.2	0.55	15.3	6.8
Large intestine	0.82	1.2	1.6	0.87	1.9	1.5
Salivary glands	0.87	0.4	0.9	0.91	0.9	0.6
Tonsils	0.92	0.3	0.4	0.82	0.4	0.6
Liver	0.85	5.0	4.1	0.86	4.1	3.7
Gall bladder	0.84	2.5	1.6	0.91	0.4	0.7
Pancreas	0.83	5.2	2.3	0.85	6.6	2.4
Heart	0.94	1.5	1.1	0.93	2.2	1.7
Kidneys	0.81	5.4	2.8	0.84	5.3	3.3
Ureters	0.61	0.6	1.1	0.73	0.7	0.8
Urinary bladder	0.94	0.5	1.1	0.95	0.6	0.8
Gonads	0.87	0.2	0.6	0.86	0.2	0.7
Prostate / uterus	0.90	0.5	0.8	0.90	0.4	0.9
Adrenals	0.46	1.0	2.0	0.83	0.6	0.9
Breasts	0.83	0.5	0.7	0.91	0.4	0.6
Brain	0.96	0.9	1.0	0.97	0.4	3.8
Pituitary glands	0.81	0.5	0.5	0.73	0.3	0.6
Spinal cord	0.86	0.9	0.5	0.84	0.4	0.5
Spleen	0.78	4.8	2.6	0.80	4.3	2.3
Thymus	0.88	0.2	0.8	0.77	2.0	1.3
Thyroid	0.77	2.0	1.1	0.88	0.6	0.6
ET	0.76	0.5	1.3	0.76	0.5	1.1
Trachea	0.87	0.5	0.9	0.85	2.3	1.0
Lungs	0.90	3.0	3.8	0.90	1.6	2.7

1226 6.3. Compatibility with Monte Carlo codes

1227 6.3.1. Monte Carlo codes

1228 (81)Most of the major general-purpose Monte Carlo simulation codes such as Geant4,
 1229 MCNP6, PHITS and FLUKA can now directly implement polygon mesh (PM) or tetrahedral
 1230 mesh (TM) geometries. The Geant4 code implements both PM and TM geometries by using
 1231 the *G4TessellatedSolid* class and *G4Tet* class, respectively (Agostinelli et al., 2003). The
 1232 MCNP6 code, as a merger of the MCNP5 and MCNPX versions, provides a new feature for
 1233 implementation of unstructured mesh geometries including TM geometries. Note that since the
 1234 version 1.1 beta of the MCNP6, the unstructured mesh geometry can support the transport of
 1235 most particles available in the MCNP6 code (Goorley et al., 2013), whereas in the previous
 1236 version (i.e. ver. 1.0), the transport of only neutrons and gammas was supported (Martz et al.,
 1237 2014). The PHITS code, since version 2.82, provides a new feature for implementation of TM
 1238 geometries (Sato et al., 2013). The FLUKA code can implement the PM geometry via FluDAG
 1239 (<http://svalinn.github.io/DAGMC/index.html>).

1240 **6.3.2. Computation time and memory usage**

1241 (82) Computation time was measured for Geant4 (ver. 10.02), MCNP6 (ver. 2.0 prerelease)
 1242 and PHITS (ver. 2.92) coupled with the female phantom of the TM format. The estimation was
 1243 performed on a single core of the Intel® Xeon® CPU X5660 (@ 2.80 GHz and 128 GB
 1244 memory). First, the estimated initialisation times for all Monte Carlo codes were found to be a
 1245 few minutes, which are negligible compared to the total computation time, on the order of a
 1246 day, which is a typical value for dose calculations. (Furuta et al., 2017).

1247 (83) Run time was also measured with a single core of the same server computer to achieve
 1248 2% of relative error in effective dose for the left-lateral (LLAT) irradiation geometry of particle
 1249 beams; photons and electrons (10 keV–10 GeV) and neutrons (10^{-9} MeV–20 MeV). For
 1250 Geant4, the physics library of the *G4EmLivermorePhysics* was used to transport photons and
 1251 electrons. To transport neutrons, the physics models and cross-sections of the
 1252 *NeutronHPThermalScattering*, *NeutronHPElastic*, *ParticleHPInelastic*, *Neutron-HPCapture*
 1253 and *NeutronHPFission* were used. A secondary cut value of 1 μm was applied to photons and
 1254 electrons. For the PHITS code, the physics library of *AcelibJ40* was used to transport photons,
 1255 electrons and neutrons. For the MCNP6 code, the physics libraries of MCPLIB84, EL03 and
 1256 ENDF70 were used to transport photons, electrons and neutrons, respectively. Considering that
 1257 a secondary cut value of 1 μm was used for the Geant4 calculations, the equivalent energy cut
 1258 values were used in the PHITS and MCNP6 codes. The ‘implicit capture’ variance reduction
 1259 technique was turned off for both PHITS and MCNP6 codes.

1260 (84) The Geant4 result showed that for photons, the measured run times were within the range
 1261 of 1–30 minutes for all of the considered energies. For electrons, the run times were less than
 1262 1 hour for energies higher than 0.06 MeV, but for the lower energies (≤ 0.06), the run times
 1263 were much longer, i.e. 20–60 hours. These long run times are due to the facts that these low-
 1264 energy electrons cannot penetrate the skin dead layer and that only the secondary photons,
 1265 produced from electron interactions, contribute to skin dose, and eventually effective dose. For
 1266 neutrons, the run times were within the range of 2–30 hours for all of the considered energies.

1267 (85) The run times of the PHITS code for photons and electrons were generally much longer,
 1268 i.e. 3–20 times when compared to the Geant4 code. Similarly, the run times of the MCNP6
 1269 code were also longer, i.e. 6–30 times than those of the Geant4 code. For neutrons, the run
 1270 times of the PHITS code were shorter by 2–8 times than those of the Geant4 code, whereas
 1271 those of the MCNP6 were 3–4 times longer than those of the Geant4 code.

1272 (86) Memory usage was also measured for the three Monte Carlo codes. The Geant4 required
 1273 ~10.6 GB, which is slightly smaller than that, ~13.7 GB, of MCNP6. PHITS, when compared
 1274 to Geant4 and MCNP6, required much smaller memory, i.e. ~1.2 GB, which is due to the fact
 1275 that PHITS, in contrast to other codes, uses dynamic allocation for most of the memory needed
 1276 for implementing the MRCP. In general, considering memory usage, all of the above Monte
 1277 Carlo codes can run the MRCPs in a personal computer equipped with 64 GB at maximum.
 1278

1279 7. DOSIMETRIC IMPACT OF THE ADULT MESH-TYPE REFERENCE 1280 PHANTOMS

1281 (87) In order to investigate the impact of the improved representation of the organs and tissues
1282 in the adult mesh-type reference computational phantoms (MRCPs) on dose coefficient (DC)
1283 calculations, DCs of organ dose and effective dose and specific absorbed fractions (SAFs) were
1284 calculated for some selected external and internal exposure cases using the MRCPs. The
1285 calculated values were then compared with the values provided in *Publications 116* and *133*
1286 (ICRP, 2010, 2016) which were calculated by using the *Publication 110* phantoms (ICRP,
1287 2009) and the stylised models adopted in the previous *Publications* (ICRP, 1994a, 2006, 2016).

1288 (88) In Annex H, the DCs of the MRCPs for external exposure to photons, neutrons, electrons
1289 and helium ions are compared with the *Publication 116* values. For photons, with some
1290 exceptions at very low energies, the DCs of the MRCPs were found to be very close to the
1291 *Publication 116* values for both organ dose and effective dose. For neutrons, the organ DCs of
1292 the MRCPs show some differences from the *Publication 116* values, but are very close to the
1293 values calculated using the *Publication 110* phantoms and the Geant4 code that was the same
1294 code used in the calculation of the MRCP DCs. This result indicates that the differences from
1295 the *Publication 116* values are not mainly due to the difference in phantom geometry or
1296 material composition, but just to the difference in Monte Carlo codes and cross-section data /
1297 physics models used in the calculations. Note that for neutrons, the *Publication 116* values
1298 were calculated using four Monte Carlo codes (MCNPX, PHITS, FLUKA and Geant4) and
1299 then the final reference values of the dose coefficients were taken as averaged values following
1300 an extensive smoothing process (ICRP, 2010).

1301 (89) For charged particles (i.e. electrons and alphas) in Annex H, the DCs of the MRCPs for
1302 some organs (e.g. RBM, breasts and skin) showed large differences from the *Publication 116*
1303 values, which are mainly due to the improved representation of the thin tissues (e.g. cortical
1304 bone and skin) in the MRCPs over the voxel-type *Publication 110* phantoms (see Chapter 2).
1305 Large differences were also found in effective dose DCs for electrons (< 1 MeV) and helium
1306 ions (< 10 MeV/u); these differences are mainly caused by the differences of the skin DCs due
1307 to the consideration of the 50- μm -thick skin target layer in the MRCPs. Note that in real
1308 situations of electron exposures, polyenergetic electrons are generally encountered, for which
1309 the differences in effective doses are much less significant. For example, the difference in
1310 effective dose between the MRCPs and the *Publication 110* phantoms resulting from the
1311 isotropic (ISO) irradiation of beta radiations (^{14}C , ^{186}Re , ^{32}P , $^{90}\text{Sr}/^{90}\text{Y}$ and ^{106}Rh) are less than
1312 2 times, except for ^{14}C for which the difference is ~ 4 times. Note that ^{14}C emits very low energy
1313 electrons (0.15 MeV maximum) and thus is generally not of concern for external exposures. In
1314 real situations of helium ion exposures, short-range alpha exposures are mostly encountered,
1315 which are practically unimportant for radiation protection purposes.

1316 (90) In Annex I, the specific absorbed fractions (SAFs) of the MRCPs for photons and
1317 electrons are compared with the *Publication 133* values for selected source organs/tissues (=
1318 cortical bone, liver, lungs and thyroid). For photons, with some exceptions, the SAFs of the
1319 MRCPs were found to be very close to the *Publication 133* values. One exception was the
1320 RBM as a target, where the SAFs of the MRCPs were much smaller than the *Publication 133*
1321 values at low energies. These differences are due mainly to the fact that in the MRCPs, the
1322 spongiosa is fully enclosed by the cortical bone, whereas this is not the case for the *Publication*
1323 *110* phantoms (see Fig. 6.5). In contrast, for the colon \leftarrow cortical bone case, the SAFs of the
1324 MRCPs were found to be greater than the *Publication 133* values, which is again due mainly
1325 to the difference of the distribution of the cortical bone; that is, in the *Publication 110* phantoms,

1326 the cortical bone does not fully enclose the spongiosa and is not uniformly distributed,
1327 especially in the ribs, where the cortical bone is rarely distributed in the regions that are very
1328 close to the colon.

1329 (91) For electrons in Annex I, the SAFs of the MRCPs were found to be very close to the
1330 *Publication 133* values for all of the self-irradiation cases. However, large differences were
1331 found for most cross-fire irradiation cases, which is due mainly to the different geometry
1332 formats of the phantoms (smooth surface of the MRCPs vs. stair-stepped surface of the
1333 *Publication 110* phantoms). The significances of these differences on the effective dose will
1334 be dependent on the biokinetics or chemical form of ingested or inhaled radionuclide.

1335 (92) In Nguyen et al. (2015), the lens DCs of the MRCPs for external exposure to photons and
1336 electrons were compared with the *Publication 116* values that were produced with both the
1337 *Publication 110* voxel phantoms and the mathematical eye model of Behrens et al. (2009). The
1338 comparison was complicated because different phantoms were used for different cases in
1339 *Publication 116*. For photons, the lens DCs of the MRCPs were not found to be much different
1340 from the *Publication 116* values for all of the irradiation geometries, except for the PA
1341 geometry and low energies (< 0.1 MeV), in which cases the lens DCs of the MRCPs were
1342 smaller than the *Publication 116* values. These differences are not very important in practice,
1343 and are due mainly to the differences in head structure and composition between the MRCPs
1344 and the mathematical head phantom (incorporating the eye model) used to produce the
1345 *Publication 116* values (ICRP 2010). For electrons, generally the lens DCs of the MRCPs were
1346 found to be very close to the *Publication 116* values at the energies ≥ 2 MeV, but at the lower
1347 energies (< 2 MeV), relatively large differences were found. The largest differences were once
1348 again found in the PA geometry, which result is due to the differences in head structure and
1349 composition between the MRCPs and the *Publication 110* phantoms used to produce the
1350 *Publication 116* values (ICRP 2010). For the AP irradiation geometry, which is the most
1351 important irradiation geometry in radiation protection, the differences were much smaller, and
1352 significant differences were observed only at very low energies (< 0.7 MeV), where primary
1353 electrons cannot reach to the lens and thus very low energy secondary photons are the only
1354 contribution to lens dose. More detailed discussions on the comparison of the lens DCs can be
1355 found in Nguyen et al. (2015).

1356 (93) In Kim et al. (2017), the electron SAFs of the MRCPs for the alimentary and respiratory
1357 tract systems were compared with the *Publication 133* values that were calculated using the
1358 supplementary stylised models (ICRP, 1994a, 2006, 2016). Generally, a good agreement was
1359 observed for the oral mucosa, oesophagus and bronchi (BB) region. In contrast, for the stomach,
1360 small intestine, large intestine, extrathoracic (ET) region and bronchiole (bb) region, relatively
1361 large differences were observed due mainly to the anatomical differences of these organs as
1362 described by the MRCPs and the stylised models. With some exceptions (stomach and
1363 bronchioles (bb) for the alveolar-interstitial region as a source), the MRCPs tend to
1364 overestimate SAFs when compared to the *Publication 133* values; the maximum difference
1365 was about 16 times for the large intestine for the contents as a source. More detailed discussions
1366 on the comparison of the SAFs for the alimentary and respiratory tract systems can be found
1367 in Kim et al. (2017).

1368 (94) The male MRCP was used to calculate the SAFs for alphas and electrons for the urinary
1369 bladder wall \leftarrow urinary bladder content case, and then the calculated values were compared
1370 with the values which were calculated using a stylised model for the male (Eckerman and
1371 Veinot, 2018). Note that the values of the MRCP were not compared with the values in
1372 *Publication 133* because these values were calculated for the entire wall of the urinary bladder,
1373 not for the radiosensitive basal layer of the wall. The MRCP values were found to be slightly

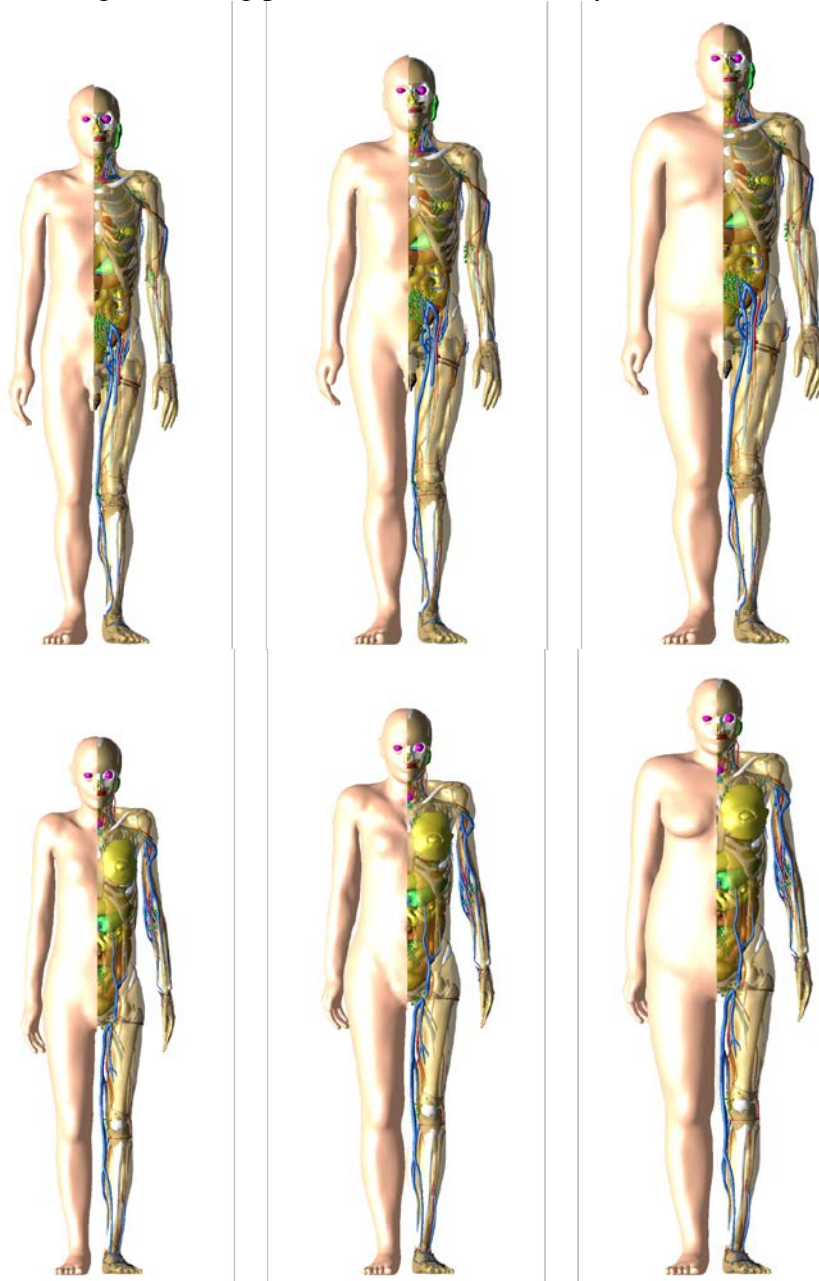
1374 less than the values of the stylised model, the differences being less than a few percent, which
1375 is mainly due to the slight difference (~ 6%) in the target mass between the MRCP urinary
1376 bladder model and the idealised spherical stylised model used in Eckerman and Veniot (2018).
1377

1378 **8. APPLICATION: CALCULATION OF DOSE COEFFICIENTS FOR**
1379 **INDUSTRIAL RADIOGRAPHY SOURCES**

1380 (95) Accidents involving industrial radiography sources could result in very high radiation
1381 doses to workers, causing serious injuries and even death (IAEA, 2011). In addition, members
1382 of the public could be accidentally exposed if industrial radiography sources are not properly
1383 controlled or regulated. According to the IAEA (1998), industrial radiography accounts for
1384 approximately half of all reported accidents for nuclear-related industries, in both developed
1385 and developing countries. Radiation accidents could result in high radiation doses inducing
1386 acute radiation syndrome (ARS), which can be classified into hematopoietic (3–5 Gy),
1387 gastrointestinal (5–15 Gy) and cerebrovascular (> 15 Gy) syndromes (ICRP, 2007). In order to
1388 effectively treat patients (i.e. exposed individuals) with ARS, it is necessary to perform medical
1389 triage accurately and quickly, whereby those patients who will develop symptoms are
1390 separately identified from those who do not require medical intervention (Gougelet et al.,
1391 2010). Individual radiation doses can be estimated using various dosimetry techniques based
1392 on biological, physical or computational approaches. However, all of the existing dosimetry
1393 techniques have limitations, and thus none of them can be used as a stand-alone tool in a
1394 satisfactory manner for most radiation accident scenarios (Ainsbury et al., 2011). For example,
1395 biological and physical dosimetry techniques generally require several days for sample
1396 collection and analysis. Moreover, these techniques are impractical for use in a large-scale
1397 accident involving a multitude of exposed individuals (Gougelet et al., 2010; Rea et al., 2010;
1398 Swartz et al., 2014; Kulka et al., 2017) and are generally limited to estimating the whole-body
1399 dose, without information on organ/tissue specific doses or their dose distribution (Ainsbury et
1400 al., 2011). Note that the knowledge of the whole-body dose may not be sufficient, especially
1401 in partial-body or localised exposures (Ainsbury et al., 2011; Lu et al., 2017). Organ/tissue
1402 doses or dose distributions can be estimated using computational dosimetry techniques (e.g.
1403 Monte Carlo simulations with computational human phantoms), if reliable information on the
1404 accident scenario is available, including the source geometry and duration of exposure (Lu et
1405 al., 2017), which are often unclear immediately following accidental irradiation situations
1406 (Clairand et al., 2006; Ainsbury et al., 2011). Due to the fact that no single technique fully
1407 meets the criteria of an ideal dosimeter for use in accidental situations, an integrated approach
1408 using multiple dosimetry techniques is considered to be the best strategy (Ainsbury et al., 2011;
1409 Sullivan et al., 2013; Ainsbury et al., 2017). Doses calculated with computational
1410 anthropomorphic phantoms can be used as one of the dose estimators, particularly as an ‘initial,
1411 rapid estimator’.

1412 (96) For dose estimation of individuals exposed to such high doses, consideration of the
1413 reference person may be insufficient, particularly when the body size of the individual involved
1414 in the accident is significantly different from that of the phantom representing the reference
1415 person. In such cases, the dose could be better approximated by using DCs calculated with a
1416 non-reference computational phantom whose body size is close to that of the actual person. To
1417 demonstrate this approach, non-reference adult male and female phantoms, representing the
1418 10th and 90th percentiles of the Caucasian population, were developed in this report. The 10th
1419 percentile phantoms, which represent small persons, were constructed by decreasing the size
1420 of the MRCPs to the 10th percentile standing height and the 10th percentile body mass (male:
1421 1.672 m and 55.9 kg and female: 1.549 m and 44.2 kg). Similarly, the 90th percentile phantoms,
1422 which represent large persons, were constructed by increasing the size of the MRCPs to the
1423 90th percentile standing height and the 90th percentile body mass (male: 1.858 m and 108.4 kg
1424 and female: 1.717 m and 94.1 kg). Figure 8.1 shows the 10th and 90th percentile phantoms,

1425 along with the MRCPs. The height and mass values were derived from the PeopleSize 2008
 1426 Professional data (<http://www.openerg.com>). The torso, arms, and legs were scaled considering
 1427 the lean body mass (LBM) (Deurenberg et al., 1991; Pieterman et al., 2002). The head was
 1428 scaled separately, using the PeopleSize 2008 Professional data and the US Army
 1429 Anthropometric Survey (ANSUR II) data (Gordon et al., 2014). More detailed information on
 1430 scaling can be found in Lee et al. (2018). The internal organs and tissues of the phantoms were
 1431 modified via the scaling/deforming procedures as described by Lee et al. (2018).



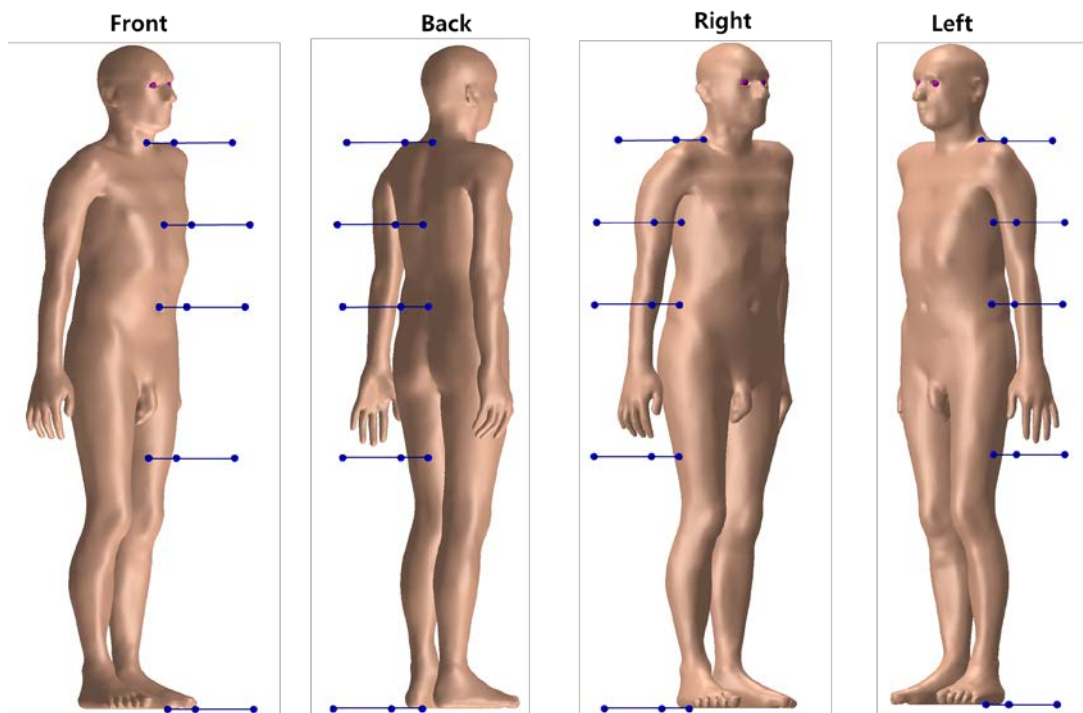
1432

1433

1434 Fig. 8.1. Computational phantoms: 10th percentile phantom (left), MRCP (middle) and 90th percentile.

1435 (97) In order to evaluate accidental exposures from industrial radiography sources, dose
 1436 coefficients (DCs) were calculated using the adult MRCPs as well as the 10th and 90th percentile
 1437 phantoms, implemented into the Geant4 Monte Carlo code (ver. 10.02) (Agostinelli et al.,
 1438 2003). The most commonly used industrial radiography sources, i.e. ¹⁹²Ir, ¹³⁷Cs/^{137m}Ba and

1439 ^{60}Co , were simulated as point sources placed near each of the mesh-type phantoms. ^{192}Ir emits
 1440 gamma rays with energies up to 0.820 MeV and a mean energy of 0.377 MeV, ^{137}Cs emits
 1441 0.662 MeV gamma rays, and ^{60}Co emits 1.33 and 1.17 MeV gamma rays. The point sources
 1442 were assumed to be located at three different distances (0.005, 0.1 and 0.3 m) in four directions
 1443 (anterior, posterior, right lateral and left lateral) at five levels (ground, middle thigh and lower,
 1444 middle and upper torso) (see Fig. 8.2). In addition, three longer distances (1, 1.5 and 3 m) were
 1445 modelled in the four directions at the lower torso level. The source distance used in the
 1446 calculations is the distance from the surface of the phantom, except for the anterior and
 1447 posterior directions at the ground and middle thigh levels, for which the distance is calculated
 1448 from the centre of the imaginary segment tangent to the surfaces of the left and right legs at the
 1449 given level.
 1450
 1451



1452
 1453 Fig. 8.2. Source locations at three distances (0.005, 0.1 and 0.3 m) at five levels (ground, middle thigh
 1454 and lower, middle and upper torso) in four directions (anterior, posterior, right lateral and left lateral).

1455
 1456 (98) In order to consider the doses of those organs/tissues that might manifest acute
 1457 radiation syndrome, the doses for red bone marrow (RBM), brain, lungs, small and large
 1458 intestine were calculate as organ/tissue-averaged absorbed dose per source disintegration (Gy
 1459 $\text{s}^{-1} \text{Bq}^{-1}$). The RBM DCs were calculated by using the fluence-to-absorbed dose response
 1460 functions (DRF) reported in Annex D of *Publication 116* (ICRP, 2010). In addition, the DCs
 1461 of effective dose (effective dose per source disintegration) were calculated and could be used
 1462 for the dosimetry of individuals who are exposed at lower doses related to stochastic effects.
 1463 Effective doses cannot be calculated using non-reference phantoms (i.e., 10th and 90th
 1464 percentile phantoms) and, therefore, in this report, the DCs of effective doses were calculated
 1465 using only the MRCs. The statistical errors of the calculated values were less than 5% for all
 1466 cases. A complete set of the DCs calculated with the MRCs and the 10th and 90th percentile
 1467 phantoms are given in Annex J.

1468 (99) Furthermore, the influence of different postures during exposure was investigated by
1469 calculating DCs using a set of non-standing phantoms (walking, sitting, bending, kneeling and
1470 squatting postures) that were constructed by modifying the MRCPs. For this purpose, the DCs
1471 were calculated for the lowest-energy source (i.e. ^{192}Ir) located 1 m from the phantom surface
1472 in the four directions of the lower-torso level. The calculated DCs of the non-standing
1473 phantoms were then compared with those of the standing MRCPs. The results of this limited
1474 investigation showed that the influence of different postures on the DC is not very large:
1475 generally less than 30%. It was, therefore, decided not to calculate the DCs of the non-standing
1476 phantoms.

1477 (100) Note that the DCs in this report were calculated assuming point sources, not considering
1478 the source geometry. The user can consider the self-shielding effect of the source by applying,
1479 to the values in Annex J, the source self-shielding factors which were calculated for different
1480 thicknesses of radioactive material and capsule wall. The calculated values are given in Annex
1481 J.

1482

1483

REFERENCES

- 1484 Agostinelli, S., Allison, J., Amako, K., et al., 2003. GEANT4—a simulation toolkit. Nucl. Instrum.
 1485 Methods. Phys. Res. A, 506, 250–303.
- 1486 Ainsbury, E.A., Bakhanova, E., Barquinero, J.F., et al., 2011. Review of retrospective dosimetry
 1487 techniques for external ionizing radiation exposures. Radiat. Prot. Dosim. 47, 573–592.
- 1488 Ainsbury, E.A., Badie, C., Barnard, S., et al., 2017. Integration of new biological and physical
 1489 retrospective dosimetry methods into EU emergency response plans – a joint RENEB and
 1490 EURADOS inter-laboratory comparison. Int. J. Radiat. Biol. 93, 99–109.
- 1491 Apostolakis, J., Asai, M., Cosmo, G., et al., 2008. Parallel geometries in Geant4: foundation and recent
 1492 enhancements. IEEE. Nucl. Sci. Symp. Conf. Rec, pp. 883–886.
- 1493 Behrens, R., Dietze, G., Zankl, M., 2009. Dose conversion coefficients for electron exposure of the
 1494 human eye lens. Phys. Med. Biol. 54, 4069–87.
- 1495 Bolch, W., Lee, C., Wayson, M., et al., 2010. Hybrid computational phantoms for medical dose
 1496 reconstruction. Radiat. Environ. Biophys. 49, 155–168.
- 1497 Brash, J.C., Jamieson, E.B., 1943. Cunningham’s Textbook of Anatomy. Oxford University Press,
 1498 New York.
- 1499 Clairand, I., Trompier, F., Bottollier-Depois, J.F., et al., 2006. EX vivo ESR measurements associated
 1500 with Monte Carlo calculations for accident dosimetry: application to the 2001 Georgian accident.
 1501 Radiat. Prot. Dosim. 119, 500–505.
- 1502 Colin, P., Koenig, P., Ouzzane, A., et al., 2009. Environmental factors involved in carcinogenesis of
 1503 urothelial cell carcinomas of the upper urinary tract. BJU Int. 104, 1436–1440.
- 1504 Cristy, M., 1980. Mathematical phantoms representing children of various ages for use in estimates of
 1505 internal dose. ORNL Report TM-367. Oak Ridge National Laboratory, Oak Ridge, TN.
- 1506 Cristy, M., Eckerman, K.F., 1987. Specific absorbed fractions of energy at various ages from internal
 1507 photon sources. Part I: Methods. ORNL Report TM-8381/V1. Oak Ridge National Laboratory, Oak
 1508 Ridge, TN.
- 1509 Deurenberg, P., Weststrate, J. A., Seidell, J. C., 1991. Body mass index as a measure of body fatness:
 1510 age- and sex-specific prediction formulas. Br. J. Nutr. 65, 105–114.
- 1511 Dice, L.R., 1945. Measures of the amount of ecologic association between species. Ecology 26, 297–
 1512 302.
- 1513 Eckerman, K.F., Veinot, K.G., 2018. Transitional Epithelium of Urinary Bladder – Dosimetric Data for
 1514 Cell at Risk. IEEE TRPMS, (submitted).
- 1515 Edelsbrunner, H., Kirkpatrick, D., Seidel, R., 1983. On the shape of a set of points in the plane. IEEE
 1516 Trans. Inf. Theory 29, 551–559.
- 1517 Furuta, T., Sato, T., Han, M.C., et al., 2017. Implementation of tetrahedral-mesh geometry in Monte
 1518 Carlo radiation transport code PHITS. Phys. Med. Biol. 62, 4798–4810.
- 1519 GEO kompakt, 2005. Das Wunder Mensch, Gruner+Jahr, Hamburg.
- 1520 Goorley, J.T., James, M.R., Booth, T.E., et al. 2013. Initial MCNP6 release overview-MCNP6 version
 1521 1.0. Report LA-UR-13-22934. Los Alamos National Laboratory, Los Alamos, NM.
- 1522 Gordon, C. C., Blackwell, C. L., Bradtmiller, B., et al. 2014. 2012 Anthropometric Survey of U.S. Army
 1523 Personnel: Methods and Summary Statistics. NATICK/TR-15/007. Natick, MA: U.S. Army Natick
 1524 Soldier Research, Development, and Engineering Center.
- 1525 Gougelet, R.M., Rea, M.E., Nicolalde, R.J., et al., 2010. The View from the Trenches Part 1: Emergency
 1526 Medical Response Plans and the Need for EPR Screening. Health Phys. 98, 118–127.
- 1527 Hausdorff, F., 1918. Dimension und äußeres Maß. Math. Ann. 79, 157–179.
- 1528 Han, M.C., Yeom, Y.S., Kim, C.H., et al., 2015. New approach based on tetrahedral-mesh geometry
 1529 for accurate 4D Monte Carlo patient-dose calculation. Phys. Med. Biol. 60, 1601–1612.
- 1530 IAEA, 1998. Lessons Learned from Accidents in Industrial Radiography. Safety Standards Series No.
 1531 7. International Atomic Energy Agency, Vienna.
- 1532 IAEA, 2011. Radiation Safety in Industrial Radiography. Safety Standards Series No. SSG-11.
 1533 International Atomic Energy Agency, Vienna.

- 1534 ICRP, 1975. Report on the Task Group on Reference Man. ICRP Publication 23. Pergamon Press,
1535 Oxford.
- 1536 ICRP, 1977. Recommendations of the International Commission on Radiological Protection. ICRP
1537 Publication 26. Ann. ICRP 1(3).
- 1538 ICRP, 1979. Limits for Intakes of Radionuclides by Workers. Part 1. ICRP Publication 30. Ann. ICRP
1539 2 (3/4).
- 1540 ICRP, 1988. Radiation Dose to Patients from Radiopharmaceuticals. ICRP Publication 53. Ann. ICRP
1541 18 (1-4).
- 1542 ICRP, 1990. Age-dependent Doses to Members of the Public from Intake of Radionuclides - Part 1.
1543 ICRP Publication 56. Ann. ICRP 20 (2).
- 1544 ICRP, 1991a. 1990 Recommendations of the International Commission on Radiological Protection.
1545 ICRP Publication 60. Ann. ICRP 21 (1-3).
- 1546 ICRP, 1991b. Annuals Limits on Intake of Radionuclides by Workers Based on the 1990
1547 Recommendations. ICRP Publication 61. Ann. ICRP 21 (4).
- 1548 ICRP, 1993. Age-dependent Doses to Members of the Public from Intake of Radionuclides - Part 2
1549 Ingestion Dose Coefficients. ICRP Publication 67. Ann. ICRP 23 (3/4).
- 1550 ICRP, 1994a. Human Respiratory Tract Model for Radiological Protection. ICRP Publication 66. Ann.
1551 ICRP 24 (1-3).
- 1552 ICRP, 1994b. Dose Coefficients for Intakes of Radionuclides by Workers. ICRP Publication 68. Ann.
1553 ICRP 24 (4).
- 1554 ICRP, 1995a. Age-dependent Doses to Members of the Public from Intake of Radionuclides - Part 3
1555 Ingestion Dose Coefficients. ICRP Publication 69. Ann. ICRP 25 (1).
- 1556 ICRP, 1995b. Age-dependent Doses to Members of the Public from Intake of Radionuclides - Part 4
1557 Inhalation Dose Coefficients. ICRP Publication 71. Ann. ICRP 25 (3-4).
- 1558 ICRP, 1996a. Age-dependent Doses to the Members of the Public from Intake of Radionuclides - Part
1559 5 Compilation of Ingestion and Inhalation Coefficients. ICRP Publication 72. Ann. ICRP 26 (1).
- 1560 ICRP, 1996b. Conversion Coefficients for use in Radiological Protection against External Radiation.
1561 ICRP Publication 74. Ann. ICRP 26 (3/4).
- 1562 ICRP, 1998. Radiation Dose to Patients from Radiopharmaceuticals (Addendum to ICRP Publication
1563 53). ICRP Publication 80. Ann. ICRP 28 (3).
- 1564 ICRP, 2002. Basic Anatomical and Physiological Data for Use in Radiological Protection Reference
1565 Values. ICRP Publication 89. Ann. ICRP 32 (3-4).
- 1566 ICRP, 2006. Human Alimentary Tract Model for Radiological Protection. ICRP Publication 100. Ann.
1567 ICRP 36 (1-2).
- 1568 ICRP, 2007. The 2007 Recommendations of the International Commission on Radiological Protection.
1569 ICRP Publication 103. Ann. ICRP 37 (2-4).
- 1570 ICRP, 2009. Adult Reference Computational Phantoms. ICRP Publication 110. Ann. ICRP 39 (2).
- 1571 ICRP, 2010. Conversion Coefficients for Radiological Protection Quantities for External Radiation
1572 Exposures. ICRP Publication 116, Ann. ICRP 40 (2-5).
- 1573 ICRP, 2015. Occupational Intakes of Radionuclides: Part 1. ICRP Publication 130. Ann. ICRP 44(2).
- 1574 ICRP, 2016. The ICRP Computational Framework for Internal Dose Assessment for Reference Adults:
1575 Specific Absorbed Fractions. ICRP Publication 133. Ann. ICRP 45(2).
- 1576 ICRP, 2017a. Occupational Intakes of Radionuclides: Part 2. ICRP Publication 134. Ann. ICRP 45(3/4).
- 1577 ICRP, 2017b. Occupational Intakes of Radionuclides: Part 3. ICRP Publication 137. Ann. ICRP 46(3/4).
- 1578 ICRU, 1992. Photon, Electron, Proton, and Neutron Interaction Data for Body Tissues. ICRU Report
1579 46. International Commission on Radiation Units and Measurements, Bethesda, MD.
- 1580 Kim, C.H., Jeong, J.H., Bolch, W.E., et al., 2011. A polygon-surface reference Korean male phantom
1581 (PSRK-Man) and its direct implementation in Geant4 Monte Carlo simulation. Phys. Med. Biol. 56,
1582 3137–3161.
- 1583 Kim, H.S., Yeom, Y.S., Nguyen, T.T., et al., 2017. Inclusion of thin target and source regions in
1584 alimentary and respiratory tract systems of mesh-type ICRP adult reference phantoms. Phys. Med.
1585 Biol. 62, 2132–2152.

- 1586 Kramer, R., Zankl, M., Williams, G., et al., 1982. The calculation of Dose from External Photon
1587 Exposures Using Reference Human Phantoms and Monte Carlo Methods. Part I: The male (Adam)
1588 and Female (Eva) Adult Mathematical Phantoms. GSF-Report S-885. GSF - National Research
1589 Center for Environment and Health, Neuherberg.
- 1590 Kulka, U., Abend, M., Ainsbury, E., et al., 2017. RENEB – Running the European Network of
1591 biological dosimetry and physical retrospective dosimetry. *Int. J. Radiat. Biol.* 93, 2–14.
- 1592 Lázaro Elias, S., 2011. Modelling of realistic Blood Vessel Geometry.
- 1593 Lee, C., Lodwick, D., Hasenauer, D., et al., 2007. Hybrid computational phantoms of the male and
1594 female newborn patient: NURBS-based whole-body models. *Phys. Med. Biol.* 52, 3309–3333.
- 1595 Lee, C., Lodwick, D., Hurtado, J., et al., 2010. The UF family of reference hybrid phantoms for
1596 computational radiation dosimetry. *Phys. Med. Biol.* 55, 339–363.
- 1597 Lee, C., Lamart, S., Moroz, B.E., 2013. Computational lymphatic node models in pediatric and adult
1598 hybrid phantoms for radiation dosimetry. *Phys. Med. Biol.* 58, N59–N82.
- 1599 Lee, H., et al., 2018. A set of body-size dependent phantoms constructed based on mesh-type ICRP
1600 reference phantoms. *Phys. Med. Biol.* (will be submitted in 2018).
- 1601 Lu, W., Wu, Z., Qiu, R., et al., 2017. Physical Dosimetric Reconstruction of a Radiological Accident at
1602 Nanjing (China) for Clinical Treatment Using Thudose. *Health Phys.* 113, 327–334.
- 1603 Martz, R., 2014. The MCNP6 book on unstructured mesh geometry: User’s guide. Report LA-UR-11-
1604 05668. Los Alamos National Laboratory, Los Alamos, NM.
- 1605 Möller, T.B., Reif, E., 1993. Taschenatlas der Schnittbildanatomie – Computertomographie und
1606 Kernspintomographie. Band II: Thorax, Abdomen, Becken. Georg Thieme Verlag, Stuttgart, New
1607 York.
- 1608 Möller, T.B., Reif, E., 1997. Taschenatlas der Schnittbildanatomie – Computertomographie und
1609 Kernspintomographie. Band I: Kopf, Hals, Wirbelsäule, Gelenke. Georg Thieme Verlag, Stuttgart,
1610 New York.
- 1611 Nguyen, T.T., Yeom, Y.S., Kim, H.S., et al., 2015. Incorporation of detailed eye model into polygon-
1612 mesh versions of ICRP-110 reference phantoms. *Phys. Med. Biol.* 60, 8695–8707.
- 1613 Park, J.S., Chung, M.S., Hwang, S.B., et al., 2005. Visible Korean Human: Improved Serially Sectioned
1614 Images of the Entire Body. *IEEE Trans. Med. Imaging* 24, 352–360.
- 1615 Pieterman, R., Willemsen, A., Appel, Milo., et al., 2002. Visualisation and assessment of the protein
1616 synthesis rate of lung cancer using carbon-11 tyrosine and positron emission tomography. *Eur. J.*
1617 *Nucl. Med.* 29, 243–247.
- 1618 Rea, M.E., Gougelet, R.M., Nicolalde, R.J. et al., 2010. Proposed triage categories for large-scale
1619 radiation incidents using high-accuracy biodosimetry method. *Health Phys.* 98, 136-144.
- 1620 Sato, T., Niita, K., Matsuda, N., et al., 2013. Particle and Heavy Ion Transport code System, PHITS,
1621 version 2.52. *J. Nucl. Sci. Technol.* 50, 913–923.
- 1622 Si, H., 2015. TetGen, a Delaunay-Based Quality Tetrahedral Mesh Generator. *ACM Trans. Math.*
1623 *Softw.* 41, 1–36.
- 1624 Snyder, W.S., Ford, M.R., Warner, G.G., et al., 1969. Estimates of Absorbed Fractions for
1625 Monoenergetic Photon Sources Uniformly Distributed in Various Organs of a Heterogeneous
1626 Phantom. *J. Nucl. Med.* 10: Suppl. No. 3, 7-52.
- 1627 Snyder, W.S., Ford, M.R., Warner, G.G., 1978. Estimates of Specific Absorbed Fractions for
1628 Monoenergetic Photon Sources Uniformly Distributed in Various Organs of a Heterogeneous
1629 Phantom. MIRD Pamphlet No. 5, Revised. Society of Nuclear Medicine, New York.
- 1630 Sullivan, J.M., Prasanna, P.G.S., Grace, M.B., et al., 2013. Assessment of Biodosimetry Methods for a
1631 Mass-Casualty Radiological Incident: Medical Response and Management Considerations. *Health*
1632 *Phys.* 105, 540–554.
- 1633 Stabin, M.G., Watson, E.E., Cristy, M., et al., 1995. Mathematical models and specific absorbed
1634 fractions of photon energy in the nonpregnant adult female and at the end of each trimester of
1635 pregnancy. ORNL Report TM-12907. Oak Ridge National Laboratory, Oak Ridge, TN.
- 1636 Swartz, H.M., Williams, B.B., Flood, A.B., 2014. Overview of the principles and practice of
1637 biodosimetry. *Radiat. Environ. Biophys.* 53, 221–232.

- 1638 Tawhai, M.H., Pullan, A.J., Hunter, P.J., 2000. Generation of an Anatomically Based Three-
1639 Dimensional Model of the Conducting Airways. *Ann. Biomed. Eng.* 28, 793–802.
- 1640 Yeom, Y.S., Han, M.C., Kim, C.H., et al., 2013. Conversion of ICRP male reference phantom to
1641 polygon-surface phantom. *Phys. Med. Biol.* 58, 6985–7007.
- 1642 Yeom, Y.S., Jeong, J.H., Han, M.C., et al., 2014. Tetrahedral-mesh-based computational human
1643 phantom for fast Monte Carlo dose calculations. *Phys. Med. Biol.* 59, 3173–3185.
- 1644 Yeom, Y.S., Kim, H.S., Nguyen, T.T., et al., 2016a. New small-intestine modeling method for surface-
1645 based computational human phantoms. *J. Radiol. Prot.* 36, 230–245.
- 1646 Yeom, Y.S., Wang, Z.J., Nguyen, T.T., et al., 2016b. Development of skeletal system for mesh-type
1647 ICRP reference adult phantoms. *Phys. Med. Biol.* 61, 7054–7073.
- 1648 Zankl, M., Wittmann, A., 2001. The adult male voxel model “Golem” segmented from whole-body CT
1649 patient data. *Radiat. Environ. Biophys.* 40, 153–162.
- 1650 Zankl, M., Becker, J., Fill, U., et al., 2005. GSF male and female adult voxel models representing ICRP
1651 Reference Man – the present status. In : *The Monte Carlo Method : Versatility Unbounded in a*
1652 *Dynamic Computing World.* Chattanooga, TN.
- 1653

1654 **ANNEX A. LIST OF ORGAN ID, MEDIUM, DENSITY AND MASS OF**
 1655 **EACH ORGAN/TISSUE**

1656 Table A.1. List of organ ID, medium, density and mass of each organ/tissue in TM-version phantoms.

Organ ID	Organ/tissue	Medium	Density (g/cm ³)		Mass (g)	
			Male	Female	Male	Female
100	Adrenal, left	1	1.036	1.035	8.683	6.817
200	Adrenal, right	1	1.036	1.035	8.683	8.649
300	ET ₁ , 0 ~ 8 μm	2	1.031	1.031	0.022	0.009
301	ET ₁ , 8 ~ 40 μm	2	1.031	1.031	0.090	0.035
302	ET ₁ , 40 ~ 50 μm	2	1.031	1.031	0.028	0.011
303	ET ₁ , 50 μm ~ surface	2	1.031	1.031	11.291	4.375
400	ET ₂ , -15 ~ 0 μm	52	1.000	1.000	0.141	0.104
401	ET ₂ , 0 ~ 40 μm	2	1.031	1.031	0.390	0.288
402	ET ₂ , 40 ~ 50 μm	2	1.031	1.031	0.098	0.072
403	ET ₂ , 50 ~ 55 μm	2	1.031	1.031	0.049	0.036
404	ET ₂ , 55 ~ 65 μm	2	1.031	1.031	0.098	0.072
405	ET ₂ , 65 μm ~ surface	2	1.031	1.031	28.808	14.180
500	Oral mucosa, tongue	3	1.050	1.050	0.086	0.066
501	Oral mucosa, mouth floor	3	1.050	1.050	0.023	0.016
600	Oral mucosa, lips and cheeks	3	1.050	1.050	0.023	0.019
700	Trachea	2	1.031	1.031	10.364	8.201
800	BB ₁ [†] , -11 ~ -6 μm	52	1.000	1.000	0.025	0.010
801	BB ₁ [†] , -6 ~ 0 μm	2	1.031	1.031	0.031	0.013
802	BB ₁ [†] , 0 ~ 10 μm	2	1.031	1.031	0.052	0.021
803	BB ₁ [†] , 10 ~ 35 μm	2	1.031	1.031	0.130	0.053
804	BB ₁ [†] , 35 ~ 40 μm	2	1.031	1.031	0.026	0.011
805	BB ₁ [†] , 40 ~ 50 μm	2	1.031	1.031	0.052	0.021
806	BB ₁ [†] , 50 ~ 60 μm	2	1.031	1.031	0.052	0.021
807	BB ₁ [†] , 60 ~ 70 μm	2	1.031	1.031	0.053	0.021
808	BB ₁ [†] , 70 μm ~ surface	2	1.031	1.031	2.777	1.179
900	Blood in large arteries, head	4	1.060	1.060	1.504	1.908
910	Blood in large veins, head	4	1.060	1.060	6.935	3.007
1000	Blood in large arteries, trunk	4	1.060	1.060	193.183	117.872
1010	Blood in large veins, trunk	4	1.060	1.060	444.040	239.807
1100	Blood in large arteries, arms	4	1.060	1.060	32.467	46.314
1110	Blood in large veins, arms	4	1.060	1.060	167.306	139.583
1200	Blood in large arteries, legs	4	1.060	1.060	108.846	79.906
1210	Blood in large veins, legs	4	1.060	1.060	389.719	355.601
1300	Humeri, upper, cortical	5	1.904	1.904	159.456	113.682
1400	Humeri, upper, spongiosa	7	1.233	1.185	145.689	107.717
1500	Humeri, upper, medullary cavity	6	0.981	0.981	34.244	20.516
1600	Humeri, lower, cortical	5	1.904	1.904	106.461	103.295
1700	Humeri, lower, spongiosa	8	1.109	1.117	50.890	50.264
1800	Humeri, lower, medullary cavity	6	0.981	0.981	37.397	20.493
1900	Ulnae and radii, cortical	5	1.904	1.904	273.498	156.708
2000	Ulnae and radii, spongiosa	8	1.109	1.117	154.981	86.883
2100	Ulnae and radii, medullary cavity	6	0.981	0.981	22.996	34.068
2200	Wrists and hand bones, cortical	5	1.904	1.904	181.529	105.132
2300	Wrists and hand bones, spongiosa	8	1.109	1.117	118.927	69.360
2400	Clavicles, cortical	5	1.904	1.904	48.252	32.825
2500	Clavicles, spongiosa	9	1.157	1.192	45.057	38.798
2600	Cranium, cortical	5	1.904	1.904	568.469	407.670
2700	Cranium, spongiosa	10	1.165	1.252	382.073	391.311
2800	Femora, upper, cortical	5	1.904	1.904	253.548	244.126
2900	Femora, upper, spongiosa	11	1.125	1.046	413.232	232.804
3000	Femora, upper, medullary cavity	6	0.981	0.981	26.045	39.516
3100	Femora, lower, cortical	5	1.904	1.904	307.761	240.929
3200	Femora, lower, spongiosa	8	1.109	1.117	373.652	166.334
3300	Femora, lower, medullary cavity	6	0.981	0.981	82.179	56.762
3400	Tibiae, cortical	5	1.904	1.904	536.651	544.845
3500	Tibiae, spongiosa	8	1.109	1.117	621.408	558.529
3600	Tibiae, medullary cavity	6	0.981	0.981	79.815	88.883
3700	Ankles and foot, cortical	5	1.904	1.904	234.882	173.476
3800	Ankles and foot, spongiosa	8	1.109	1.117	432.615	257.451
3900	Mandible, cortical	5	1.904	1.904	76.877	45.394
4000	Mandible, spongiosa	12	1.271	1.189	56.287	33.479
4100	Pelvis, cortical	5	1.904	1.904	402.595	262.460
4200	Pelvis, spongiosa	13	1.121	1.105	619.672	455.599
4300	Ribs, cortical	5	1.904	1.904	368.797	164.514

4400	Ribs, spongiosa	14	1.170	1.087	457.351	277.325
4500	Scapulae, cortical	5	1.904	1.904	223.333	121.664
4600	Scapulae, spongiosa	15	1.201	1.125	156.670	96.730
4700	Cervical spine, cortical	5	1.904	1.904	103.943	71.596
4800	Cervical spine, spongiosa	16	1.049	1.129	78.915	75.601
4900	Thoracic spine, cortical	5	1.904	1.904	289.440	205.828
5000	Thoracic spine, spongiosa	17	1.070	1.080	345.222	271.915
5100	Lumbar spine, cortical	5	1.904	1.904	188.047	156.175
5200	Lumbar spine, spongiosa	18	1.108	1.165	291.584	264.976
5300	Sacrum, cortical	5	1.904	1.904	110.320	80.240
5400	Sacrum, spongiosa	19	1.033	1.052	192.224	154.840
5500	Sternum, cortical	5	1.904	1.904	9.991	1.685
5600	Sternum, spongiosa	20	1.041	1.073	61.420	51.347
5700	Cartilage, costal	21	1.099	1.099	56.331	41.959
5800	Cartilage, discs	21	1.099	1.099	82.063	69.351
6100	Brain	22	1.041	1.041	1517.390	1349.568
6200	Breast, left, adipose tissue	23	0.953	0.952	7.769	153.663
6300	Breast, left, glandular tissue	24	1.021	1.021	5.180	102.491
6400	Breast, right, adipose tissue	23	0.953	0.952	7.769	153.663
6500	Breast, right, glandular tissue	24	1.021	1.021	5.180	102.491
6600	Eye lens, sensitive, left	25	1.060	1.060	0.039	0.039
6601	Eye lens, insensitive, left	25	1.060	1.060	0.189	0.189
6700	Cornea, left	26	1.100	1.087	1.113	1.100
6701	Aqueous, left	27	1.025	1.014	0.308	0.304
6702	Vitreous, left	28	1.031	1.019	6.122	6.051
6800	Eye lens, sensitive, right	25	1.060	1.060	0.039	0.039
6801	Eye lens, insensitive, right	25	1.060	1.060	0.189	0.189
6900	Cornea, right	26	1.100	1.087	1.113	1.100
6901	Aqueous, right	27	1.025	1.014	0.308	0.304
6902	Vitreous, right	28	1.031	1.019	6.122	6.051
7000	Gall bladder wall	2	1.031	1.031	10.364	8.201
7100	Gall bladder contents	29	1.030	1.030	58.000	48.000
7200	Stomach wall, 0 ~ 60 µm	30	1.037	1.036	1.784	1.561
7201	Stomach wall, 60 ~ 100 µm	30	1.037	1.036	1.193	1.044
7202	Stomach wall, 100 ~ 300 µm	30	1.037	1.036	6.008	5.256
7203	Stomach wall, 300 µm ~ surface	30	1.037	1.036	185.286	165.012
7300	Stomach contents	33	1.040	1.040	250.000	230.000
7400	Small intestine wall, 0 ~ 130 µm	31	1.037	1.036	14.547	12.341
7401	Small intestine wall, 130 ~ 150 µm	31	1.037	1.036	2.264	1.922
7402	Small intestine wall, 150 ~ 200 µm	31	1.037	1.036	5.692	4.831
7403	Small intestine wall, 200 µm ~ surface	31	1.037	1.036	840.096	736.674
7500	Small intestine contents, -500 ~ 0 µm	33	1.040	1.040	53.337	45.227
7501	Small intestine contents, centre ~ -500 µm	33	1.040	1.040	296.663	234.773
7600	Ascending colon wall, 0 ~ 280 µm	32	1.037	1.036	3.071	4.451
7601	Ascending colon wall, 280 ~ 300 µm	32	1.037	1.036	0.223	0.322
7602	Ascending colon wall, 300 µm ~ surface	32	1.037	1.036	116.634	107.784
7700	Ascending colon contents	33	1.040	1.040	55.000	100.007
7800	Transverse colon wall, right, 0 ~ 280 µm	32	1.037	1.036	3.993	3.680
7801	Transverse colon wall, right, 280 ~ 300 µm	32	1.037	1.036	0.289	0.266
7802	Transverse colon wall, right, 300 µm ~ surface	32	1.037	1.036	75.671	64.847
7900	Transverse colon contents, right	33	1.040	1.040	95.000	59.995
8000	Transverse colon wall, left, 0 ~ 280 µm	32	1.037	1.036	2.824	2.196
8001	Transverse colon wall, left, 280 ~ 300 µm	32	1.037	1.036	0.205	0.160
8002	Transverse colon wall, left, 300 µm ~ surface	32	1.037	1.036	76.924	66.428
8100	Transverse colon contents, left	33	1.040	1.040	40.000	30.005
8200	Descending colon wall, 0 ~ 280 µm	32	1.037	1.036	2.779	3.021
8201	Descending colon wall, 280 ~ 300 µm	32	1.037	1.036	0.203	0.220
8202	Descending colon wall, 300 µm ~ surface	32	1.037	1.036	116.946	109.320
8300	Descending colon contents	33	1.040	1.040	35.000	50.003
8400	Sigmoid colon wall, 0 ~ 280 µm	32	1.037	1.036	4.451	4.222
8401	Sigmoid colon wall, 280 ~ 300 µm	32	1.037	1.036	0.324	0.306
8402	Sigmoid colon wall, 300 µm ~ surface	32	1.037	1.036	48.527	51.761
8500	Sigmoid colon contents	33	1.040	1.040	75.000	79.993
8600	Rectum wall	32	1.037	1.036	39.976	31.268
8700	Heart wall	34	1.051	1.051	385.839	290.890
8800	Blood in heart chamber	4	1.060	1.060	510.000	370.000
8900	Kidney, left, cortex	35	1.053	1.052	162.338	149.091
9000	Kidney, left, medulla	35	1.053	1.052	38.359	37.441
9100	Kidney, left, pelvis	35	1.053	1.052	7.652	7.494
9200	Kidney, right, cortex	35	1.053	1.052	166.542	125.147
9300	Kidney, right, medulla	35	1.053	1.052	39.362	31.440
9400	Kidney, right, pelvis	35	1.053	1.052	7.892	6.292
9500	Liver	36	1.060	1.060	2360.000	1810.000

9700	Lung (AD), left	37	0.415	0.413	545.877	427.256
9900	Lung (AD), right	37	0.415	0.413	652.861	522.518
10000	Lymphatic nodes, ET	38	1.032	1.032	15.949	12.695
10100	Lymphatic nodes, thoracic	38	1.032	1.032	15.949	12.695
10200	Lymphatic nodes, head	38	1.032	1.032	5.510	4.385
10300	Lymphatic nodes, trunk	38	1.032	1.032	130.203	103.641
10400	Lymphatic nodes, arms	38	1.032	1.032	11.019	8.771
10500	Lymphatic nodes, legs	38	1.032	1.032	11.019	8.771
10600	Muscle, head	39	1.050	1.050	1200.827	445.022
10700	Muscle, trunk	39	1.050	1.050	14841.796	8324.736
10800	Muscle, arms	39	1.050	1.050	2843.360	1479.783
10900	Muscle, legs	39	1.050	1.050	10890.597	7676.898
11000	Oesophagus wall, 0 ~ 190 µm	40	1.037	1.036	1.919	1.871
11001	Oesophagus wall, 190 ~ 200 µm	40	1.037	1.036	0.103	0.101
11002	Oesophagus wall, 200 µm ~ surface	40	1.037	1.036	49.783	41.247
11003	Oesophagus contents	33	1.040	1.040	22.870	21.240
11100	Ovary, left	41		1.051		6.318
11200	Ovary, right	41		1.051		6.318
11300	Pancreas	42	1.044	1.043	173.631	144.552
11400	Pituitary gland	2	1.031	1.031	0.622	0.615
11500	Prostate	43	1.031		17.618	
11600	RST, head	44	0.939	0.946	975.621	844.542
11700	RST, trunk	44	0.939	0.946	11176.903	11513.384
11800	RST, arms	44	0.939	0.946	1549.842	2171.515
11900	RST, legs	44	0.939	0.946	4510.159	7795.947
12000	Salivary glands, left	2	1.031	1.031	44.045	35.880
12100	Salivary glands, right	2	1.031	1.031	44.045	35.880
12200	Skin, head, insensitive	45	1.089	1.088	259.230	155.582
12201	Skin, head, sensitive, 50 ~ 100 µm	45	1.089	1.088	8.470	6.325
12300	Skin, trunk, insensitive	45	1.089	1.088	1271.128	871.564
12301	Skin, trunk, sensitive, 50 ~ 100 µm	45	1.089	1.088	38.418	32.368
12400	Skin, arms, insensitive	45	1.089	1.088	575.708	380.941
12401	Skin, arms, sensitive, 50 ~ 100 µm	45	1.089	1.088	18.843	15.599
12500	Skin, legs, insensitive	45	1.089	1.088	1259.982	924.625
12501	Skin, legs, sensitive, 50 ~ 100 µm	45	1.089	1.088	37.790	35.025
12600	Spinal cord	2	1.031	1.031	37.952	19.098
12700	Spleen	46	1.060	1.060	228.400	187.400
12800	Teeth	47	2.688	2.690	50.727	40.562
12801	Teeth, retention region	33	1.040	1.040	0.043	0.036
12900	Testis, left	41	1.041		18.617	
13000	Testis, right	41	1.041		18.617	
13100	Thymus	2	1.031	1.031	25.909	20.503
13200	Thyroid	48	1.051	1.051	23.351	19.455
13300	Tongue, upper (food)	3	1.050	1.050	20.993	20.995
13301	Tongue, lower	3	1.050	1.050	54.552	40.415
13400	Tonsils	2	1.031	1.031	3.109	3.075
13500	Ureter, left	2	1.031	1.031	8.809	7.689
13600	Ureter, right	2	1.031	1.031	7.773	7.689
13700	Urinary bladder wall, insensitive	49	1.040	1.040	49.028	38.546
13701	Urinary bladder wall, sensitive, 75/69 [‡] ~ 193/185 [‡] µm	49	1.040	1.040	2.071	2.259
13800	Urinary bladder contents	50	1.040	1.040	200.000	200.000
13900	Uterus	43		1.021		81.993
14000	Air inside body	51	0.001	0.001	0.140	0.036

1657 [†] Only the main bronchi (BB₁) was defined in the TM-version phantoms. The other generations of the bronchi (BB) and all generations of the
 1658 bronchioles (bb) were modelled in CSG format (see Chapter 5.3).

1659 [‡] Male/female.

1660

1661 Table A.2. List of organ ID, medium, density and mass of each organ/tissue in PM-version phantoms.

Organ ID	Organ/tissue	Medium	Density (g/cm ³)		Mass (g)	
			Male	Female	Male	Female
100	Adrenal, left	1	1.036	1.035	8.683	6.817
200	Adrenal, right	1	1.036	1.035	8.683	8.649
300	ET ₁ , 8 μm	2	1.031	1.031	0.022	0.009
301	ET ₁ , 40 μm	2	1.031	1.031	0.090	0.035
302	ET ₁ , 50 μm	2	1.031	1.031	0.028	0.011
303	ET ₁ , surface	2	1.031	1.031	11.291	4.375
400	ET ₂ , 0 μm	52	1.000	1.000	0.141	0.104
401	ET ₂ , 40 μm	2	1.031	1.031	0.390	0.288
402	ET ₂ , 50 μm	2	1.031	1.031	0.098	0.072
403	ET ₂ , 55 μm	2	1.031	1.031	0.049	0.036
404	ET ₂ , 65 μm	2	1.031	1.031	0.098	0.072
405	ET ₂ , surface	2	1.031	1.031	28.808	14.180
500	Oral mucosa, tongue	3	1.050	1.050	0.086	0.066
501	Oral mucosa, mouth floor	3	1.050	1.050	0.023	0.016
600	Oral mucosa, lips and cheeks	3	1.050	1.050	0.023	0.019
700	Trachea	2	1.031	1.031	10.364	8.201
800	BB ₁ [†] , -6 μm	52	1.000	1.000	0.025	0.010
801	BB ₁ [†] , 0 μm	2	1.031	1.031	0.031	0.013
802	BB ₁ [†] , 10 μm	2	1.031	1.031	0.052	0.021
803	BB ₁ [†] , 35 μm	2	1.031	1.031	0.130	0.053
804	BB ₁ [†] , 40 μm	2	1.031	1.031	0.026	0.011
805	BB ₁ [†] , 50 μm	2	1.031	1.031	0.052	0.021
806	BB ₁ [†] , 60 μm	2	1.031	1.031	0.052	0.021
807	BB ₁ [†] , 70 μm	2	1.031	1.031	0.053	0.021
808	BB ₁ [†] , surface	2	1.031	1.031	2.777	1.179
900	Blood in large arteries	4	1.060	1.060	336.000	246.000
910	Blood in large veins	4	1.060	1.060	1008.000	737.998
1300	Humeri, cortical	5	1.904	1.904	265.917	216.977
1400	Humeri, upper, spongiosa	7	1.233	1.185	145.689	107.717
1700	Humeri, lower, spongiosa	8	1.109	1.117	50.890	50.264
1800	Humeri, medullary cavity	6	0.981	0.981	71.641	41.009
1900	Ulnae and radii, cortical	5	1.904	1.904	273.498	156.708
2000	Ulnae and radii, spongiosa	8	1.109	1.117	154.981	86.883
2100	Ulnae and radii, medullary cavity	6	0.981	0.981	22.996	34.068
2200	Wrists and hand bones, cortical	5	1.904	1.904	181.529	105.132
2300	Wrists and hand bones, spongiosa	8	1.109	1.117	118.927	69.360
2400	Clavicles, cortical	5	1.904	1.904	48.252	32.825
2500	Clavicles, spongiosa	9	1.157	1.192	45.057	38.798
2600	Cranium, cortical	5	1.904	1.904	568.469	407.670
2700	Cranium, spongiosa	10	1.165	1.252	382.073	391.311
2800	Femora, cortical	5	1.904	1.904	561.309	485.055
2900	Femora, upper, spongiosa	11	1.125	1.046	413.232	232.804
3200	Femora, lower, spongiosa	8	1.109	1.117	373.652	166.334
3300	Femora, medullary cavity	6	0.981	0.981	108.224	96.278
3400	Tibiae, cortical	5	1.904	1.904	536.651	544.845
3500	Tibiae, spongiosa	8	1.109	1.117	621.408	558.529
3600	Tibiae, medullary cavity	6	0.981	0.981	79.815	88.883
3700	Ankles and foot, cortical	5	1.904	1.904	234.882	173.476
3800	Ankles and foot, spongiosa	8	1.109	1.117	432.615	257.451
3900	Mandible, cortical	5	1.904	1.904	76.877	45.394
4000	Mandible, spongiosa	12	1.271	1.189	56.287	33.479
4100	Pelvis, cortical	5	1.904	1.904	402.595	262.460
4200	Pelvis, spongiosa	13	1.121	1.105	619.672	455.599
4300	Ribs, cortical	5	1.904	1.904	368.797	164.514
4400	Ribs, spongiosa	14	1.170	1.087	457.351	277.325
4500	Scapulae, cortical	5	1.904	1.904	223.333	121.664
4600	Scapulae, spongiosa	15	1.201	1.125	156.670	96.730
4700	Cervical spine, cortical	5	1.904	1.904	103.943	71.596
4800	Cervical spine, spongiosa	16	1.049	1.129	78.915	75.601
4900	Thoracic spine, cortical	5	1.904	1.904	289.440	205.828
5000	Thoracic spine, spongiosa	17	1.070	1.080	345.222	271.915
5100	Lumbar spine, cortical	5	1.904	1.904	188.047	156.175
5200	Lumbar spine, spongiosa	18	1.108	1.165	291.584	264.976
5300	Sacrum, cortical	5	1.904	1.904	110.320	80.240
5400	Sacrum, spongiosa	19	1.033	1.052	192.224	154.840
5500	Sternum, cortical	5	1.904	1.904	9.991	1.685
5600	Sternum, spongiosa	20	1.041	1.073	61.420	51.347
5700	Cartilage, costal	21	1.099	1.099	56.331	41.959
5800	Cartilage, discs	21	1.099	1.099	82.063	69.351

6100	Brain	22	1.041	1.041	1517.390	1349.568
6200	Breast, left, adipose tissue	23	0.953	0.952	7.769	153.663
6300	Breast, left, glandular tissue	24	1.021	1.021	5.180	102.491
6400	Breast, right, adipose tissue	23	0.953	0.952	7.769	153.663
6500	Breast, right, glandular tissue	24	1.021	1.021	5.180	102.491
6600	Eye lens, sensitive, left	25	1.060	1.060	0.039	0.039
6601	Eye lens, insensitive, left	25	1.060	1.060	0.189	0.189
6700	Cornea, left	26	1.100	1.087	1.113	1.100
6701	Aqueous, left	27	1.025	1.014	0.308	0.304
6702	Vitreous, left	28	1.031	1.019	6.122	6.051
6800	Eye lens, sensitive, right	25	1.060	1.060	0.039	0.039
6801	Eye lens, insensitive, right	25	1.060	1.060	0.189	0.189
6900	Cornea, right	26	1.100	1.087	1.113	1.100
6901	Aqueous, right	27	1.025	1.014	0.308	0.304
6902	Vitreous, right	28	1.031	1.019	6.122	6.051
7000	Gall bladder wall	2	1.031	1.031	10.364	8.201
7100	Gall bladder contents	29	1.030	1.030	58.000	48.000
7200	Stomach wall, 60 µm	30	1.037	1.036	1.784	1.561
7201	Stomach wall, 100 µm	30	1.037	1.036	1.193	1.044
7202	Stomach wall, 300 µm	30	1.037	1.036	6.008	5.256
7203	Stomach wall, surface	30	1.037	1.036	185.286	165.012
7300	Stomach contents	33	1.040	1.040	250.000	230.000
7400	Small intestine wall, 130 µm	31	1.037	1.036	14.547	12.341
7401	Small intestine wall, 150 µm	31	1.037	1.036	2.264	1.922
7402	Small intestine wall, 200 µm	31	1.037	1.036	5.692	4.831
7403	Small intestine wall, surface	31	1.037	1.036	840.096	736.674
7500	Small intestine contents, -500 µm	33	1.040	1.040	53.337	45.227
7501	Small intestine contents, 0 µm	33	1.040	1.040	296.663	234.773
7600	Ascending colon wall, 280 µm	32	1.037	1.036	3.071	4.451
7601	Ascending colon wall, 300 µm	32	1.037	1.036	0.223	0.322
7602	Ascending colon wall, surface	32	1.037	1.036	116.634	107.784
7700	Ascending colon contents	33	1.040	1.040	55.000	100.007
7800	Transverse colon wall, right, 280 µm	32	1.037	1.036	3.993	3.680
7801	Transverse colon wall, right, 300 µm	32	1.037	1.036	0.289	0.266
7802	Transverse colon wall, right, surface	32	1.037	1.036	75.671	64.847
7900	Transverse colon contents, right	33	1.040	1.040	95.000	59.995
8000	Transverse colon wall, left, 280 µm	32	1.037	1.036	2.824	2.196
8001	Transverse colon wall, left, 300 µm	32	1.037	1.036	0.205	0.160
8002	Transverse colon wall, left, surface	32	1.037	1.036	76.924	66.428
8100	Transverse colon contents, left	33	1.040	1.040	40.000	30.005
8200	Descending colon wall, 280 µm	32	1.037	1.036	2.779	3.021
8201	Descending colon wall, 300 µm	32	1.037	1.036	0.203	0.220
8202	Descending colon wall, surface	32	1.037	1.036	116.946	109.320
8300	Descending colon contents	33	1.040	1.040	35.000	50.003
8400	Sigmoid colon wall, 280 µm	32	1.037	1.036	4.451	4.222
8401	Sigmoid colon wall, 300 µm	32	1.037	1.036	0.324	0.306
8402	Sigmoid colon wall, surface	32	1.037	1.036	48.527	51.761
8500	Sigmoid colon contents	33	1.040	1.040	75.000	79.993
8600	Rectum wall	32	1.037	1.036	39.976	31.268
8700	Heart wall	34	1.051	1.051	385.839	290.890
8800	Blood in heart chamber	4	1.060	1.060	510.000	370.000
8900	Kidney, left, cortex	35	1.053	1.052	162.338	149.091
9000	Kidney, left, medulla	35	1.053	1.052	38.359	37.441
9100	Kidney, left, pelvis	35	1.053	1.052	7.652	7.494
9200	Kidney, right, cortex	35	1.053	1.052	166.542	125.147
9300	Kidney, right, medulla	35	1.053	1.052	39.362	31.440
9400	Kidney, right, pelvis	35	1.053	1.052	7.892	6.292
9500	Liver	36	1.060	1.060	2360.000	1810.000
9700	Lung (AD), left	37	0.415	0.413	545.877	427.256
9900	Lung (AD), right	37	0.415	0.413	652.861	522.518
10000	Lymphatic nodes, ET	38	1.032	1.032	15.949	12.695
10001	Lymphatic nodes, cervical	38	1.032	1.032	5.510	4.386
10002	Lymphatic nodes, axillary	38	1.032	1.032	6.670	5.309
10003	Lymphatic nodes, breast	38	1.032	1.032	11.019	8.771
10004	Lymphatic nodes, thoracic	38	1.032	1.032	15.949	12.695
10005	Lymphatic nodes, cubital	38	1.032	1.032	11.019	8.771
10006	Lymphatic nodes, mesentery	38	1.032	1.032	101.495	80.789
10007	Lymphatic nodes, inguinal	38	1.032	1.032	11.019	8.771
10008	Lymphatic nodes, popliteal	38	1.032	1.032	11.019	8.771
10600	Muscle	39	1.050	1.050	29776.580	17926.439
11000	Oesophagus wall, 190 µm	40	1.037	1.036	1.919	1.871
11001	Oesophagus wall, 200 µm	40	1.037	1.036	0.103	0.101
11002	Oesophagus wall, surface	40	1.037	1.036	49.783	41.247

11003	Oesophagus contents	33	1.040	1.040	22.870	21.240
11100	Ovary, left	41		1.051		6.318
11200	Ovary, right	41		1.051		6.318
11300	Pancreas	42	1.044	1.043	173.631	144.552
11400	Pituitary gland	2	1.031	1.031	0.622	0.615
11500	Prostate	43	1.031		17.618	
11600	RST	44	0.939	0.946	18212.525	22325.388
12000	Salivary glands, left	2	1.031	1.031	44.045	35.880
12100	Salivary glands, right	2	1.031	1.031	44.045	35.880
12200	Skin, surface	45	1.089	1.088	103.981	89.399
12201	Skin, 50 µm	45	1.089	1.088	103.521	89.317
12202	Skin, 100 µm	45	1.089	1.088	3262.067	2243.313
12600	Spinal cord	2	1.031	1.031	37.952	19.098
12700	Spleen	46	1.060	1.060	228.400	187.400
12800	Teeth	47	2.688	2.690	50.727	40.562
12801	Teeth, retention region	33	1.040	1.040	0.043	0.036
12900	Testis, left	41	1.041		18.617	
13000	Testis, right	41	1.041		18.617	
13100	Thymus	2	1.031	1.031	25.909	20.503
13200	Thyroid	48	1.051	1.051	23.351	19.455
13300	Tongue, upper (food)	3	1.050	1.050	20.993	20.995
13301	Tongue, lower, surface	3	1.050	1.050	1.648	1.269
13302	Tongue, lower, -200 µm	3	1.050	1.050	52.904	39.146
13400	Tonsils	2	1.031	1.031	3.109	3.075
13500	Ureter, left	2	1.031	1.031	8.809	7.689
13600	Ureter, right	2	1.031	1.031	7.773	7.689
13700	Urinary bladder wall	49	1.040	1.040	47.719	37.209
13701	Urinary bladder wall, 75/69 [‡] µm	49	1.040	1.040	1.309	1.337
13702	Urinary bladder wall, 193/185 [‡] µm	49	1.040	1.040	2.071	2.259
13800	Urinary bladder contents	50	1.040	1.040	200.000	200.000
13900	Uterus	43		1.021		81.993
14000	ET ₁ contents, 0 µm (air)	51	0.001	0.001	0.008	0.000198
14001	ET ₂ contents, -15 µm (air)	51	0.001	0.001	0.029	0.014
14002	Trachea contents (air)	51	0.001	0.001	0.015	0.011
14003	BB ₁ contents [†] , -11 µm (air)	51	0.001	0.001	0.016	0.004
14004	Air, remaining	51	0.001	0.001	0.072	0.007

1662 [†] Only the main bronchi (BB₁) was defined in the PM-version phantoms. The other generations of the bronchi (BB) and all generations of the
 1663 bronchioles (bb) were modelled in CSG format (see Chapter 5.3).

1664 [‡] Male/female.

1665
1666

ANNEX B. LIST OF MEDIA AND THEIR ELEMENTAL COMPOSITION

1667 Table B.1. List of media, their elemental compositions (percentage by mass) and their densities for the
1668 adult male mesh-type reference phantom.

Medium no.		H	C	N	O	Na	Mg	P	S	Cl	K	Ca	Fe	I	Density (g/cm ³)
1	Adrenal	10.4	22.8	2.8	63.0	0.1		0.2	0.3	0.2	0.2				1.036
2	ET, Trachea, BB, bb, Gall bladder wall, Pituitary gland, Salivary glands, Spinal cord, Thymus, Tonsils, Ureter	10.5	25.1	2.7	60.7	0.1		0.2	0.3	0.2	0.2				1.031
3	Oral mucosa, Tongue	10.2	14.2	3.4	71.1	0.1		0.2	0.3	0.1	0.4				1.050
4	Blood	10.2	11.0	3.3	74.5	0.1		0.1	0.2	0.3	0.2		0.1		1.060
5	Cortical bone	3.6	15.9	4.2	44.8	0.3	0.2	9.4	0.3			21.3			1.904
6	Medullary cavity	11.5	63.6	0.7	23.9	0.1			0.1	0.1					0.981
7	Humeri, upper, spongiosa	8.1	35.4	2.8	41.0	0.2	0.1	3.7	0.2	0.1	0.1	8.3			1.233
8	Humeri, lower, Ulnae and radii, Wrists and hand bones, Femora, lower, Tibiae, Ankles and foot, spongiosa	9.6	50.4	1.7	30.8	0.1		2.2	0.2	0.1		4.9			1.109
9	Clavicles, spongiosa	8.9	40.9	2.5	38.5	0.1		2.7	0.2	0.1	0.1	6.0			1.157
10	Cranium, spongiosa	8.8	39.5	2.6	39.5	0.1	0.1	2.8	0.2	0.1	0.1	6.2			1.165
11	Femora, upper, spongiosa	9.3	44.1	2.3	36.5	0.1	0.1	2.2	0.2	0.1	0.1	5.0			1.125
12	Mandible, spongiosa	7.7	33.2	3.0	42.0	0.2	0.1	4.1	0.2	0.1	0.1	9.3			1.271
13	Pelvis, spongiosa	9.4	40.9	2.6	40.0	0.1	0.1	2.0	0.2	0.1	0.1	4.5			1.121
14	Ribs, spongiosa	8.8	34.6	3.1	44.4	0.1	0.1	2.6	0.2	0.1	0.1	5.8	0.1		1.170
15	Scapulae, spongiosa	8.4	37.3	2.7	40.4	0.1	0.1	3.3	0.2	0.1	0.1	7.3			1.201
16	Cervical spine, spongiosa	10.3	41.6	2.8	42.8	0.1		0.6	0.2	0.2	0.1	1.2	0.1		1.049
17	Thoracic spine, spongiosa	10.0	40.3	2.8	43.1	0.1		1.0	0.2	0.2	0.1	2.1	0.1		1.070
18	Lumbar spine, spongiosa	9.5	38.0	3.0	43.6	0.1		1.6	0.2	0.2	0.1	3.6	0.1		1.108
19	Sacrum, spongiosa	10.5	42.6	2.7	42.6	0.1		0.3	0.2	0.2	0.1	0.6	0.1		1.033
20	Sternum, spongiosa	10.4	42.1	2.8	42.7			0.5	0.2	0.2	0.1	0.9	0.1		1.041
21	Cartilage	9.6	9.9	2.2	74.4	0.5		2.2	0.9	0.3					1.099
22	Brain	10.7	14.3	2.3	71.3	0.2		0.4	0.2	0.3	0.3				1.041
23	Breast, adipose tissue	11.4	58.1	0.8	29.4	0.1			0.1	0.1					0.953
24	Breast, glandular tissue	10.6	32.4	3.0	53.5	0.1		0.1	0.2	0.1					1.021
25	Eye lens	9.6	19.5	5.7	64.6	0.1		0.1	0.3	0.1					1.060
26	Cornea	10.1	12.5	3.7	73.2	0.1		0.1	0.2	0.1					1.100
27	Aqueous	11.2	0.4	0.1	88.3										1.025
28	Vitreous	11.2	0.4	0.1	88.3										1.031
29	Gall bladder contents	10.5	25.6	2.7	60.2	0.1		0.2	0.3	0.2	0.2				1.030
30	Stomach wall	10.5	11.4	2.5	75.0	0.1		0.1	0.1	0.2	0.1				1.037
31	Small intestine wall	10.5	11.4	2.5	75.0	0.1		0.1	0.1	0.2	0.1				1.037
32	Colon wall	10.5	11.4	2.5	75.0	0.1		0.1	0.1	0.2	0.1				1.037
33	GI contents	10.0	22.2	2.2	64.4	0.1		0.2	0.3	0.1	0.4	0.1			1.040
34	Heart wall	10.4	13.5	2.9	72.2	0.1		0.2	0.2	0.2	0.3				1.051
35	Kidney	10.3	12.6	3.1	72.9	0.2		0.2	0.2	0.2	0.2	0.1			1.053
36	Liver	10.2	13.2	3.1	72.3	0.2		0.2	0.3	0.2	0.3				1.060
37	Lung	10.2	10.8	3.2	74.8	0.1		0.1	0.2	0.3	0.2		0.1		0.415
38	Lymphatic nodes	10.8	4.5	1.2	82.7	0.3			0.1	0.4					1.032
39	Muscle	10.2	14.2	3.4	71.1	0.1		0.2	0.3	0.1	0.4				1.050
40	Oesophagus	10.4	22.3	2.8	63.5	0.1		0.2	0.3	0.2	0.2				1.037



DRAFT REPORT FOR MC APPROVAL FOR CONSULTATION

41	Gonads	10.6	9.9	2.1	76.5	0.2		0.1	0.2	0.2	0.2				1.041
42	Pancreas	10.5	15.8	2.4	70.4	0.2		0.2	0.1	0.2	0.2				1.044
43	Prostate	10.5	25.1	2.7	60.7	0.1		0.2	0.3	0.2	0.2				1.031
44	RST	11.2	51.7	1.1	35.5	0.1		0.1	0.2	0.1					0.939
45	Skin	10.0	19.9	4.2	65.0	0.2		0.1	0.2	0.3	0.1				1.089
46	Spleen	10.3	11.2	3.2	74.3	0.1		0.2	0.2	0.2	0.3				1.060
47	Teeth	2.3	9.5	2.9	42.6		0.7	13.5				28.5			2.688
48	Thyroid	10.4	11.8	2.5	74.5	0.2		0.1	0.1	0.2	0.1		0.1		1.051
49	Urinary bladder wall	10.5	9.6	2.6	76.1	0.2		0.2	0.2	0.3	0.3				1.040
50	Urine	10.7	0.3	1.0	87.3	0.4		0.1			0.2				1.040
51	Air inside body			80.0	20.0										0.001
52	Water	11.2			88.8										1.000

1669

1670

1671 Table B.2. List of media, their elemental compositions (percentage by mass) and their densities for the
 1672 adult female mesh-type reference phantom.

Medium no.		H	C	N	O	Na	Mg	P	S	Cl	K	Ca	Fe	I	Density (g/cm ³)
1	Adrenal	10.4	23.3	2.8	62.5	0.1		0.2	0.3	0.2	0.2				1.035
2	ET, Trachea, BB, bb, Gall bladder wall, Pituitary gland, Salivary glands, Spinal cord, Thymus, Tonsils, Ureter	10.5	25.2	2.7	60.6	0.1		0.2	0.3	0.2	0.2				1.031
3	Oral mucosa, Tongue	10.2	14.2	3.4	71.1	0.1		0.2	0.3	0.1	0.4				1.050
4	Blood	10.2	11.0	3.3	74.5	0.1		0.1	0.2	0.3	0.2		0.1		1.060
5	Cortical bone	3.6	15.9	4.2	44.8	0.3	0.2	9.4	0.3			21.3			1.904
6	Medullary cavity	11.5	63.7	0.7	23.8	0.1			0.1	0.1					0.981
7	Humeri, upper, spongiosa	8.6	39.2	2.6	39.0	0.1	0.1	3.1	0.2	0.1	0.1	6.9			1.185
8	Humeri, lower, Ulnae and radii, Wrists and hand bones, Femora, lower, Tibiae, Ankles and foot, spongiosa	9.5	49.8	1.7	31.1	0.1		2.3	0.2	0.1		5.2			1.117
9	Clavicles, spongiosa	8.5	38.8	2.6	39.2	0.1	0.1	3.2	0.2	0.1	0.1	7.1			1.192
10	Cranium, spongiosa	7.9	34.5	2.9	41.3	0.2	0.1	3.9	0.2	0.1	0.1	8.8			1.252
11	Femora, upper, spongiosa	10.4	50.1	1.9	34.2	0.1		0.9	0.2	0.1	0.1	2.0			1.046
12	Mandible, spongiosa	8.6	38.3	2.7	39.8	0.1	0.1	3.1	0.2	0.1	0.1	6.9			1.189
13	Pelvis, spongiosa	9.6	42.2	2.5	39.4	0.1		1.8	0.2	0.1	0.1	3.9	0.1		1.105
14	Ribs, spongiosa	9.8	39.4	2.9	43.1	0.1		1.3	0.2	0.2	0.1	2.8	0.1		1.087
15	Scapulae, spongiosa	9.3	42.6	2.4	38.2	0.1		2.2	0.2	0.1	0.1	4.8			1.125
16	Cervical spine, spongiosa	9.2	37.1	3.0	43.6	0.1		2.0	0.2	0.2	0.1	4.4	0.1		1.129
17	Thoracic spine, spongiosa	9.8	39.9	2.9	43.0	0.1		1.2	0.2	0.2	0.1	2.5	0.1		1.080
18	Lumbar spine, spongiosa	8.8	35.2	3.1	44.0	0.1	0.1	2.6	0.2	0.1	0.1	5.7			1.165
19	Sacrum, spongiosa	10.2	41.6	2.8	42.6	0.1		0.7	0.2	0.2	0.1	1.4	0.1		1.052
20	Sternum, spongiosa	10.0	40.3	2.8	42.9	0.1		1.1	0.2	0.2	0.1	2.2	0.1		1.073
21	Cartilage	9.6	9.9	2.2	74.4	0.5		2.2	0.9	0.3					1.099
22	Brain	10.7	14.4	2.2	71.3	0.2		0.4	0.2	0.3	0.3				1.041
23	Breast, adipose tissue	11.4	58.6	0.8	28.9	0.1			0.1	0.1					0.952
24	Breast, glandular tissue	10.6	32.7	3.0	53.2	0.1		0.1	0.2	0.1					1.021
25	Eye lens	9.6	19.5	5.7	64.6	0.1		0.1	0.3	0.1					1.060
26	Cornea	10.1	12.6	3.7	73.1	0.1		0.1	0.2	0.1					1.087
27	Aqueous	11.2	0.3	0.1	88.4										1.014
28	Vitreous	11.2	0.3	0.1	88.4										1.019
29	Gall bladder contents	10.5	25.6	2.7	60.2	0.1		0.2	0.3	0.2	0.2				1.030
30	Stomach wall	10.6	11.4	2.4	75.0	0.1		0.1	0.1	0.2	0.1				1.036
31	Small intestine wall	10.5	11.4	2.5	75.0	0.1		0.1	0.1	0.2	0.1				1.036
32	Colon wall	10.5	11.4	2.5	75.0	0.1		0.1	0.1	0.2	0.1				1.036
33	GI contents	10.0	22.2	2.2	64.4	0.1		0.2	0.3	0.1	0.4	0.1			1.040
34	Heart wall	10.4	13.5	2.9	72.2	0.1		0.2	0.2	0.2	0.3				1.051
35	Kidney	10.3	12.7	3.0	72.9	0.2		0.2	0.2	0.2	0.2	0.1			1.052
36	Liver	10.2	13.2	3.1	72.3	0.2		0.2	0.3	0.2	0.3				1.060
37	Lung	10.2	10.8	3.2	74.8	0.1		0.1	0.2	0.3	0.2		0.1		0.413
38	Lymphatic nodes	10.8	4.5	1.2	82.7	0.3			0.1	0.4					1.032
39	Muscle	10.2	14.2	3.4	71.1	0.1		0.2	0.3	0.1	0.4				1.050
40	Oesophagus	10.5	22.8	2.8	62.9	0.1		0.2	0.3	0.2	0.2				1.036
41	Gonads	10.5	9.5	2.5	76.5	0.2		0.2	0.2	0.2	0.2				1.051
42	Pancreas	10.5	15.9	2.4	70.3	0.2		0.2	0.1	0.2	0.2				1.043
43	Uterus	10.6	31.0	2.4	55.2	0.1		0.2	0.2	0.1	0.2				1.021
44	RST	11.2	54.5	1	32.9	0.1		0.1	0.1	0.1					0.946



DRAFT REPORT FOR MC APPROVAL FOR CONSULTATION

45	Skin	10.0	19.9	4.2	65.0	0.2		0.1	0.2	0.3	0.1		1.088
46	Spleen	10.3	11.2	3.2	74.2	0.1		0.3	0.2	0.2	0.3		1.060
47	Teeth	2.3	9.5	2.9	42.6		0.7	13.5				28.5	2.690
48	Thyroid	10.4	11.8	2.5	74.5	0.2		0.1	0.1	0.2	0.1	0.1	1.051
49	Urinary bladder wall	10.5	9.6	2.6	76.1	0.2		0.2	0.2	0.3	0.3		1.040
50	Urine	10.7	0.3	1.0	87.3	0.4		0.1			0.2		1.040
51	Air inside body				80.0	20.0							0.001
52	Water	11.2			88.8								1.000

1673

1674

1675 **ANNEX C. LIST OF ANATOMICAL SOURCE REGIONS, ACRONYMS**
 1676 **AND ID NUMBERS**

1677 Table C.1. List of anatomical source regions, their acronyms and corresponding ID numbers in the
 1678 phantoms.

Source region	Acronym	ID number(s)
Oral cavity	O-cavity	13300
Oral mucosa	O-mucosa	500, 501, 600
Teeth surface	Teeth-S	12801
Teeth volume	Teeth-V	12800
Tongue	Tongue	500, 13300, 13301
Tonsils	Tonsils	13400
Oesophagus fast	Oesophag-f	11003
Oesophagus slow	Oesophag-s	11003
Oesophagus	Oesophagus-w	11000, 11001, 11002
Stomach contents	St-cont	7300
Stomach wall	St-wall	7200, 7201, 7202, 7203
Stomach mucosa	St-mucosa	7200, 7201, 7202
Small intestine contents	SI-cont	7501
Small intestine villi	SI-villi	7500
Small intestine wall	SI-wall	7400, 7401, 7402, 7403
Small intestine mucosa	SI-mucosa	7400, 7401, 7402
Right colon contents	RC-cont	7700, 7900
Right colon wall	RC-wall	7600, 7601, 7602, 7800, 7801, 7802
Right colon mucosa	RC-mucosa	7600, 7601, 7800, 7801
Left colon contents	LC-cont	8100, 8300
Left colon wall	LC-wall	8000, 8001, 8002, 8200, 8201, 8202
Left colon mucosa	LC-mucosa	8000, 8001, 8200, 8201
Rectosigmoid colon contents	RS-cont	8500
Rectosigmoid colon wall	RS-wall	8400, 8401, 8402, 8600
Rectosigmoid colon mucosa	RS-mucosa	8400, 8401
ET1 surface	ET1-sur	300
ET2 surface	ET2-sur	400
ET1 wall	ET1-wall	300, 301, 302, 303
ET2 wall	ET2-wall	401, 402, 403, 404, 405
ET2 bound region	ET2-bnd	401, 402, 403
ET2 sequestered region	ET2-seq	404
Extrathoracic lymph nodes	LN-ET	10000
Bronchial – fast	Bronchi-f	800
Bronchial – slow	Bronchi-s	801
Bronchi bound region	Bronchi-b	802, 803, 804, 805, 806
Bronchi sequestered region	Bronchi-q	807
Bronchiolar – fast	Brchiole-f	810
Bronchiolar – slow	Brchiole-s	811
Bronchiolar bound region	Brchiole-b	812, 813, 814
Bronchiolar sequestered region	Brchiole-q	815
Alveolar-interstitium	AI	9700, 9900
Thoracic lymph nodes	LN-Th	10100
Right lung lobe	RLung	9900
Left lung lobe	LLung	9700
RLung + LLung	Lungs	9700, 9900
Right adrenal gland	RArenal	200
Left adrenal gland	LArenal	100
RArenal + LArenal	Adrenals	100, 200
Blood vessels of head	HBlood	900, 910

Blood vessels of trunk	TBlood	1000, 1010
Blood vessels of arms	ABlood	1100, 1110
Blood vessels of legs	LBlood	1200, 1210
Blood in heart	Ht-cont	8800
Total blood	Blood	†
Cortical bone surface	C-bone-S	‡
Cortical bone volume	C-bone-V	‡
Trabecular bone surface	T-bone-S	¶
Trabecular bone volume	T-bone-V	¶
Cortical bone marrow	C-marrow	§
Trabecular bone marrow	T-marrow	‡†
Brain	Brain	6100
Right breast adipose	RBreast-a	6400
Right breast glandular	RBreast-g	6500
Left breast adipose	LBreast-a	6200
Left breast glandular	LBreast-g	6300
RBreast-a + RBreast-g	RBreast	6400, 6500
LBreast-a + LBreast-g	LBreast	6200, 6300
RBreast-a + LBreast-a	Breast-a	6200, 6400
RBreast-g + LBreast-g	Breast-g	6300, 6500
Breast-a + Breast-g	Breast	6200, 6300, 6400, 6500
Lens of eye	Eye-lens	6600, 6601, 6800, 6801
Gall bladder	GB-wall	7000
Gall bladder contents	GB-cont	7100
Heart	Ht-wall	8700
Right kidney cortex	RKidney-C	9200
Right kidney medulla	RKidney-M	9300
Right kidney pelvis	RKidney-P	9400
Right kidney C+M+P	RKidney	9200, 9300, 9400
Left kidney cortex	LKidney-C	8900
Left kidney medulla	LKidney-M	9000
Left kidney pelvis	LKidney-P	9100
Left kidney C+M+P	LKidney	8900, 9000, 9100
RKidney + LKidney	Kidneys	8900, 9000, 9100, 9200, 9300, 9400
Liver	Liver	9500
Systemic lmyph nodes	LN-Sys	10200, 10300, 10400, 10500
Muscle	Muscle	10600, 10700, 10800, 10900
Right ovary	ROvary	11200
Left ovary	LOvary	11100
ROvary + LOvary	Ovaries	11100, 11200
Pancreas	Pancreas	11300
Pituitary gland	P-gland	11400
Prostate	Prostate	11500
Salivary glands	S-glands	12000, 12100
Skin	Skin	12200, 12201, 12300, 12301, 12400, 12401, 12500, 12501
Spinal cord	Sp-cord	12600
Spleen	Spleen	12700
Testes	Testes	12900, 13000
Thymus	Thymus	13100
Thyroid	Thyroid	13200
Ureters	Ureters	13500, 13600
Urinary bladder	UB-wall	13700, 13701
Urinary bladder content	UB-cont	13800
Uterus/cervix	Uterus	13900
Adipose/residual tissue	Adipose	11600, 11700, 11800, 11900
Total body tissues (total body minus contents of walled organs)	T-body	*

	Soft tissue (T-body – mineral bone)	S-tissue	**
1679	† Blood: 900, 910, 1000, 1010, 1100, 1110, 1200, 1210, 8800, plus blood included in the organs and tissues.		
1680	‡ Cortical bone mineral: 1300, 1600, 1900, 2200, 2400, 2600, 2800, 3100, 3400, 3700, 3900, 4100, 4300, 4500, 4700, 4900, 5100, 5300, 5500.		
1681	¶ Trabecular bone mineral: mineral bone fraction of 1400, 1700, 2000, 2300, 2500, 2700, 2900, 3200, 3500, 3800, 4000, 4200, 4400, 4600, 4800, 5000, 5200, 5400, 5600.		
1682	§ Cortical bone marrow: 1500, 1800, 2100, 3000, 3300, 3600.		
1683	†† Trabecular bone marrow: marrow fraction of 1400, 1700, 2000, 2300, 2500, 2700, 2900, 3200, 3500, 3800, 4000, 4200, 4400, 4600, 4800, 5000, 5200, 5400, 5600 (red and yellow marrow).		
1684	* Total body tissues: 100-7000, 7200-7203, 7400-7403, 7600-7602, 7800-7802, 8000-8002, 8200-8202, 8400-8402, 8600-11002, 11100-13701, 13900.		
1685	** Soft tissue: 100-1210, 1500, 1800, 2100, 3000, 3300, 3600, 5700-7000, 7200-7203, 7400-7403, 7600-7602, 7800-7802, 8000-8002, 8200-8202, 8400-8402, 8600-11002, 11100-12700, 12900-13701, 13900, plus soft tissue fraction of 1400, 1700, 2000, 2300, 2500, 2700, 2900, 3200, 3500, 3800, 4000, 4200, 4400, 4600, 4800, 5000, 5200, 5400, 5600.		
1686			
1687			
1688			
1689			
1690			
1691			
1692			

1693 **ANNEX D. LIST OF ANATOMICAL TARGET REGIONS, ACRONYMS**
 1694 **AND ID NUMBERS**

1695 **Table D.1. List of target regions, their acronyms and corresponding ID numbers in the phantoms.**

Target region	Acronym	ID number(s)
Red (active) marrow	R-marrow	†
Colon wall	Colon	7600, 7601, 7602, 7800, 7801, 7802, 8000, 8001, 8002, 8200, 8201, 8202, 8400, 8401, 8402, 8600
Stem cells of colon	Colon-stem	7601, 7801, 8001, 8201, 8401
RLung + LLung	Lungs	9700, 9900
Stomach wall	St-wall	7200, 7201, 7202, 7203
Stem cells of stomach	St-stem	7201
Breast-a + Breast-g	Breast	6200, 6300, 6400, 6500
ROvary + LOvary	Ovaries	11100, 11200
Testes	Testes	12900, 13000
Urinary bladder wall	UB-wall	13700, 13701
Urinary bladder basal cells	UB-basal	13701
Oesophagus wall	Oesophagus	11000, 11001, 11002
Oesophagus basal cells	Oesophagus-bas	11001
Liver	Liver	9500
Thyroid	Thyroid	13200
50- μ m endosteal region	Endost-BS	‡
Brain	Brain	6100
Salivary glands	S-glands	12000, 12100
Skin	Skin	12200, 12201, 12300, 12301, 12400, 12401, 12500, 12501
Basal cells of skin	Skin-bas	12201, 12301, 12401, 12501
RAdrenal + LAdrenal	Adrenals	100, 200
ET region	ET	300, 301, 302, 303, 401, 402, 403, 404, 405
Gall bladder wall	GB-wall	7000
Heart wall	Ht-wall	8700
RKidney + LKidney	Kidneys	8900, 9000, 9100, 9200, 9300, 9400
Systemic lymph nodes	LN-Sys	10200, 10300, 10400, 10500
Muscle	Muscle	10600, 10700, 10800, 10900
Oral mucosa	O-mucosa	500, 501, 600
Pancreas	Pancreas	11300
Prostate	Prostate	11500
Small intestine wall	SI-wall	7400, 7401, 7402, 7403
Stem cells of small intestine	SI-stem	7401
Spleen	Spleen	12700
Thymus	Thymus	13100
Uterus/cervix	Uterus	13900
Tongue	Tongue	500, 13300, 13301
Tonsils	Tonsils	13400
Right colon wall (ascending + right transverse)	RC-wall	7600, 7601, 7602, 7800, 7801, 7802
Left colon wall (left transverse + descending)	LC-wall	8000, 8001, 8002, 8200, 8201, 8202
Rectosigmoid colon wall (sigmoid + rectum)	RS-wall	8400, 8401, 8402, 8600
Stem cells of right colon (ascending + right transverse)	RC-stem	7601, 7801
Stem cells of left colon (left transverse + descending)	LC-stem	8001, 8201
Stem cells of rectosigmoid colon (sigmoid + rectum)	RSig-stem	8401
Basal cells of anterior nasal passages	ET1-bas	302
Basal cells of posterior nasal passages + pharynx	ET2-bas	402
Extrathoracic lymph nodes	LN-ET	10000
Bronchi basal cells	Bronch-bas	804, 805
Bronchi secretory cells	Bronch-sec	803, 804

Bronchiolar secretory cells	Brciol-sec	813
Alveolar-interstitial	AI	9700, 9900
Thoracic lymph nodes	LN-Th	10100
Right lung lobe	RLung	9900
Left lung lobe	LLung	9700
Right adrenal gland	RAdrenal	200
Left adrenal gland	LAdrenal	100
Right breast adipose	RBreast-a	6400
Right breast glandular	RBreast-g	6500
Left breast adipose	LBreast-a	6200
Left breast glandular	LBreast-g	6300
RBreast-a + RBreast-g	RBreast	6400, 6500
LBreast-a + LBreast-g	LBreast	6200, 6300
RBreast-a + LBreast-a	Breast-a	6200, 6400
RBreast-g + LBreast-g	Breast-g	6300, 6500
Entire lenses of eye	Lens-ent	6600, 6601, 6800, 6801
Sensitive lenses of eye	Lens-sen	6600, 6800
Right kidney cortex	RKidney-C	9200
Right kidney medulla	RKidney-M	9300
Right kidney pelvis	RKidney-P	9400
Right kidney C+M+P	RKidney	9200, 9300, 9400
Left kidney cortex	LKidney-C	8900
Left kidney medulla	LKidney-M	9000
Left kidney pelvis	LKidney-P	9100
Left kidney C+M+P	LKidney	8900, 9000, 9100
Right ovary	ROvary	11200
Left ovary	LOvary	11100
Pituitary gland	P-gland	11400
Spinal cord	Sp-cord	12600
Ureters	Ureters	13500, 13600
Adipose/residual tissue	Adipose	11600, 11700, 11800, 11900

1696 † Red bone marrow fraction in organ IDs 1400, 2500, 2700, 2900, 4000, 4200, 4400, 4600, 4800, 5000, 5200, 5400, 5600.

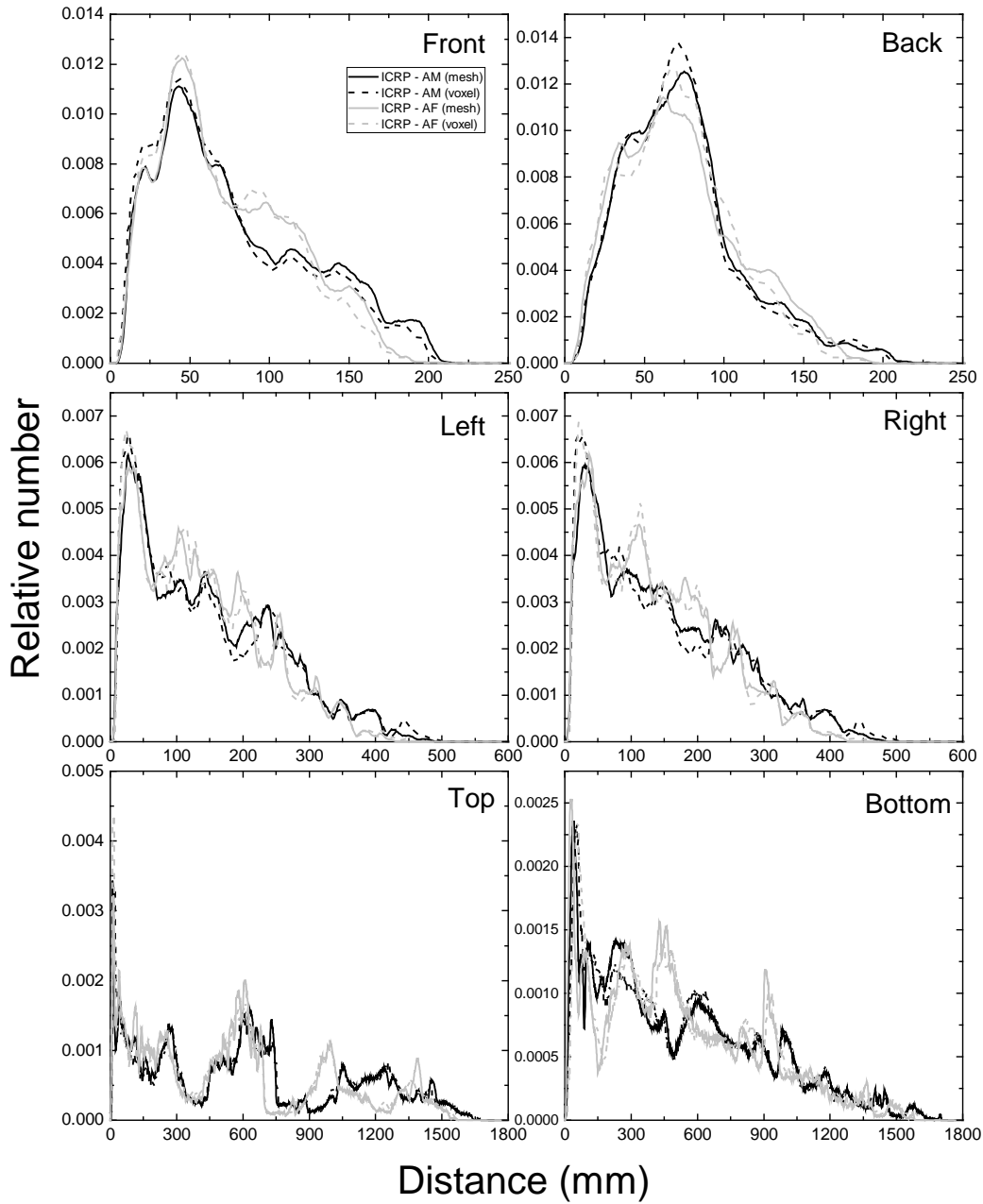
1697 ‡ Endosteum fraction in organ IDs 1400, 1500, 1700, 1800, 2000, 2100, 2300, 2500, 2700, 2900, 3000, 3200, 3300, 3500, 3600, 3800, 4000,
1698 4200, 4400, 4600, 4800, 5000, 5200, 5400, 5600.

1699

1700
1701**ANNEX E. ORGAN DEPTH DISTRIBUTIONS OF SELECTED
ORGANS/TISSUES**1702
1703
1704
1705
1706
1707
1708
1709
1710

(E1) In Figs. E.1–E.13, organ depth distributions (ODDs) of the adult mesh-type reference computational phantoms and the *Publication 110* phantoms are shown for the selected organs and tissues (i.e. spongiosa, colon wall, lungs, stomach wall, breasts, gonads, urinary bladder wall, oesophagus, liver, thyroid, brain, salivary glands and skin). For the ODD calculation, ten million points were randomly sampled in the considered organ/tissue, and the distances from the sampled points to the outer surface (e.g. front, back, left, etc.) of the phantoms were calculated. The ODDs represent a depth of an organ/tissue below the outer surface of the phantoms, significantly influencing dose calculation for external exposure.

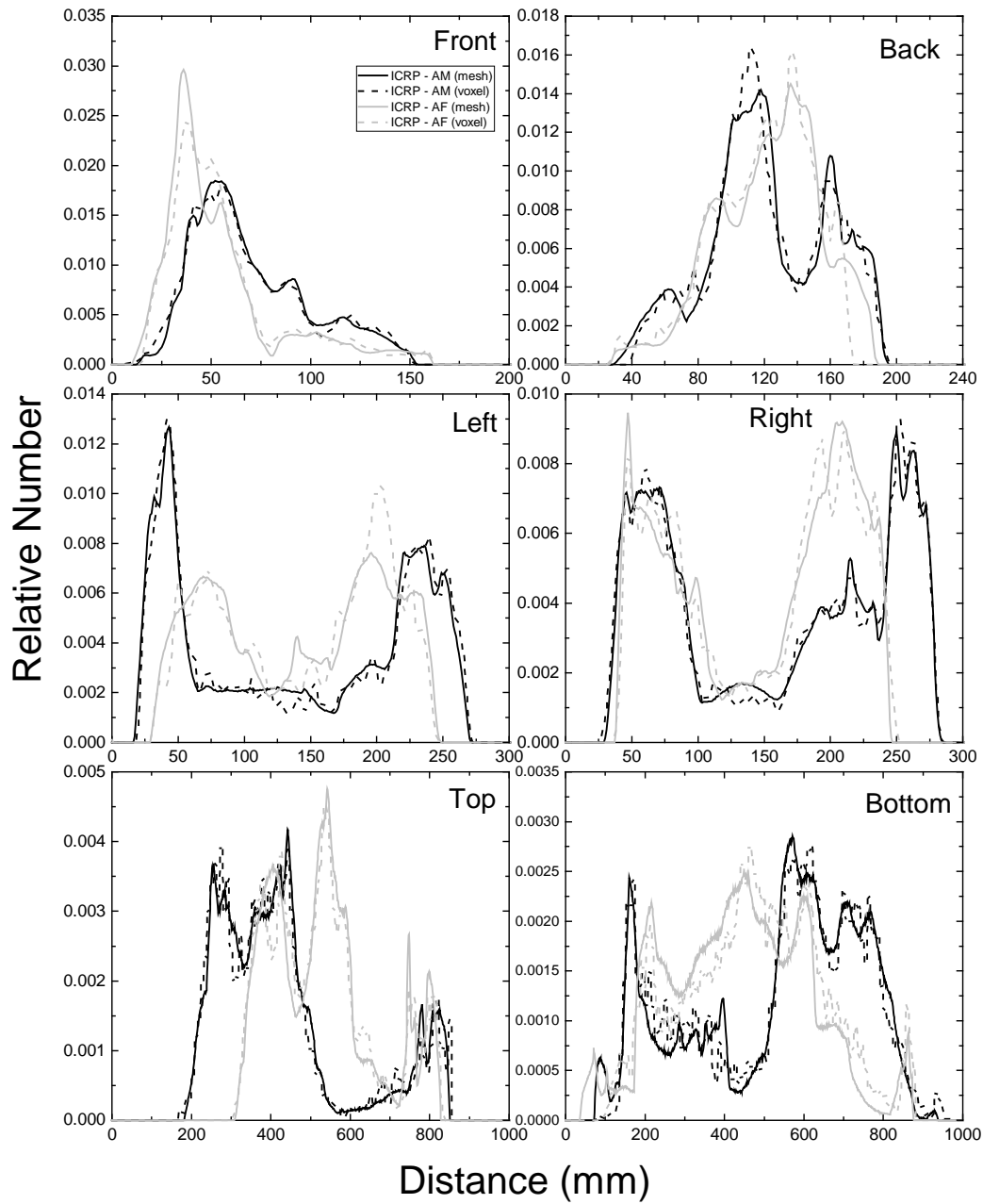
Spongiosa



1711
 1712
 1713
 1714
 1715
 1716
 1717

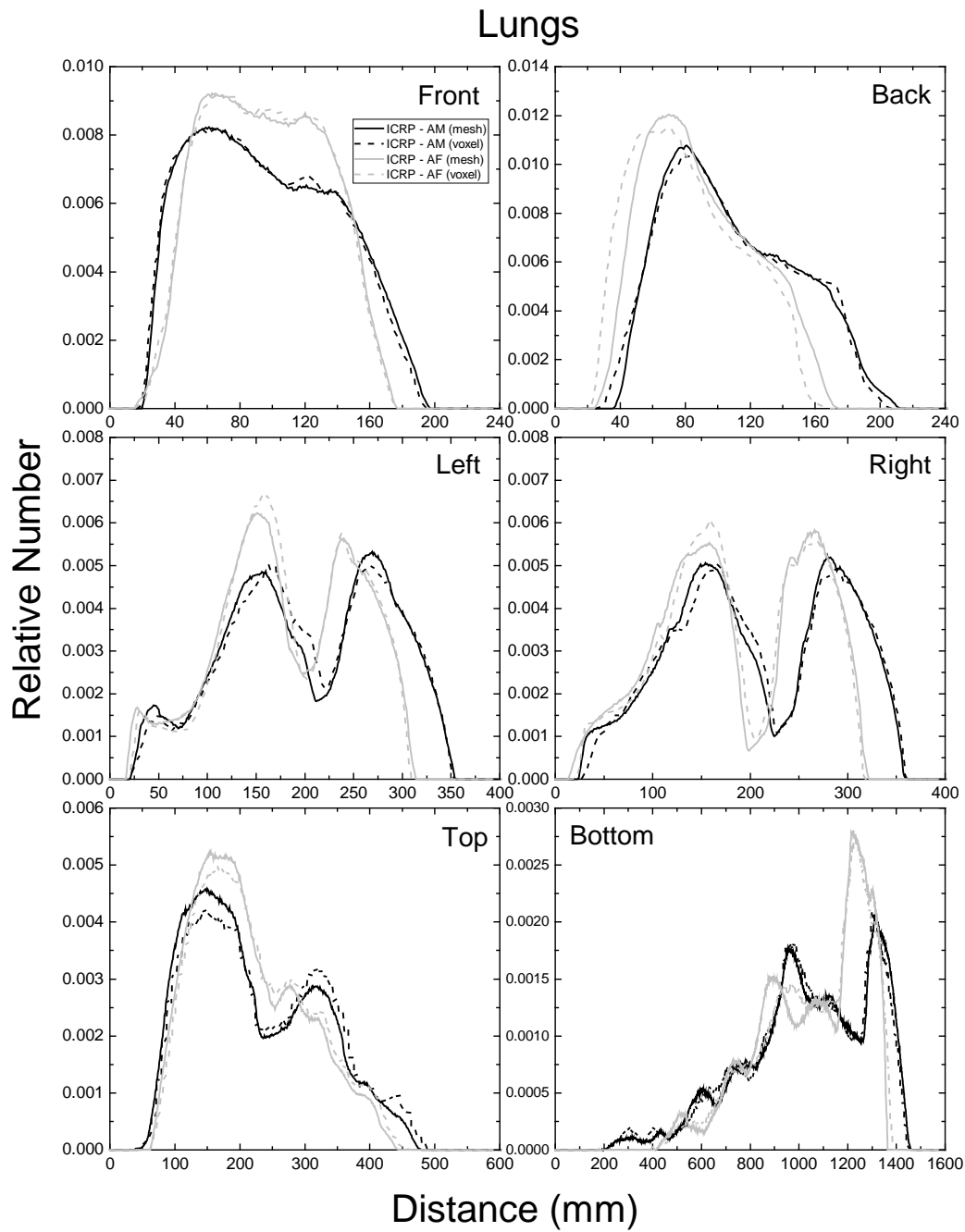
Fig. E.1. Distribution of depths of 10 million randomly sampled points in the spongiosa below the body surfaces at: front, back, left, right, top and bottom.

Colon Wall



1718
1719
1720
1721
1722

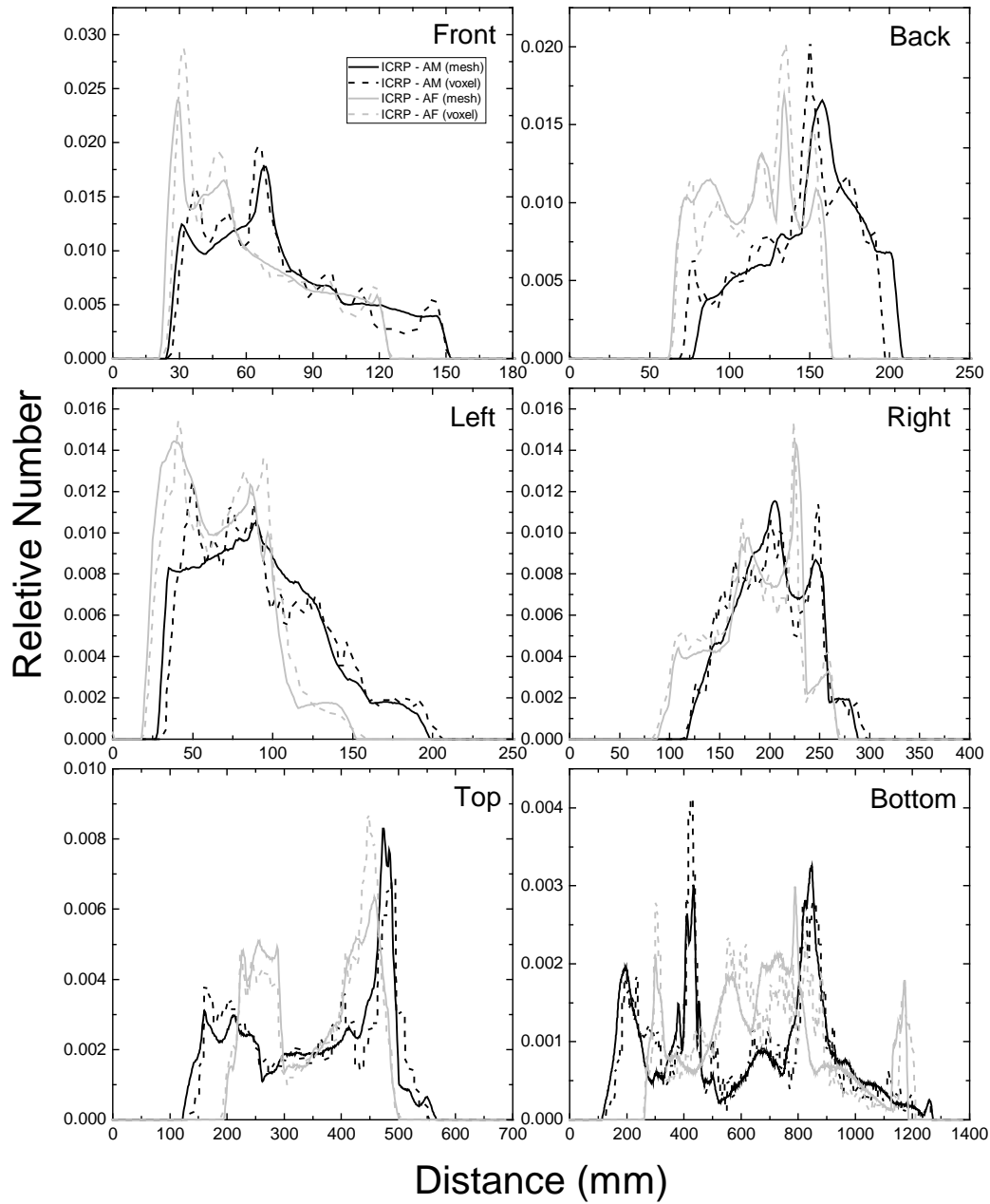
Fig. E.2. Distribution of depths of 10 million randomly sampled points in the colon wall below the body surfaces at: front, back, left, right, top and bottom.



1723
1724
1725
1726
1727

Fig. E.3. Distribution of depths of 10 million randomly sampled points in the lungs below the body surfaces at: front, back, left, right, top and bottom.

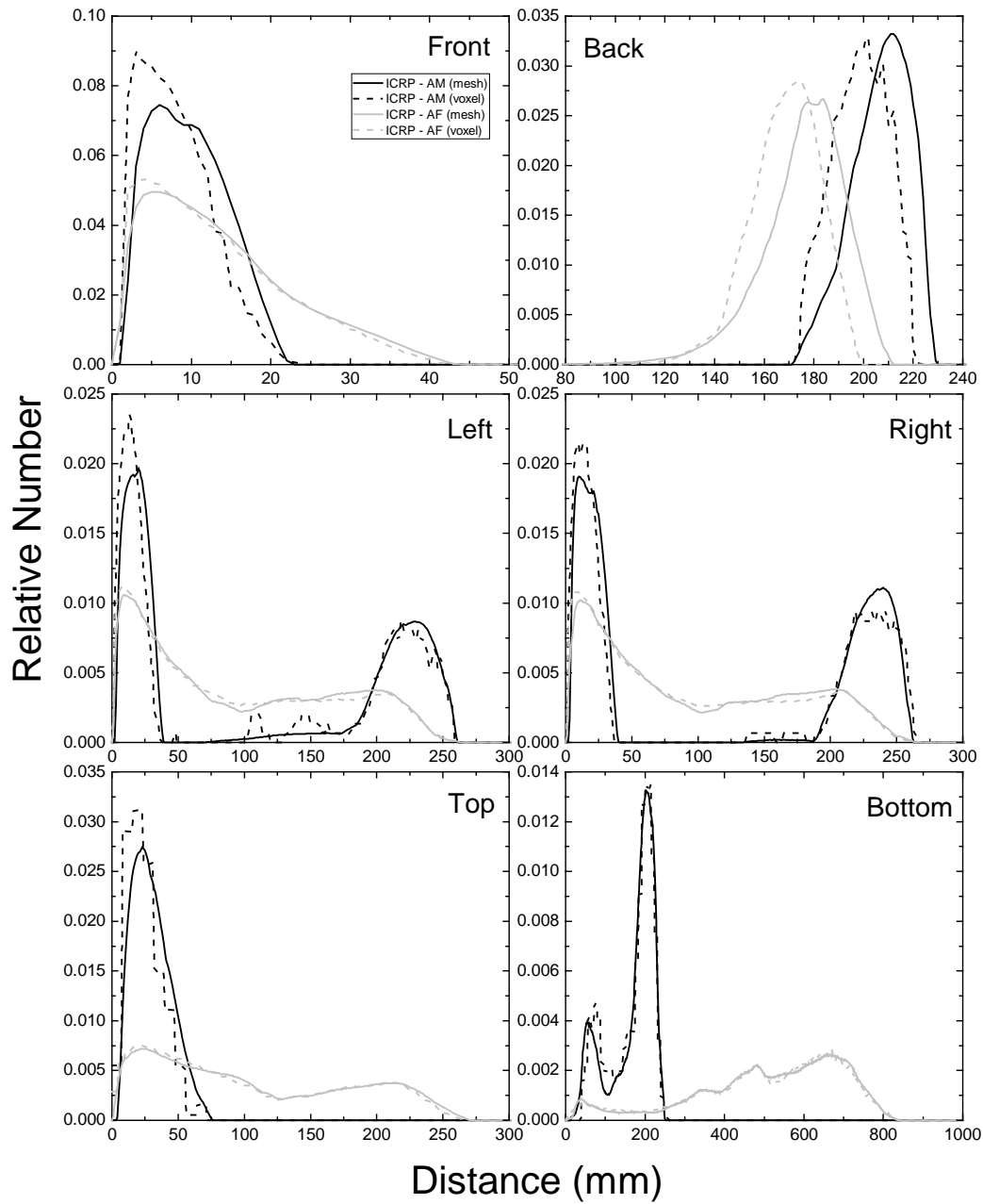
Stomach Wall



1728
1729
1730
1731
1732

Fig. E.4. Distribution of depths of 10 million randomly sampled points in the stomach wall below the body surfaces at: front, back, left, right, top and bottom.

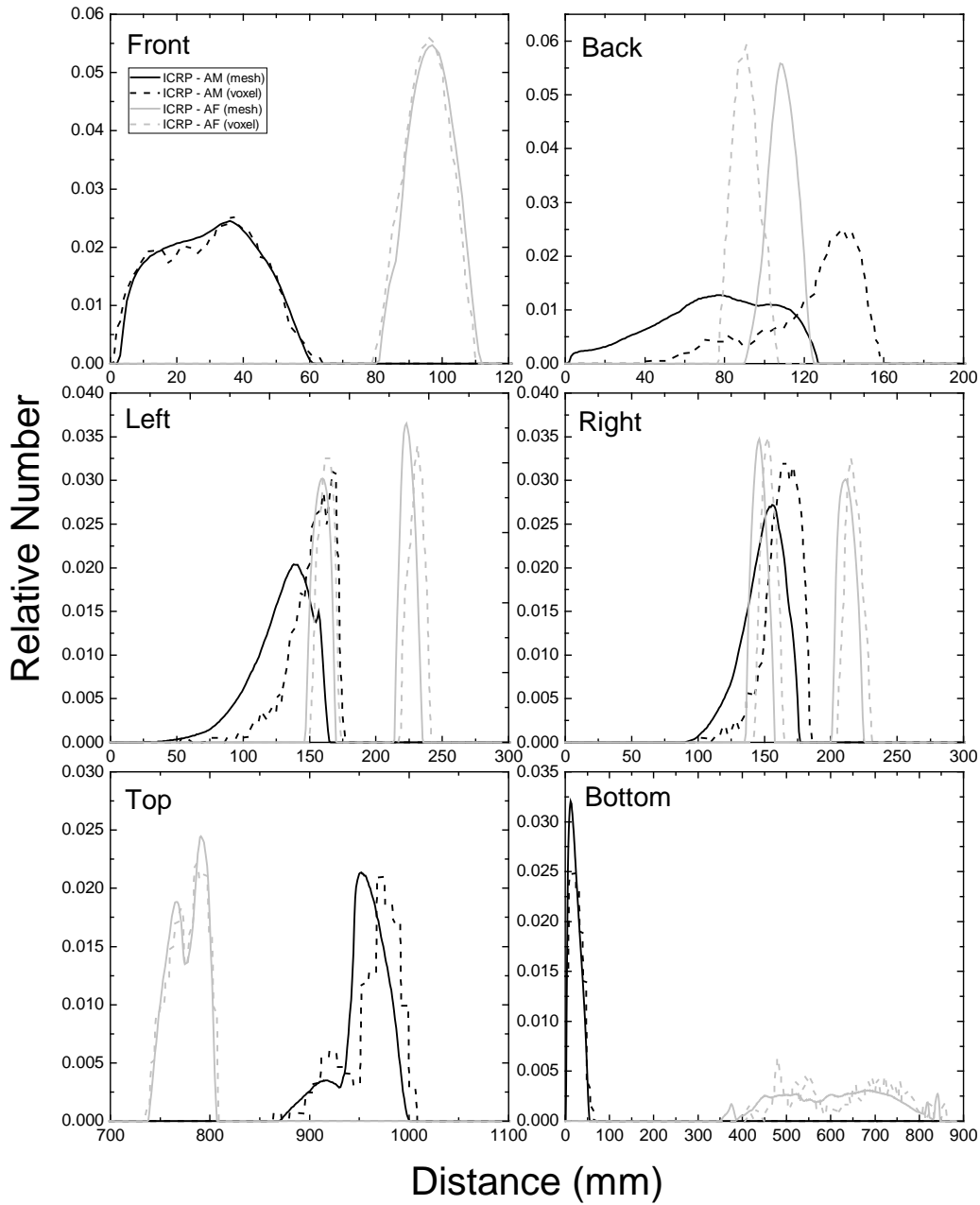
Breasts



1733
1734
1735
1736

Fig. E.5. Distribution of depths of 10 million randomly sampled points in the breasts below the body surfaces at: front, back, left, right, top and bottom.

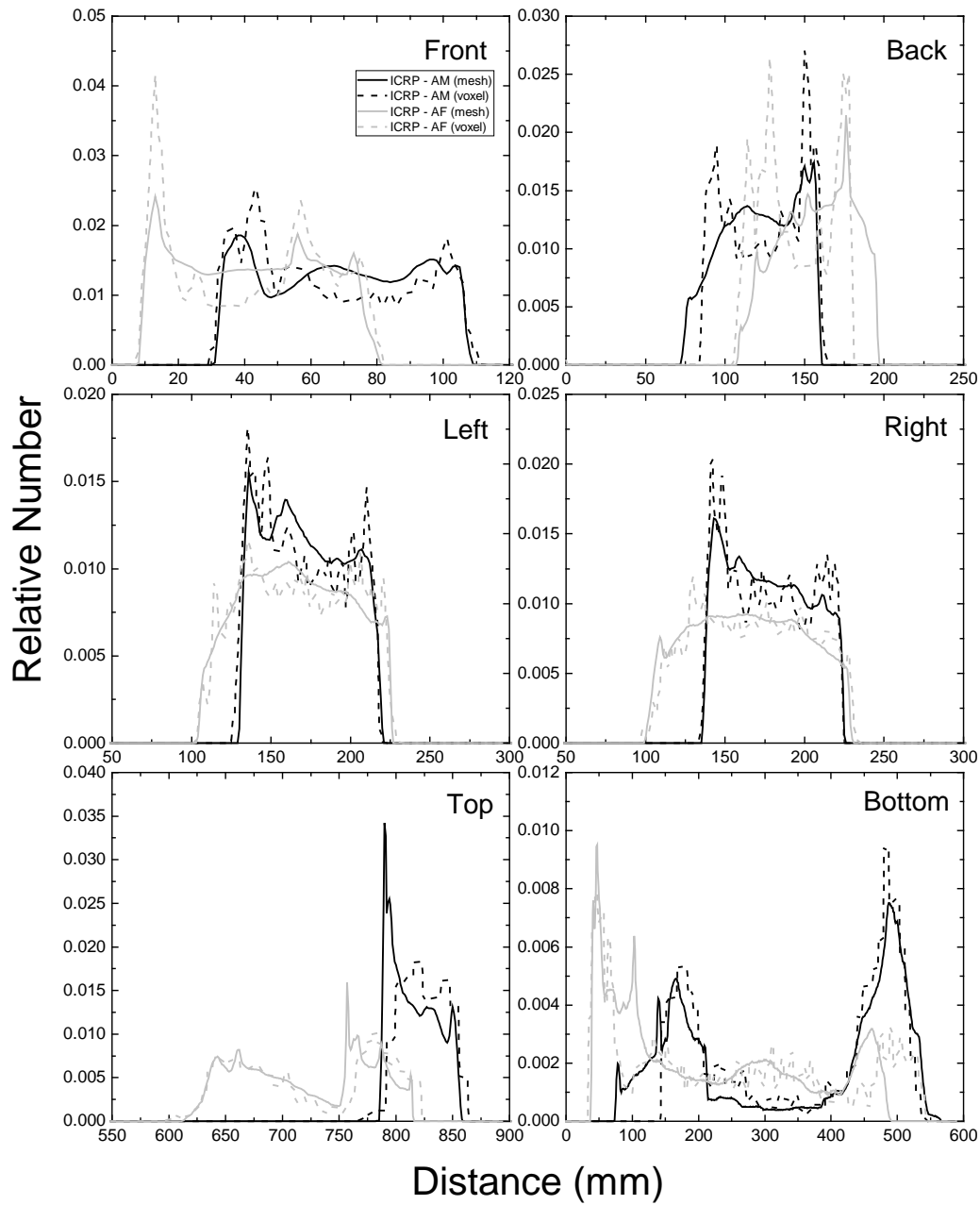
Gonads



1737
 1738
 1739
 1740
 1741

Fig. E.6. Distribution of depths of 10 million randomly sampled points in the gonads below the body surfaces at: front, back, left, right, top and bottom.

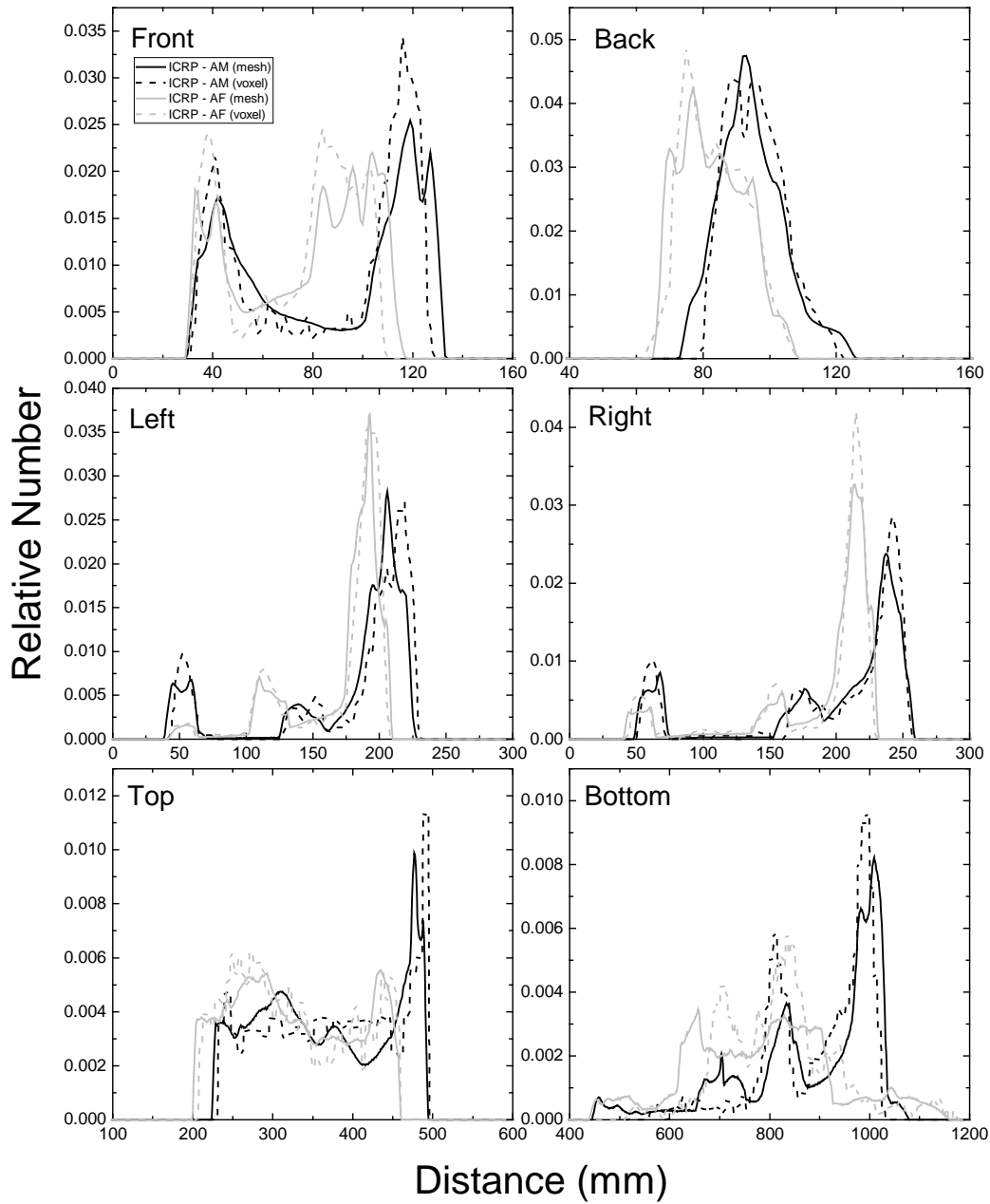
Urinary Bladder Wall



1742
1743
1744
1745

Fig. E.7. Distribution of depths of 10 million randomly sampled points in the urinary bladder wall below the body surfaces at: front, back, left, right, top and bottom.

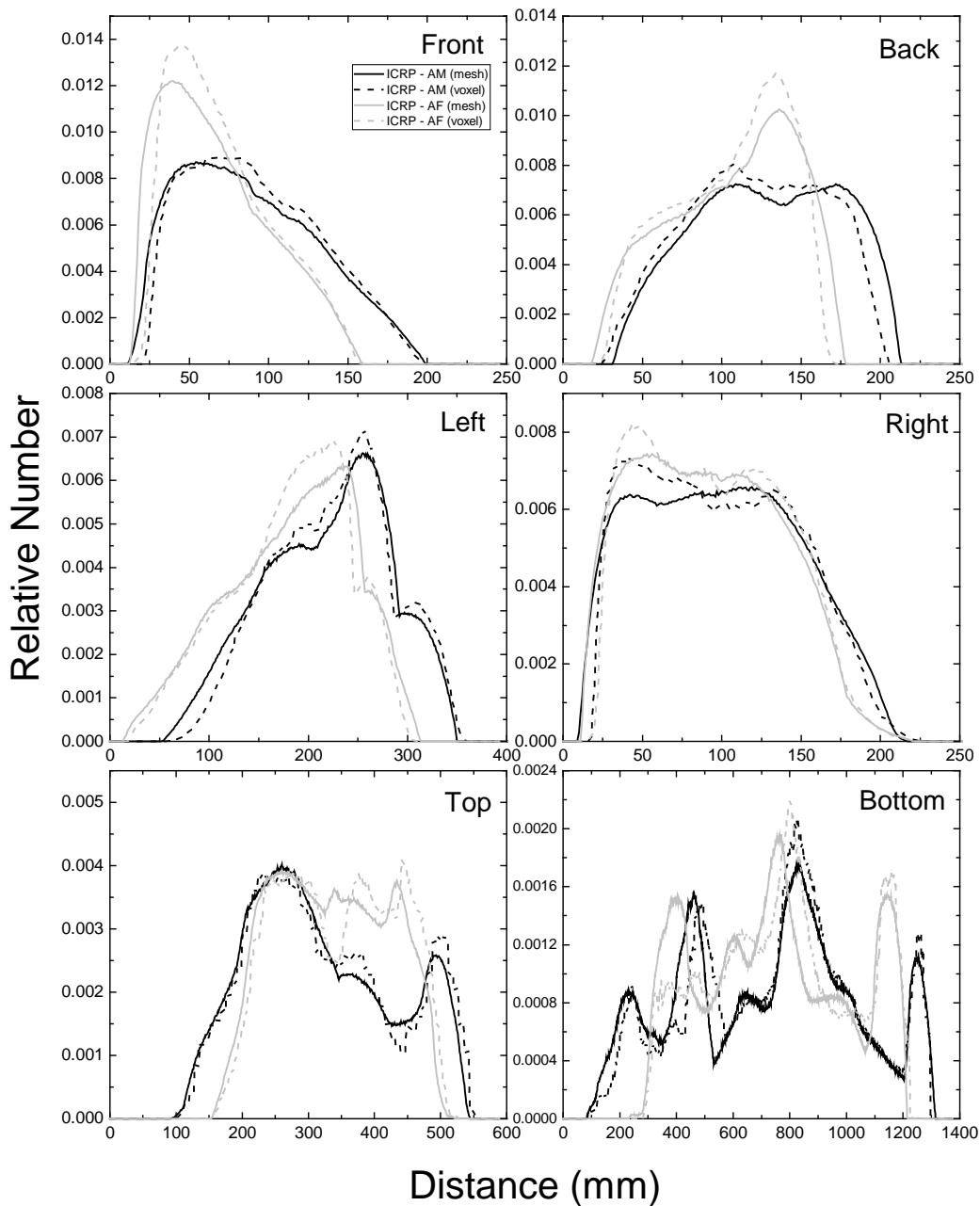
Oesophagus



1746
1747
1748
1749

Fig. E.8. Distribution of depths of 10 million randomly sampled points in the oesophagus below the body surfaces at: front, back, left, right, top and bottom.

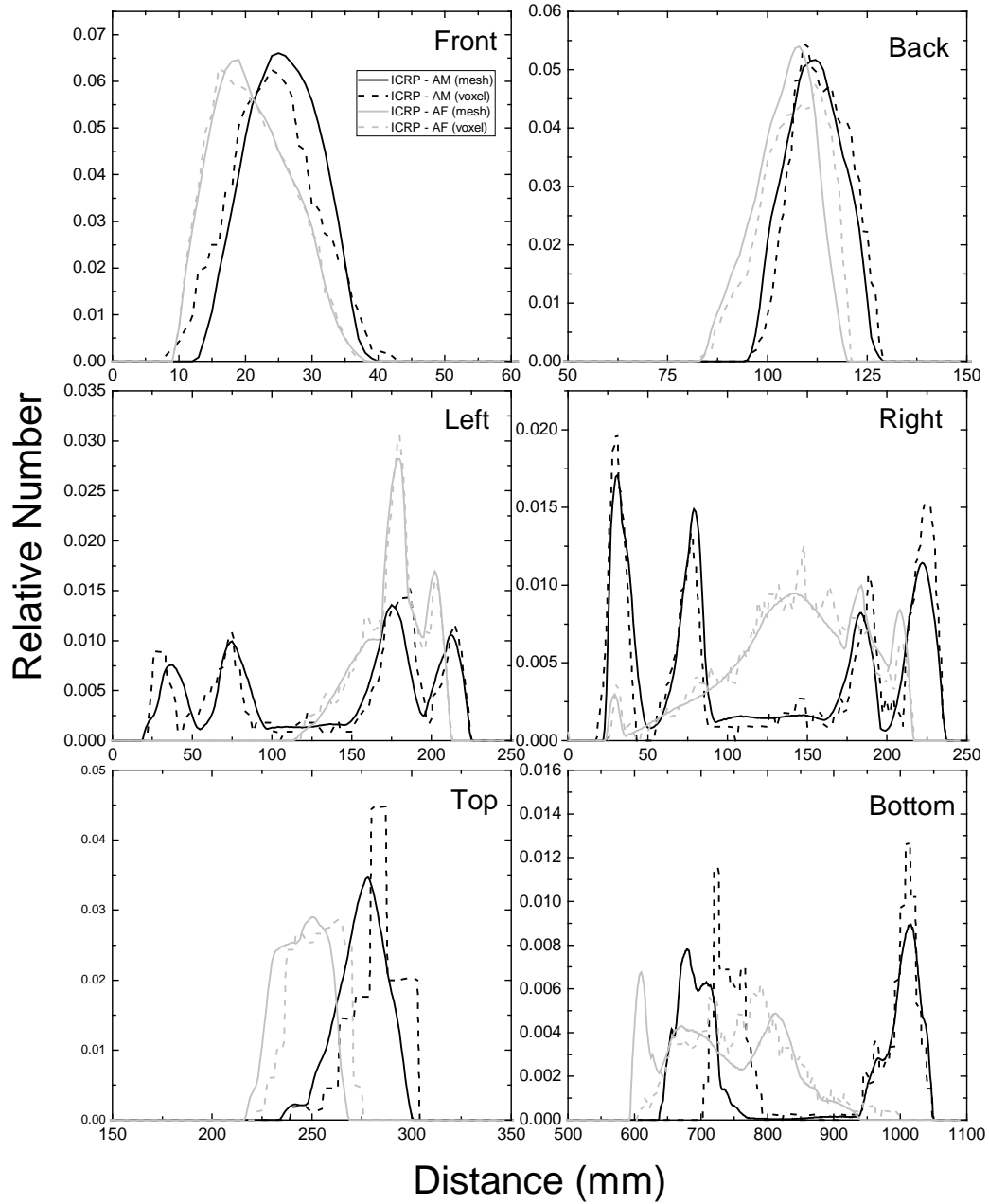
Liver



1750
1751
1752
1753

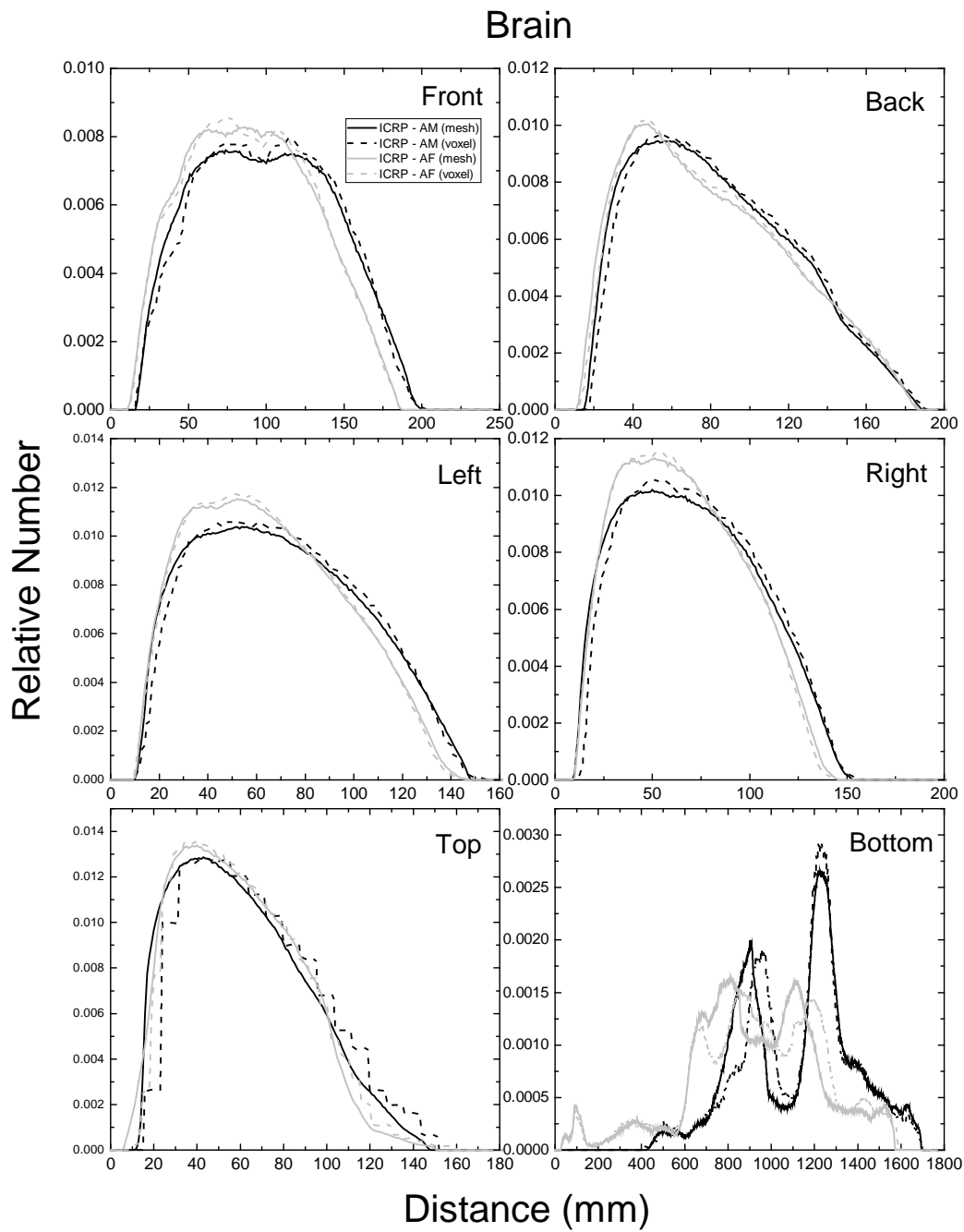
Fig. E.9. Distribution of depths of 10 million randomly sampled points in the liver below the body surfaces at: front, back, left, right, top and bottom.

Thyroid



1754
1755
1756
1757

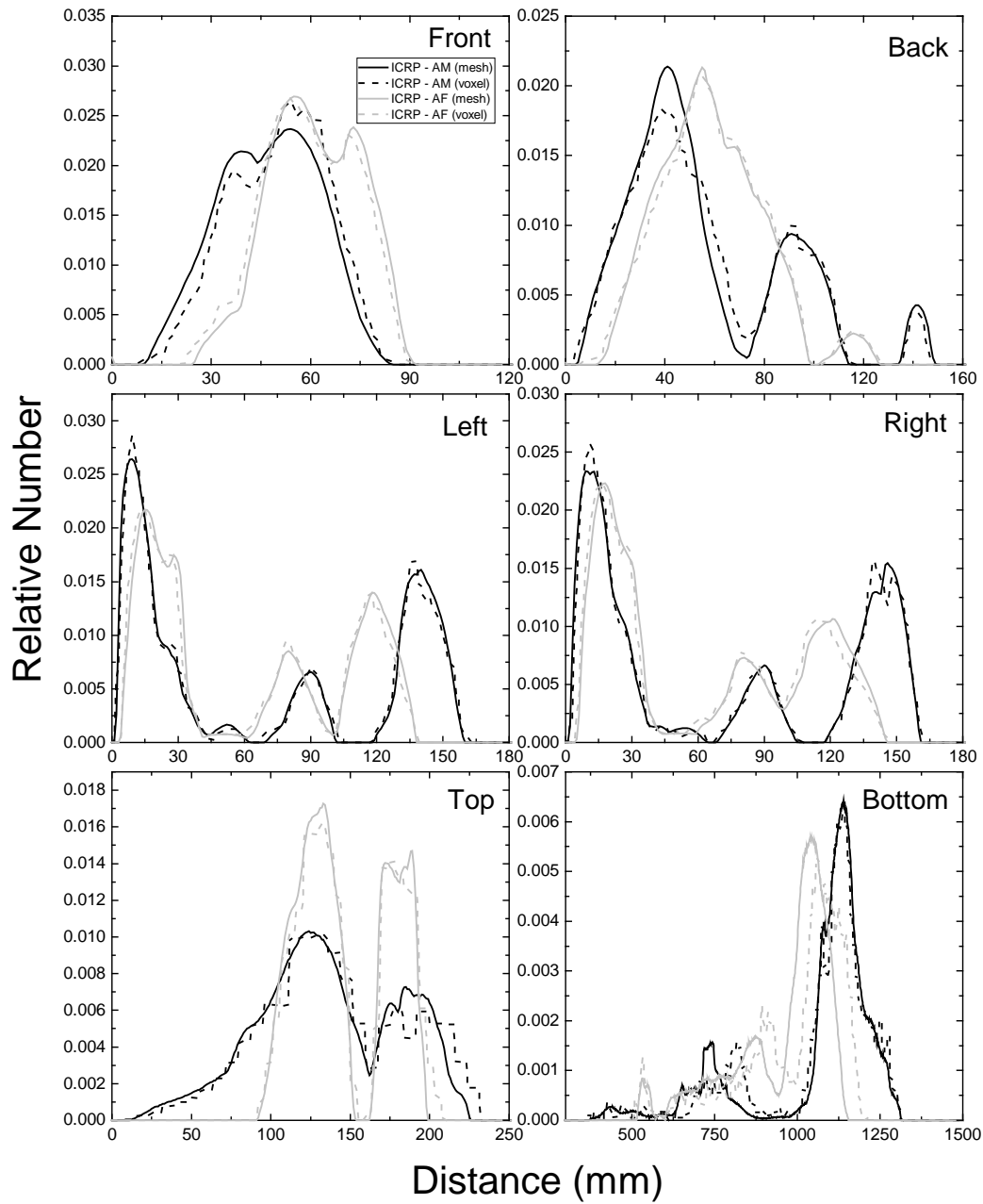
Fig. E.10. Distribution of depths of 10 million randomly sampled points in the thyroid below the body surfaces at: front, back, left, right, top and bottom.



1758
 1759
 1760
 1761
 1762

Fig. E.11. Distribution of depths of 10 million randomly sampled points in the brain below the body surfaces at: front, back, left, right, top and bottom.

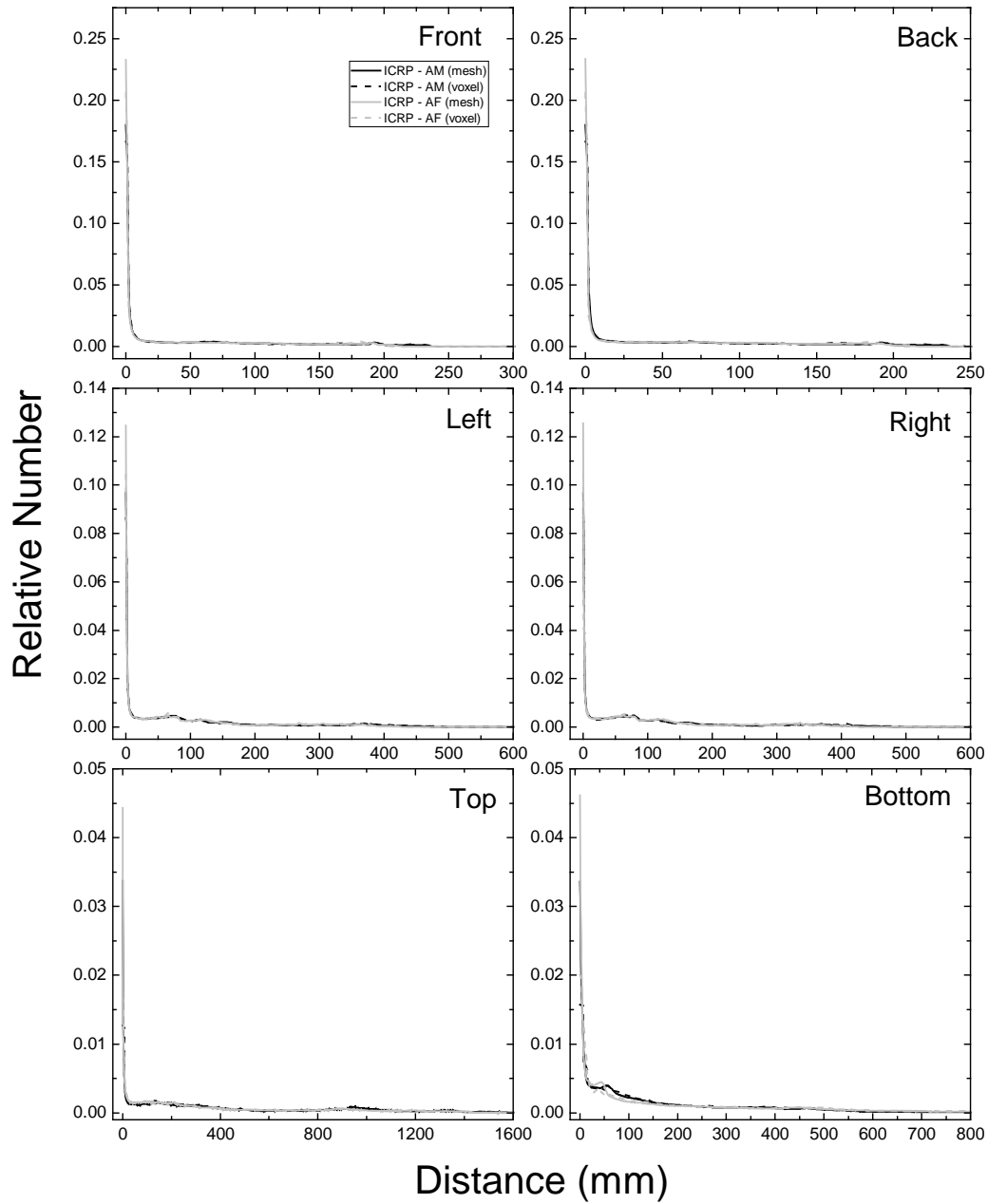
Salivary Glands



1763
1764
1765
1766
1767

Fig. E.12. Distribution of depths of 10 million randomly sampled points in the salivary glands below the body surfaces at: front, back, left, right, top and bottom.

Skin

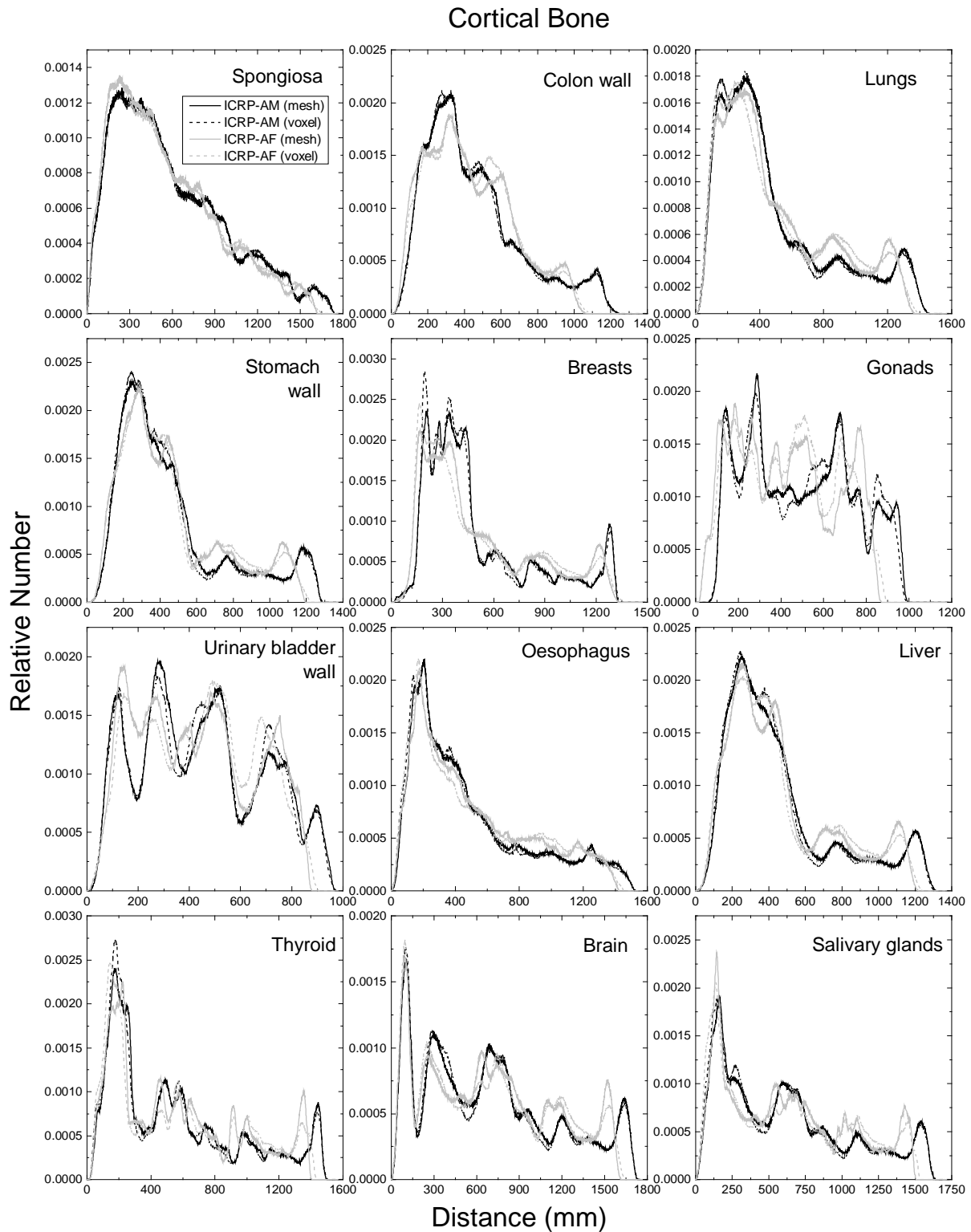


1768
1769
1770
1771

Fig. E.13. Distribution of depths of 10 million randomly sampled points in the skin below the body surfaces at: front, back, left, right, top and bottom.

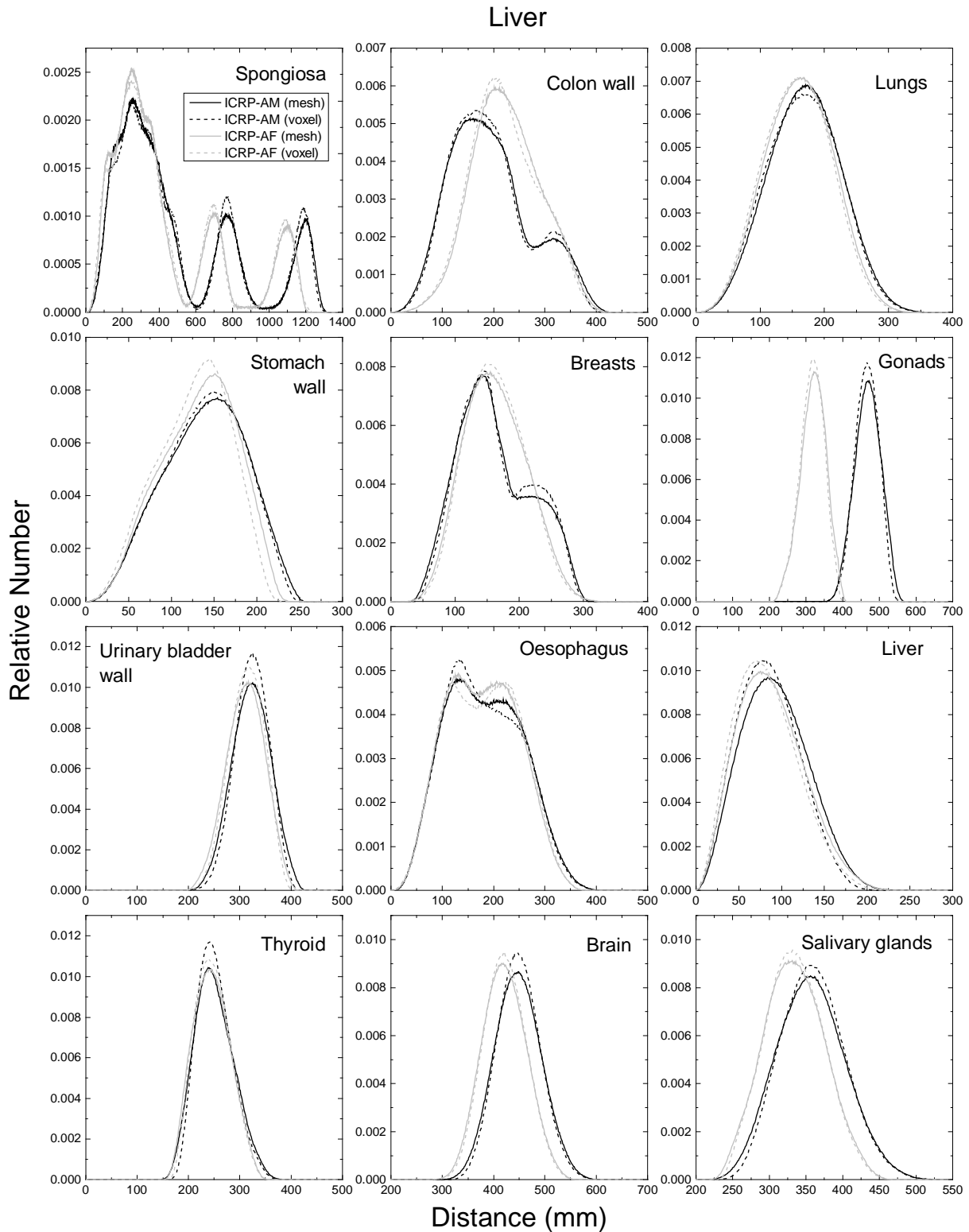
1772
1773**ANNEX F. CHORD-LENGTH DISTRIBUTIONS BETWEEN
SELECTED ORGAN PAIRS (SOURCE/TARGET TISSUES)**

1774 (F1) In Figs. F.1–F.5, chord-length distributions (CLDs) of the adult mesh-type reference
1775 computational phantoms and the *Publication 110* phantoms are shown for the selected
1776 organ/tissue pairs (i.e. source/target regions): source regions (cortical bone, liver, lungs, thyroid
1777 and urinary bladder contents); target regions (spongiosa, colon wall, lungs, stomach wall,
1778 breasts, gonads, urinary bladder wall, oesophagus, liver, thyroid, brain and salivary glands).
1779 For the CLD calculation, ten million point pairs were randomly sampled in the target and source
1780 regions considered, and distances of the points pairs were calculated. The CLDs represent a
1781 distance between the target and source regions, significantly influencing dose calculation for
1782 internal exposure.
1783



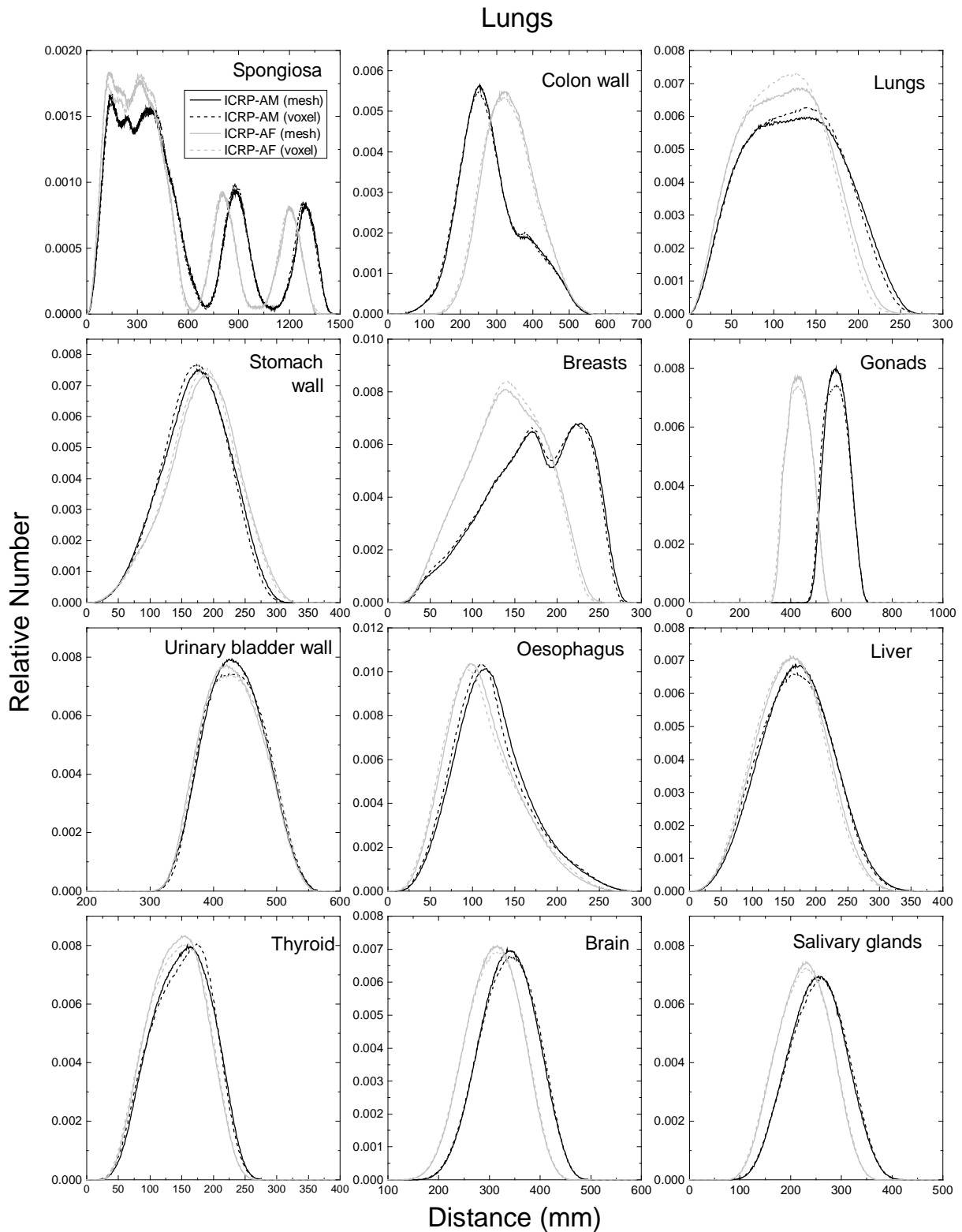
1784
1785
1786
1787
1788
1789

Fig. F.1. Distribution of distances between 10 million randomly sampled point pairs in the cortical bone (a source region and the spongiosa, colon wall, lungs, stomach wall, breasts, gonads, urinary bladder wall, oesophagus, liver, thyroid, brain and salivary glands (target regions)).



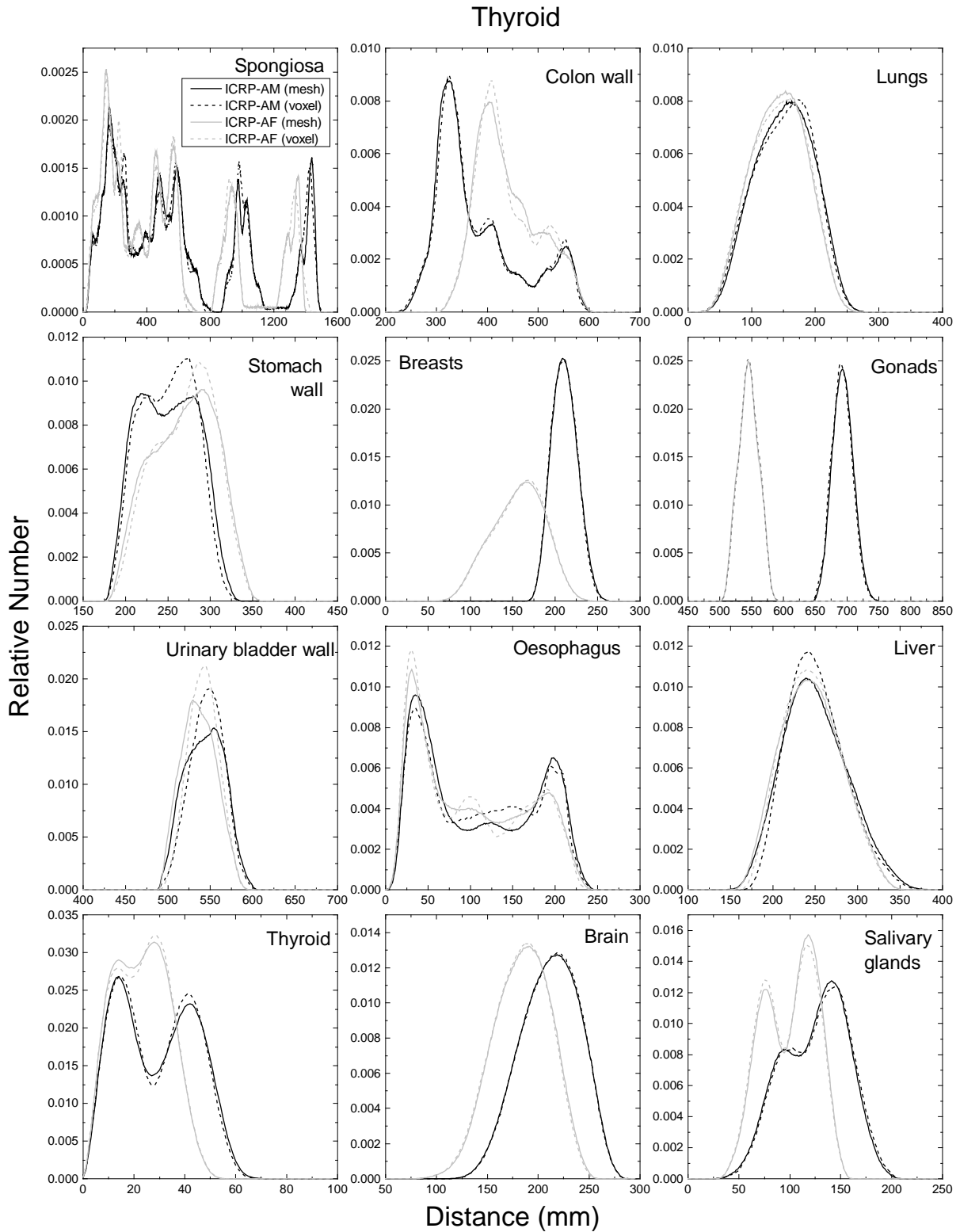
1790
1791
1792
1793
1794
1795

Fig. F.2. Distribution of distances between 10 million randomly sampled point pairs in the liver (a source region) and the spongiosa, colon wall, lungs, stomach wall, breasts, gonads, urinary bladder wall, oesophagus, liver, thyroid, brain and salivary glands (target regions).



1796
1797
1798
1799
1800
1801

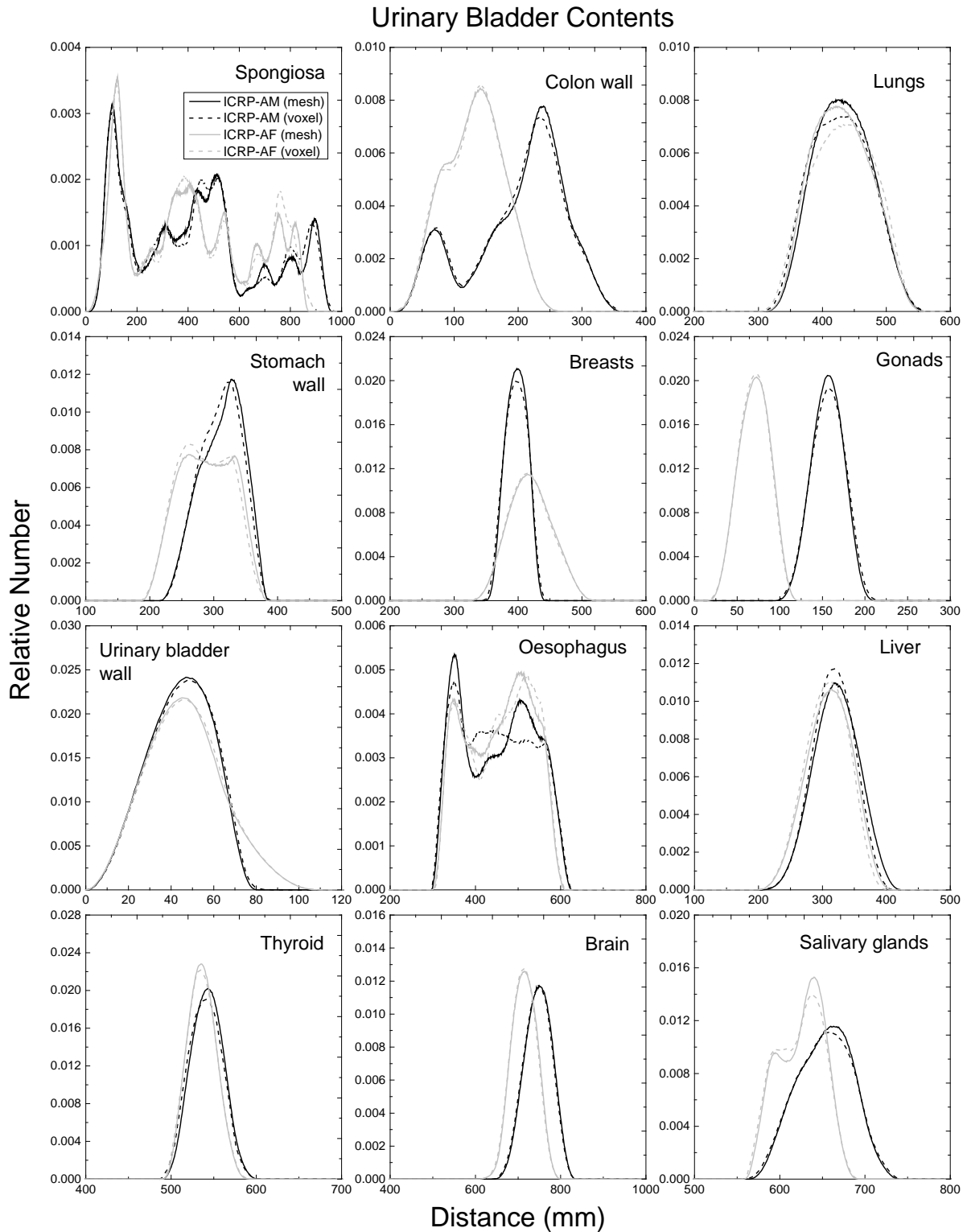
Fig. F.3. Distribution of distances between 10 million randomly sampled point pairs in the lungs (a source region) and the spongiosa, colon wall, lungs, stomach wall, breasts, gonads, urinary bladder wall, oesophagus, liver, thyroid, brain and salivary glands (target regions).



1802
1803
1804
1805
1806
1807

Fig. F.4. Distribution of distances between 10 million randomly sampled point pairs in the thyroid (a source region) and the spongiosa, colon wall, lungs, stomach wall, breasts, gonads, urinary bladder wall, oesophagus, liver, thyroid, brain and salivary glands (target regions).

1808



1809
1810
1811
1812
1813
1814

Fig. F.5. Distribution of distances between 10 million randomly sampled point pairs in the urinary bladder contents (a source region) and the spongiosa, colon wall, lungs, stomach wall, breasts, gonads, urinary bladder wall, oesophagus, liver, thyroid, brain and salivary glands (target regions)

1815

ANNEX G. CROSS-SECTIONAL IMAGES

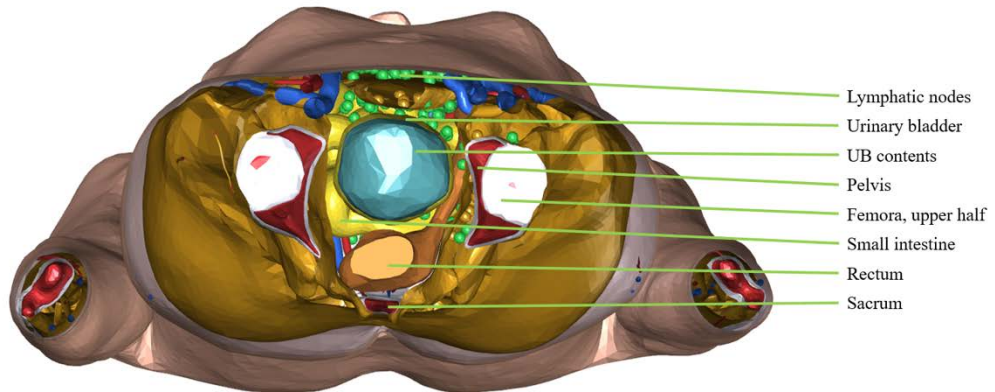
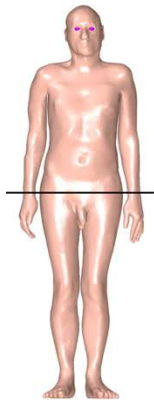
1816

G.1. Images of the adult mesh-type reference computation phantom for male

1817

1818

G.1.1. Transverse (axial) images

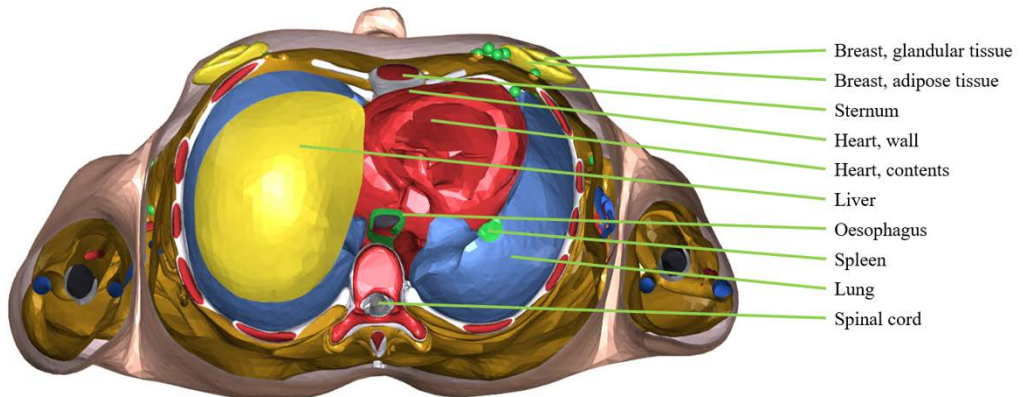


1819

1820

1821

1822

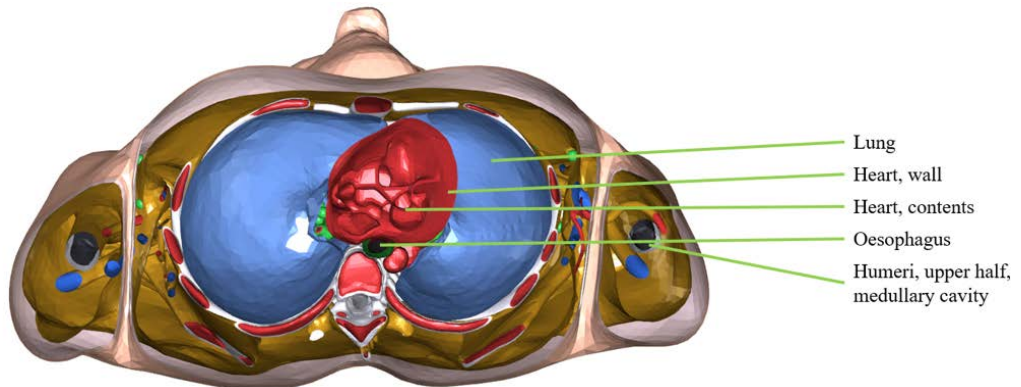


1823

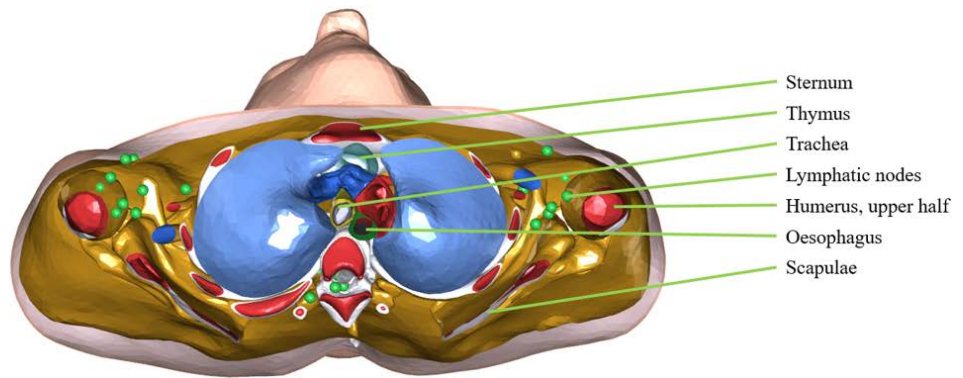
1824

1825

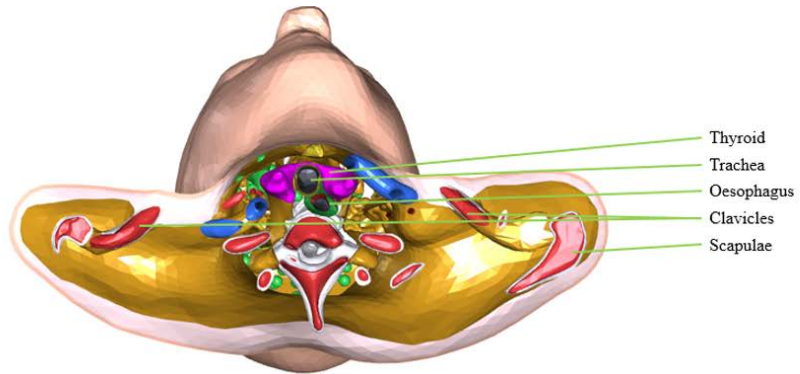
1826



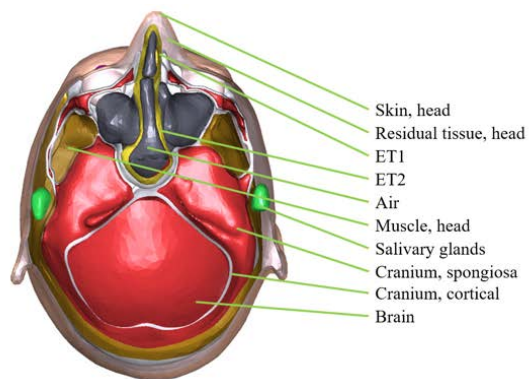
1827



1828
1829
1830
1831

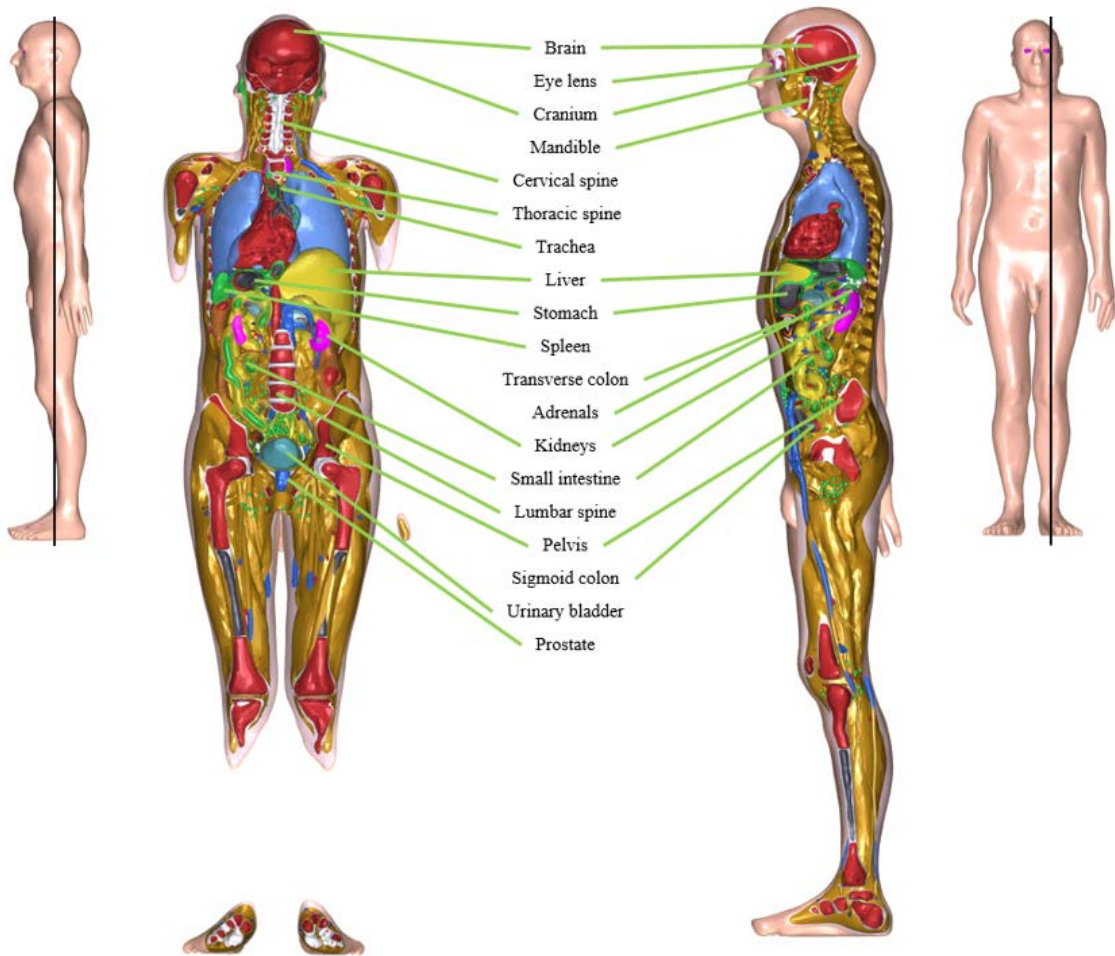


1832
1833
1834
1835



1836
1837

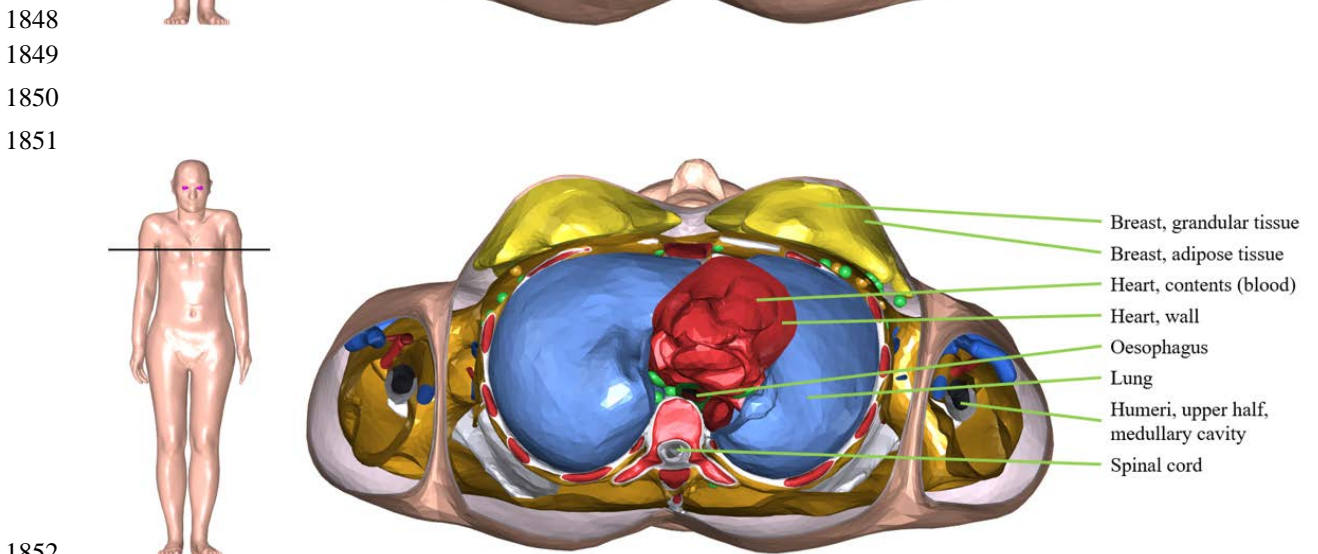
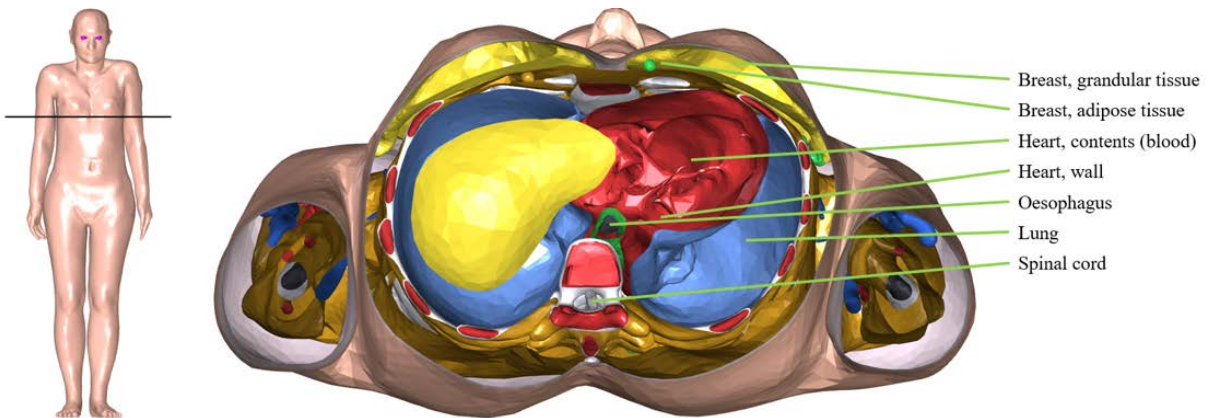
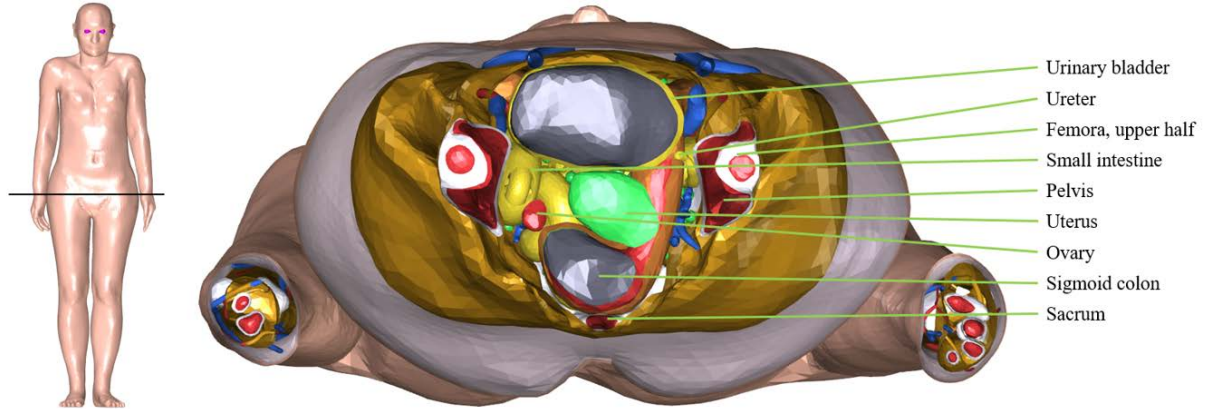
1838 **G.1.2. Coronal and sagittal images**



1839
1840

1841 **G.2. Images of the adult mesh-type reference computational phantom for**
 1842 **female**

1843 **G.2.1. Transverse (axial) images**

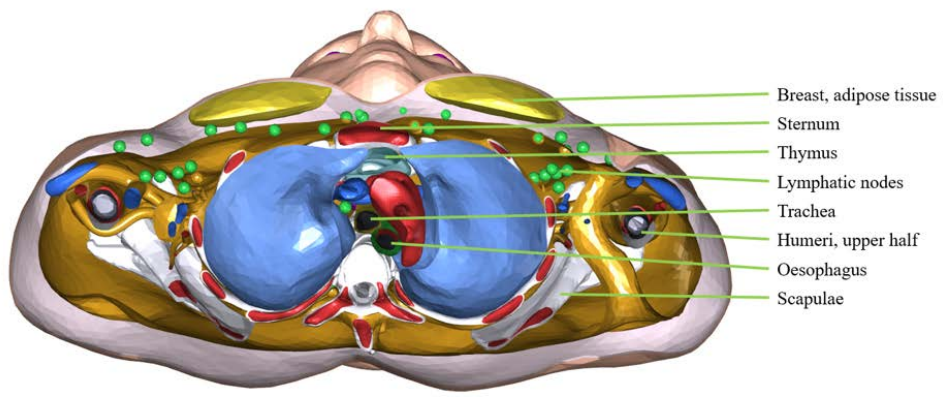


1852

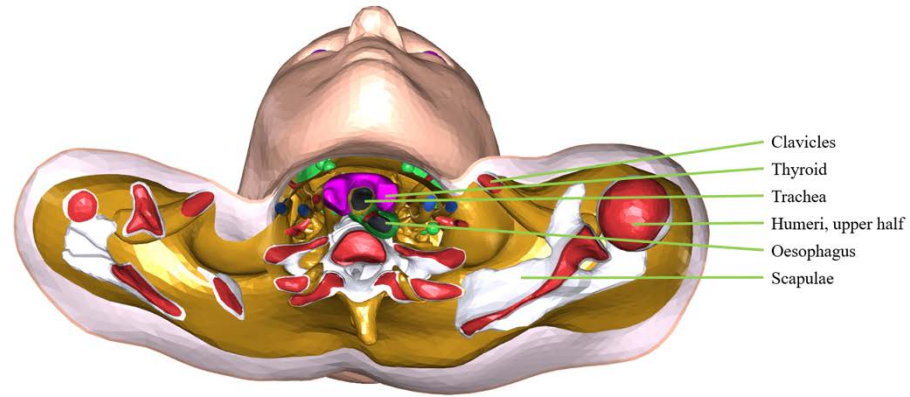
1853

1854

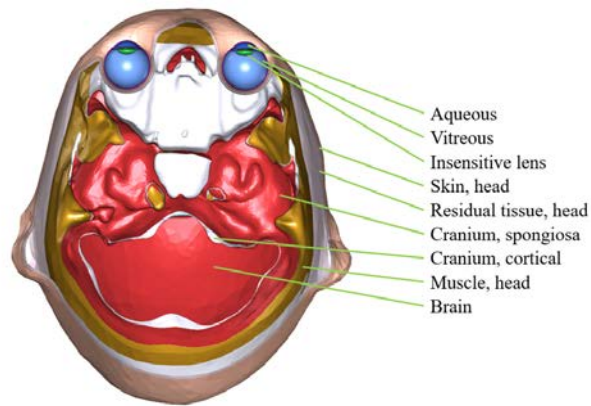
1855



1856
1857
1858
1859

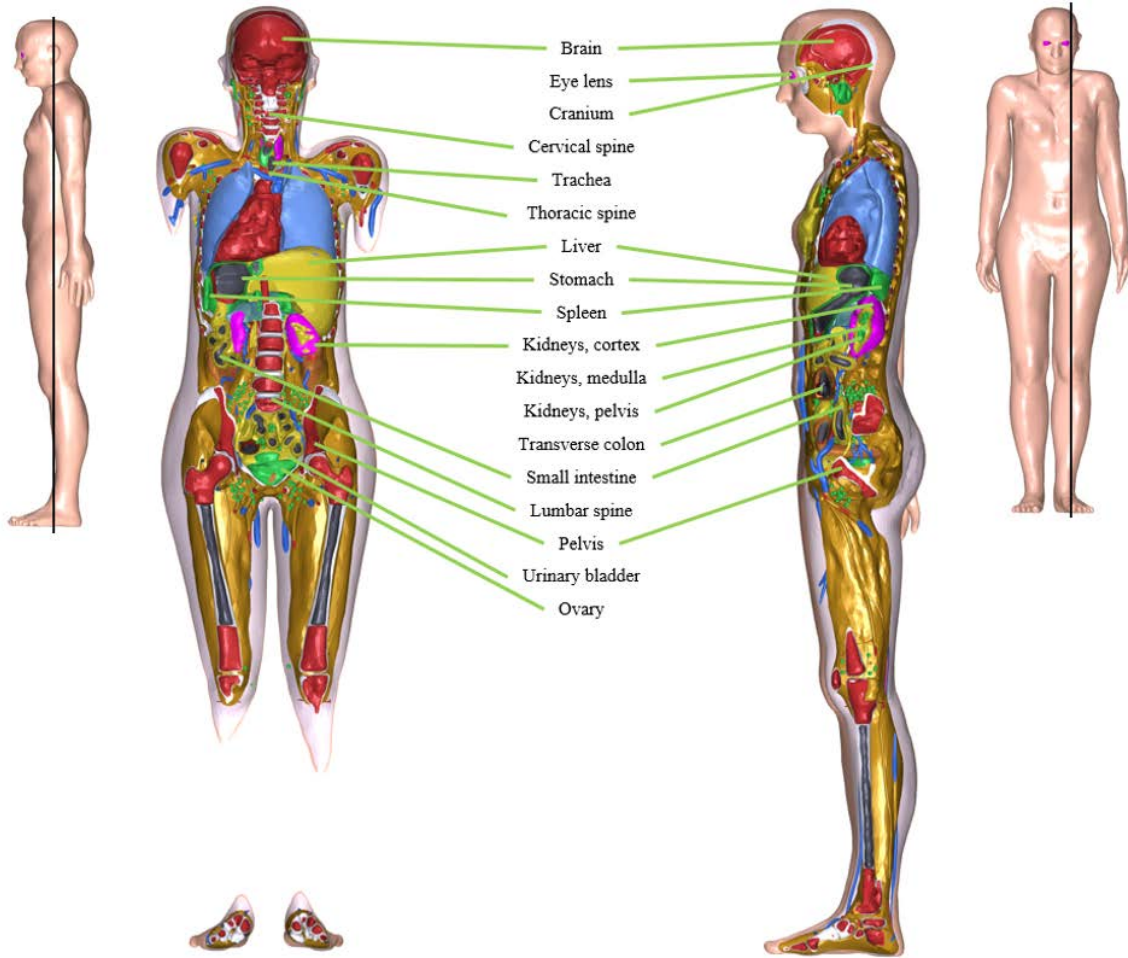


1860
1861
1862
1863



1864
1865
1866

1867 **G.2.2. Coronal and sagittal images**



1868
1869

1870
1871

ANNEX H. COMPARISON OF DOSE COEFFICIENTS FOR EXTERNAL EXPOSURE

1872 (H1) In order to investigate the impact of the improved morphology of the adult mesh-type
1873 reference computational phantoms (MRCPs) on the calculation of dose coefficients (DCs) for
1874 external exposures, the DCs for effective dose in terms of effective dose per fluence (pSv cm^2)
1875 were calculated using the MRCPs and subsequently compared with the reference values given
1876 in *Publication 116* that were produced with the *Publication 110* (ICRP, 2009) phantoms. For
1877 these calculations, a broad parallel beam of photons, neutrons, electrons and helium ions was
1878 assumed to be incident to the phantoms in the same irradiation geometries as considered in
1879 *Publication 116* (ICRP, 2010). Three Monte Carlo simulation codes, i.e. Geant4 (ver. 10.02),
1880 PHITS (ver. 2.92) and MCNP6 (ver. 2.0 prerelease), were used in the calculations. The Geant4
1881 code was used for all of the energy points considered for the comparison, while the PHITS and
1882 MCNP6 codes were used only for some energy points for spot-check purposes. In order to
1883 facilitate the analysis, the effective dose DCs were also calculated using the *Publication 110*
1884 phantoms and the Geant4 code. For the Geant4 code, the physics libraries of
1885 *G4EmLivermorePhysics* and the *FTFP_BERT_HP* were used to transport all particles (Geant4
1886 Physics Reference Manual). In addition, the thermal neutron scattering treatment $S(\alpha, \beta)$ for
1887 hydrogen (H) in light water at 300 K was applied for accurate transport of thermal neutrons. A
1888 range of 1 μm for the secondary production cut was applied to all of the particles. For both the
1889 PHITS and MCNP6 codes, the default physics models and cross-section data were used to
1890 transport all of the particles, and the thermal neutron scattering treatment was also applied. For
1891 the MCNP6 code, the default cut energies were used, which were also applied to set cut
1892 energies for the PHITS code. Note that absorbed doses to the skeletal target tissues (red bone
1893 marrow and endosteum) were taken as the mass-weighted average of the regional spongiosa
1894 and medullary cavity doses following the same approach used in *Publication 116* (ICRP, 2010).

1895 H.1. Uncharged particles

1896 (H2) Prior to the comparison of the effective dose DCs, the organ DCs in terms of organ-
1897 averaged absorbed dose per fluence (pGy cm^2) were compared with the *Publication 116* values
1898 for some selected organs (red bone marrow, colon, lungs, stomach, breasts and skin). The
1899 selected organs have the highest tissue-weighting factor (0.12) except for the skin which was
1900 selected in order to investigate the effect of the 50- μm -thick skin target layer of the MRCPs in
1901 skin dose calculation.

1902 (H3) Figures H.1 and H.2 present the calculated organ DCs for uncharged particles (i.e.
1903 photons and neutrons, respectively) for the anterior-posterior (AP) irradiation geometry, along
1904 with the *Publication 116* values and DC values calculated with the *Publication 110* phantoms
1905 and the Geant4 code. For all of the calculated organ DCs shown in these figures, the statistical
1906 error is less than 5%.

1907 (H4) For photons, it can be seen that with some exceptions at the lowest energy (0.01 MeV),
1908 the organ DCs of the MRCPs were very close to both the *Publication 116* values and the DC
1909 values calculated using the *Publication 110* phantoms and the Geant4 code. The differences
1910 were generally less than 2%. For the 0.01 MeV photons, larger differences were found and the
1911 results show that the differences are mainly due to the difference in the geometry or material
1912 composition of the phantoms. It can also be seen that the female values show relatively less
1913 difference than the male values, which seems due to the fact that the *Publication 110* female

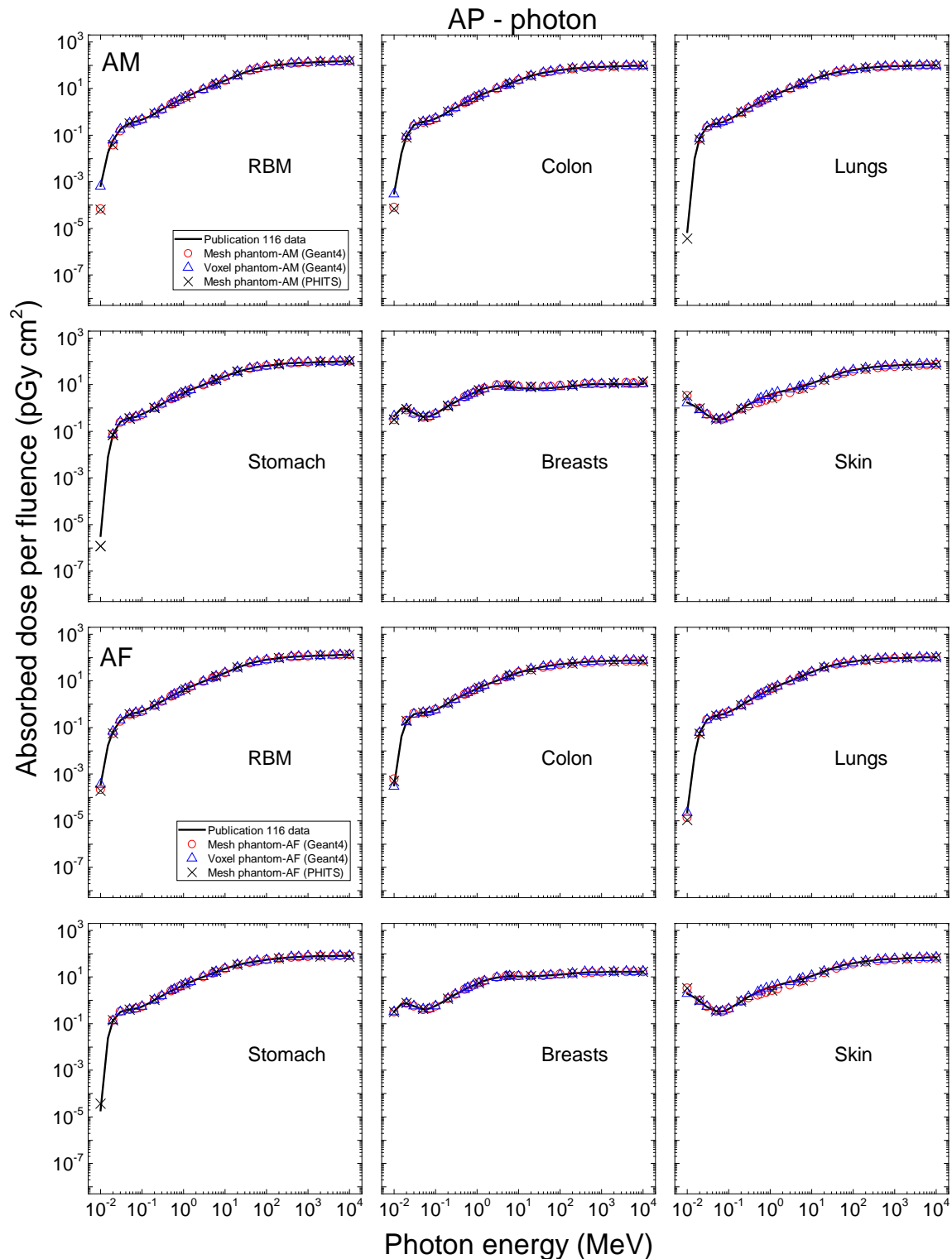
1914 phantom has higher voxel resolution ($1.775 \times 1.775 \times 4.8 \text{ mm}^3$) than the male phantom (2.137
1915 $\times 2.137 \times 8 \text{ mm}^3$).

1916 (H5) Relatively large differences can be seen in the skin DCs over the entire energy range,
1917 which is due mainly to the consideration of the 50- μm -thick skin target layer in the MRCPs.
1918 Note that the 50- μm -thick skin target layer is explicitly modelled and used in the MRCPs, while
1919 the entire skin is used in the *Publication 110* phantoms. For the energies $< 0.03 \text{ MeV}$, the skin
1920 DCs of the MRCPs are greater than the *Publication 110* values, e.g. by a factor of ~ 2 at 0.01
1921 MeV . This difference is due to the fact that the low-energy photons establish the maximum
1922 dose very close to the 50- μm -thick skin target layer and that then, the dose rapidly decreases
1923 with depth within the skin by attenuation. On the other hand, for energies in the $0.2\text{--}10 \text{ MeV}$
1924 range, the skin DCs of the MRCPs are lower, e.g. by a factor of ~ 2 at 1 MeV . This reversal
1925 phenomenon is due to the fact that the high-energy photon beam establishes a dose build-up,
1926 resulting in the maximum dose at a depth much deeper than the depth of the 50- μm -thick skin
1927 target layer.

1928 (H6) For neutrons, except for the skin DCs, the organ DCs of the MRCPs show relatively
1929 large differences from the *Publication 116* values, generally less than 20%, but are very close
1930 to the DC values calculated using the *Publication 110* phantoms and the Geant4 code, the
1931 differences being less than 5% for most cases. These results indicate that for neutrons, the
1932 differences from the *Publication 116* values are not mainly due to the difference in phantom
1933 geometry or material composition, but due to the difference in the Monte Carlo codes or cross
1934 section data / physics models used in the calculations. Note that the DCs of the MRCPs were
1935 calculated using the Geant4 code, but that the *Publication 116* values were calculated by using
1936 four different codes (MCNPX, PHITS, FLUKA and Geant4) for neutrons and then the
1937 calculated values were averaged and went through a smoothing process (ICRP, 2010). As
1938 expected, for the skin DCs, the DCs of the MRCPs tend to deviate from both the *Publication*
1939 *116* values and the DCs calculated with the *Publication 110* phantoms and the Geant4 code,
1940 due mainly to the consideration of the 50- μm -thick skin target layer in the MRCPs.

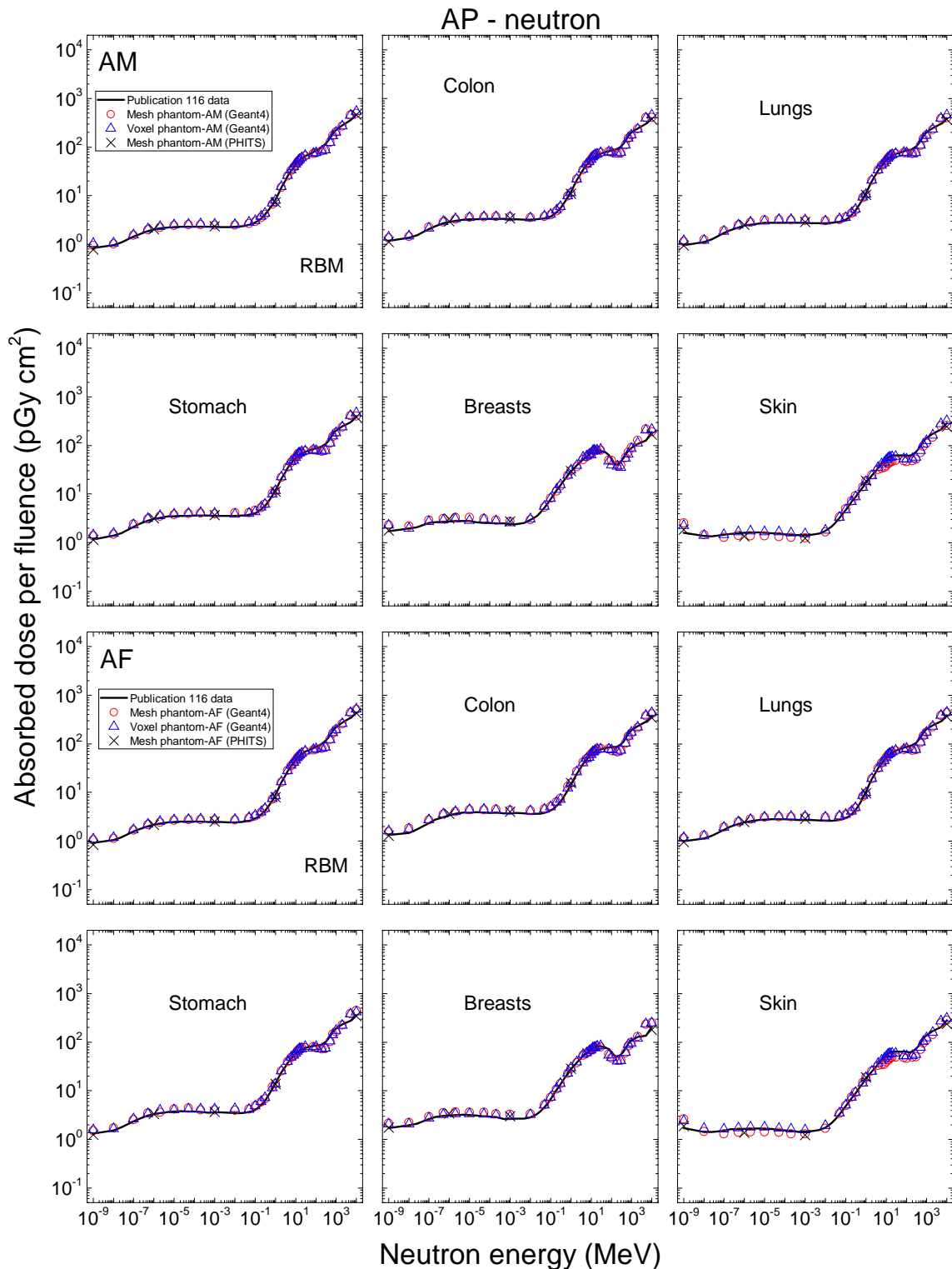
1941 (H7) Figures H.3 and H.4 present the effective dose DCs for the AP, PA, LL, RL, ROT and
1942 ISO irradiation geometries calculated with the MRCPs, along with the *Publication 116* values
1943 and DCs calculated with the *Publication 110* phantoms and Geant4 code. For all of the
1944 calculated effective dose DCs shown in these figures, the statistical error is less than 0.5%. It
1945 can be seen that for photons and neutrons, the effective dose DCs of the MRCPs are very close
1946 to both the *Publication 116* values and the DC values calculated with the *Publication 110*
1947 phantoms and the Geant4 code. For photons, with some exceptions at low energies (< 0.03
1948 MeV), the differences are less than 2%. This result indicates that the relatively large differences
1949 of the skin DCs due to the consideration of the 50- μm -thick skin target layer in the MRCPs do
1950 not significantly affect the effective dose DCs for photons; this is because the doses of the other
1951 organs/tissues are more important than that of the skin, which has a small tissue-weighting
1952 factor ($w_T = 0.01$). For neutrons, the differences from the *Publication 116* values are less than
1953 10% for most cases, but the differences from the values calculated with the *Publication 110*
1954 phantoms and the Geant4 code are much smaller ($< 2\%$ for most cases). These slightly larger
1955 differences from the *Publication 116* values are again due mainly to the different Monte Carlo
1956 codes or cross-section data / physics models used in the calculations, not to differences in
1957 phantom geometry or material composition.

1958



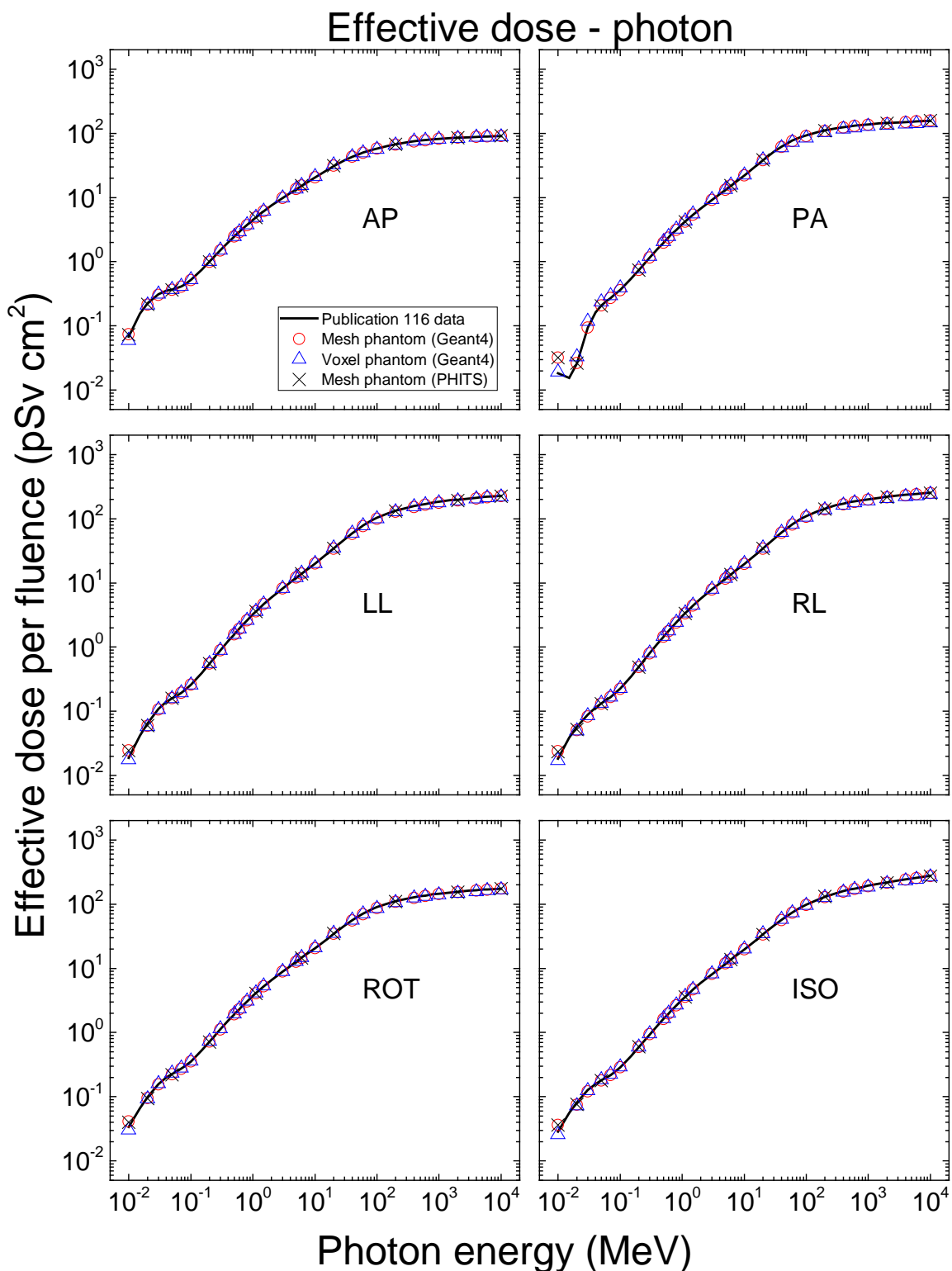
1959
1960
1961
1962
1963
1964
1965

Fig. H.1. Absorbed dose per fluence (pGy cm²) to the RBM, colon, lungs, stomach, breasts and skin in the anterior-posterior (AP) geometry for photon exposures calculated with the adult mesh-type reference phantoms (MRCPs), along with the *Publication 116* values (ICRP, 2010) and the values calculated with the *Publication 110* phantoms and the Geant4 code: adult male, AM (upper) and adult female, AF (lower).



1966
1967
1968
1969
1970
1971

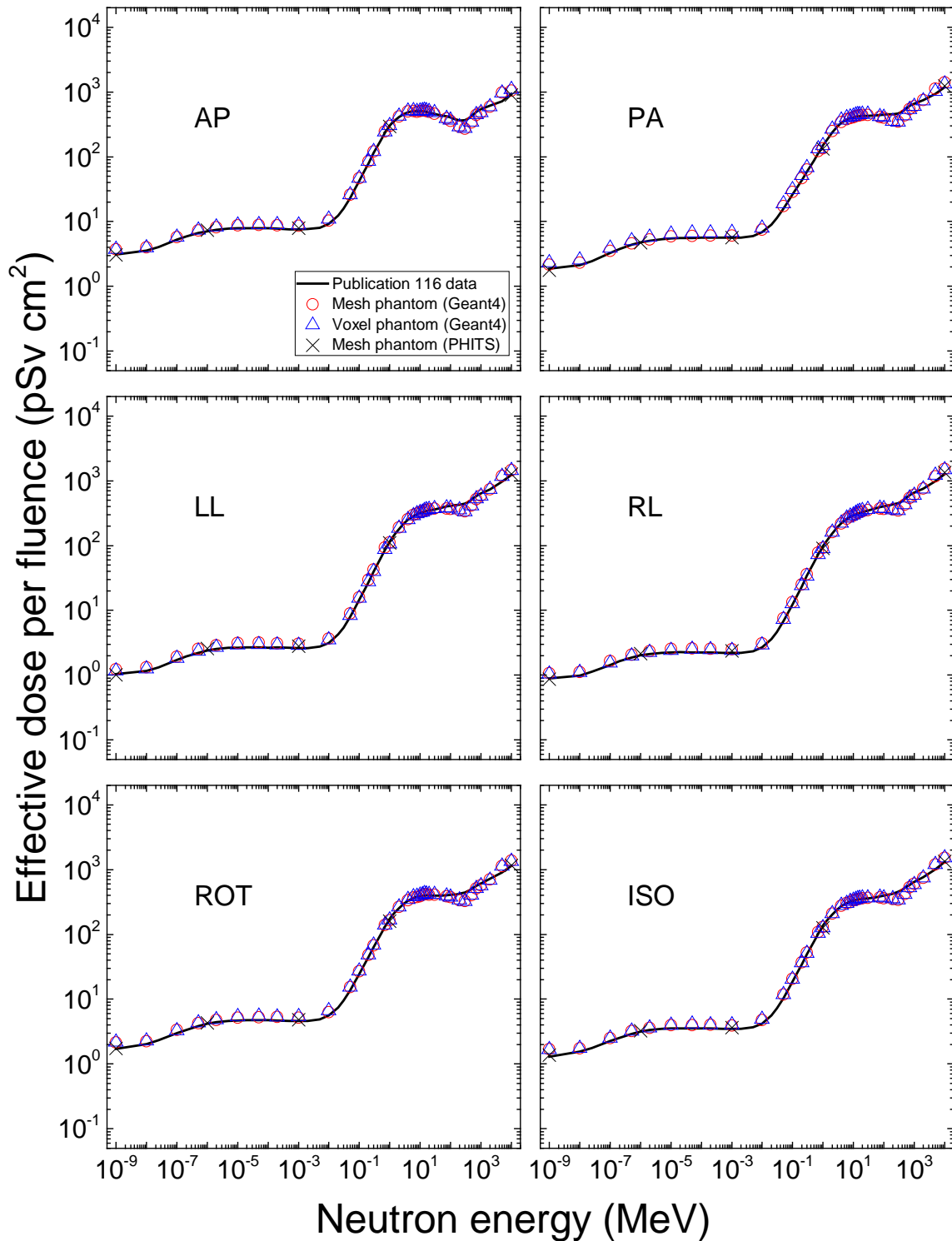
Fig. H.2. Absorbed dose per fluence (pGy cm^2) to the RBM, colon, lungs, stomach, breasts and skin in the AP geometry for neutron exposures calculated with the adult mesh-type reference phantoms (MRCPs), along with the *Publication 116* values (ICRP, 2010) and the values calculated with the *Publication 110* phantoms and the Geant4 code: adult male, AM (upper) and adult female, AF (lower).



1972
1973
1974
1975

Fig. H.3. Effective dose per fluence (pSv cm²) for photon exposures calculated with the adult mesh-type reference phantoms (MRCPs), along with the *Publication 116* values (ICRP, 2010) and the values calculated with the *Publication 110* phantoms and the Geant4 code.

Effective dose - neutron



1976
1977
1978
1979
1980

Fig. H.4. Effective dose per fluence (pSv cm²) for neutron exposures calculated with the adult mesh-type reference phantoms (MRCPs), along with the *Publication 116* values (ICRP, 2010) and the values calculated with the *Publication 110* phantoms and the Geant4 code.

1981 **H.2. Charged particles**

1982 (H8) Figures H.5–H.6 present the calculated organ DCs for charged particles (i.e. electrons
1983 and helium ions) in terms of organ-averaged absorbed dose per fluence (pGy cm^2), along with
1984 the *Publication 116* values and DC values calculated with the *Publication 110* phantoms and
1985 Geant4 code for the selected organs (red bone marrow, colon, lungs, stomach, breasts and skin)
1986 in the ISO irradiation geometry. The statistical errors of the organ DCs presented in the figures
1987 are all less than 5%.

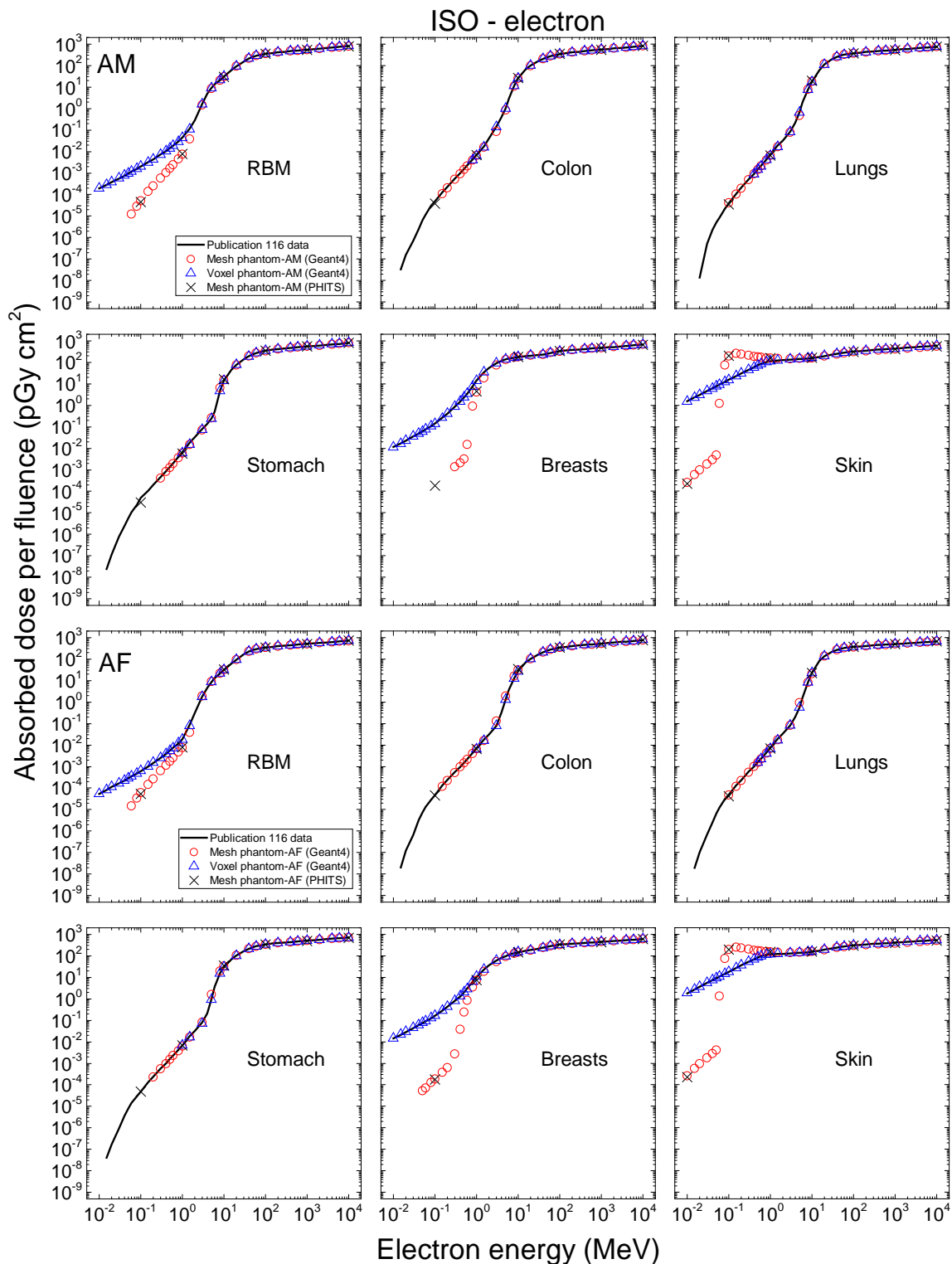
1988 (H9) For electrons, it can be seen that the organ DCs of the MRCs for the colon, lungs and
1989 stomach are not much different from the *Publication 116* values, whereas there are large
1990 differences in the DCs for the RBM, breasts and skin. The differences in the DCs for the RBM
1991 and breasts are due to the improvement in the MRCs; that is, the skin and cortical bone of the
1992 MRCs are continuous and fully cover the body and the spongiosa regions, respectively,
1993 whereas this is not the case in the *Publication 110* phantoms due to their finite voxel resolutions
1994 (see Figs. 6.4 and 6.5).

1995 (H10) The skin DCs, when compared to the RBM and breast DCs, show larger differences,
1996 which is mainly due to the consideration of the 50- μm -thick skin target layer in the MRCs.
1997 For electron energies < 0.08 MeV, the skin DCs of the MRCs are much lower than the
1998 *Publication 116* values; this is due to the fact that for the MRCs, the low-energy electrons
1999 cannot penetrate the dead layer of the skin and, therefore, only the bremsstrahlung photons
2000 contribute to the energy deposition in the thin target layer. For higher energies up to 1 MeV,
2001 on the other hand, the skin DCs of the MRCs are greater, e.g. by a factor of ~ 13 at 0.1 MeV,
2002 which is due to the fact that the electrons penetrate the dead layer and establish the maximum
2003 dose within the thin target layer.

2004 (H11) For helium ions, it can be seen that except for the skin, the organ DCs of the MRCs
2005 are generally not much different from the *Publication 116* values. Relatively large differences
2006 are shown at very low energies, due mainly to the geometrical difference between the MRCs
2007 and the *Publication 110* phantoms. The skin DCs for helium ions show larger differences,
2008 which is again due to the consideration of the 50- μm -thick skin target layer in the MRCs. For
2009 the helium ions < 10 MeV/u, except for 1 MeV/u, the skin DCs of the MRCs are significantly
2010 greater, e.g. by a factor of ~ 16 at 3 MeV/u, which is due to the establishment of the Bragg peak
2011 in the 50- μm -thick target layer. For 1 MeV/u (i.e. 4 MeV), the skin DCs of the MRCs are
2012 essentially zero, whereas the *Publication 116* values show some significant values. Note that
2013 the 4-MeV helium ions do not penetrate the dead layer and deposit essentially their entire
2014 energy there, which fact is reflected in the results of the MRCs.

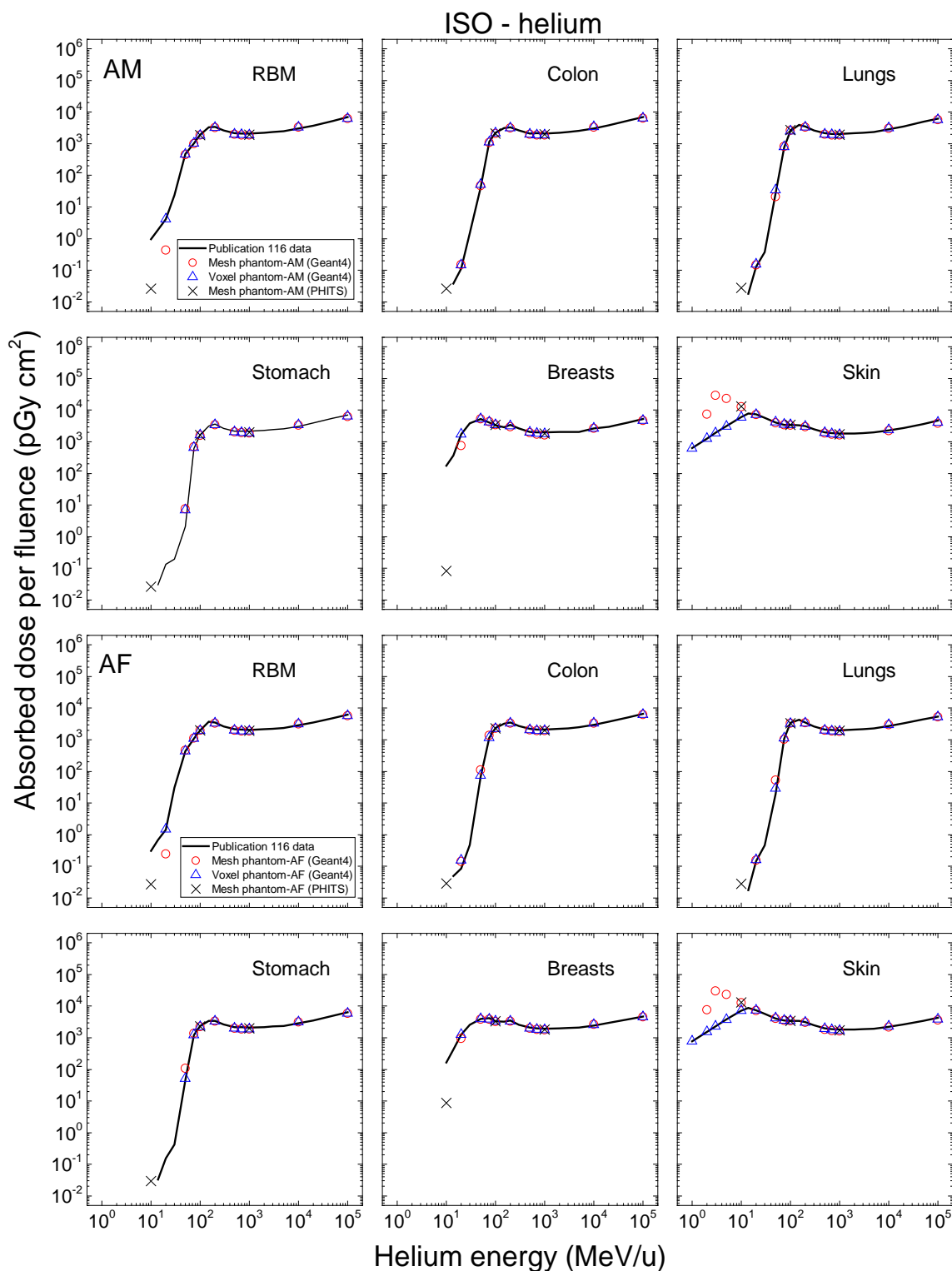
2015 (H12) Figures H.7 and H.8 present the effective dose DCs for the AP, PA and ISO irradiation
2016 geometries calculated with the MRCs, along with the *Publication 116* values. For all of the
2017 calculated effective dose DCs shown in these figures, the statistical error is less than 0.5%. It
2018 can be seen that for high energy electrons and helium ions (i.e. > 1 MeV for electrons and > 10
2019 MeV/u for helium ions), the effective dose DCs of the MRCs are generally close to both the
2020 *Publication 116* values and the values calculated with the *Publication 110* phantoms and
2021 Geant4 code. For the lower energies, on the other hand, the effective dose DCs show large
2022 differences, due mainly to the differences in the skin DCs. For electrons, the effective dose
2023 DCs of the MRCs for the energies (≤ 0.06 MeV) are smaller than the *Publication 116* values,
2024 but for the higher energies up to 1 MeV, greater by up to a factor of ~ 12 (at 0.1 MeV). For
2025 helium ions, for 1 MeV/u, the effective dose DCs of the MRCs are essentially zero, which is
2026 due to the effect of the dead layer defined in the MRCs, whereas the *Publication 116* values

2027 show some significant values. For the higher energies up to 10 MeV, the effective dose DCs
2028 of the MRCs are greater than the *Publication 116* values by up to a factor of ~14 (at 3 MeV/u).
2029 (H13) However, it is also true that the difference is overly exaggerated as we consider only
2030 monoenergetic electron beams; in real exposure situations, generally polyenergetic electrons
2031 (e.g. beta spectra) are encountered, where the differences in effective doses are much less
2032 significant. For example, the difference of effective dose between the MRCs and the
2033 *Publication 110* phantoms resulting from the isotropic (ISO) irradiation of the beta radiation
2034 sources (^{14}C , ^{186}Re , ^{32}P , $^{90}\text{Sr}/^{90}\text{Y}$ and ^{106}Rh) is less than ~2 times, except for ^{14}C , for which the
2035 difference is ~4 times. Note that ^{14}C emits very low-energy electrons (maximum energy: 0.15
2036 MeV) and thus is generally not of concern for external exposures. In real situations of helium
2037 ion exposures, alpha exposures are mostly encountered but practically considered not to be
2038 important for radiation protection purposes, considering that they can be easily shielded by a
2039 thin piece of paper or several centimetre-thick air.

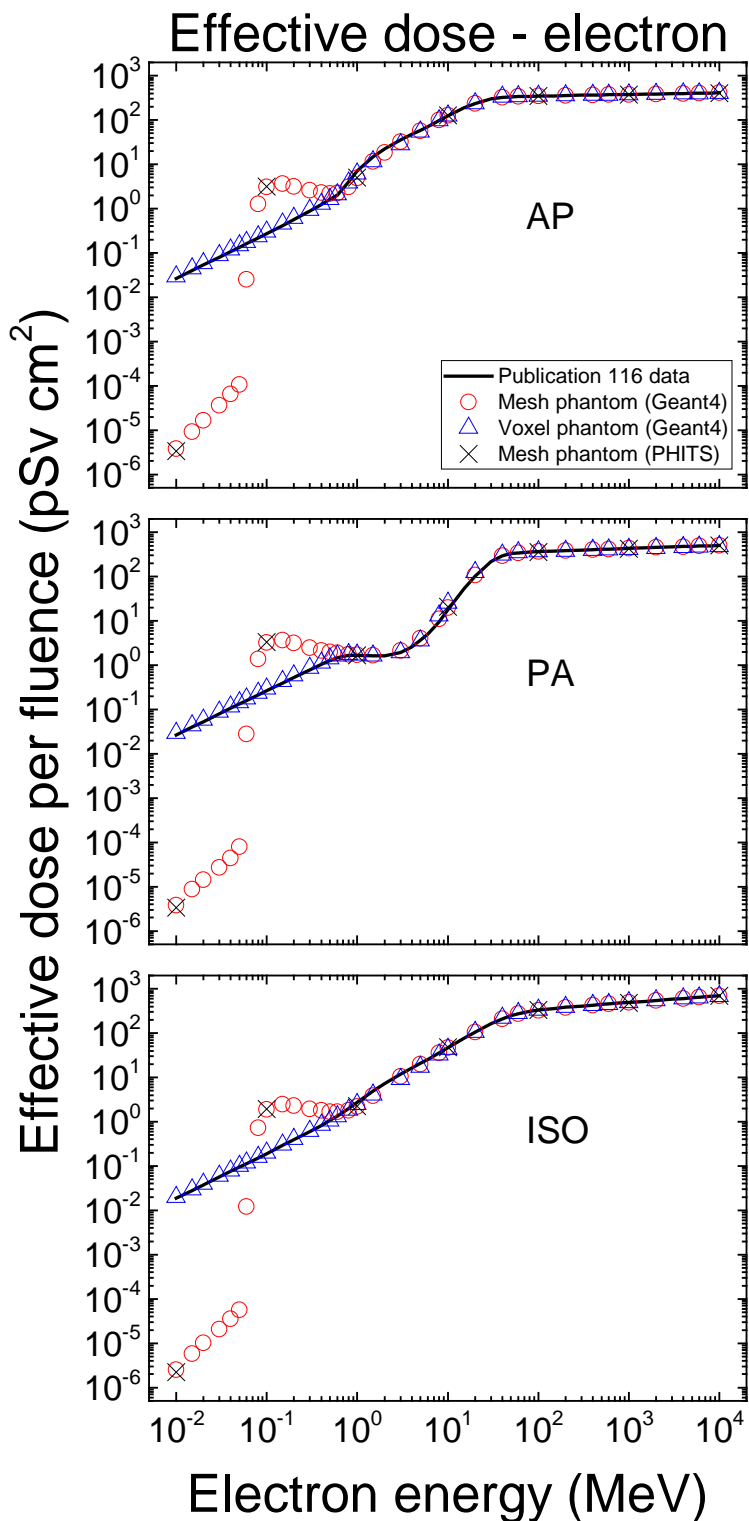


2040
2041
2042
2043
2044

Fig. H.5. Absorbed dose per fluence (pGy cm²) to the RBM, colon, lungs, stomach, breasts and skin in the ISO geometry for electron exposures calculated with the adult mesh-type reference phantoms (MRCPs), along with the *Publication 116* values (ICRP, 2010) and the values calculated with the *Publication 110* phantoms and the Geant4 code: adult male, AM (upper) and adult female, AF (lower).

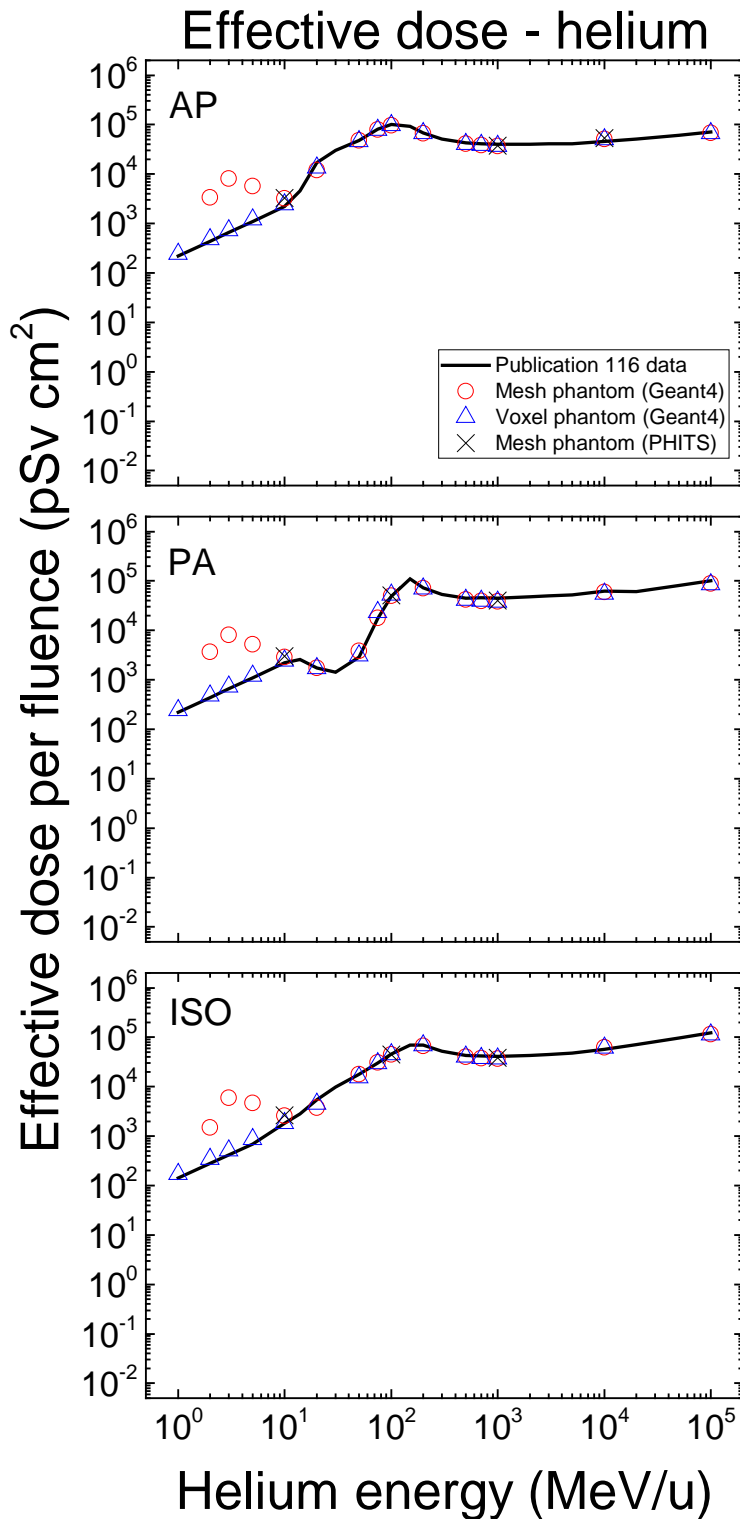


2045
 2046 Fig. H.6. Absorbed dose per fluence (pGy cm²) to the RBM, colon, lungs, stomach, breasts and skin
 2047 in the ISO geometry for helium ion exposures calculated with the adult mesh-type reference phantoms
 2048 (MRCPs), along with the *Publication 116* values (ICRP, 2010) and the values calculated with the
 2049 *Publication 110* phantoms and the Geant4 code: adult male, AM (upper) and adult female, AF (lower).
 2050



2051
2052
2053
2054

Fig. H.7. Effective dose per fluence (pSv cm²) for electron exposures calculated with the adult mesh-type reference phantoms (MRCPs), along with the *Publication 116* values (ICRP, 2010) and the values calculated with the *Publication 110* phantoms and the Geant4 code.



2055
 2056
 2057
 2058
 2059
 2060

Fig. H.8. Effective dose per fluence (pSv cm²) for helium ion exposures calculated with the adult mesh-type reference phantoms (MRCPs), along with the *Publication 116* values (ICRP, 2010) and the values calculated with the *Publication 110* phantoms and the Geant4 code.

2061 **ANNEX I. COMPARISON OF SPECIFIC ABSORBED FRACTIONS**

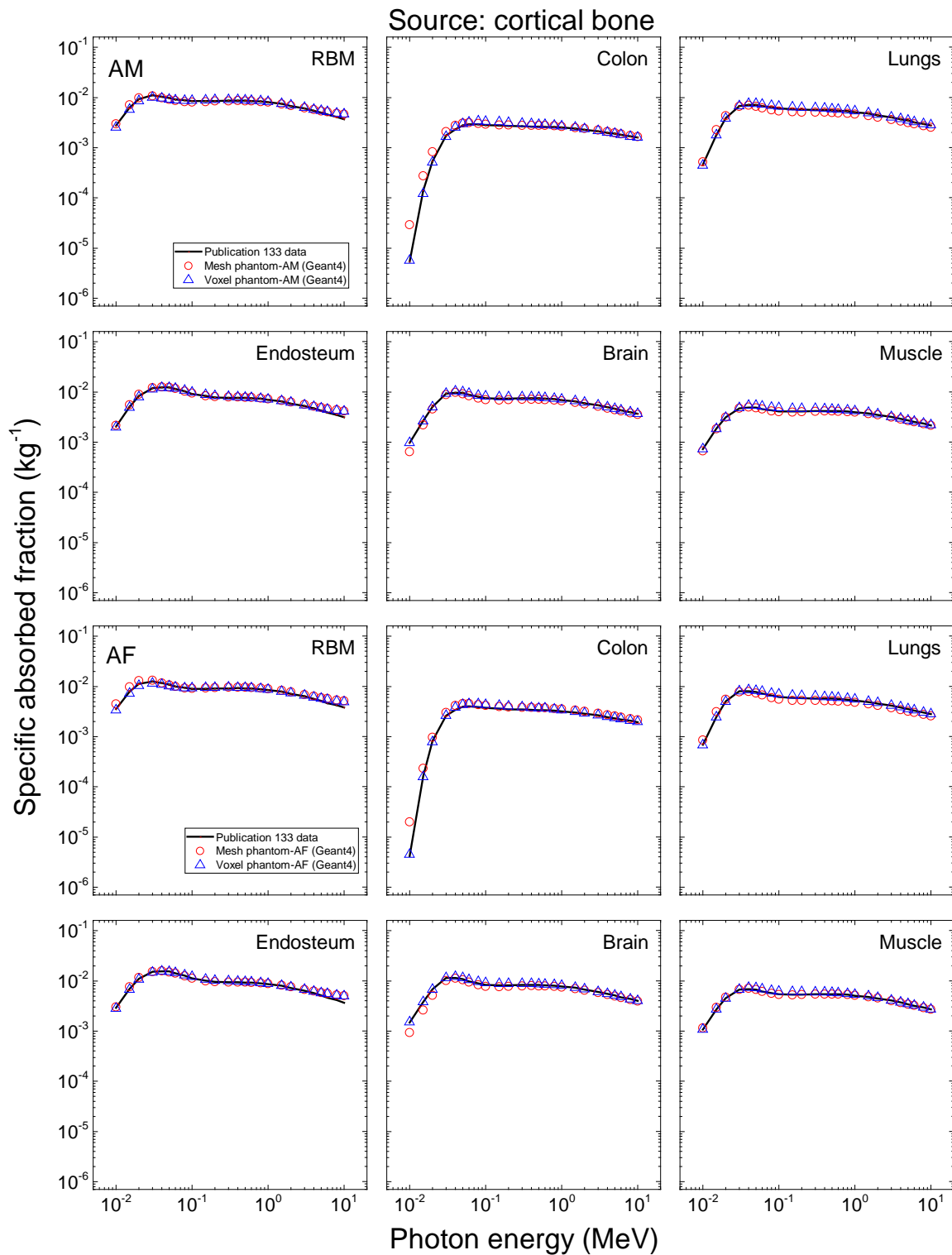
2062 (I1) In order to investigate the impact of the improved internal morphology of the adult mesh-
2063 type reference computational phantoms (MRCPs) on the calculation of dose coefficients (DCs)
2064 for internal exposures, the specific absorbed fractions (SAFs) for photons and electrons were
2065 calculated using the MRCPs for comparison with the values in *Publication 133* (ICRP, 2016a).
2066 For the calculations, the cortical bone, liver, lungs and thyroid were selected as source
2067 organs/tissues. The Geant4 code (ver. 10.02) was used for all the energy points considered for
2068 the comparison, while the PHITS (ver. 2.92) and MCNP6 (ver. 2.0 prerelease) codes were used
2069 only for some energies for spot-check purposes. The SAFs were also calculated using the
2070 *Publication 110* phantoms and the Geant4 code to facilitate the analysis. For the Geant4 code,
2071 the physics library of the G4EmLivermorePhysics to transport photons and electrons was used
2072 with a range of 1 μm for the secondary production cut (Geant4 Physics Reference Manual).
2073 For both the PHITS and MCNP6 codes, the default physics models and cross-section data were
2074 used to transport photons and electrons. For the MCNP6 code, the default cut energies were
2075 used, which were also applied to set cut energies for the PHITS code. Note that for photons,
2076 absorbed doses to the red bone marrow and endosteum were calculated based on the fluence-
2077 to-absorbed dose response functions (DRF) reported in Annex D of *Publication 116* (ICRP,
2078 2010) as recommended in Section 4.4 of *Publication 133* (ICRP, 2016a).

2079 (I2) The SAFs of the MRCPs were compared with the *Publication 133* values for six target
2080 organs/tissues which were selected considering the contribution to effective dose. Figures I.1–
2081 I.8 present the SAFs of the MRCPs for the selected source and target organs/tissues for photons
2082 and electrons, along with the *Publication 133* values. The statistical errors of the calculated
2083 values presented in the figures are less than 5%.

2084 (I3) For photons, it can be seen that the SAFs of the MRCPs are generally not much different
2085 from the *Publication 133* values. Large differences, however, can be seen when the RBM is a
2086 target, where the SAFs of the MRCPs are much smaller than the *Publication 133* values at low
2087 energies. These differences are due mainly to the fact that in the MRCPs, the spongiosa is fully
2088 enclosed by cortical bone, whereas this is not the case in the voxel-type *Publication 110*
2089 reference phantoms (see Fig. 6.5). Even for the cortical bone as a source and the colon as a
2090 target, the SAFs show large differences, for which the values of the MRCPs are greater by a
2091 factor of ~ 5 at 0.01 MeV for the male phantom, which is again due to the difference in the
2092 distribution of the cortical bone; that is, in the *Publication 110* phantoms, the cortical bone
2093 dose not fully enclose the spongiosa and is not uniformly distributed, especially in the ribs
2094 where the cortical bone is rarely distributed in the regions that are very close to the colon.

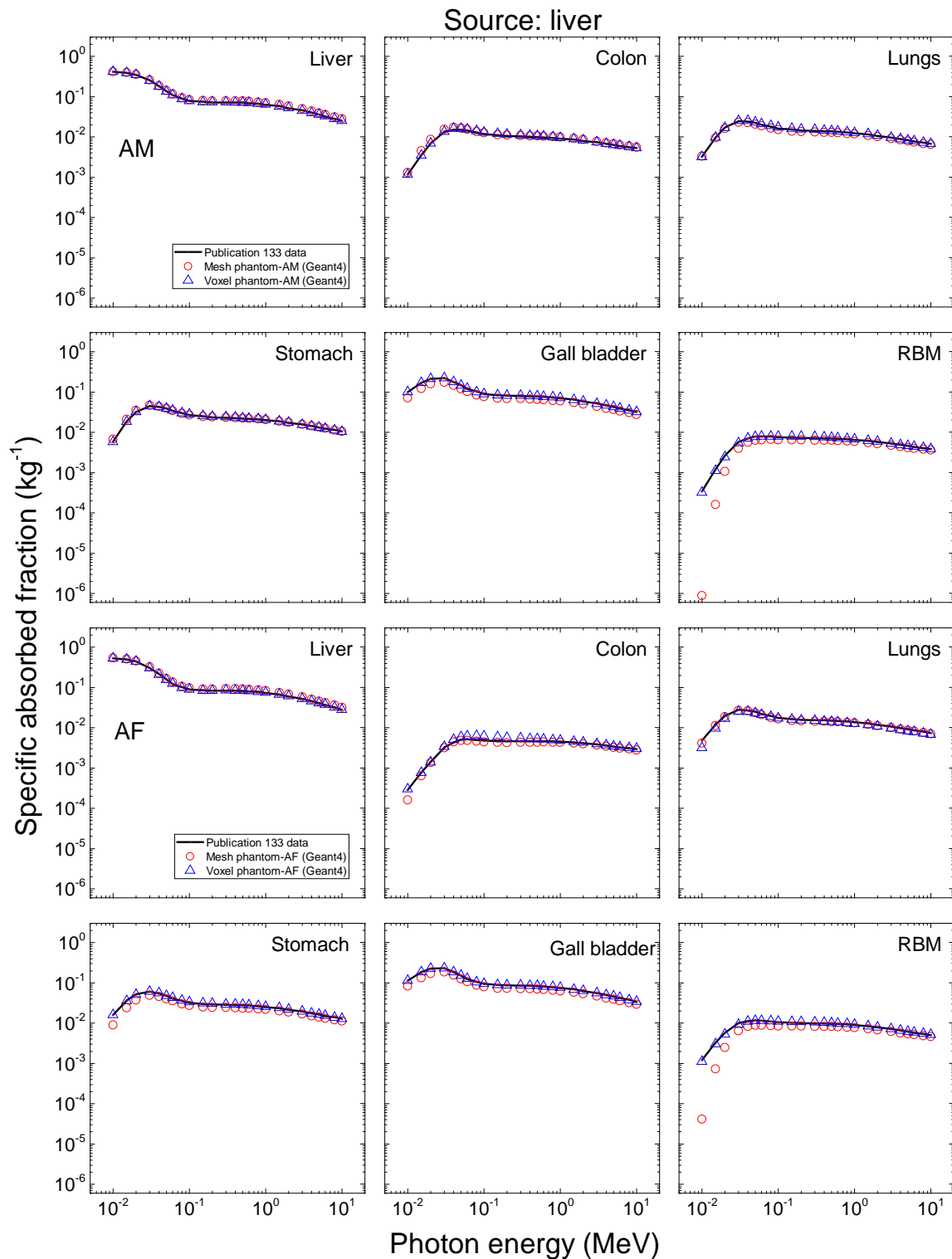
2095 (I4) For electrons, it can be seen that the SAFs of the MRCPs are close to the *Publication 133*
2096 values for self-irradiation cases (e.g. liver \leftarrow liver), whereas for cross-fire-irradiation cases (e.g.
2097 RBM \leftarrow liver), the SAFs show significant differences. For most of the cross-fire-irradiation
2098 cases, the SAFs of the MRCPs are generally smaller than the *Publication 133* values, which is
2099 mainly due to the fact that the contact area between the adjacent source and target
2100 organs/tissues of the MRCPs (smooth-surfaces) is smaller than that of the *Publication 110*
2101 phantoms (stair-stepped-surfaces, see Fig. 6.3). The differences were even larger when the
2102 thyroid is a source and the oesophagus and the thymus are a target, which is mainly due to the
2103 fact that the MRCPs overcome an anatomical limitation of the *Publication 110* phantoms
2104 wherein the thyroid slightly contacts the oesophagus for both the male and the female and the
2105 thymus only for the male (see Chapter 3.1). Larger differences can also be seen for the RBM
2106 as a target, which is due to the fact that in the MRCPs, the cortical bone fully encloses the

2107 spongiosa, whereas this is not the case in the *Publication 110* phantoms. Exceptionally, the
2108 SAFs of the MRCPs are generally greater than the *Publication 133* values only for the colon
2109 ← cortical bone case, which is again due to the fact that in the *Publication 110* phantoms, the
2110 cortical bone is not uniformly distributed, especially in the ribs where the cortical bone is rarely
2111 distributed in the regions that are very close to the colon.
2112



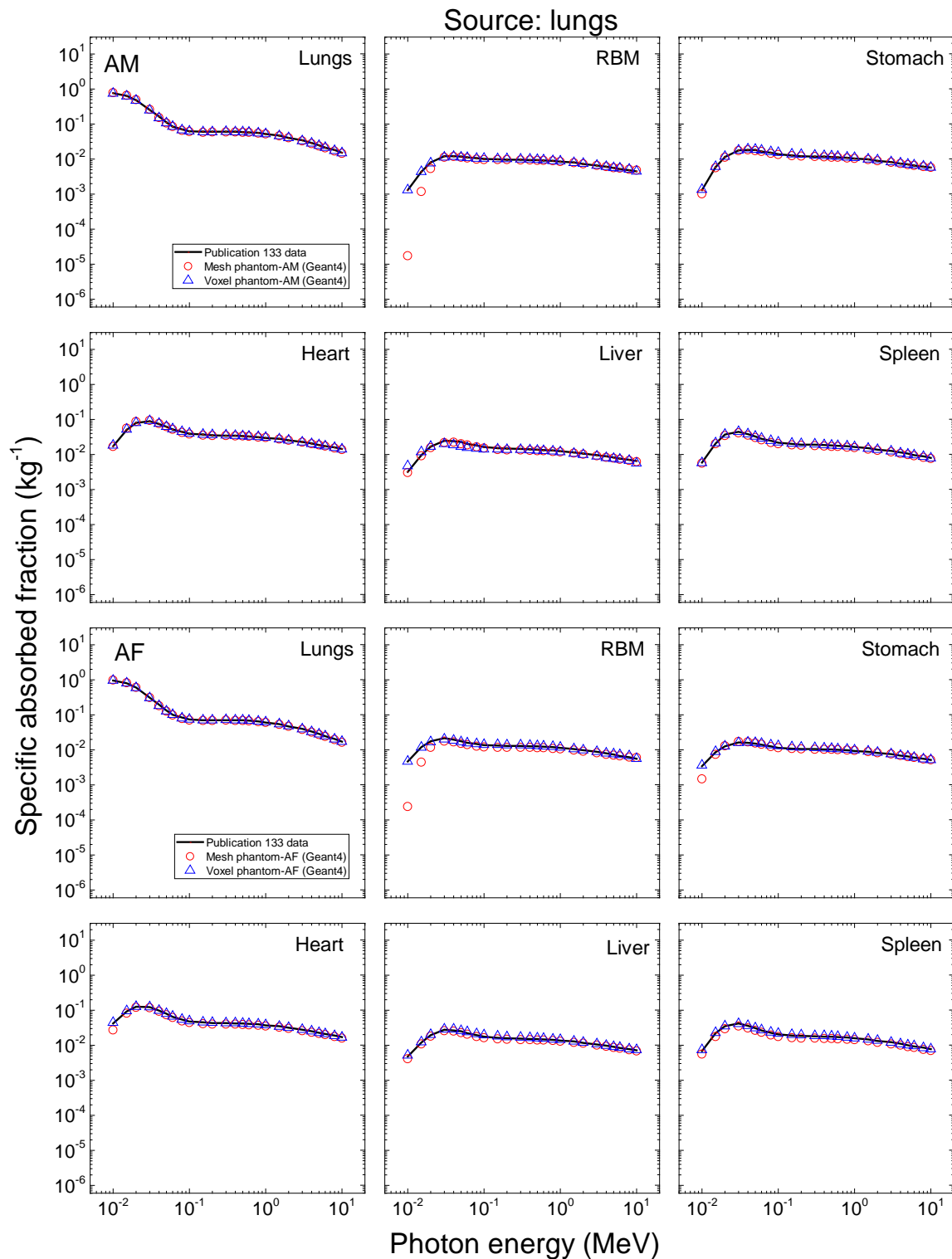
2113
2114
2115
2116
2117
2118

Fig. I.1. Specific absorbed fractions (SAFs) for cortical bone as a source and RBM, colon, lungs, endosteum, brain and muscle as a target for photon exposures calculated with the adult mesh-type reference phantoms (MRCPs), along with the *Publication 133* values (ICRP, 2016a) and the values calculated with the *Publication 110* phantoms and the Geant4 code: adult male, AM (upper) and adult female, AF (lower).



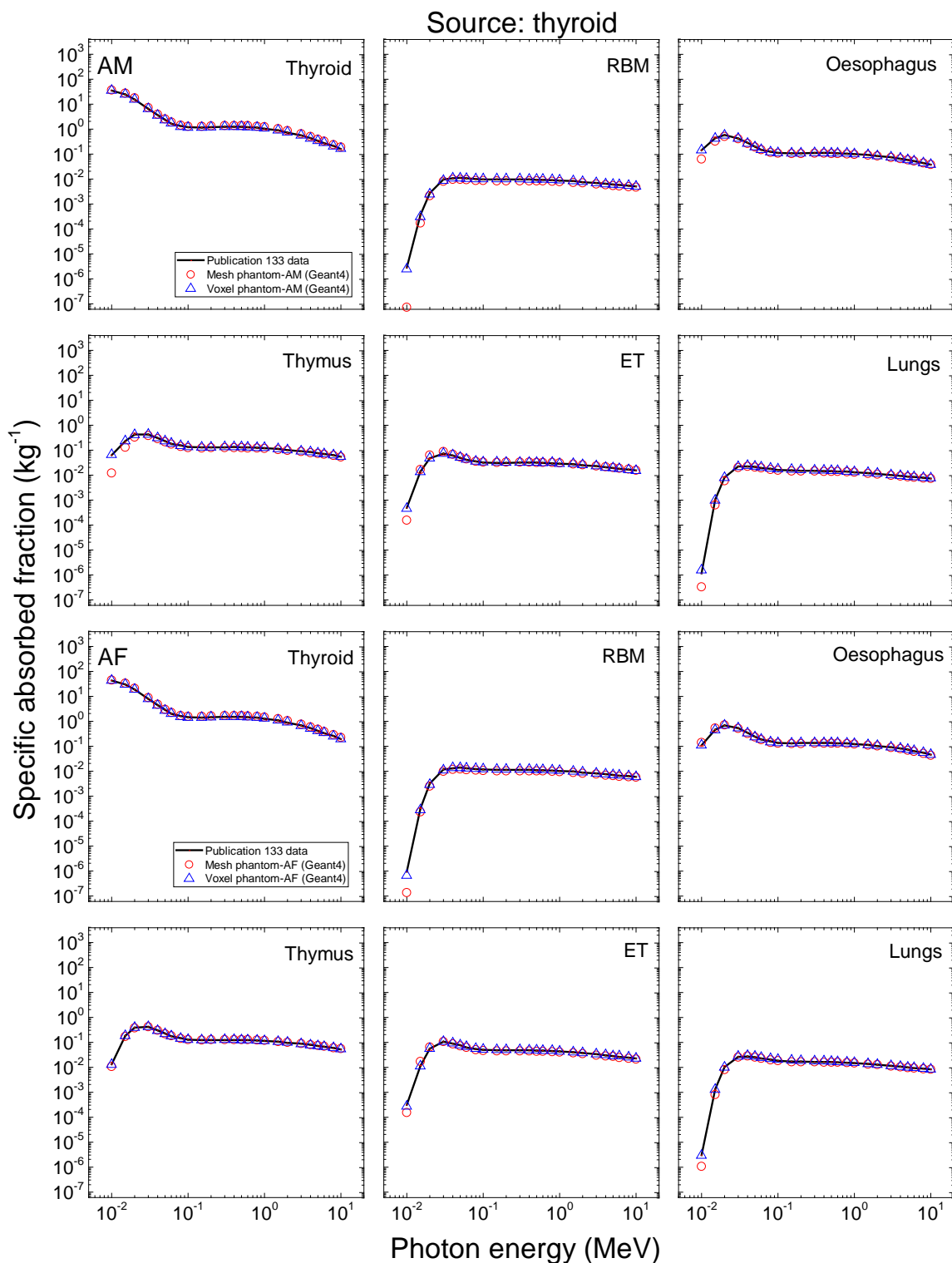
2119
2120
2121
2122
2123
2124

Fig. I.2. Specific absorbed fractions (SAFs) for liver as a source and liver, colon, lungs, stomach, gall bladder and RBM as a target for photon exposures calculated with the adult mesh-type reference phantoms (MRCPs), along with the *Publication 133* values (ICRP, 2016a) and the values calculated with the *Publication 110* phantoms and the Geant4 code: adult male, AM (upper) and adult female, AF (lower).

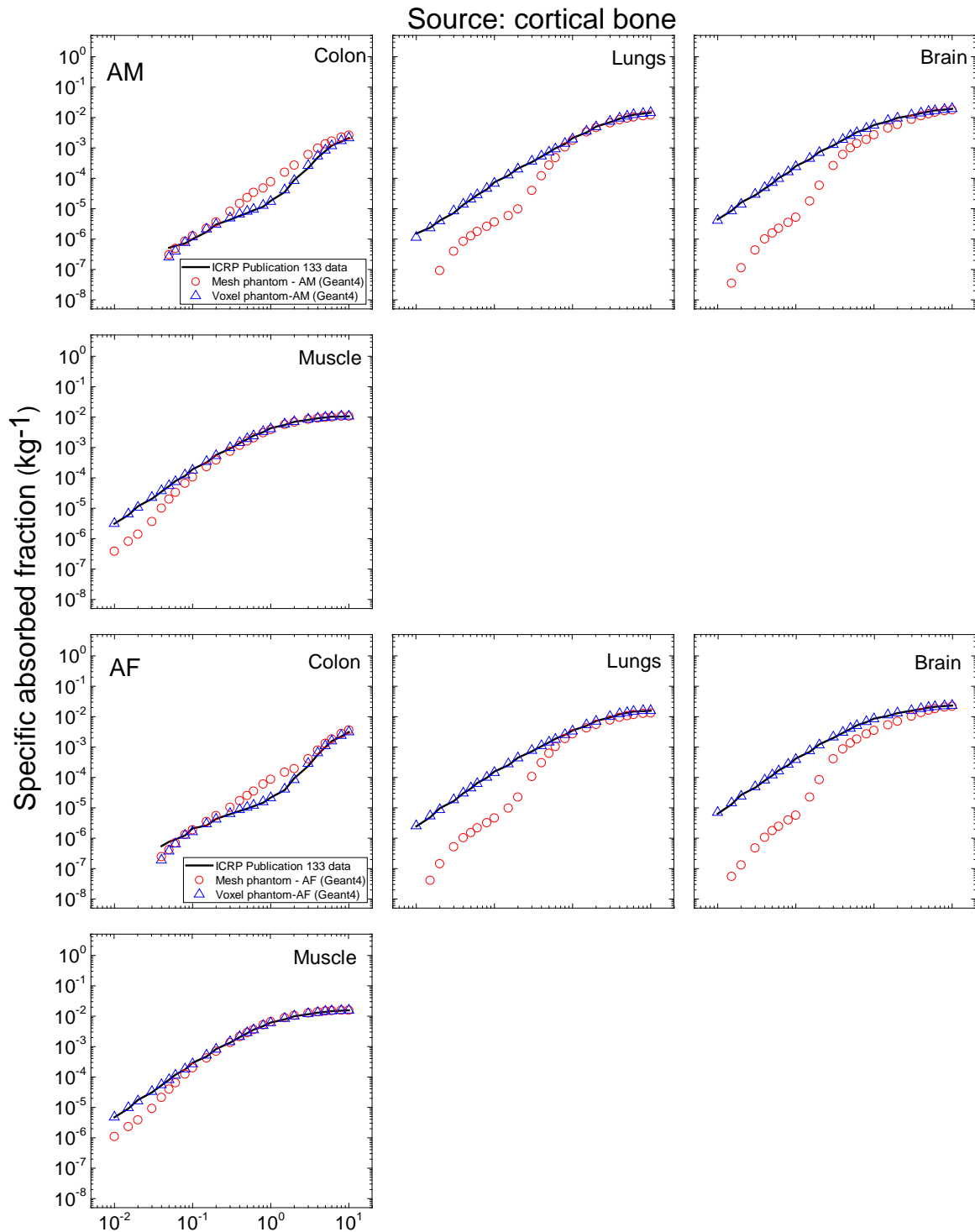


2125
2126
2127
2128
2129

Fig. I.3. Specific absorbed fractions (SAFs) for lungs as a source and lungs, RBM, stomach, heart, liver and spleen as a target for photon exposures calculated with the adult mesh-type reference phantoms (MRCPs), along with the *Publication 133* values (ICRP, 2016a) and the values calculated with the *Publication 110* phantoms and the Geant4 code: adult male, AM (upper) and adult female, AF (lower).

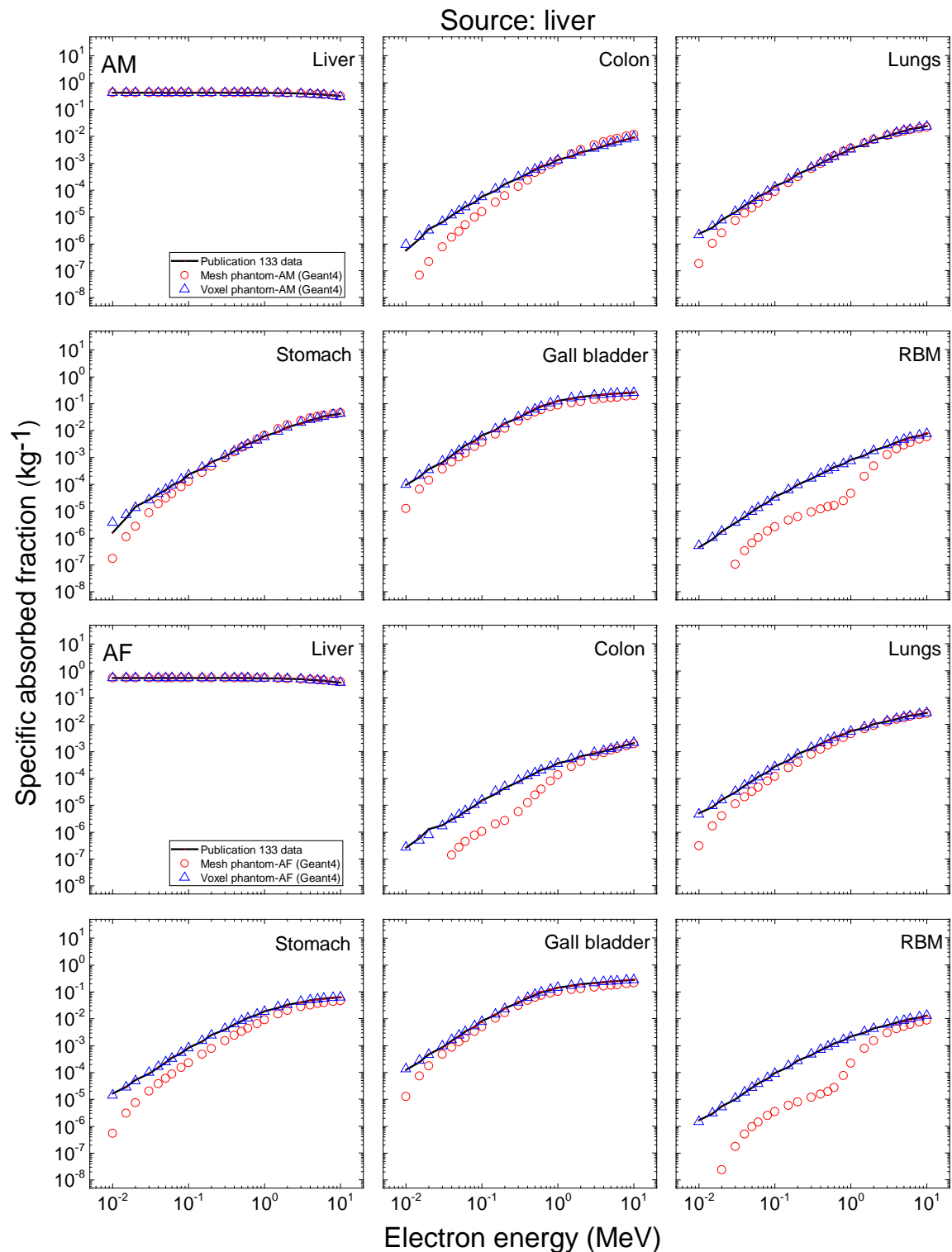


2130
 2131 Fig. I.4. Specific absorbed fractions (SAFs) for thyroid as a source and thyroid, RBM, oesophagus,
 2132 thymus, extrathoracic (ET) region and lungs as a target for photon exposures calculated with the adult
 2133 mesh-type reference phantoms (MRCPs), along with the *Publication 133* values (ICRP, 2016a) and the
 2134 values calculated with the *Publication 110* phantoms and the Geant4 code: adult male, AM (upper) and
 2135 adult female, AF (lower).
 2136



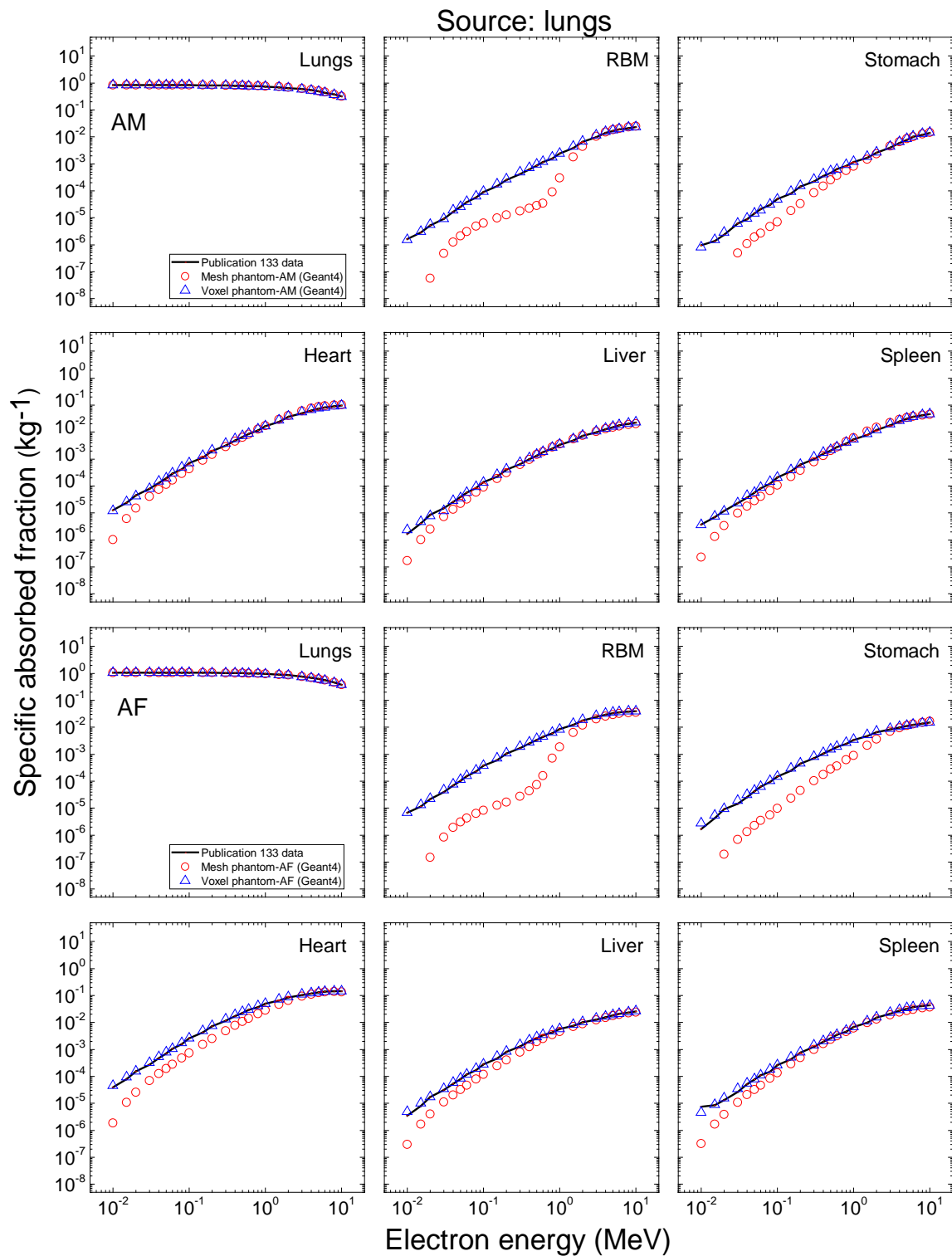
2137
2138
2139
2140
2141
2142
2143
2144
2145

Fig. I.5. Specific absorbed fractions (SAFs) for cortical bone as a source and colon, lungs, brain and muscle as a target for electron exposures calculated with the adult mesh-type reference phantoms (MRCPs), along with the *Publication 133* values (ICRP, 2016a) and the values calculated with the *Publication 110* phantoms and the Geant4 code: adult male, AM (upper) and adult female, AF (lower). Note that SAFs for the RBM and endosteum as a target are not given here because these values of *Publication 133* were calculated not using the *Publication 110* phantoms but using the absorbed fractions (AFs) calculated by using the micro-CT imaging data for 38 cored samples of spongiosa provided by Hough et al. (2011).



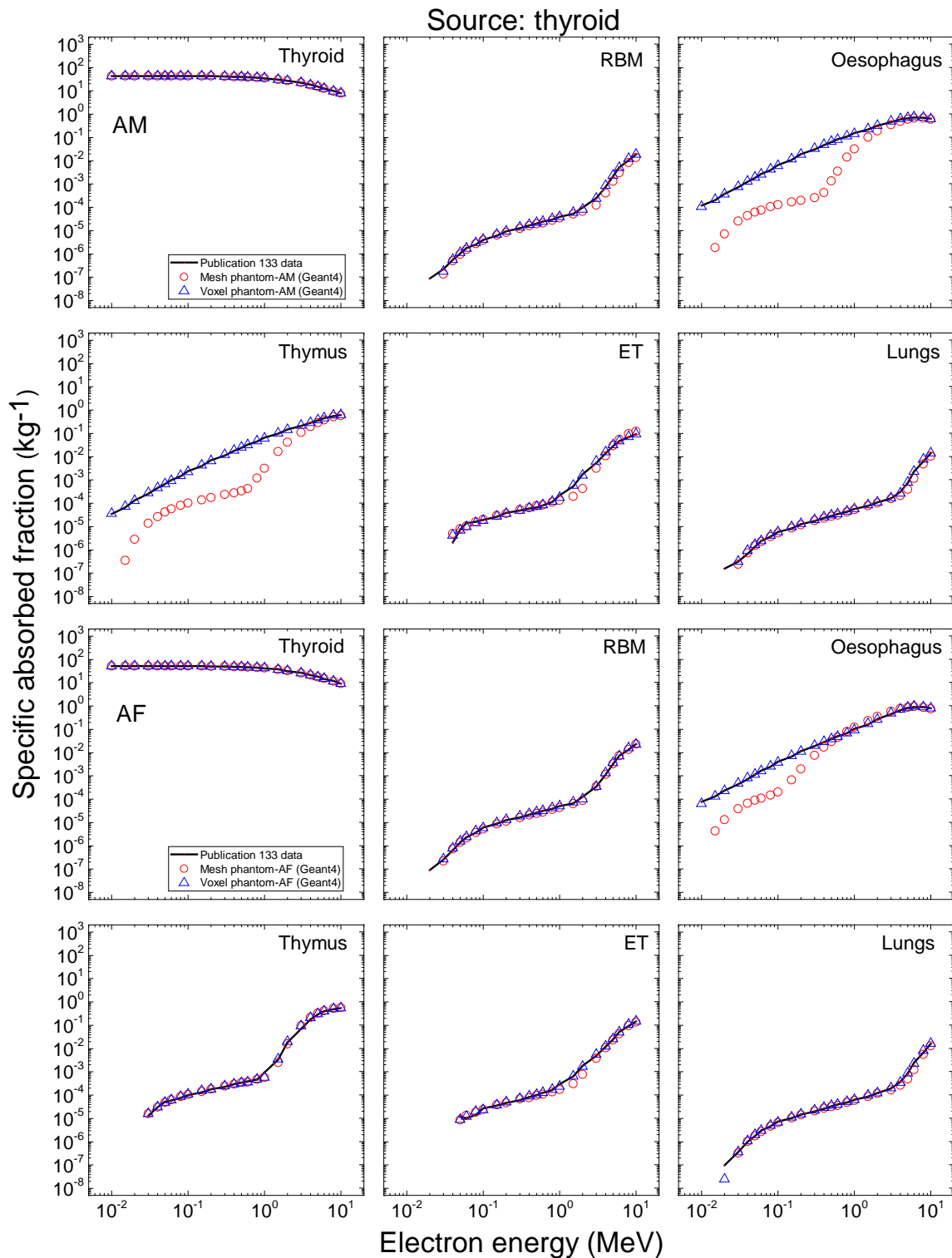
2146
2147
2148
2149
2150
2151

Fig. I.6. Specific absorbed fractions (SAFs) for liver as a source and liver, colon, lungs, stomach, gall bladder and RBM as a target for electron exposures calculated with the adult mesh-type reference phantoms (MRCPs), along with the *Publication 133* values (ICRP, 2016a) and the values calculated with the *Publication 110* phantoms and the Geant4 code: adult male, AM (upper) and adult female, AF (lower).



2152
2153
2154
2155
2156

Fig. I.7. Specific absorbed fractions (SAFs) for lungs as a source and lungs, RBM, stomach, heart, liver and spleen as a target for electron exposures calculated with the adult mesh-type reference phantoms (MRCPs), along with the *Publication 133* values (ICRP, 2016a) and the values calculated with the *Publication 110* phantoms and the Geant4 code: adult male, AM (upper) and adult female, AF (lower).



2157
2158
2159
2160
2161
2162
2163

Fig. I.8. Specific absorbed fractions (SAFs) for thyroid as a source and thyroid, RBM, oesophagus, thymus, extrathoracic (ET) region and lungs as a target for electron exposures calculated with the adult mesh-type reference phantoms (MRCPs), along with the *Publication 133* values (ICRP, 2016a) and the values calculated with the *Publication 110* phantoms and the Geant4 code: adult male, AM (upper) and adult female, AF (lower).

2164
2165**ANNEX J. DOSE COEFFICIENTS FOR INDUSTRIAL
RADIOGRAPHY SOURCES**

2166 (J1) Tables J.1–J.15 list the dose coefficients (DCs) ($\text{Gy s}^{-1} \text{Bq}^{-1}$) of red bone marrow, brain,
2167 lungs, small intestine and large intestine for the ^{192}Ir , $^{137}\text{Cs}/^{137\text{m}}\text{Ba}$, and ^{60}Co point sources.
2168 Table J.16 lists the DCs of effective dose ($\text{Sv s}^{-1} \text{Bq}^{-1}$) for the same sources. The data are for
2169 point sources located at three source distances (0.005, 0.1 and 0.3 m) in four directions
2170 (anterior, right lateral, posterior and left lateral) at five levels (ground, middle thigh and lower,
2171 middle and upper torso) as described in Chapter 8 (see Fig. 8.2). In addition, three longer
2172 distances (1, 1.5 and 3 m) were calculated in the four directions at the lower-torso level. Table
2173 J.17 lists the source self-shielding factors for different thicknesses of radioactive material (1,
2174 2, 3 and 4 mm) and capsule wall (1 and 2 mm) for the three isotopes.

Table J.1. ¹⁹²Ir: RBM absorbed dose per source disintegration Gy s⁻¹ Bq⁻¹).

Level (see Fig. 8.2)	Distance (m)	Gender	Direction											
			Anterior			Right lateral			Posterior			Left lateral		
			10%ile	MRCP	90%ile	10%ile	MRCP	90%ile	10%ile	MRCP	90%ile	10%ile	MRCP	90%ile
Ground	0.005	Male	3.72E-18	2.96E-18	2.11E-18	1.22E-18	1.03E-18	7.70E-19	2.85E-18	2.30E-18	1.56E-18	1.29E-18	1.14E-18	8.06E-19
		Female	6.03E-18	4.25E-18	3.21E-18	2.48E-18	1.68E-18	1.38E-18	3.38E-18	1.91E-18	1.74E-18	2.57E-18	1.73E-18	1.39E-18
	0.1	Male	5.88E-18	4.46E-18	2.94E-18	1.94E-18	1.50E-18	1.00E-18	6.13E-18	4.66E-18	3.22E-18	2.20E-18	1.75E-18	1.13E-18
		Female	8.50E-18	6.08E-18	4.38E-18	2.49E-18	1.68E-18	1.36E-18	7.05E-18	4.55E-18	3.32E-18	2.91E-18	1.95E-18	1.54E-18
	0.3	Male	9.09E-18	6.87E-18	4.78E-18	4.13E-18	3.03E-18	1.88E-18	1.08E-17	8.17E-18	6.26E-18	4.09E-18	3.20E-18	2.00E-18
		Female	1.20E-17	9.04E-18	6.41E-18	5.22E-18	3.67E-18	2.32E-18	1.28E-17	9.38E-18	6.96E-18	5.57E-18	3.87E-18	2.67E-18
Middle thigh	0.005	Male	7.89E-17	6.59E-17	5.51E-17	3.89E-17	3.38E-17	2.50E-17	8.63E-17	6.90E-17	5.83E-17	3.88E-17	3.41E-17	2.58E-17
		Female	1.45E-16	1.18E-16	9.75E-17	6.66E-17	5.39E-17	4.18E-17	1.39E-16	1.13E-16	9.44E-17	6.97E-17	5.67E-17	4.61E-17
	0.1	Male	8.18E-17	6.62E-17	5.26E-17	4.78E-17	3.83E-17	2.78E-17	9.32E-17	7.52E-17	6.26E-17	4.69E-17	3.96E-17	2.79E-17
		Female	1.24E-16	1.03E-16	7.92E-17	6.82E-17	5.48E-17	4.04E-17	1.25E-16	1.04E-16	8.07E-17	6.88E-17	5.43E-17	4.28E-17
	0.3	Male	5.94E-17	5.13E-17	3.71E-17	3.15E-17	2.60E-17	1.99E-17	6.90E-17	5.95E-17	5.04E-17	3.14E-17	2.59E-17	1.95E-17
		Female	7.59E-17	6.60E-17	4.67E-17	4.17E-17	3.48E-17	2.62E-17	8.00E-17	6.92E-17	5.58E-17	4.11E-17	3.35E-17	2.59E-17
Lower torso	0.005	Male	5.36E-16	4.01E-16	1.91E-16	4.63E-16	3.56E-16	1.96E-16	1.33E-15	1.13E-15	9.46E-16	4.31E-16	3.59E-16	1.83E-16
		Female	6.36E-16	4.79E-16	2.94E-16	4.83E-16	4.32E-16	2.01E-16	1.38E-15	1.19E-15	9.15E-16	4.50E-16	4.05E-16	2.17E-16
	0.1	Male	2.65E-16	2.19E-16	1.18E-16	2.29E-16	1.88E-16	1.22E-16	5.08E-16	4.52E-16	3.98E-16	2.20E-16	1.88E-16	1.16E-16
		Female	3.18E-16	2.66E-16	1.63E-16	2.40E-16	2.16E-16	1.22E-16	5.28E-16	4.72E-16	3.90E-16	2.25E-16	2.03E-16	1.29E-16
	0.3	Male	1.12E-16	9.77E-17	6.13E-17	7.98E-17	6.78E-17	5.04E-17	1.62E-16	1.49E-16	1.36E-16	7.31E-17	6.25E-17	4.38E-17
		Female	1.23E-16	1.10E-16	7.37E-17	8.32E-17	7.52E-17	5.11E-17	1.65E-16	1.53E-16	1.34E-16	7.80E-17	6.93E-17	4.96E-17
	1	Male	2.01E-17	1.88E-17	1.42E-17	1.31E-17	1.18E-17	9.78E-18	2.50E-17	2.37E-17	2.26E-17	1.28E-17	1.16E-17	9.37E-18
		Female	2.15E-17	2.01E-17	1.55E-17	1.41E-17	1.27E-17	1.02E-17	2.52E-17	2.41E-17	2.24E-17	1.38E-17	1.25E-17	1.03E-17
	1.5	Male	9.92E-18	9.32E-18	7.32E-18	6.42E-18	5.77E-18	4.95E-18	1.19E-17	1.13E-17	1.09E-17	6.29E-18	5.69E-18	4.78E-18
		Female	1.05E-17	9.90E-18	7.90E-18	6.87E-18	6.27E-18	5.19E-18	1.21E-17	1.15E-17	1.09E-17	6.73E-18	6.18E-18	5.24E-18
	3	Male	2.67E-18	2.57E-18	2.11E-18	1.73E-18	1.58E-18	1.38E-18	3.12E-18	3.00E-18	2.93E-18	1.72E-18	1.56E-18	1.35E-18
		Female	2.83E-18	2.70E-18	2.21E-18	1.86E-18	1.71E-18	1.47E-18	3.17E-18	3.03E-18	2.89E-18	1.85E-18	1.68E-18	1.47E-18
Middle torso	0.005	Male	6.06E-16	4.33E-16	2.96E-16	7.37E-16	5.45E-16	4.17E-16	1.24E-15	1.06E-15	8.64E-16	6.17E-16	4.83E-16	3.62E-16
		Female	8.39E-16	7.28E-16	3.47E-16	1.00E-15	8.34E-16	5.52E-16	1.72E-15	1.43E-15	1.00E-15	9.02E-16	6.99E-16	5.16E-16
	0.1	Male	2.60E-16	2.11E-16	1.52E-16	2.29E-16	1.95E-16	1.53E-16	4.52E-16	4.02E-16	3.46E-16	2.03E-16	1.77E-16	1.38E-16
		Female	3.29E-16	2.90E-16	1.73E-16	2.67E-16	2.26E-16	1.71E-16	5.23E-16	4.65E-16	3.77E-16	2.66E-16	2.23E-16	1.77E-16
	0.3	Male	1.09E-16	9.52E-17	7.07E-17	7.92E-17	6.89E-17	5.52E-17	1.55E-16	1.42E-16	1.29E-16	7.08E-17	6.11E-17	4.68E-17
		Female	1.31E-16	1.20E-16	8.04E-17	9.03E-17	7.93E-17	6.15E-17	1.69E-16	1.56E-16	1.36E-16	8.69E-17	7.49E-17	5.86E-17
Upper torso	0.005	Male	7.72E-16	6.37E-16	5.36E-16	8.14E-16	6.28E-16	5.21E-16	8.69E-16	6.54E-16	5.34E-16	7.80E-16	6.30E-16	5.18E-16
		Female	9.99E-16	8.53E-16	7.02E-16	7.19E-16	4.80E-16	3.48E-16	1.06E-15	8.26E-16	6.63E-16	4.87E-16	3.57E-16	2.32E-16
	0.1	Male	3.32E-16	2.90E-16	2.52E-16	4.30E-16	3.61E-16	3.22E-16	3.62E-16	3.05E-16	2.59E-16	3.77E-16	3.22E-16	2.97E-16
		Female	3.94E-16	3.56E-16	2.95E-16	1.77E-16	1.40E-16	1.12E-16	4.00E-16	3.45E-16	2.93E-16	1.45E-16	1.18E-16	8.80E-17
	0.3	Male	1.12E-16	1.01E-16	8.58E-17	8.73E-17	7.60E-17	6.54E-17	1.38E-16	1.24E-16	1.10E-16	7.39E-17	6.43E-17	5.78E-17
		Female	1.29E-16	1.19E-16	9.45E-17	6.74E-17	5.68E-17	4.53E-17	1.44E-16	1.31E-16	1.16E-16	6.19E-17	5.27E-17	4.10E-17

Table J.2. ¹⁹²Ir: Brain absorbed dose per source disintegration (Gy s⁻¹ Bq⁻¹).

Level	Distance (m)	Gender	Direction											
			Anterior			Right lateral			Posterior			Left lateral		
			10%ile	MRCP	90%ile	10%ile	MRCP	90%ile	10%ile	MRCP	90%ile	10%ile	MRCP	90%ile
Ground	0.005	Male	3.40E-19	1.80E-19	8.83E-20	9.88E-20	8.11E-20	6.28E-20	1.24E-19	1.02E-19	8.10E-20	1.09E-19	9.00E-20	6.61E-20
		Female	1.82E-18	1.01E-18	1.44E-19	1.12E-19	8.94E-20	7.05E-20	1.23E-19	9.17E-20	6.88E-20	1.21E-19	9.67E-20	7.24E-20
	0.1	Male	1.10E-18	5.43E-19	1.23E-19	1.49E-19	1.13E-19	8.32E-20	3.94E-19	1.96E-19	1.05E-19	1.63E-19	1.18E-19	8.51E-20
		Female	3.38E-18	2.32E-18	5.70E-19	2.09E-19	1.25E-19	8.23E-20	2.78E-19	1.49E-19	7.65E-20	2.83E-19	1.25E-19	9.49E-20
	0.3	Male	3.26E-18	2.25E-18	1.14E-18	8.43E-19	3.73E-19	1.13E-19	2.43E-18	1.39E-18	6.84E-19	7.21E-19	3.60E-19	1.22E-19
		Female	5.81E-18	4.58E-18	2.19E-18	2.26E-18	1.21E-18	1.52E-19	1.84E-18	9.05E-19	5.00E-19	2.22E-18	1.10E-18	2.09E-19
Middle thigh	0.005	Male	2.01E-19	1.72E-19	1.29E-19	1.79E-19	1.25E-19	1.05E-19	2.48E-19	1.81E-19	1.63E-19	1.77E-19	1.17E-19	9.59E-20
		Female	4.82E-19	3.68E-19	2.16E-19	2.67E-19	2.23E-19	1.44E-19	3.53E-19	3.07E-19	2.02E-19	2.27E-19	2.03E-19	1.36E-19
	0.1	Male	2.69E-18	1.19E-18	2.60E-19	9.53E-19	5.27E-19	3.21E-19	2.59E-18	1.14E-18	7.61E-19	1.33E-18	6.52E-19	3.35E-19
		Female	1.05E-17	8.34E-18	1.84E-18	4.16E-18	2.73E-18	6.57E-19	2.76E-18	1.92E-18	1.11E-18	3.70E-18	2.12E-18	6.63E-19
	0.3	Male	1.16E-17	9.23E-18	6.17E-18	4.47E-18	3.01E-18	1.69E-18	1.24E-17	8.50E-18	5.92E-18	3.27E-18	2.10E-18	1.31E-18
		Female	1.90E-17	1.77E-17	1.03E-17	9.20E-18	7.05E-18	3.09E-18	1.16E-17	8.39E-18	5.39E-18	9.47E-18	7.16E-18	3.12E-18
Lower torso	0.005	Male	3.08E-18	2.49E-18	1.99E-18	4.34E-18	4.20E-18	2.75E-18	2.42E-18	2.13E-18	1.46E-18	3.84E-18	3.05E-18	2.40E-18
		Female	1.49E-17	1.22E-17	3.22E-18	7.29E-18	6.20E-18	3.54E-18	4.15E-18	3.75E-18	2.58E-18	7.15E-18	5.03E-18	3.47E-18
	0.1	Male	2.97E-17	2.52E-17	2.00E-17	1.26E-17	9.87E-18	7.50E-18	2.16E-17	1.43E-17	7.85E-18	9.28E-18	7.29E-18	5.93E-18
		Female	4.65E-17	4.28E-17	2.43E-17	2.18E-17	1.76E-17	9.02E-18	1.52E-17	1.08E-17	6.41E-18	2.19E-17	1.75E-17	9.16E-18
	0.3	Male	3.16E-17	2.84E-17	2.32E-17	2.54E-17	1.85E-17	1.29E-17	3.95E-17	3.64E-17	2.94E-17	2.04E-17	1.38E-17	1.04E-17
		Female	4.35E-17	3.98E-17	3.31E-17	2.94E-17	2.24E-17	1.55E-17	3.95E-17	3.46E-17	2.60E-17	2.99E-17	2.33E-17	1.60E-17
	1	Male	1.32E-17	1.25E-17	1.07E-17	1.57E-17	1.50E-17	1.35E-17	1.53E-17	1.49E-17	1.39E-17	1.51E-17	1.44E-17	1.28E-17
		Female	1.53E-17	1.45E-17	1.32E-17	1.62E-17	1.58E-17	1.41E-17	1.57E-17	1.53E-17	1.44E-17	1.59E-17	1.56E-17	1.39E-17
	1.5	Male	7.28E-18	7.02E-18	6.28E-18	8.63E-18	8.31E-18	7.79E-18	8.31E-18	8.02E-18	7.68E-18	8.50E-18	8.14E-18	7.51E-18
		Female	8.14E-18	7.85E-18	7.32E-18	8.78E-18	8.69E-18	7.94E-18	8.52E-18	8.21E-18	7.87E-18	8.80E-18	8.63E-18	8.03E-18
	3	Male	2.19E-18	2.13E-18	1.97E-18	2.54E-18	2.51E-18	2.43E-18	2.39E-18	2.40E-18	2.29E-18	2.56E-18	2.49E-18	2.36E-18
		Female	2.30E-18	2.25E-18	2.15E-18	2.63E-18	2.60E-18	2.49E-18	2.45E-18	2.42E-18	2.36E-18	2.62E-18	2.58E-18	2.46E-18
Middle torso	0.005	Male	7.54E-17	6.78E-17	4.16E-17	3.05E-17	2.77E-17	2.16E-17	2.18E-17	1.91E-17	1.40E-17	2.80E-17	2.38E-17	1.84E-17
		Female	7.91E-17	7.98E-17	3.70E-17	4.51E-17	3.92E-17	2.90E-17	2.56E-17	2.43E-17	1.94E-17	4.02E-17	3.54E-17	2.89E-17
	0.1	Male	7.94E-17	7.14E-17	6.11E-17	3.32E-17	2.76E-17	1.96E-17	1.01E-16	8.81E-17	7.13E-17	2.99E-17	2.27E-17	1.62E-17
		Female	1.16E-16	1.06E-16	8.98E-17	4.10E-17	2.93E-17	2.19E-17	9.33E-17	7.68E-17	5.89E-17	4.60E-17	3.28E-17	2.70E-17
	0.3	Male	5.90E-17	5.23E-17	4.44E-17	7.32E-17	6.65E-17	5.56E-17	7.37E-17	6.90E-17	6.14E-17	6.70E-17	5.93E-17	4.78E-17
		Female	8.28E-17	7.75E-17	6.42E-17	7.85E-17	6.79E-17	5.44E-17	7.92E-17	7.46E-17	6.64E-17	7.66E-17	6.50E-17	5.06E-17
Upper torso	0.005	Male	4.50E-16	4.25E-16	3.89E-16	5.17E-16	5.27E-16	4.82E-16	5.20E-16	4.98E-16	4.52E-16	4.65E-16	4.61E-16	4.13E-16
		Female	6.99E-16	6.82E-16	6.54E-16	5.45E-16	4.62E-16	3.97E-16	6.44E-16	5.92E-16	5.34E-16	4.84E-16	4.00E-16	3.33E-16
	0.1	Male	2.99E-16	2.71E-16	2.38E-16	4.49E-16	4.02E-16	3.71E-16	4.04E-16	3.65E-16	3.31E-16	3.80E-16	3.45E-16	3.13E-16
		Female	5.11E-16	4.65E-16	4.24E-16	3.12E-16	2.65E-16	2.33E-16	4.07E-16	3.65E-16	3.33E-16	2.85E-16	2.45E-16	2.08E-16
	0.3	Male	1.42E-16	1.32E-16	1.24E-16	1.73E-16	1.57E-16	1.48E-16	1.47E-16	1.36E-16	1.27E-16	1.49E-16	1.37E-16	1.28E-16
		Female	1.89E-16	1.80E-16	1.71E-16	1.23E-16	1.10E-16	1.01E-16	1.41E-16	1.29E-16	1.23E-16	1.14E-16	1.04E-16	9.28E-17

Table J.3. ¹⁹²Ir: Lung absorbed dose per source disintegration (Gy s⁻¹ Bq⁻¹).

Level	Distance (m)	Gender	Direction											
			Anterior			Right lateral			Posterior			Left lateral		
			10%ile	MRCP	90%ile	10%ile	MRCP	90%ile	10%ile	MRCP	90%ile	10%ile	MRCP	90%ile
Ground	0.005	Male	1.00E-18	8.21E-19	3.65E-19	2.88E-19	2.24E-19	1.56E-19	6.10E-19	4.39E-19	2.82E-19	3.86E-19	3.04E-19	1.76E-19
		Female	8.91E-19	6.05E-19	4.43E-19	2.92E-19	2.17E-19	1.63E-19	6.00E-19	3.51E-19	2.62E-19	3.10E-19	2.36E-19	1.75E-19
	0.1	Male	1.87E-18	1.47E-18	6.01E-19	6.44E-19	3.94E-19	2.39E-19	2.19E-18	1.35E-18	9.06E-19	1.02E-18	6.49E-19	3.05E-19
		Female	2.00E-18	1.38E-18	7.54E-19	5.20E-19	3.34E-19	2.42E-19	2.61E-18	1.41E-18	7.34E-19	5.74E-19	3.77E-19	2.71E-19
	0.3	Male	4.06E-18	3.08E-18	1.39E-18	2.46E-18	1.56E-18	6.85E-19	6.29E-18	4.45E-18	3.21E-18	3.52E-18	2.31E-18	9.99E-19
		Female	5.69E-18	4.09E-18	1.90E-18	3.62E-18	2.29E-18	8.01E-19	9.53E-18	6.70E-18	4.37E-18	3.86E-18	2.32E-18	9.30E-19
Middle thigh	0.005	Male	2.36E-18	2.09E-18	1.83E-18	1.27E-18	8.30E-19	6.42E-19	3.37E-18	2.31E-18	2.09E-18	1.45E-18	8.51E-19	6.20E-19
		Female	4.00E-18	3.75E-18	3.03E-18	2.25E-18	1.93E-18	1.33E-18	5.25E-18	4.74E-18	3.49E-18	2.12E-18	1.85E-18	1.31E-18
	0.1	Male	9.35E-18	7.61E-18	3.39E-18	6.38E-18	4.04E-18	2.56E-18	1.90E-17	1.27E-17	1.02E-17	1.27E-17	7.11E-18	3.77E-18
		Female	1.38E-17	1.10E-17	5.14E-18	1.77E-17	1.34E-17	5.25E-18	3.49E-17	2.72E-17	1.82E-17	1.68E-17	1.15E-17	5.07E-18
	0.3	Male	2.08E-17	1.64E-17	1.02E-17	1.79E-17	1.43E-17	9.66E-18	3.33E-17	2.68E-17	2.13E-17	1.92E-17	1.53E-17	1.08E-17
		Female	3.40E-17	2.88E-17	1.64E-17	2.72E-17	2.31E-17	1.42E-17	4.93E-17	4.22E-17	3.23E-17	2.53E-17	2.15E-17	1.43E-17
Lower torso	0.005	Male	9.82E-17	8.60E-17	5.54E-17	8.70E-17	8.52E-17	5.30E-17	1.05E-16	9.91E-17	7.46E-17	1.03E-16	8.70E-17	6.13E-17
		Female	9.83E-17	9.17E-17	6.90E-17	1.15E-16	1.03E-16	5.94E-17	1.51E-16	1.43E-16	1.09E-16	1.14E-16	9.39E-17	6.29E-17
	0.1	Male	1.23E-16	1.02E-16	7.87E-17	1.30E-16	1.12E-16	8.34E-17	1.83E-16	1.59E-16	1.26E-16	1.46E-16	1.27E-16	9.53E-17
		Female	1.60E-16	1.36E-16	8.85E-17	1.57E-16	1.45E-16	9.56E-17	2.25E-16	2.02E-16	1.55E-16	1.55E-16	1.39E-16	9.92E-17
	0.3	Male	1.04E-16	8.96E-17	6.19E-17	6.80E-17	5.93E-17	4.65E-17	1.22E-16	1.09E-16	9.53E-17	6.62E-17	5.99E-17	4.52E-17
		Female	1.08E-16	9.78E-17	6.59E-17	8.00E-17	7.14E-17	5.13E-17	1.41E-16	1.30E-16	1.10E-16	7.26E-17	6.60E-17	4.84E-17
	1	Male	2.33E-17	2.16E-17	1.69E-17	1.26E-17	1.16E-17	9.70E-18	2.38E-17	2.20E-17	2.11E-17	1.26E-17	1.20E-17	9.56E-18
		Female	2.23E-17	2.11E-17	1.51E-17	1.45E-17	1.33E-17	1.05E-17	2.63E-17	2.48E-17	2.37E-17	1.39E-17	1.29E-17	1.06E-17
	1.5	Male	1.15E-17	1.08E-17	8.69E-18	6.11E-18	5.69E-18	4.76E-18	1.14E-17	1.08E-17	1.04E-17	6.08E-18	5.76E-18	4.83E-18
		Female	1.09E-17	1.07E-17	7.76E-18	7.07E-18	6.39E-18	5.32E-18	1.26E-17	1.21E-17	1.14E-17	6.82E-18	6.30E-18	5.30E-18
	3	Male	3.12E-18	3.05E-18	2.58E-18	1.65E-18	1.53E-18	1.29E-18	3.06E-18	2.87E-18	2.79E-18	1.67E-18	1.59E-18	1.30E-18
		Female	3.01E-18	2.94E-18	2.22E-18	1.88E-18	1.74E-18	1.49E-18	3.32E-18	3.20E-18	3.06E-18	1.86E-18	1.69E-18	1.49E-18
Middle torso	0.005	Male	1.29E-15	9.76E-16	7.14E-16	1.58E-15	1.23E-15	9.48E-16	1.53E-15	1.31E-15	1.05E-15	1.86E-15	1.46E-15	1.10E-15
		Female	1.66E-15	1.41E-15	8.11E-16	2.29E-15	1.93E-15	1.40E-15	2.19E-15	1.83E-15	1.40E-15	2.40E-15	1.87E-15	1.38E-15
	0.1	Male	5.83E-16	4.76E-16	3.36E-16	4.42E-16	3.80E-16	3.20E-16	6.54E-16	5.62E-16	4.88E-16	4.41E-16	3.91E-16	3.24E-16
		Female	6.38E-16	5.59E-16	3.33E-16	5.43E-16	4.45E-16	3.68E-16	8.21E-16	7.16E-16	5.94E-16	5.41E-16	4.46E-16	3.80E-16
	0.3	Male	1.76E-16	1.56E-16	1.21E-16	1.04E-16	9.31E-17	7.86E-17	1.85E-16	1.65E-16	1.53E-16	9.72E-17	8.99E-17	7.20E-17
		Female	1.79E-16	1.67E-16	1.07E-16	1.23E-16	1.09E-16	9.25E-17	2.17E-16	1.98E-16	1.78E-16	1.18E-16	1.03E-16	8.44E-17
Upper torso	0.005	Male	1.16E-15	9.80E-16	8.16E-16	1.36E-15	1.11E-15	9.27E-16	1.05E-15	8.53E-16	6.95E-16	1.19E-15	9.80E-16	8.15E-16
		Female	1.40E-15	1.21E-15	9.38E-16	5.32E-16	4.03E-16	3.05E-16	1.24E-15	1.06E-15	8.48E-16	4.02E-16	3.23E-16	2.28E-16
	0.1	Male	7.14E-16	6.27E-16	5.32E-16	4.64E-16	3.86E-16	3.47E-16	6.05E-16	5.09E-16	4.29E-16	3.65E-16	3.06E-16	2.74E-16
		Female	7.24E-16	6.54E-16	5.17E-16	2.27E-16	1.77E-16	1.41E-16	6.66E-16	5.76E-16	4.98E-16	1.89E-16	1.49E-16	1.10E-16
	0.3	Male	2.24E-16	2.05E-16	1.81E-16	1.17E-16	9.76E-17	8.40E-17	1.97E-16	1.72E-16	1.56E-16	1.02E-16	8.62E-17	7.67E-17
		Female	2.10E-16	1.99E-16	1.60E-16	8.72E-17	7.08E-17	5.86E-17	2.08E-16	1.89E-16	1.74E-16	7.94E-17	6.56E-17	5.30E-17

Table J.4. ¹⁹²Ir: Small intestine absorbed dose per source disintegration (Gy s⁻¹ Bq⁻¹).

Level	Distance (m)	Gender	Direction											
			Anterior			Right lateral			Posterior			Left lateral		
			10%ile	MRCP	90%ile	10%ile	MRCP	90%ile	10%ile	MRCP	90%ile	10%ile	MRCP	90%ile
Ground	0.005	Male	8.61E-18	6.63E-18	5.23E-18	1.21E-18	1.07E-18	1.17E-18	1.83E-18	1.55E-18	1.01E-18	1.40E-18	1.29E-18	1.20E-18
		Female	1.35E-17	9.70E-18	7.86E-18	4.47E-18	3.31E-18	2.57E-18	6.60E-18	3.22E-18	2.99E-18	3.62E-18	2.57E-18	2.15E-18
	0.1	Male	1.28E-17	1.00E-17	7.34E-18	1.46E-18	1.16E-18	1.20E-18	3.71E-18	2.92E-18	1.98E-18	1.95E-18	1.63E-18	1.35E-18
		Female	1.71E-17	1.27E-17	9.99E-18	2.70E-18	1.92E-18	1.89E-18	1.01E-17	6.72E-18	5.20E-18	3.22E-18	2.24E-18	2.09E-18
	0.3	Male	1.75E-17	1.50E-17	9.77E-18	3.31E-18	2.24E-18	1.91E-18	7.04E-18	5.02E-18	3.96E-18	4.61E-18	3.26E-18	2.36E-18
		Female	2.17E-17	1.72E-17	1.23E-17	4.14E-18	2.98E-18	2.63E-18	1.35E-17	1.02E-17	8.22E-18	6.01E-18	3.96E-18	3.40E-18
Middle thigh	0.005	Male	6.50E-17	5.45E-17	5.62E-17	1.82E-17	1.55E-17	1.19E-17	5.80E-17	4.46E-17	3.96E-17	1.78E-17	1.52E-17	1.19E-17
		Female	2.08E-16	1.79E-16	1.55E-16	6.36E-17	5.23E-17	3.98E-17	1.93E-16	1.63E-16	1.37E-16	6.54E-17	5.43E-17	4.34E-17
	0.1	Male	1.21E-16	1.04E-16	7.69E-17	3.10E-17	2.27E-17	1.94E-17	6.34E-17	5.19E-17	4.36E-17	3.50E-17	2.48E-17	2.06E-17
		Female	2.14E-16	1.86E-16	1.35E-16	6.64E-17	5.15E-17	4.09E-17	1.51E-16	1.29E-16	1.05E-16	7.28E-17	5.50E-17	4.63E-17
	0.3	Male	1.08E-16	1.00E-16	6.31E-17	3.28E-17	2.55E-17	2.11E-17	5.27E-17	4.34E-17	3.67E-17	4.38E-17	3.58E-17	2.55E-17
		Female	1.38E-16	1.24E-16	8.49E-17	4.40E-17	3.51E-17	2.84E-17	8.94E-17	7.48E-17	6.14E-17	5.75E-17	4.68E-17	3.60E-17
Lower torso	0.005	Male	4.00E-15	2.91E-15	1.15E-15	9.33E-16	6.70E-16	4.00E-16	1.21E-15	9.89E-16	8.16E-16	1.45E-15	1.18E-15	5.90E-16
		Female	3.04E-15	2.36E-15	1.35E-15	7.27E-16	6.27E-16	2.95E-16	1.69E-15	1.42E-15	1.11E-15	1.12E-15	1.03E-15	5.47E-16
	0.1	Male	1.04E-15	8.71E-16	4.54E-16	3.41E-16	2.73E-16	1.74E-16	4.96E-16	4.26E-16	3.70E-16	4.89E-16	4.26E-16	2.51E-16
		Female	9.26E-16	7.82E-16	5.11E-16	2.94E-16	2.59E-16	1.40E-16	6.63E-16	5.72E-16	4.76E-16	4.41E-16	4.05E-16	2.47E-16
	0.3	Male	2.41E-16	2.20E-16	1.42E-16	9.96E-17	8.52E-17	6.07E-17	1.46E-16	1.33E-16	1.20E-16	1.31E-16	1.18E-16	7.94E-17
		Female	2.28E-16	2.05E-16	1.50E-16	9.21E-17	8.13E-17	5.20E-17	1.75E-16	1.57E-16	1.41E-16	1.22E-16	1.13E-16	7.91E-17
	1	Male	2.89E-17	2.78E-17	2.12E-17	1.45E-17	1.31E-17	9.92E-18	2.05E-17	1.88E-17	1.77E-17	1.83E-17	1.70E-17	1.31E-17
		Female	2.86E-17	2.68E-17	2.15E-17	1.34E-17	1.23E-17	8.87E-18	2.28E-17	2.13E-17	1.96E-17	1.75E-17	1.64E-17	1.29E-17
	1.5	Male	1.33E-17	1.27E-17	1.01E-17	6.93E-18	6.29E-18	4.90E-18	9.56E-18	8.90E-18	8.56E-18	8.67E-18	8.10E-18	6.41E-18
		Female	1.32E-17	1.27E-17	1.03E-17	6.58E-18	5.97E-18	4.44E-18	1.06E-17	9.88E-18	9.36E-18	8.36E-18	7.79E-18	6.38E-18
	3	Male	3.41E-18	3.34E-18	2.74E-18	1.82E-18	1.67E-18	1.34E-18	2.54E-18	2.33E-18	2.23E-18	2.25E-18	2.09E-18	1.74E-18
		Female	3.45E-18	3.31E-18	2.71E-18	1.75E-18	1.61E-18	1.28E-18	2.75E-18	2.59E-18	2.40E-18	2.22E-18	2.02E-18	1.76E-18
Middle torso	0.005	Male	4.36E-16	3.62E-16	2.86E-16	2.09E-16	1.72E-16	1.41E-16	3.01E-16	2.57E-16	2.06E-16	4.16E-16	3.44E-16	2.80E-16
		Female	3.78E-16	3.48E-16	2.50E-16	1.75E-16	1.51E-16	1.22E-16	2.63E-16	2.28E-16	1.74E-16	3.79E-16	3.47E-16	2.78E-16
	0.1	Male	3.65E-16	2.94E-16	2.25E-16	1.70E-16	1.46E-16	1.13E-16	2.30E-16	1.92E-16	1.57E-16	2.77E-16	2.33E-16	1.91E-16
		Female	3.74E-16	3.27E-16	2.14E-16	1.55E-16	1.30E-16	9.31E-17	2.51E-16	2.18E-16	1.66E-16	2.94E-16	2.55E-16	2.02E-16
	0.3	Male	1.68E-16	1.44E-16	1.11E-16	8.00E-17	6.88E-17	5.29E-17	1.07E-16	9.35E-17	8.17E-17	1.05E-16	9.14E-17	7.36E-17
		Female	1.70E-16	1.55E-16	1.12E-16	7.42E-17	6.76E-17	4.59E-17	1.24E-16	1.10E-16	9.27E-17	1.11E-16	9.84E-17	7.75E-17
Upper torso	0.005	Male	4.49E-17	4.21E-17	3.45E-17	4.14E-17	3.65E-17	2.92E-17	3.02E-17	2.76E-17	2.13E-17	4.47E-17	4.08E-17	3.25E-17
		Female	3.30E-17	3.35E-17	2.30E-17	1.59E-17	1.39E-17	1.01E-17	2.23E-17	2.22E-17	1.73E-17	1.74E-17	1.65E-17	1.20E-17
	0.1	Male	6.90E-17	5.86E-17	4.22E-17	2.12E-17	1.89E-17	1.54E-17	4.51E-17	3.77E-17	2.89E-17	2.26E-17	2.02E-17	1.73E-17
		Female	6.39E-17	5.70E-17	2.73E-17	2.17E-17	1.76E-17	1.06E-17	5.03E-17	4.42E-17	3.20E-17	5.02E-17	4.22E-17	2.40E-17
	0.3	Male	8.60E-17	7.07E-17	5.36E-17	3.88E-17	3.14E-17	2.03E-17	5.50E-17	4.53E-17	3.70E-17	5.13E-17	4.25E-17	2.88E-17
		Female	8.76E-17	7.84E-17	5.18E-17	3.47E-17	2.99E-17	1.90E-17	6.25E-17	5.56E-17	4.33E-17	5.25E-17	4.51E-17	3.24E-17

Table J.5. ¹⁹²Ir: Large intestine absorbed dose per source disintegration (Gy s⁻¹ Bq⁻¹).

Level	Distance (m)	Gender	Direction											
			Anterior			Right lateral			Posterior			Left lateral		
			10%ile	MRCP	90%ile	10%ile	MRCP	90%ile	10%ile	MRCP	90%ile	10%ile	MRCP	90%ile
Ground	0.005	Male	7.38E-18	6.19E-18	3.58E-18	1.31E-18	1.18E-18	1.00E-18	3.93E-18	3.04E-18	2.32E-18	1.25E-18	1.25E-18	9.12E-19
		Female	1.62E-17	1.13E-17	9.16E-18	6.01E-18	4.17E-18	3.47E-18	7.20E-18	3.62E-18	3.60E-18	5.05E-18	3.70E-18	3.09E-18
	0.1	Male	1.17E-17	9.27E-18	5.41E-18	1.50E-18	1.19E-18	1.01E-18	5.69E-18	4.51E-18	3.51E-18	2.45E-18	2.05E-18	1.20E-18
		Female	2.17E-17	1.56E-17	1.21E-17	3.65E-18	2.59E-18	2.47E-18	1.01E-17	6.97E-18	5.76E-18	4.37E-18	3.11E-18	2.69E-18
	0.3	Male	1.65E-17	1.38E-17	7.62E-18	3.69E-18	2.69E-18	1.88E-18	8.16E-18	6.19E-18	5.20E-18	6.93E-18	5.35E-18	2.58E-18
		Female	2.71E-17	2.14E-17	1.50E-17	5.40E-18	3.77E-18	3.43E-18	1.35E-17	1.00E-17	8.33E-18	7.01E-18	4.54E-18	4.07E-18
Middle thigh	0.005	Male	6.37E-17	5.42E-17	4.96E-17	1.92E-17	1.63E-17	1.21E-17	7.97E-17	6.45E-17	5.79E-17	1.98E-17	1.70E-17	1.27E-17
		Female	2.66E-16	2.21E-16	1.93E-16	7.37E-17	5.98E-17	4.60E-17	2.43E-16	2.00E-16	1.71E-16	8.17E-17	6.71E-17	5.44E-17
	0.1	Male	9.58E-17	8.24E-17	5.40E-17	3.02E-17	2.25E-17	1.86E-17	7.76E-17	6.66E-17	5.68E-17	4.32E-17	3.03E-17	2.13E-17
		Female	2.74E-16	2.38E-16	1.64E-16	7.54E-17	5.84E-17	4.85E-17	1.69E-16	1.44E-16	1.20E-16	8.67E-17	6.52E-17	5.60E-17
	0.3	Male	9.36E-17	8.34E-17	5.13E-17	3.85E-17	3.05E-17	2.20E-17	5.87E-17	4.86E-17	4.21E-17	4.80E-17	4.13E-17	2.64E-17
		Female	1.62E-16	1.50E-16	1.03E-16	5.56E-17	4.43E-17	3.60E-17	8.24E-17	6.98E-17	5.96E-17	6.17E-17	4.83E-17	4.06E-17
Lower torso	0.005	Male	1.57E-15	1.28E-15	7.02E-16	1.57E-15	1.12E-15	5.81E-16	8.38E-16	6.98E-16	5.75E-16	1.40E-15	1.18E-15	5.93E-16
		Female	4.40E-15	3.14E-15	1.72E-15	1.34E-15	1.21E-15	5.09E-16	1.25E-15	1.01E-15	7.95E-16	1.48E-15	1.38E-15	6.73E-16
	0.1	Male	8.19E-16	6.89E-16	3.86E-16	4.48E-16	3.73E-16	2.28E-16	4.42E-16	3.78E-16	3.29E-16	5.16E-16	4.63E-16	2.81E-16
		Female	1.11E-15	9.38E-16	6.12E-16	4.13E-16	3.83E-16	2.02E-16	5.27E-16	4.45E-16	3.69E-16	4.36E-16	4.12E-16	2.50E-16
	0.3	Male	2.21E-16	2.00E-16	1.37E-16	1.20E-16	1.05E-16	7.52E-17	1.43E-16	1.25E-16	1.14E-16	1.40E-16	1.27E-16	9.20E-17
		Female	2.55E-16	2.34E-16	1.76E-16	1.14E-16	1.05E-16	6.63E-17	1.52E-16	1.34E-16	1.19E-16	1.16E-16	1.07E-16	7.53E-17
	1	Male	2.84E-17	2.65E-17	2.16E-17	1.63E-17	1.47E-17	1.18E-17	2.07E-17	1.90E-17	1.79E-17	1.89E-17	1.79E-17	1.44E-17
		Female	3.04E-17	2.96E-17	2.45E-17	1.58E-17	1.48E-17	1.07E-17	2.04E-17	1.89E-17	1.80E-17	1.62E-17	1.52E-17	1.21E-17
	1.5	Male	1.33E-17	1.26E-17	1.04E-17	7.58E-18	7.04E-18	5.69E-18	9.78E-18	8.77E-18	8.71E-18	8.75E-18	8.31E-18	6.97E-18
		Female	1.41E-17	1.41E-17	1.14E-17	7.50E-18	7.07E-18	5.39E-18	9.65E-18	9.08E-18	8.35E-18	7.71E-18	7.30E-18	5.85E-18
	3	Male	3.31E-18	3.29E-18	2.86E-18	2.03E-18	1.87E-18	1.56E-18	2.54E-18	2.34E-18	2.32E-18	2.29E-18	2.15E-18	1.88E-18
		Female	3.67E-18	3.57E-18	3.06E-18	1.99E-18	1.89E-18	1.43E-18	2.49E-18	2.29E-18	2.22E-18	2.03E-18	1.94E-18	1.62E-18
Middle torso	0.005	Male	6.25E-16	5.24E-16	4.22E-16	3.37E-16	2.72E-16	2.34E-16	2.98E-16	2.50E-16	1.98E-16	7.78E-16	6.33E-16	5.32E-16
		Female	2.26E-16	2.12E-16	1.67E-16	1.61E-16	1.52E-16	1.32E-16	1.59E-16	1.39E-16	1.07E-16	1.55E-16	1.45E-16	1.17E-16
	0.1	Male	4.54E-16	3.80E-16	3.03E-16	2.66E-16	2.23E-16	1.83E-16	2.28E-16	1.89E-16	1.55E-16	4.08E-16	3.49E-16	2.94E-16
		Female	3.49E-16	2.99E-16	1.92E-16	1.91E-16	1.72E-16	1.18E-16	1.81E-16	1.52E-16	1.20E-16	1.90E-16	1.62E-16	1.24E-16
	0.3	Male	1.72E-16	1.51E-16	1.26E-16	1.02E-16	8.87E-17	7.33E-17	1.04E-16	9.03E-17	8.05E-17	1.23E-16	1.10E-16	9.37E-17
		Female	1.81E-16	1.72E-16	1.19E-16	9.07E-17	8.49E-17	5.82E-17	1.01E-16	8.90E-17	7.37E-17	9.27E-17	8.29E-17	6.18E-17
Upper torso	0.005	Male	6.23E-17	5.69E-17	4.83E-17	5.13E-17	4.47E-17	3.65E-17	3.96E-17	3.50E-17	2.73E-17	5.81E-17	5.24E-17	4.31E-17
		Female	2.21E-17	2.26E-17	1.55E-17	1.16E-17	1.05E-17	7.70E-18	1.39E-17	1.37E-17	1.05E-17	1.06E-17	1.00E-17	7.20E-18
	0.1	Male	9.74E-17	8.23E-17	5.74E-17	2.58E-17	2.24E-17	1.84E-17	5.46E-17	4.54E-17	3.52E-17	2.74E-17	2.43E-17	2.00E-17
		Female	5.57E-17	4.62E-17	1.96E-17	3.24E-17	2.82E-17	1.28E-17	3.50E-17	2.92E-17	2.21E-17	4.14E-17	3.52E-17	2.13E-17
	0.3	Male	9.66E-17	8.37E-17	6.62E-17	5.46E-17	4.69E-17	3.03E-17	5.64E-17	4.70E-17	3.84E-17	7.18E-17	6.09E-17	4.39E-17
		Female	9.21E-17	8.46E-17	5.30E-17	4.39E-17	3.93E-17	2.48E-17	5.02E-17	4.34E-17	3.38E-17	4.33E-17	3.76E-17	2.64E-17

Table J.6. ¹³⁷Cs: RBM absorbed dose per source disintegration (Gy s⁻¹ Bq⁻¹).

Level	Distance (m)	Gender	Direction											
			Anterior			Right lateral			Posterior			Left lateral		
			10%ile	MRCP	90%ile	10%ile	MRCP	90%ile	10%ile	MRCP	90%ile	10%ile	MRCP	90%ile
Ground	0.005	Male	3.19E-18	2.57E-18	1.82E-18	1.12E-18	9.19E-19	6.81E-19	2.42E-18	1.96E-18	1.32E-18	1.22E-18	1.03E-18	7.24E-19
		Female	5.08E-18	3.66E-18	2.80E-18	2.18E-18	1.46E-18	1.21E-18	2.85E-18	1.64E-18	1.47E-18	2.27E-18	1.53E-18	1.23E-18
	0.1	Male	4.91E-18	3.76E-18	2.52E-18	1.74E-18	1.34E-18	8.89E-19	5.09E-18	3.90E-18	2.74E-18	1.95E-18	1.54E-18	1.01E-18
		Female	6.93E-18	5.02E-18	3.70E-18	2.24E-18	1.51E-18	1.20E-18	5.89E-18	3.88E-18	2.86E-18	2.57E-18	1.73E-18	1.35E-18
	0.3	Male	7.04E-18	5.46E-18	3.87E-18	3.43E-18	2.60E-18	1.64E-18	8.31E-18	6.43E-18	5.00E-18	3.48E-18	2.73E-18	1.74E-18
		Female	9.23E-18	7.02E-18	5.10E-18	4.51E-18	3.13E-18	2.03E-18	9.83E-18	7.34E-18	5.59E-18	4.72E-18	3.28E-18	2.30E-18
Middle thigh	0.005	Male	6.03E-17	5.06E-17	4.20E-17	3.25E-17	2.81E-17	2.08E-17	6.54E-17	5.29E-17	4.46E-17	3.23E-17	2.83E-17	2.15E-17
		Female	1.06E-16	8.65E-17	7.11E-17	5.38E-17	4.36E-17	3.39E-17	1.02E-16	8.35E-17	6.89E-17	5.61E-17	4.58E-17	3.69E-17
	0.1	Male	6.00E-17	4.92E-17	3.91E-17	3.73E-17	3.03E-17	2.21E-17	6.82E-17	5.58E-17	4.63E-17	3.68E-17	3.12E-17	2.22E-17
		Female	8.91E-17	7.44E-17	5.73E-17	5.26E-17	4.26E-17	3.15E-17	9.03E-17	7.55E-17	5.92E-17	5.30E-17	4.23E-17	3.31E-17
	0.3	Male	4.22E-17	3.67E-17	2.71E-17	2.45E-17	2.04E-17	1.57E-17	4.83E-17	4.20E-17	3.58E-17	2.43E-17	2.04E-17	1.55E-17
		Female	5.37E-17	4.71E-17	3.39E-17	3.15E-17	2.67E-17	2.03E-17	5.57E-17	4.89E-17	3.98E-17	3.14E-17	2.60E-17	2.03E-17
Lower torso	0.005	Male	3.77E-16	2.85E-16	1.41E-16	3.34E-16	2.58E-16	1.45E-16	9.16E-16	7.77E-16	6.50E-16	3.12E-16	2.59E-16	1.36E-16
		Female	4.51E-16	3.42E-16	2.11E-16	3.48E-16	3.10E-16	1.48E-16	9.50E-16	8.16E-16	6.24E-16	3.25E-16	2.92E-16	1.59E-16
	0.1	Male	1.88E-16	1.57E-16	8.83E-17	1.65E-16	1.36E-16	8.96E-17	3.44E-16	3.08E-16	2.71E-16	1.59E-16	1.36E-16	8.59E-17
		Female	2.24E-16	1.88E-16	1.19E-16	1.72E-16	1.55E-16	9.04E-17	3.57E-16	3.20E-16	2.66E-16	1.63E-16	1.47E-16	9.49E-17
	0.3	Male	7.83E-17	6.87E-17	4.48E-17	5.83E-17	5.00E-17	3.80E-17	1.09E-16	1.00E-16	9.21E-17	5.40E-17	4.68E-17	3.33E-17
		Female	8.55E-17	7.65E-17	5.32E-17	6.08E-17	5.52E-17	3.84E-17	1.11E-16	1.04E-16	9.09E-17	5.73E-17	5.14E-17	3.76E-17
	1	Male	1.40E-17	1.30E-17	1.01E-17	9.71E-18	8.74E-18	7.35E-18	1.68E-17	1.59E-17	1.53E-17	9.54E-18	8.65E-18	7.11E-18
		Female	1.48E-17	1.38E-17	1.10E-17	1.03E-17	9.45E-18	7.65E-18	1.70E-17	1.62E-17	1.52E-17	1.02E-17	9.33E-18	7.71E-18
	1.5	Male	6.85E-18	6.48E-18	5.23E-18	4.74E-18	4.29E-18	3.72E-18	8.02E-18	7.67E-18	7.43E-18	4.67E-18	4.26E-18	3.65E-18
		Female	7.16E-18	6.78E-18	5.57E-18	5.05E-18	4.64E-18	3.88E-18	8.10E-18	7.75E-18	7.34E-18	4.98E-18	4.56E-18	3.92E-18
	3	Male	1.86E-18	1.77E-18	1.49E-18	1.29E-18	1.18E-18	1.05E-18	2.10E-18	2.05E-18	1.98E-18	1.27E-18	1.17E-18	1.02E-18
		Female	1.92E-18	1.84E-18	1.57E-18	1.37E-18	1.27E-18	1.11E-18	2.13E-18	2.04E-18	1.96E-18	1.35E-18	1.26E-18	1.11E-18
Middle torso	0.005	Male	4.31E-16	3.10E-16	2.12E-16	5.16E-16	3.82E-16	2.91E-16	8.66E-16	7.41E-16	5.99E-16	4.33E-16	3.39E-16	2.53E-16
		Female	5.89E-16	5.13E-16	2.45E-16	6.99E-16	5.79E-16	3.79E-16	1.19E-15	9.88E-16	6.92E-16	6.29E-16	4.88E-16	3.58E-16
	0.1	Male	1.85E-16	1.51E-16	1.10E-16	1.67E-16	1.42E-16	1.12E-16	3.09E-16	2.76E-16	2.37E-16	1.50E-16	1.30E-16	1.02E-16
		Female	2.33E-16	2.05E-16	1.26E-16	1.95E-16	1.66E-16	1.26E-16	3.57E-16	3.18E-16	2.58E-16	1.94E-16	1.63E-16	1.29E-16
	0.3	Male	7.63E-17	6.68E-17	5.11E-17	5.84E-17	5.12E-17	4.15E-17	1.05E-16	9.65E-17	8.78E-17	5.31E-17	4.59E-17	3.57E-17
		Female	9.10E-17	8.35E-17	5.77E-17	6.66E-17	5.89E-17	4.65E-17	1.14E-16	1.05E-16	9.23E-17	6.43E-17	5.60E-17	4.43E-17
Upper torso	0.005	Male	5.35E-16	4.42E-16	3.70E-16	5.67E-16	4.38E-16	3.64E-16	6.09E-16	4.60E-16	3.75E-16	5.46E-16	4.41E-16	3.63E-16
		Female	6.86E-16	5.87E-16	4.81E-16	5.10E-16	3.42E-16	2.48E-16	7.45E-16	5.79E-16	4.63E-16	3.52E-16	2.60E-16	1.70E-16
	0.1	Male	2.31E-16	2.02E-16	1.75E-16	3.09E-16	2.59E-16	2.30E-16	2.51E-16	2.13E-16	1.82E-16	2.72E-16	2.32E-16	2.13E-16
		Female	2.74E-16	2.48E-16	2.06E-16	1.31E-16	1.04E-16	8.29E-17	2.77E-16	2.40E-16	2.03E-16	1.08E-16	8.85E-17	6.62E-17
	0.3	Male	7.83E-17	7.05E-17	6.07E-17	6.49E-17	5.66E-17	4.85E-17	9.50E-17	8.51E-17	7.61E-17	5.50E-17	4.83E-17	4.32E-17
		Female	8.95E-17	8.34E-17	6.71E-17	4.99E-17	4.22E-17	3.37E-17	9.82E-17	8.96E-17	7.97E-17	4.58E-17	3.94E-17	3.08E-17

Table J.7. ¹³⁷Cs/^{137m}Ba: Brain absorbed dose per source disintegration (unit: Gy s⁻¹ Bq⁻¹).

Level	Distance (m)	Gender	Direction												
			Anterior			Right lateral			Posterior			Left lateral			
			10%ile	MRCP	90%ile	10%ile	MRCP	90%ile	10%ile	MRCP	90%ile	10%ile	MRCP	90%ile	
Ground	0.005	Male	2.96E-19	1.57E-19	6.01E-20	5.21E-20	4.35E-20	3.11E-20	8.87E-20	6.46E-20	4.30E-20	6.04E-20	4.84E-20	3.49E-20	
		Female	1.40E-18	7.77E-19	1.06E-19	6.67E-20	4.95E-20	3.47E-20	9.02E-20	5.83E-20	4.08E-20	6.67E-20	5.11E-20	3.40E-20	
	0.1	Male	9.55E-19	4.85E-19	1.18E-19	1.03E-19	7.30E-20	4.94E-20	3.80E-19	2.05E-19	1.05E-19	1.17E-19	8.28E-20	4.88E-20	
		Female	2.74E-18	1.88E-18	5.05E-19	1.48E-19	8.12E-20	4.75E-20	3.17E-19	1.61E-19	7.95E-20	2.00E-19	8.69E-20	5.88E-20	
	0.3	Male	2.72E-18	1.84E-18	1.01E-18	8.40E-19	3.98E-19	1.18E-19	1.96E-18	1.18E-18	6.51E-19	7.71E-19	4.16E-19	1.45E-19	
		Female	4.79E-18	3.86E-18	1.87E-18	2.02E-18	1.04E-18	1.61E-19	1.67E-18	9.42E-19	5.54E-19	2.04E-18	9.88E-19	2.21E-19	
Middle thigh	0.005	Male	1.84E-19	1.64E-19	1.30E-19	1.42E-19	9.49E-20	7.35E-20	2.65E-19	1.81E-19	1.52E-19	1.29E-19	8.40E-20	6.43E-20	
		Female	5.37E-19	4.19E-19	2.40E-19	2.73E-19	2.18E-19	1.37E-19	3.94E-19	3.51E-19	2.32E-19	2.32E-19	1.99E-19	1.20E-19	
	0.1	Male	2.46E-18	1.21E-18	3.06E-19	1.10E-18	5.90E-19	3.32E-19	2.35E-18	1.23E-18	8.37E-19	1.53E-18	7.19E-19	3.67E-19	
		Female	8.49E-18	6.67E-18	1.79E-18	4.16E-18	2.90E-18	7.28E-19	2.89E-18	2.11E-18	1.34E-18	3.64E-18	2.20E-18	6.77E-19	
	0.3	Male	9.41E-18	7.74E-18	5.23E-18	4.01E-18	2.88E-18	1.80E-18	9.32E-18	6.63E-18	4.70E-18	3.11E-18	2.16E-18	1.46E-18	
		Female	1.48E-17	1.36E-17	8.70E-18	7.70E-18	6.06E-18	3.07E-18	9.47E-18	6.67E-18	4.57E-18	7.84E-18	6.30E-18	3.13E-18	
Lower torso	0.005	Male	3.44E-18	2.97E-18	2.30E-18	4.85E-18	4.95E-18	3.03E-18	2.74E-18	2.44E-18	1.71E-18	4.56E-18	3.47E-18	2.71E-18	
		Female	1.32E-17	1.11E-17	3.73E-18	7.78E-18	6.79E-18	3.88E-18	4.64E-18	4.27E-18	3.00E-18	7.71E-18	5.31E-18	3.75E-18	
	0.1	Male	2.44E-17	2.11E-17	1.73E-17	1.18E-17	9.56E-18	7.78E-18	1.70E-17	1.23E-17	7.25E-18	9.25E-18	7.74E-18	6.25E-18	
		Female	3.57E-17	3.29E-17	1.98E-17	1.90E-17	1.61E-17	9.15E-18	1.37E-17	1.03E-17	6.63E-18	1.89E-17	1.59E-17	9.44E-18	
	0.3	Male	2.44E-17	2.25E-17	1.81E-17	1.97E-17	1.49E-17	1.07E-17	2.99E-17	2.73E-17	2.28E-17	1.66E-17	1.17E-17	8.98E-18	
		Female	3.24E-17	2.94E-17	2.51E-17	2.23E-17	1.78E-17	1.31E-17	2.96E-17	2.64E-17	2.02E-17	2.29E-17	1.88E-17	1.34E-17	
	1	Male	9.82E-18	9.33E-18	7.96E-18	1.11E-17	1.06E-17	9.53E-18	1.11E-17	1.07E-17	9.98E-18	1.08E-17	1.03E-17	9.26E-18	
		Female	1.13E-17	1.08E-17	9.61E-18	1.14E-17	1.12E-17	9.90E-18	1.13E-17	1.09E-17	1.03E-17	1.15E-17	1.11E-17	9.96E-18	
	1.5	Male	5.40E-18	5.18E-18	4.80E-18	6.07E-18	5.82E-18	5.48E-18	5.86E-18	5.65E-18	5.63E-18	6.04E-18	5.81E-18	5.30E-18	
		Female	5.92E-18	5.61E-18	5.27E-18	6.20E-18	6.19E-18	5.60E-18	5.96E-18	5.76E-18	5.62E-18	6.21E-18	6.08E-18	5.76E-18	
	3	Male	1.54E-18	1.53E-18	1.47E-18	1.78E-18	1.74E-18	1.71E-18	1.70E-18	1.72E-18	1.67E-18	1.82E-18	1.76E-18	1.67E-18	
		Female	1.67E-18	1.64E-18	1.56E-18	1.83E-18	1.80E-18	1.75E-18	1.73E-18	1.70E-18	1.71E-18	1.83E-18	1.81E-18	1.74E-18	
	Middle torso	0.005	Male	6.12E-17	5.77E-17	3.63E-17	2.86E-17	2.44E-17	1.99E-17	2.05E-17	1.79E-17	1.36E-17	2.61E-17	2.27E-17	1.75E-17
			Female	6.31E-17	6.55E-17	3.31E-17	3.84E-17	3.54E-17	2.59E-17	2.51E-17	2.28E-17	1.81E-17	3.71E-17	3.31E-17	2.50E-17
0.1		Male	6.29E-17	5.71E-17	4.86E-17	3.13E-17	2.49E-17	1.92E-17	7.57E-17	6.73E-17	5.45E-17	2.59E-17	2.08E-17	1.56E-17	
		Female	8.67E-17	8.11E-17	6.89E-17	3.57E-17	2.79E-17	2.08E-17	6.99E-17	6.06E-17	4.73E-17	4.03E-17	3.04E-17	2.48E-17	
0.3		Male	4.42E-17	3.97E-17	3.41E-17	5.20E-17	4.74E-17	4.08E-17	5.31E-17	5.04E-17	4.50E-17	4.81E-17	4.37E-17	3.58E-17	
		Female	6.09E-17	5.66E-17	4.78E-17	5.71E-17	4.97E-17	4.05E-17	5.70E-17	5.46E-17	4.89E-17	5.53E-17	4.79E-17	3.77E-17	
Upper torso	0.005	Male	3.42E-16	3.23E-16	2.98E-16	3.81E-16	3.80E-16	3.45E-16	3.85E-16	3.68E-16	3.34E-16	3.43E-16	3.32E-16	3.01E-16	
		Female	5.20E-16	5.05E-16	4.78E-16	3.80E-16	3.20E-16	2.76E-16	4.64E-16	4.26E-16	3.84E-16	3.42E-16	2.84E-16	2.36E-16	
	0.1	Male	2.30E-16	2.09E-16	1.86E-16	3.15E-16	2.82E-16	2.59E-16	2.89E-16	2.60E-16	2.36E-16	2.69E-16	2.42E-16	2.20E-16	
		Female	3.79E-16	3.45E-16	3.17E-16	2.18E-16	1.87E-16	1.63E-16	2.91E-16	2.60E-16	2.37E-16	1.99E-16	1.73E-16	1.46E-16	
	0.3	Male	1.04E-16	9.66E-17	9.05E-17	1.19E-16	1.09E-16	1.03E-16	1.04E-16	9.62E-17	9.14E-17	1.04E-16	9.69E-17	9.13E-17	
		Female	1.36E-16	1.30E-16	1.24E-16	8.58E-17	7.62E-17	7.02E-17	9.89E-17	9.21E-17	8.64E-17	7.96E-17	7.25E-17	6.50E-17	

Table J.8. ¹³⁷Cs/^{137m}Ba: Lung absorbed dose per source disintegration (unit: Gy s⁻¹ Bq⁻¹).

Level	Distance (m)	Gender	Direction											
			Anterior			Right lateral			Posterior			Left lateral		
			10%ile	MRCP	90%ile	10%ile	MRCP	90%ile	10%ile	MRCP	90%ile	10%ile	MRCP	90%ile
Ground	0.005	Male	9.67E-19	7.98E-19	4.08E-19	2.13E-19	1.67E-19	1.20E-19	5.18E-19	3.90E-19	2.35E-19	2.75E-19	2.27E-19	1.36E-19
		Female	8.72E-19	6.66E-19	4.44E-19	2.51E-19	1.90E-19	1.38E-19	5.94E-19	3.30E-19	2.52E-19	2.61E-19	1.96E-19	1.47E-19
	0.1	Male	1.83E-18	1.42E-18	6.49E-19	4.51E-19	2.95E-19	1.81E-19	1.81E-18	1.12E-18	7.49E-19	7.91E-19	5.08E-19	2.36E-19
		Female	1.87E-18	1.31E-18	7.49E-19	4.17E-19	2.88E-19	2.04E-19	2.20E-18	1.25E-18	7.06E-19	4.92E-19	3.26E-19	2.30E-19
	0.3	Male	3.61E-18	2.67E-18	1.31E-18	2.08E-18	1.29E-18	5.93E-19	4.94E-18	3.57E-18	2.59E-18	2.88E-18	1.94E-18	8.58E-19
		Female	4.65E-18	3.46E-18	1.67E-18	3.06E-18	1.78E-18	6.93E-19	7.49E-18	5.31E-18	3.50E-18	3.20E-18	1.81E-18	7.92E-19
Middle thigh	0.005	Male	2.78E-18	2.44E-18	2.17E-18	1.30E-18	9.79E-19	7.31E-19	3.62E-18	2.71E-18	2.35E-18	1.45E-18	9.86E-19	7.39E-19
		Female	4.64E-18	4.41E-18	3.50E-18	2.53E-18	2.20E-18	1.57E-18	5.62E-18	5.15E-18	3.86E-18	2.46E-18	2.17E-18	1.58E-18
	0.1	Male	9.08E-18	7.48E-18	3.73E-18	5.81E-18	3.85E-18	2.40E-18	1.57E-17	1.07E-17	8.60E-18	1.07E-17	6.22E-18	3.37E-18
		Female	1.31E-17	1.07E-17	5.10E-18	1.47E-17	1.12E-17	4.94E-18	2.77E-17	2.17E-17	1.49E-17	1.43E-17	9.98E-18	4.69E-18
	0.3	Male	1.70E-17	1.35E-17	8.71E-18	1.43E-17	1.17E-17	8.26E-18	2.48E-17	2.06E-17	1.63E-17	1.50E-17	1.24E-17	8.87E-18
		Female	2.66E-17	2.23E-17	1.34E-17	2.11E-17	1.77E-17	1.16E-17	3.48E-17	3.07E-17	2.37E-17	1.97E-17	1.68E-17	1.15E-17
Lower torso	0.005	Male	8.16E-17	7.11E-17	4.70E-17	7.10E-17	6.79E-17	4.22E-17	8.59E-17	8.03E-17	6.17E-17	8.25E-17	7.03E-17	4.88E-17
		Female	8.28E-17	7.71E-17	5.75E-17	9.09E-17	8.14E-17	4.72E-17	1.21E-16	1.13E-16	8.62E-17	9.17E-17	7.50E-17	4.97E-17
	0.1	Male	9.50E-17	7.97E-17	6.11E-17	9.80E-17	8.42E-17	6.30E-17	1.35E-16	1.17E-16	9.32E-17	1.08E-16	9.34E-17	7.04E-17
		Female	1.19E-16	1.03E-16	6.80E-17	1.14E-16	1.06E-16	7.15E-17	1.61E-16	1.44E-16	1.13E-16	1.14E-16	1.02E-16	7.35E-17
	0.3	Male	7.38E-17	6.37E-17	4.54E-17	5.10E-17	4.43E-17	3.49E-17	8.40E-17	7.51E-17	6.66E-17	4.97E-17	4.45E-17	3.43E-17
		Female	7.52E-17	6.83E-17	4.84E-17	5.77E-17	5.28E-17	3.77E-17	9.69E-17	8.93E-17	7.55E-17	5.36E-17	4.82E-17	3.65E-17
	1	Male	1.58E-17	1.49E-17	1.17E-17	9.46E-18	8.68E-18	7.31E-18	1.63E-17	1.51E-17	1.42E-17	9.70E-18	9.04E-18	7.45E-18
		Female	1.52E-17	1.43E-17	1.08E-17	1.08E-17	9.80E-18	7.90E-18	1.76E-17	1.69E-17	1.61E-17	1.04E-17	9.68E-18	7.90E-18
	1.5	Male	7.74E-18	7.40E-18	6.13E-18	4.62E-18	4.29E-18	3.63E-18	7.74E-18	7.29E-18	7.16E-18	4.69E-18	4.41E-18	3.74E-18
		Female	7.53E-18	7.09E-18	5.56E-18	5.16E-18	4.75E-18	4.02E-18	8.52E-18	8.07E-18	7.82E-18	5.07E-18	4.77E-18	3.94E-18
	3	Male	2.09E-18	2.02E-18	1.80E-18	1.25E-18	1.19E-18	1.01E-18	2.12E-18	1.95E-18	1.92E-18	1.26E-18	1.18E-18	1.02E-18
		Female	2.06E-18	2.00E-18	1.58E-18	1.40E-18	1.29E-18	1.13E-18	2.25E-18	2.17E-18	2.12E-18	1.37E-18	1.28E-18	1.10E-18
Middle torso	0.005	Male	9.04E-16	6.79E-16	4.93E-16	1.09E-15	8.32E-16	6.41E-16	1.06E-15	8.99E-16	7.23E-16	1.27E-15	9.92E-16	7.41E-16
		Female	1.14E-15	9.71E-16	5.51E-16	1.56E-15	1.30E-15	9.32E-16	1.51E-15	1.26E-15	9.55E-16	1.65E-15	1.27E-15	9.29E-16
	0.1	Male	3.99E-16	3.25E-16	2.35E-16	3.17E-16	2.67E-16	2.24E-16	4.43E-16	3.87E-16	3.32E-16	3.11E-16	2.77E-16	2.29E-16
		Female	4.41E-16	3.88E-16	2.35E-16	3.85E-16	3.18E-16	2.57E-16	5.60E-16	4.86E-16	4.01E-16	3.78E-16	3.17E-16	2.62E-16
	0.3	Male	1.19E-16	1.07E-16	8.34E-17	7.59E-17	6.85E-17	5.81E-17	1.25E-16	1.14E-16	1.04E-16	7.33E-17	6.64E-17	5.42E-17
		Female	1.22E-16	1.14E-16	7.61E-17	9.09E-17	8.03E-17	6.72E-17	1.47E-16	1.35E-16	1.21E-16	8.69E-17	7.57E-17	6.26E-17
Upper torso	0.005	Male	8.00E-16	6.68E-16	5.56E-16	9.41E-16	7.65E-16	6.40E-16	7.38E-16	6.03E-16	4.90E-16	8.25E-16	6.82E-16	5.66E-16
		Female	9.52E-16	8.21E-16	6.35E-16	3.99E-16	3.05E-16	2.30E-16	8.76E-16	7.42E-16	5.94E-16	3.10E-16	2.49E-16	1.76E-16
	0.1	Male	4.84E-16	4.21E-16	3.61E-16	3.50E-16	2.92E-16	2.59E-16	4.24E-16	3.49E-16	2.98E-16	2.81E-16	2.36E-16	2.07E-16
		Female	4.94E-16	4.43E-16	3.51E-16	1.77E-16	1.38E-16	1.11E-16	4.62E-16	4.00E-16	3.41E-16	1.49E-16	1.18E-16	8.76E-17
	0.3	Male	1.50E-16	1.38E-16	1.23E-16	9.02E-17	7.55E-17	6.48E-17	1.33E-16	1.18E-16	1.08E-16	7.82E-17	6.66E-17	6.00E-17
		Female	1.43E-16	1.34E-16	1.11E-16	6.58E-17	5.34E-17	4.47E-17	1.42E-16	1.28E-16	1.18E-16	5.94E-17	4.99E-17	4.03E-17

Table J.9. ¹³⁷Cs/^{137m}Ba: Small intestine absorbed dose per source disintegration (unit: Gy s⁻¹ Bq⁻¹).

Level	Distance (m)	Gender	Direction											
			Anterior			Right lateral			Posterior			Left lateral		
			10%ile	MRCP	90%ile	10%ile	MRCP	90%ile	10%ile	MRCP	90%ile	10%ile	MRCP	90%ile
Ground	0.005	Male	7.11E-18	5.63E-18	4.38E-18	1.16E-18	1.02E-18	9.44E-19	1.54E-18	1.36E-18	8.59E-19	1.30E-18	1.13E-18	9.42E-19
		Female	1.10E-17	8.26E-18	6.65E-18	4.05E-18	2.95E-18	2.19E-18	5.45E-18	2.69E-18	2.47E-18	3.18E-18	2.20E-18	1.78E-18
	0.1	Male	1.02E-17	8.10E-18	6.02E-18	1.42E-18	1.12E-18	9.80E-19	3.30E-18	2.61E-18	1.78E-18	1.81E-18	1.43E-18	1.15E-18
		Female	1.37E-17	1.03E-17	8.18E-18	2.52E-18	1.75E-18	1.58E-18	8.34E-18	5.70E-18	4.40E-18	3.03E-18	2.13E-18	1.82E-18
	0.3	Male	1.29E-17	1.11E-17	7.54E-18	2.95E-18	2.11E-18	1.61E-18	5.86E-18	4.38E-18	3.44E-18	3.94E-18	2.84E-18	2.06E-18
		Female	1.59E-17	1.31E-17	9.44E-18	3.91E-18	2.95E-18	2.33E-18	1.07E-17	8.20E-18	6.78E-18	5.33E-18	3.64E-18	3.02E-18
Middle thigh	0.005	Male	5.33E-17	4.52E-17	4.42E-17	1.79E-17	1.53E-17	1.18E-17	4.81E-17	3.75E-17	3.30E-17	1.75E-17	1.50E-17	1.19E-17
		Female	1.54E-16	1.33E-16	1.14E-16	5.52E-17	4.54E-17	3.44E-17	1.43E-16	1.21E-16	1.01E-16	5.69E-17	4.73E-17	3.75E-17
	0.1	Male	8.87E-17	7.72E-17	5.74E-17	2.75E-17	2.08E-17	1.71E-17	5.01E-17	4.15E-17	3.47E-17	3.04E-17	2.26E-17	1.82E-17
		Female	1.52E-16	1.32E-16	9.72E-17	5.46E-17	4.39E-17	3.37E-17	1.10E-16	9.44E-17	7.72E-17	5.96E-17	4.63E-17	3.83E-17
	0.3	Male	7.34E-17	6.85E-17	4.46E-17	2.62E-17	2.10E-17	1.72E-17	3.87E-17	3.24E-17	2.73E-17	3.36E-17	2.79E-17	2.07E-17
		Female	9.39E-17	8.39E-17	5.99E-17	3.48E-17	2.76E-17	2.29E-17	6.28E-17	5.40E-17	4.44E-17	4.40E-17	3.60E-17	2.83E-17
Lower torso	0.005	Male	2.72E-15	1.98E-15	7.82E-16	6.58E-16	4.77E-16	2.85E-16	8.36E-16	6.83E-16	5.60E-16	1.01E-15	8.23E-16	4.13E-16
		Female	2.09E-15	1.62E-15	9.17E-16	5.25E-16	4.49E-16	2.14E-16	1.16E-15	9.72E-16	7.55E-16	7.97E-16	7.26E-16	3.87E-16
	0.1	Male	7.00E-16	5.88E-16	3.13E-16	2.44E-16	1.96E-16	1.26E-16	3.43E-16	2.91E-16	2.55E-16	3.40E-16	2.96E-16	1.77E-16
		Female	6.26E-16	5.29E-16	3.48E-16	2.14E-16	1.87E-16	1.04E-16	4.51E-16	3.91E-16	3.25E-16	3.11E-16	2.85E-16	1.76E-16
	0.3	Male	1.60E-16	1.45E-16	9.62E-17	7.31E-17	6.25E-17	4.47E-17	1.01E-16	8.99E-17	8.23E-17	9.24E-17	8.30E-17	5.78E-17
		Female	1.50E-16	1.38E-16	1.01E-16	6.76E-17	6.04E-17	3.98E-17	1.21E-16	1.08E-16	9.48E-17	8.86E-17	8.10E-17	5.73E-17
	1	Male	1.95E-17	1.86E-17	1.44E-17	1.08E-17	9.57E-18	7.60E-18	1.41E-17	1.29E-17	1.25E-17	1.29E-17	1.21E-17	9.61E-18
		Female	1.92E-17	1.79E-17	1.49E-17	1.03E-17	9.41E-18	7.03E-18	1.57E-17	1.46E-17	1.36E-17	1.26E-17	1.18E-17	9.69E-18
	1.5	Male	8.88E-18	8.56E-18	7.02E-18	5.13E-18	4.70E-18	3.75E-18	6.79E-18	6.18E-18	6.08E-18	6.14E-18	5.80E-18	4.69E-18
		Female	8.71E-18	8.34E-18	6.90E-18	4.99E-18	4.54E-18	3.44E-18	7.32E-18	6.76E-18	6.35E-18	6.05E-18	5.66E-18	4.64E-18
	3	Male	2.30E-18	2.19E-18	1.82E-18	1.39E-18	1.29E-18	1.04E-18	1.76E-18	1.67E-18	1.64E-18	1.60E-18	1.53E-18	1.29E-18
		Female	2.31E-18	2.19E-18	1.86E-18	1.33E-18	1.23E-18	9.63E-19	1.88E-18	1.81E-18	1.69E-18	1.60E-18	1.44E-18	1.28E-18
Middle torso	0.005	Male	3.19E-16	2.61E-16	2.09E-16	1.62E-16	1.31E-16	1.06E-16	2.22E-16	1.88E-16	1.52E-16	2.97E-16	2.48E-16	1.98E-16
		Female	2.78E-16	2.59E-16	1.83E-16	1.38E-16	1.18E-16	9.15E-17	2.00E-16	1.71E-16	1.29E-16	2.78E-16	2.50E-16	1.97E-16
	0.1	Male	2.56E-16	2.08E-16	1.59E-16	1.30E-16	1.08E-16	8.55E-17	1.63E-16	1.40E-16	1.14E-16	1.94E-16	1.64E-16	1.35E-16
		Female	2.61E-16	2.31E-16	1.52E-16	1.18E-16	1.00E-16	7.16E-17	1.80E-16	1.54E-16	1.19E-16	2.09E-16	1.84E-16	1.43E-16
	0.3	Male	1.12E-16	9.88E-17	7.79E-17	5.92E-17	5.14E-17	4.02E-17	7.43E-17	6.64E-17	5.83E-17	7.53E-17	6.63E-17	5.29E-17
		Female	1.14E-16	1.05E-16	7.70E-17	5.60E-17	5.00E-17	3.62E-17	8.55E-17	7.63E-17	6.44E-17	7.93E-17	7.10E-17	5.61E-17
Upper torso	0.005	Male	3.84E-17	3.53E-17	2.91E-17	3.49E-17	3.17E-17	2.53E-17	2.75E-17	2.43E-17	1.90E-17	3.80E-17	3.45E-17	2.86E-17
		Female	2.86E-17	2.99E-17	2.06E-17	1.62E-17	1.41E-17	1.03E-17	2.09E-17	2.03E-17	1.54E-17	1.74E-17	1.59E-17	1.19E-17
	0.1	Male	5.66E-17	4.84E-17	3.36E-17	2.03E-17	1.78E-17	1.49E-17	3.65E-17	3.11E-17	2.37E-17	2.16E-17	1.92E-17	1.61E-17
		Female	5.13E-17	4.63E-17	2.39E-17	1.98E-17	1.60E-17	1.01E-17	3.95E-17	3.47E-17	2.51E-17	4.06E-17	3.46E-17	1.98E-17
	0.3	Male	6.11E-17	5.19E-17	3.99E-17	3.16E-17	2.65E-17	1.75E-17	4.05E-17	3.43E-17	2.77E-17	3.96E-17	3.41E-17	2.36E-17
		Female	6.19E-17	5.51E-17	3.83E-17	2.79E-17	2.38E-17	1.55E-17	4.66E-17	4.02E-17	3.17E-17	3.81E-17	3.40E-17	2.47E-17

Table J.10. ¹³⁷Cs/^{137m}Ba: Large intestine absorbed dose per source disintegration (unit: Gy s⁻¹ Bq⁻¹).

Level	Distance (m)	Gender	Direction											
			Anterior			Right lateral			Posterior			Left lateral		
			10%ile	MRCP	90%ile	10%ile	MRCP	90%ile	10%ile	MRCP	90%ile	10%ile	MRCP	90%ile
Ground	0.005	Male	6.34E-18	5.22E-18	3.21E-18	1.20E-18	1.07E-18	8.35E-19	3.05E-18	2.41E-18	1.81E-18	1.17E-18	1.04E-18	7.55E-19
		Female	1.31E-17	9.34E-18	7.52E-18	5.36E-18	3.76E-18	2.99E-18	5.53E-18	2.91E-18	2.80E-18	4.72E-18	3.35E-18	2.68E-18
	0.1	Male	9.28E-18	7.59E-18	4.70E-18	1.44E-18	1.09E-18	8.92E-19	4.52E-18	3.57E-18	2.79E-18	2.20E-18	1.74E-18	1.07E-18
		Female	1.68E-17	1.23E-17	9.68E-18	3.46E-18	2.46E-18	2.10E-18	8.00E-18	5.51E-18	4.57E-18	4.08E-18	2.93E-18	2.31E-18
	0.3	Male	1.21E-17	1.03E-17	6.21E-18	3.52E-18	2.37E-18	1.69E-18	6.30E-18	4.87E-18	4.06E-18	5.61E-18	4.38E-18	2.29E-18
		Female	1.95E-17	1.59E-17	1.12E-17	5.15E-18	3.58E-18	2.94E-18	1.05E-17	7.79E-18	6.62E-18	6.42E-18	4.31E-18	3.57E-18
Middle thigh	0.005	Male	5.19E-17	4.39E-17	3.97E-17	1.79E-17	1.53E-17	1.14E-17	6.01E-17	4.91E-17	4.36E-17	1.86E-17	1.60E-17	1.22E-17
		Female	1.94E-16	1.62E-16	1.39E-16	6.30E-17	5.14E-17	3.93E-17	1.74E-16	1.44E-16	1.22E-16	6.98E-17	5.72E-17	4.57E-17
	0.1	Male	7.14E-17	6.29E-17	4.20E-17	2.65E-17	2.03E-17	1.66E-17	5.74E-17	4.91E-17	4.13E-17	3.56E-17	2.60E-17	1.87E-17
		Female	1.92E-16	1.67E-16	1.17E-16	6.31E-17	4.93E-17	3.95E-17	1.22E-16	1.03E-16	8.58E-17	6.97E-17	5.45E-17	4.53E-17
	0.3	Male	6.40E-17	5.79E-17	3.75E-17	2.94E-17	2.44E-17	1.77E-17	4.28E-17	3.49E-17	3.02E-17	3.56E-17	3.09E-17	2.07E-17
		Female	1.10E-16	1.03E-16	7.17E-17	4.24E-17	3.45E-17	2.83E-17	5.85E-17	5.15E-17	4.23E-17	4.69E-17	3.80E-17	3.13E-17
Lower torso	0.005	Male	1.09E-15	8.88E-16	4.90E-16	1.10E-15	7.80E-16	4.06E-16	5.91E-16	4.01E-16	4.01E-16	9.87E-16	8.22E-16	4.17E-16
		Female	3.03E-15	2.17E-15	1.16E-15	9.52E-16	8.54E-16	3.58E-16	8.70E-16	7.01E-16	5.45E-16	1.04E-15	9.65E-16	4.70E-16
	0.1	Male	5.65E-16	4.71E-16	2.65E-16	3.10E-16	2.57E-16	1.59E-16	3.10E-16	2.65E-16	2.27E-16	3.58E-16	3.16E-16	1.94E-16
		Female	7.45E-16	6.34E-16	4.14E-16	2.92E-16	2.69E-16	1.45E-16	3.62E-16	3.11E-16	2.57E-16	3.09E-16	2.89E-16	1.79E-16
	0.3	Male	1.49E-16	1.35E-16	9.27E-17	8.46E-17	7.42E-17	5.32E-17	1.00E-16	8.98E-17	7.96E-17	9.80E-17	8.89E-17	6.47E-17
		Female	1.70E-16	1.55E-16	1.17E-16	8.02E-17	7.70E-17	4.89E-17	1.05E-16	9.34E-17	8.35E-17	8.22E-17	7.71E-17	5.54E-17
	1	Male	1.90E-17	1.79E-17	1.42E-17	1.17E-17	1.05E-17	8.52E-18	1.43E-17	1.33E-17	1.24E-17	1.32E-17	1.24E-17	1.02E-17
		Female	2.05E-17	1.96E-17	1.61E-17	1.15E-17	1.07E-17	7.95E-18	1.41E-17	1.35E-17	1.23E-17	1.19E-17	1.09E-17	8.87E-18
	1.5	Male	8.70E-18	8.35E-18	7.08E-18	5.61E-18	5.18E-18	4.23E-18	6.78E-18	6.25E-18	6.04E-18	6.30E-18	5.82E-18	4.96E-18
		Female	9.30E-18	9.22E-18	7.62E-18	5.51E-18	5.32E-18	4.00E-18	6.76E-18	6.50E-18	5.87E-18	5.49E-18	5.29E-18	4.36E-18
	3	Male	2.34E-18	2.15E-18	1.87E-18	1.44E-18	1.41E-18	1.14E-18	1.85E-18	1.66E-18	1.63E-18	1.65E-18	1.51E-18	1.36E-18
		Female	2.32E-18	2.34E-18	2.02E-18	1.46E-18	1.39E-18	1.10E-18	1.78E-18	1.68E-18	1.55E-18	1.45E-18	1.44E-18	1.19E-18
Middle torso	0.005	Male	4.51E-16	3.77E-16	3.02E-16	2.51E-16	2.02E-16	1.68E-16	2.23E-16	1.87E-16	1.47E-16	5.45E-16	4.49E-16	3.70E-16
		Female	1.72E-16	1.62E-16	1.25E-16	1.30E-16	1.22E-16	9.82E-17	1.24E-16	1.11E-16	8.28E-17	1.27E-16	1.12E-16	9.28E-17
	0.1	Male	3.20E-16	2.70E-16	2.13E-16	1.90E-16	1.58E-16	1.29E-16	1.64E-16	1.37E-16	1.12E-16	2.79E-16	2.42E-16	2.03E-16
		Female	2.46E-16	2.11E-16	1.37E-16	1.41E-16	1.29E-16	8.93E-17	1.33E-16	1.13E-16	8.77E-17	1.40E-16	1.22E-16	9.29E-17
	0.3	Male	1.17E-16	1.03E-16	8.76E-17	7.24E-17	6.42E-17	5.29E-17	7.48E-17	6.39E-17	5.63E-17	8.62E-17	7.72E-17	6.52E-17
		Female	1.22E-16	1.16E-16	8.10E-17	6.56E-17	6.09E-17	4.29E-17	7.14E-17	6.31E-17	5.27E-17	6.78E-17	6.08E-17	4.59E-17
Upper torso	0.005	Male	5.23E-17	4.71E-17	3.84E-17	4.32E-17	3.84E-17	3.03E-17	3.57E-17	3.11E-17	2.41E-17	4.82E-17	4.44E-17	3.59E-17
		Female	2.04E-17	2.15E-17	1.45E-17	1.19E-17	1.10E-17	7.83E-18	1.38E-17	1.32E-17	1.00E-17	1.11E-17	1.03E-17	7.77E-18
	0.1	Male	7.25E-17	6.43E-17	4.67E-17	2.40E-17	2.14E-17	1.76E-17	4.44E-17	3.70E-17	2.91E-17	2.54E-17	2.29E-17	2.02E-17
		Female	4.51E-17	3.83E-17	1.79E-17	2.75E-17	2.42E-17	1.15E-17	2.88E-17	2.58E-17	1.81E-17	3.39E-17	2.85E-17	1.81E-17
	0.3	Male	6.87E-17	6.10E-17	4.80E-17	4.33E-17	3.52E-17	2.42E-17	4.28E-17	3.52E-17	2.91E-17	5.21E-17	4.55E-17	3.31E-17
		Female	6.58E-17	5.91E-17	3.86E-17	3.28E-17	2.96E-17	1.96E-17	3.71E-17	3.17E-17	2.50E-17	3.22E-17	2.86E-17	2.03E-17

Table J.11. ⁶⁰Co: RBM absorbed dose per source disintegration (unit: Gy s⁻¹ Bq⁻¹).

Level	Distance (m)	Gender	Direction											
			Anterior			Right lateral			Posterior			Left lateral		
			10%ile	MRCP	90%ile	10%ile	MRCP	90%ile	10%ile	MRCP	90%ile	10%ile	MRCP	90%ile
Ground	0.005	Male	1.85E-17	1.49E-17	1.09E-17	7.53E-18	6.08E-18	4.54E-18	1.40E-17	1.14E-17	7.92E-18	8.09E-18	6.60E-18	4.82E-18
		Female	2.77E-17	2.06E-17	1.61E-17	1.30E-17	9.01E-18	7.59E-18	1.64E-17	9.88E-18	8.74E-18	1.36E-17	9.49E-18	7.73E-18
	0.1	Male	2.58E-17	2.04E-17	1.43E-17	1.08E-17	8.36E-18	5.78E-18	2.72E-17	2.11E-17	1.54E-17	1.20E-17	9.39E-18	6.46E-18
		Female	3.52E-17	2.66E-17	2.01E-17	1.38E-17	9.54E-18	7.59E-18	3.15E-17	2.15E-17	1.64E-17	1.54E-17	1.08E-17	8.44E-18
	0.3	Male	3.37E-17	2.69E-17	1.97E-17	1.88E-17	1.46E-17	9.67E-18	3.90E-17	3.10E-17	2.48E-17	1.89E-17	1.50E-17	1.02E-17
		Female	4.30E-17	3.38E-17	2.53E-17	2.39E-17	1.74E-17	1.19E-17	4.60E-17	3.57E-17	2.80E-17	2.48E-17	1.82E-17	1.31E-17
Middle thigh	0.005	Male	2.67E-16	2.39E-16	1.97E-16	1.71E-16	1.48E-16	1.11E-16	2.78E-16	2.50E-16	2.10E-16	1.70E-16	1.49E-16	1.13E-16
		Female	4.71E-16	3.90E-16	3.20E-16	2.70E-16	2.21E-16	1.72E-16	4.54E-16	3.77E-16	3.11E-16	2.81E-16	2.30E-16	1.85E-16
	0.1	Male	2.70E-16	2.24E-16	1.79E-16	1.81E-16	1.49E-16	1.11E-16	3.00E-16	2.51E-16	2.09E-16	1.78E-16	1.53E-16	1.12E-16
		Female	3.90E-16	3.28E-16	2.55E-16	2.49E-16	2.05E-16	1.54E-16	3.94E-16	3.32E-16	2.65E-16	2.50E-16	2.04E-16	1.60E-16
	0.3	Male	1.83E-16	1.61E-16	1.22E-16	1.16E-16	9.87E-17	7.75E-17	2.02E-16	1.81E-16	1.54E-16	1.16E-16	9.92E-17	7.70E-17
		Female	2.26E-16	2.00E-16	1.50E-16	1.47E-16	1.26E-16	9.75E-17	2.34E-16	2.08E-16	1.72E-16	1.46E-16	1.24E-16	9.83E-17
Lower torso	0.005	Male	1.63E-15	1.25E-15	6.44E-16	1.46E-15	1.14E-15	6.61E-16	3.82E-15	3.24E-15	2.71E-15	1.37E-15	1.15E-15	6.23E-16
		Female	1.94E-15	1.50E-15	9.35E-16	1.53E-15	1.36E-15	6.73E-16	3.94E-15	3.39E-15	2.59E-15	1.43E-15	1.28E-15	7.19E-16
	0.1	Male	8.15E-16	6.81E-16	4.02E-16	7.17E-16	5.97E-16	4.03E-16	1.41E-15	1.26E-15	1.11E-15	6.92E-16	5.99E-16	3.89E-16
		Female	9.44E-16	7.98E-16	5.25E-16	7.50E-16	6.76E-16	4.10E-16	1.46E-15	1.32E-15	1.09E-15	7.11E-16	6.42E-16	4.26E-16
	0.3	Male	3.28E-16	2.91E-16	1.98E-16	2.57E-16	2.23E-16	1.73E-16	4.42E-16	4.10E-16	3.76E-16	2.42E-16	2.12E-16	1.55E-16
		Female	3.54E-16	3.18E-16	2.31E-16	2.67E-16	2.45E-16	1.74E-16	4.51E-16	4.21E-16	3.72E-16	2.54E-16	2.31E-16	1.73E-16
	1	Male	5.78E-17	5.45E-17	4.38E-17	4.34E-17	3.94E-17	3.38E-17	6.72E-17	6.46E-17	6.18E-17	4.28E-17	3.94E-17	3.29E-17
		Female	6.06E-17	5.70E-17	4.71E-17	4.56E-17	4.23E-17	3.50E-17	6.84E-17	6.56E-17	6.16E-17	4.51E-17	4.18E-17	3.54E-17
	1.5	Male	2.82E-17	2.69E-17	2.24E-17	2.12E-17	1.96E-17	1.71E-17	3.21E-17	3.10E-17	2.99E-17	2.10E-17	1.95E-17	1.67E-17
		Female	2.94E-17	2.81E-17	2.37E-17	2.24E-17	2.07E-17	1.78E-17	3.25E-17	3.13E-17	2.99E-17	2.21E-17	2.06E-17	1.80E-17
	3	Male	7.69E-18	7.37E-18	6.40E-18	5.79E-18	5.36E-18	4.82E-18	8.52E-18	8.21E-18	8.05E-18	5.76E-18	5.35E-18	4.76E-18
		Female	7.93E-18	7.67E-18	6.72E-18	6.12E-18	5.72E-18	5.04E-18	8.61E-18	8.29E-18	7.99E-18	6.06E-18	5.70E-18	5.09E-18
Middle torso	0.005	Male	1.84E-15	1.35E-15	9.32E-16	2.17E-15	1.62E-15	1.24E-15	3.64E-15	3.10E-15	2.52E-15	1.83E-15	1.45E-15	1.09E-15
		Female	2.50E-15	2.17E-15	1.07E-15	2.90E-15	2.41E-15	1.59E-15	4.92E-15	4.10E-15	2.88E-15	2.63E-15	2.05E-15	1.50E-15
	0.1	Male	7.94E-16	6.53E-16	4.90E-16	7.34E-16	6.30E-16	5.05E-16	1.27E-15	1.14E-15	9.89E-16	6.70E-16	5.83E-16	4.64E-16
		Female	9.87E-16	8.77E-16	5.58E-16	8.61E-16	7.38E-16	5.68E-16	1.45E-15	1.30E-15	1.06E-15	8.44E-16	7.20E-16	5.72E-16
	0.3	Male	3.20E-16	2.83E-16	2.23E-16	2.61E-16	2.30E-16	1.91E-16	4.24E-16	3.93E-16	3.59E-16	2.40E-16	2.10E-16	1.68E-16
		Female	3.77E-16	3.48E-16	2.51E-16	2.94E-16	2.64E-16	2.13E-16	4.58E-16	4.26E-16	3.75E-16	2.87E-16	2.53E-16	2.05E-16
Upper torso	0.005	Male	2.23E-15	1.85E-15	1.55E-15	2.38E-15	1.85E-15	1.54E-15	2.57E-15	1.96E-15	1.60E-15	2.30E-15	1.87E-15	1.54E-15
		Female	2.83E-15	2.43E-15	2.00E-15	2.16E-15	1.47E-15	1.07E-15	3.13E-15	2.45E-15	1.97E-15	1.53E-15	1.14E-15	7.56E-16
	0.1	Male	9.68E-16	8.50E-16	7.38E-16	1.13E-15	1.11E-15	9.89E-16	1.05E-15	8.98E-16	7.71E-16	1.18E-15	1.01E-15	9.25E-16
		Female	1.14E-15	1.04E-15	8.72E-16	5.84E-16	4.70E-16	3.76E-16	1.15E-15	1.00E-15	8.51E-16	4.88E-16	4.03E-16	3.06E-16
	0.3	Male	3.30E-16	2.99E-16	2.61E-16	2.90E-16	2.54E-16	2.22E-16	3.90E-16	3.52E-16	3.17E-16	2.50E-16	2.20E-16	1.99E-16
		Female	3.75E-16	3.49E-16	2.91E-16	2.23E-16	1.91E-16	1.55E-16	3.99E-16	3.68E-16	3.27E-16	2.05E-16	1.79E-16	1.42E-16

Table J.12. ⁶⁰Co: Brain absorbed dose per source disintegration (unit: Gy s⁻¹ Bq⁻¹).

Level	Distance (m)	Gender	Direction											
			Anterior			Right lateral			Posterior			Left lateral		
			10%ile	MRCP	90%ile	10%ile	MRCP	90%ile	10%ile	MRCP	90%ile	10%ile	MRCP	90%ile
Ground	0.005	Male	2.11E-18	1.28E-18	5.71E-19	2.91E-19	2.17E-19	1.50E-19	7.77E-19	5.50E-19	3.34E-19	3.38E-19	2.68E-19	1.57E-19
		Female	7.25E-18	4.29E-18	9.30E-19	4.26E-19	2.94E-19	2.02E-19	8.57E-19	5.05E-19	3.59E-19	4.46E-19	3.28E-19	2.11E-19
	0.1	Male	5.59E-18	3.30E-18	9.99E-19	6.50E-19	4.57E-19	2.72E-19	2.82E-18	1.61E-18	9.65E-19	8.39E-19	5.54E-19	3.08E-19
		Female	1.40E-17	1.01E-17	3.14E-18	9.49E-19	5.59E-19	3.24E-19	2.68E-18	1.48E-18	8.57E-19	1.19E-18	6.06E-19	3.82E-19
	0.3	Male	1.42E-17	9.77E-18	5.64E-18	5.89E-18	2.98E-18	1.01E-18	1.04E-17	6.87E-18	4.16E-18	5.43E-18	3.37E-18	1.36E-18
		Female	2.30E-17	1.81E-17	1.03E-17	1.14E-17	6.40E-18	1.46E-18	9.87E-18	6.21E-18	4.17E-18	1.10E-17	6.19E-18	1.98E-18
Middle thigh	0.005	Male	1.80E-18	1.86E-18	1.52E-18	1.48E-18	1.07E-18	8.09E-19	2.11E-18	2.14E-18	1.67E-18	1.39E-18	9.09E-19	6.74E-19
		Female	5.25E-18	4.66E-18	2.86E-18	2.87E-18	2.50E-18	1.67E-18	4.33E-18	3.76E-18	2.64E-18	2.56E-18	2.21E-18	1.56E-18
	0.1	Male	1.53E-17	8.86E-18	3.14E-18	9.21E-18	5.20E-18	2.98E-18	1.60E-17	9.63E-18	6.95E-18	1.25E-17	6.13E-18	3.43E-18
		Female	4.46E-17	3.63E-17	1.15E-17	2.66E-17	2.05E-17	6.21E-18	1.98E-17	1.59E-17	1.06E-17	2.37E-17	1.57E-17	6.02E-18
	0.3	Male	4.63E-17	3.93E-17	2.79E-17	2.28E-17	1.83E-17	1.23E-17	4.47E-17	3.34E-17	2.48E-17	1.89E-17	1.52E-17	1.09E-17
		Female	6.82E-17	6.35E-17	4.47E-17	3.97E-17	3.36E-17	1.98E-17	4.57E-17	3.59E-17	2.58E-17	4.00E-17	3.38E-17	2.02E-17
Lower torso	0.005	Male	2.85E-17	2.47E-17	1.96E-17	3.62E-17	3.63E-17	2.31E-17	2.22E-17	2.10E-17	1.47E-17	3.50E-17	2.67E-17	2.16E-17
		Female	7.42E-17	6.35E-17	2.86E-17	5.41E-17	4.98E-17	2.94E-17	3.58E-17	3.22E-17	2.38E-17	5.19E-17	4.08E-17	2.85E-17
	0.1	Male	1.22E-16	1.05E-16	8.85E-17	7.24E-17	5.80E-17	4.86E-17	8.93E-17	6.71E-17	4.33E-17	6.10E-17	5.15E-17	4.25E-17
		Female	1.68E-16	1.57E-16	1.03E-16	1.00E-16	8.79E-17	5.60E-17	7.81E-17	6.24E-17	4.45E-17	9.91E-17	8.92E-17	5.84E-17
	0.3	Male	1.14E-16	1.08E-16	8.70E-17	9.23E-17	7.29E-17	5.62E-17	1.34E-16	1.24E-16	1.03E-16	8.04E-17	6.21E-17	4.89E-17
		Female	1.42E-16	1.34E-16	1.14E-16	1.06E-16	8.79E-17	6.59E-17	1.31E-16	1.18E-16	9.37E-17	1.07E-16	8.96E-17	6.75E-17
	1	Male	4.26E-17	4.14E-17	3.60E-17	4.63E-17	4.43E-17	4.03E-17	4.71E-17	4.58E-17	4.28E-17	4.58E-17	4.40E-17	3.93E-17
		Female	4.82E-17	4.62E-17	4.23E-17	4.79E-17	4.69E-17	4.20E-17	4.87E-17	4.76E-17	4.44E-17	4.79E-17	4.71E-17	4.21E-17
	1.5	Male	2.37E-17	2.30E-17	2.05E-17	2.54E-17	2.45E-17	2.28E-17	2.51E-17	2.48E-17	2.37E-17	2.50E-17	2.43E-17	2.27E-17
		Female	2.55E-17	2.50E-17	2.32E-17	2.61E-17	2.54E-17	2.36E-17	2.55E-17	2.53E-17	2.40E-17	2.57E-17	2.56E-17	2.37E-17
	3	Male	6.92E-18	6.75E-18	6.45E-18	7.55E-18	7.42E-18	7.10E-18	7.35E-18	7.27E-18	7.08E-18	7.46E-18	7.41E-18	7.15E-18
		Female	7.20E-18	7.11E-18	6.85E-18	7.59E-18	7.60E-18	7.26E-18	7.33E-18	7.28E-18	7.13E-18	7.62E-18	7.53E-18	7.31E-18
Middle torso	0.005	Male	3.00E-16	2.72E-16	1.85E-16	1.64E-16	1.41E-16	1.16E-16	1.25E-16	1.08E-16	8.56E-17	1.53E-16	1.33E-16	1.03E-16
		Female	3.25E-16	3.28E-16	1.84E-16	2.18E-16	1.95E-16	1.50E-16	1.50E-16	1.37E-16	1.13E-16	2.07E-16	1.84E-16	1.47E-16
	0.1	Male	2.95E-16	2.68E-16	2.31E-16	1.70E-16	1.36E-16	1.12E-16	3.40E-16	3.03E-16	2.51E-16	1.48E-16	1.26E-16	9.56E-17
		Female	3.96E-16	3.68E-16	3.19E-16	1.94E-16	1.55E-16	1.22E-16	3.25E-16	2.84E-16	2.29E-16	2.10E-16	1.68E-16	1.43E-16
	0.3	Male	1.99E-16	1.83E-16	1.56E-16	2.20E-16	2.03E-16	1.76E-16	2.28E-16	2.15E-16	1.93E-16	2.10E-16	1.90E-16	1.59E-16
		Female	2.67E-16	2.49E-16	2.11E-16	2.42E-16	2.19E-16	1.81E-16	2.45E-16	2.34E-16	2.10E-16	2.38E-16	2.11E-16	1.72E-16
Upper torso	0.005	Male	1.59E-15	1.49E-15	1.37E-15	1.70E-15	1.66E-15	1.53E-15	1.72E-15	1.62E-15	1.48E-15	1.55E-15	1.48E-15	1.33E-15
		Female	2.34E-15	2.26E-15	2.14E-15	1.58E-15	1.33E-15	1.14E-15	2.02E-15	1.84E-15	1.66E-15	1.43E-15	1.20E-15	9.91E-16
	0.1	Male	1.07E-15	9.83E-16	8.87E-16	1.33E-15	1.18E-15	1.09E-15	1.24E-15	1.12E-15	1.02E-15	1.15E-15	1.03E-15	9.36E-16
		Female	1.69E-15	1.55E-15	1.44E-15	9.05E-16	7.71E-16	6.79E-16	1.23E-15	1.10E-15	9.98E-16	8.30E-16	7.24E-16	6.15E-16
	0.3	Male	4.55E-16	4.28E-16	4.03E-16	4.98E-16	4.53E-16	4.31E-16	4.47E-16	4.15E-16	3.90E-16	4.40E-16	4.06E-16	3.81E-16
		Female	5.84E-16	5.60E-16	5.38E-16	3.59E-16	3.20E-16	2.89E-16	4.19E-16	3.91E-16	3.67E-16	3.33E-16	3.03E-16	2.70E-16

Table J.13. ⁶⁰Co: Lung absorbed dose per source disintegration (unit: Gy s⁻¹ Bq⁻¹).

Level	Distance (m)	Gender	Direction											
			Anterior			Right lateral			Posterior			Left lateral		
			10%ile	MRCP	90%ile	10%ile	MRCP	90%ile	10%ile	MRCP	90%ile	10%ile	MRCP	90%ile
Ground	0.005	Male	6.89E-18	5.57E-18	3.48E-18	1.47E-18	1.22E-18	8.66E-19	3.67E-18	2.88E-18	1.74E-18	1.77E-18	1.54E-18	9.86E-19
		Female	6.86E-18	5.25E-18	3.88E-18	2.04E-18	1.56E-18	1.16E-18	4.79E-18	2.78E-18	2.18E-18	2.12E-18	1.57E-18	1.25E-18
	0.1	Male	1.16E-17	9.14E-18	5.18E-18	2.85E-18	2.03E-18	1.31E-18	1.03E-17	6.69E-18	4.60E-18	4.44E-18	3.07E-18	1.66E-18
		Female	1.20E-17	9.22E-18	5.77E-18	3.13E-18	2.17E-18	1.58E-18	1.30E-17	8.10E-18	5.25E-18	3.65E-18	2.60E-18	1.88E-18
	0.3	Male	1.90E-17	1.50E-17	8.14E-18	1.15E-17	7.28E-18	3.82E-18	2.42E-17	1.81E-17	1.37E-17	1.52E-17	1.06E-17	5.35E-18
		Female	2.47E-17	1.86E-17	1.02E-17	1.65E-17	1.03E-17	4.87E-18	3.48E-17	2.58E-17	1.82E-17	1.66E-17	1.04E-17	5.45E-18
Middle thigh	0.005	Male	2.03E-17	2.00E-17	1.77E-17	1.12E-17	9.28E-18	6.96E-18	2.35E-17	2.21E-17	1.87E-17	1.20E-17	9.44E-18	7.23E-18
		Female	3.69E-17	3.46E-17	2.75E-17	2.07E-17	1.83E-17	1.39E-17	4.08E-17	3.70E-17	2.88E-17	2.10E-17	1.88E-17	1.42E-17
	0.1	Male	5.47E-17	4.72E-17	2.66E-17	3.73E-17	2.53E-17	1.71E-17	8.20E-17	5.80E-17	4.72E-17	5.64E-17	3.60E-17	2.23E-17
		Female	7.31E-17	6.42E-17	3.44E-17	8.07E-17	6.18E-17	3.22E-17	1.34E-16	1.10E-16	7.79E-17	7.59E-17	5.59E-17	3.02E-17
	0.3	Male	8.34E-17	6.97E-17	4.76E-17	7.08E-17	5.98E-17	4.33E-17	1.09E-16	9.32E-17	7.66E-17	7.42E-17	6.21E-17	4.55E-17
		Female	1.22E-16	1.04E-16	6.86E-17	9.71E-17	8.71E-17	5.84E-17	1.49E-16	1.34E-16	1.06E-16	9.40E-17	8.15E-17	5.88E-17
Lower torso	0.005	Male	4.17E-16	3.68E-16	2.51E-16	3.59E-16	3.40E-16	2.19E-16	4.37E-16	4.10E-16	3.21E-16	4.14E-16	3.54E-16	2.49E-16
		Female	4.37E-16	3.99E-16	3.00E-16	4.43E-16	4.00E-16	2.43E-16	5.84E-16	5.46E-16	4.23E-16	4.43E-16	3.80E-16	2.53E-16
	0.1	Male	4.56E-16	3.77E-16	2.93E-16	4.38E-16	3.82E-16	2.89E-16	5.89E-16	5.19E-16	4.21E-16	4.77E-16	4.21E-16	3.15E-16
		Female	5.28E-16	4.61E-16	3.18E-16	5.05E-16	4.64E-16	3.23E-16	6.90E-16	6.23E-16	4.92E-16	4.97E-16	4.54E-16	3.28E-16
	0.3	Male	3.10E-16	2.75E-16	1.99E-16	2.27E-16	2.03E-16	1.61E-16	3.49E-16	3.11E-16	2.81E-16	2.26E-16	2.05E-16	1.57E-16
		Female	3.14E-16	2.88E-16	2.13E-16	2.54E-16	2.34E-16	1.72E-16	3.92E-16	3.67E-16	3.13E-16	2.40E-16	2.18E-16	1.66E-16
	1	Male	6.39E-17	5.99E-17	4.92E-17	4.28E-17	3.96E-17	3.40E-17	6.51E-17	6.19E-17	5.96E-17	4.33E-17	4.15E-17	3.43E-17
		Female	6.25E-17	5.95E-17	4.65E-17	4.68E-17	4.40E-17	3.65E-17	7.12E-17	6.78E-17	6.47E-17	4.63E-17	4.32E-17	3.65E-17
	1.5	Male	3.15E-17	3.00E-17	2.57E-17	2.11E-17	1.94E-17	1.70E-17	3.15E-17	3.04E-17	2.92E-17	2.13E-17	2.03E-17	1.72E-17
		Female	3.06E-17	2.92E-17	2.34E-17	2.31E-17	2.13E-17	1.83E-17	3.41E-17	3.32E-17	3.14E-17	2.28E-17	2.14E-17	1.86E-17
	3	Male	8.57E-18	8.34E-18	7.40E-18	5.77E-18	5.48E-18	4.75E-18	8.44E-18	8.08E-18	7.91E-18	5.85E-18	5.50E-18	4.80E-18
		Female	8.40E-18	8.26E-18	6.69E-18	6.21E-18	5.86E-18	5.22E-18	8.99E-18	8.81E-18	8.47E-18	6.17E-18	5.79E-18	5.24E-18
Middle torso	0.005	Male	3.75E-15	2.88E-15	2.08E-15	4.43E-15	3.43E-15	2.63E-15	4.42E-15	3.74E-15	3.02E-15	5.17E-15	4.04E-15	3.03E-15
		Female	4.75E-15	4.00E-15	2.29E-15	6.34E-15	5.24E-15	3.76E-15	6.22E-15	5.16E-15	3.95E-15	6.67E-15	5.15E-15	3.76E-15
	0.1	Male	1.63E-15	1.34E-15	9.92E-16	1.33E-15	1.14E-15	9.61E-16	1.81E-15	1.58E-15	1.37E-15	1.34E-15	1.17E-15	9.70E-16
		Female	1.82E-15	1.60E-15	1.01E-15	1.61E-15	1.36E-15	1.11E-15	2.27E-15	1.98E-15	1.64E-15	1.60E-15	1.35E-15	1.12E-15
	0.3	Male	4.81E-16	4.29E-16	3.51E-16	3.38E-16	3.05E-16	2.64E-16	5.08E-16	4.63E-16	4.27E-16	3.26E-16	2.99E-16	2.48E-16
		Female	5.01E-16	4.65E-16	3.23E-16	3.91E-16	3.48E-16	3.01E-16	5.84E-16	5.41E-16	4.84E-16	3.81E-16	3.36E-16	2.85E-16
Upper torso	0.005	Male	3.32E-15	2.80E-15	2.32E-15	3.89E-15	3.20E-15	2.65E-15	3.13E-15	2.57E-15	2.10E-15	3.45E-15	2.87E-15	2.36E-15
		Female	3.89E-15	3.36E-15	2.62E-15	1.81E-15	1.39E-15	1.06E-15	3.70E-15	3.13E-15	2.53E-15	1.43E-15	1.16E-15	8.30E-16
	0.1	Male	1.93E-15	1.69E-15	1.44E-15	1.61E-15	1.33E-15	1.17E-15	1.75E-15	1.47E-15	1.26E-15	1.30E-15	1.10E-15	9.62E-16
		Female	1.98E-15	1.79E-15	1.45E-15	8.27E-16	6.56E-16	5.32E-16	1.90E-15	1.64E-15	1.42E-15	6.97E-16	5.67E-16	4.28E-16
	0.3	Male	5.90E-16	5.43E-16	4.92E-16	4.10E-16	3.52E-16	3.10E-16	5.50E-16	4.88E-16	4.45E-16	3.69E-16	3.18E-16	2.84E-16
		Female	5.74E-16	5.44E-16	4.57E-16	2.96E-16	2.48E-16	2.08E-16	5.72E-16	5.24E-16	4.82E-16	2.70E-16	2.32E-16	1.88E-16

Table J.14. ⁶⁰Co: Small intestine absorbed dose per source disintegration (unit: Gy s⁻¹ Bq⁻¹).

Level	Distance (m)	Gender	Direction											
			Anterior			Right lateral			Posterior			Left lateral		
			10%ile	MRCP	90%ile	10%ile	MRCP	90%ile	10%ile	MRCP	90%ile	10%ile	MRCP	90%ile
Ground	0.005	Male	3.81E-17	3.00E-17	2.39E-17	8.35E-18	7.19E-18	5.90E-18	9.53E-18	8.26E-18	5.37E-18	9.34E-18	7.73E-18	6.09E-18
		Female	5.56E-17	4.29E-17	3.54E-17	2.39E-17	1.79E-17	1.31E-17	2.93E-17	1.56E-17	1.38E-17	1.93E-17	1.38E-17	1.08E-17
	0.1	Male	4.89E-17	3.99E-17	3.10E-17	1.03E-17	7.94E-18	6.41E-18	1.99E-17	1.62E-17	1.12E-17	1.24E-17	9.86E-18	7.50E-18
		Female	6.54E-17	5.05E-17	4.14E-17	1.62E-17	1.18E-17	1.01E-17	4.38E-17	3.07E-17	2.46E-17	2.02E-17	1.41E-17	1.16E-17
	0.3	Male	5.60E-17	4.90E-17	3.58E-17	1.77E-17	1.31E-17	9.90E-18	3.05E-17	2.38E-17	1.91E-17	2.26E-17	1.67E-17	1.21E-17
		Female	6.94E-17	5.78E-17	4.38E-17	2.41E-17	1.78E-17	1.41E-17	5.25E-17	4.16E-17	3.47E-17	3.08E-17	2.21E-17	1.76E-17
Middle thigh	0.005	Male	2.46E-16	2.33E-16	2.16E-16	1.15E-16	9.83E-17	7.57E-17	2.18E-16	1.98E-16	1.72E-16	1.13E-16	9.77E-17	7.73E-17
		Female	6.93E-16	6.02E-16	5.09E-16	3.00E-16	2.47E-16	1.88E-16	6.43E-16	5.45E-16	4.55E-16	3.10E-16	2.59E-16	2.05E-16
	0.1	Male	3.88E-16	3.42E-16	2.61E-16	1.52E-16	1.19E-16	9.62E-17	2.38E-16	2.04E-16	1.71E-16	1.66E-16	1.29E-16	1.03E-16
		Female	6.57E-16	5.66E-16	4.28E-16	2.79E-16	2.27E-16	1.75E-16	4.91E-16	4.26E-16	3.46E-16	3.04E-16	2.43E-16	1.98E-16
	0.3	Male	3.04E-16	2.78E-16	1.95E-16	1.29E-16	1.06E-16	8.75E-17	1.76E-16	1.51E-16	1.28E-16	1.58E-16	1.35E-16	1.03E-16
		Female	3.80E-16	3.49E-16	2.59E-16	1.68E-16	1.39E-16	1.14E-16	2.71E-16	2.37E-16	1.96E-16	2.07E-16	1.73E-16	1.39E-16
Lower torso	0.005	Male	1.10E-14	8.08E-15	3.25E-15	2.84E-15	2.08E-15	1.25E-15	3.54E-15	2.90E-15	2.38E-15	4.24E-15	3.48E-15	1.78E-15
		Female	8.56E-15	6.68E-15	3.80E-15	2.28E-15	1.97E-15	9.71E-16	4.87E-15	4.07E-15	3.15E-15	3.42E-15	3.10E-15	1.69E-15
	0.1	Male	2.80E-15	2.36E-15	1.29E-15	1.04E-15	8.45E-16	5.66E-16	1.44E-15	1.24E-15	1.08E-15	1.42E-15	1.24E-15	7.65E-16
		Female	2.51E-15	2.14E-15	1.43E-15	9.43E-16	8.29E-16	4.81E-16	1.86E-15	1.62E-15	1.34E-15	1.31E-15	1.20E-15	7.59E-16
	0.3	Male	6.36E-16	5.85E-16	3.96E-16	3.17E-16	2.74E-16	2.03E-16	4.21E-16	3.86E-16	3.48E-16	3.91E-16	3.55E-16	2.52E-16
		Female	6.01E-16	5.49E-16	4.18E-16	3.02E-16	2.74E-16	1.85E-16	4.93E-16	4.52E-16	3.98E-16	3.75E-16	3.48E-16	2.55E-16
	1	Male	7.57E-17	7.31E-17	5.90E-17	4.73E-17	4.38E-17	3.53E-17	5.86E-17	5.55E-17	5.22E-17	5.53E-17	5.23E-17	4.23E-17
		Female	7.33E-17	7.08E-17	5.96E-17	4.63E-17	4.28E-17	3.28E-17	6.41E-17	6.09E-17	5.63E-17	5.43E-17	5.10E-17	4.22E-17
	1.5	Male	3.53E-17	3.39E-17	2.84E-17	2.30E-17	2.11E-17	1.75E-17	2.80E-17	2.65E-17	2.52E-17	2.65E-17	2.49E-17	2.08E-17
		Female	3.43E-17	3.37E-17	2.86E-17	2.24E-17	2.08E-17	1.62E-17	3.02E-17	2.85E-17	2.70E-17	2.57E-17	2.43E-17	2.09E-17
	3	Male	9.03E-18	8.78E-18	7.61E-18	6.16E-18	5.82E-18	4.87E-18	7.61E-18	7.13E-18	6.73E-18	6.99E-18	6.69E-18	5.78E-18
		Female	9.04E-18	8.79E-18	7.67E-18	6.05E-18	5.70E-18	4.67E-18	7.93E-18	7.58E-18	7.19E-18	6.88E-18	6.59E-18	5.77E-18
Middle torso	0.005	Male	1.42E-15	1.19E-15	9.34E-16	7.61E-16	6.24E-16	4.97E-16	1.02E-15	8.66E-16	7.00E-16	1.33E-15	1.10E-15	8.82E-16
		Female	1.27E-15	1.18E-15	8.32E-16	6.70E-16	5.82E-16	4.48E-16	9.31E-16	8.07E-16	6.02E-16	1.27E-15	1.13E-15	8.85E-16
	0.1	Male	1.08E-15	8.97E-16	6.94E-16	5.81E-16	4.84E-16	3.91E-16	7.19E-16	6.11E-16	5.11E-16	8.40E-16	7.20E-16	5.87E-16
		Female	1.09E-15	9.76E-16	6.58E-16	5.43E-16	4.69E-16	3.42E-16	7.74E-16	6.75E-16	5.28E-16	8.83E-16	7.85E-16	6.15E-16
	0.3	Male	4.53E-16	4.03E-16	3.23E-16	2.59E-16	2.29E-16	1.86E-16	3.15E-16	2.82E-16	2.47E-16	3.20E-16	2.84E-16	2.37E-16
		Female	4.64E-16	4.28E-16	3.22E-16	2.55E-16	2.28E-16	1.71E-16	3.54E-16	3.20E-16	2.72E-16	3.38E-16	3.07E-16	2.48E-16
Upper torso	0.005	Male	2.08E-16	1.92E-16	1.52E-16	1.89E-16	1.68E-16	1.37E-16	1.56E-16	1.39E-16	1.08E-16	1.99E-16	1.86E-16	1.50E-16
		Female	1.66E-16	1.63E-16	1.13E-16	1.04E-16	8.96E-17	6.73E-17	1.24E-16	1.21E-16	9.31E-17	1.08E-16	1.02E-16	7.56E-17
	0.1	Male	2.73E-16	2.36E-16	1.73E-16	1.25E-16	1.09E-16	9.03E-17	1.88E-16	1.63E-16	1.29E-16	1.28E-16	1.16E-16	9.65E-17
		Female	2.55E-16	2.34E-16	1.34E-16	1.10E-16	9.49E-17	6.15E-17	2.01E-16	1.78E-16	1.31E-16	2.05E-16	1.76E-16	1.06E-16
	0.3	Male	2.65E-16	2.27E-16	1.81E-16	1.56E-16	1.30E-16	9.06E-17	1.84E-16	1.58E-16	1.32E-16	1.89E-16	1.62E-16	1.19E-16
		Female	2.62E-16	2.43E-16	1.75E-16	1.32E-16	1.15E-16	8.10E-17	2.01E-16	1.79E-16	1.42E-16	1.73E-16	1.53E-16	1.15E-16

Table J.15. ⁶⁰Co: Large intestine absorbed dose per source disintegration (unit: Gy s⁻¹ Bq⁻¹).

Level	Distance (m)	Gender	Direction											
			Anterior			Right lateral			Posterior			Left lateral		
			10%ile	MRCP	90%ile	10%ile	MRCP	90%ile	10%ile	MRCP	90%ile	10%ile	MRCP	90%ile
Ground	0.005	Male	3.37E-17	2.78E-17	1.85E-17	8.70E-18	7.56E-18	5.60E-18	1.48E-17	1.22E-17	9.12E-18	8.36E-18	7.16E-18	5.18E-18
		Female	6.38E-17	4.79E-17	3.92E-17	3.14E-17	2.26E-17	1.81E-17	2.71E-17	1.54E-17	1.44E-17	2.82E-17	2.08E-17	1.62E-17
	0.1	Male	4.64E-17	3.85E-17	2.54E-17	1.01E-17	8.02E-18	6.05E-18	2.30E-17	1.87E-17	1.45E-17	1.43E-17	1.08E-17	7.11E-18
		Female	7.73E-17	5.95E-17	4.71E-17	2.20E-17	1.64E-17	1.31E-17	4.02E-17	2.83E-17	2.36E-17	2.61E-17	1.89E-17	1.45E-17
	0.3	Male	5.47E-17	4.56E-17	3.01E-17	2.01E-17	1.49E-17	1.05E-17	3.11E-17	2.45E-17	2.05E-17	2.86E-17	2.31E-17	1.35E-17
		Female	8.22E-17	6.92E-17	5.20E-17	2.95E-17	2.17E-17	1.80E-17	5.08E-17	3.84E-17	3.29E-17	3.44E-17	2.52E-17	2.01E-17
Middle thigh	0.005	Male	2.37E-16	2.20E-16	1.98E-16	1.11E-16	9.46E-17	7.16E-17	2.55E-16	2.31E-16	2.01E-16	1.14E-16	9.83E-17	7.62E-17
		Female	8.50E-16	7.18E-16	6.13E-16	3.39E-16	2.77E-16	2.13E-16	7.59E-16	6.33E-16	5.31E-16	3.70E-16	3.06E-16	2.45E-16
	0.1	Male	3.25E-16	2.85E-16	2.01E-16	1.47E-16	1.15E-16	9.33E-17	2.54E-16	2.23E-16	1.87E-16	1.82E-16	1.39E-16	1.03E-16
		Female	7.98E-16	7.02E-16	5.10E-16	3.13E-16	2.56E-16	2.02E-16	5.33E-16	4.55E-16	3.78E-16	3.53E-16	2.81E-16	2.30E-16
	0.3	Male	2.70E-16	2.42E-16	1.66E-16	1.38E-16	1.17E-16	8.68E-17	1.83E-16	1.58E-16	1.34E-16	1.59E-16	1.42E-16	1.01E-16
		Female	4.38E-16	4.06E-16	3.04E-16	1.99E-16	1.66E-16	1.35E-16	2.57E-16	2.25E-16	1.89E-16	2.16E-16	1.81E-16	1.51E-16
Lower torso	0.005	Male	4.58E-15	3.75E-15	2.10E-15	4.59E-15	3.28E-15	1.74E-15	2.57E-15	2.13E-15	1.74E-15	4.17E-15	3.47E-15	1.80E-15
		Female	1.24E-14	8.96E-15	4.77E-15	4.01E-15	3.62E-15	1.56E-15	3.68E-15	2.97E-15	2.29E-15	4.38E-15	4.05E-15	2.01E-15
	0.1	Male	2.27E-15	1.91E-15	1.12E-15	1.30E-15	1.07E-15	6.98E-16	1.31E-15	1.12E-15	9.64E-16	1.46E-15	1.30E-15	8.31E-16
		Female	2.98E-15	2.54E-15	1.68E-15	1.25E-15	1.15E-15	6.42E-16	1.52E-15	1.31E-15	1.08E-15	1.32E-15	1.22E-15	7.74E-16
	0.3	Male	6.02E-16	5.34E-16	3.80E-16	3.58E-16	3.07E-16	2.35E-16	4.15E-16	3.64E-16	3.39E-16	4.02E-16	3.70E-16	2.76E-16
		Female	6.64E-16	6.10E-16	4.74E-16	3.49E-16	3.30E-16	2.21E-16	4.42E-16	3.98E-16	3.54E-16	3.57E-16	3.38E-16	2.43E-16
	1	Male	7.54E-17	7.10E-17	5.91E-17	5.01E-17	4.61E-17	3.85E-17	5.97E-17	5.56E-17	5.24E-17	5.53E-17	5.28E-17	4.41E-17
		Female	7.90E-17	7.67E-17	6.45E-17	5.03E-17	4.75E-17	3.64E-17	6.05E-17	5.61E-17	5.22E-17	5.09E-17	4.82E-17	3.98E-17
	1.5	Male	3.55E-17	3.34E-17	2.84E-17	2.38E-17	2.27E-17	1.87E-17	2.88E-17	2.72E-17	2.56E-17	2.61E-17	2.50E-17	2.15E-17
		Female	3.64E-17	3.52E-17	3.07E-17	2.37E-17	2.27E-17	1.81E-17	2.87E-17	2.72E-17	2.50E-17	2.42E-17	2.34E-17	1.94E-17
	3	Male	8.92E-18	8.68E-18	7.74E-18	6.37E-18	5.94E-18	5.20E-18	7.47E-18	7.09E-18	6.84E-18	7.01E-18	6.70E-18	5.98E-18
		Female	9.26E-18	9.26E-18	8.13E-18	6.43E-18	6.20E-18	4.97E-18	7.61E-18	7.21E-18	6.66E-18	6.56E-18	6.27E-18	5.36E-18
Middle torso	0.005	Male	2.01E-15	1.69E-15	1.32E-15	1.12E-15	9.34E-16	7.68E-16	1.03E-15	8.50E-16	6.87E-16	2.34E-15	1.92E-15	1.59E-15
		Female	8.48E-16	7.98E-16	6.09E-16	6.33E-16	5.85E-16	4.67E-16	6.10E-16	5.42E-16	4.13E-16	6.23E-16	5.58E-16	4.46E-16
	0.1	Male	1.34E-15	1.13E-15	9.03E-16	8.00E-16	6.87E-16	5.59E-16	7.16E-16	6.12E-16	5.03E-16	1.16E-15	9.87E-16	8.42E-16
		Female	1.02E-15	9.01E-16	6.01E-16	6.24E-16	5.63E-16	4.12E-16	5.83E-16	5.08E-16	3.98E-16	6.08E-16	5.47E-16	4.08E-16
	0.3	Male	4.78E-16	4.24E-16	3.57E-16	3.09E-16	2.75E-16	2.30E-16	3.16E-16	2.81E-16	2.46E-16	3.58E-16	3.24E-16	2.80E-16
		Female	4.82E-16	4.60E-16	3.38E-16	2.86E-16	2.68E-16	1.98E-16	3.02E-16	2.71E-16	2.28E-16	2.91E-16	2.62E-16	2.05E-16
Upper torso	0.005	Male	2.72E-16	2.48E-16	2.03E-16	2.32E-16	2.04E-16	1.61E-16	1.95E-16	1.72E-16	1.34E-16	2.56E-16	2.32E-16	1.85E-16
		Female	1.29E-16	1.25E-16	8.74E-17	8.33E-17	7.40E-17	5.43E-17	9.10E-17	8.71E-17	6.74E-17	7.73E-17	7.04E-17	5.24E-17
	0.1	Male	3.48E-16	3.02E-16	2.23E-16	1.50E-16	1.30E-16	1.06E-16	2.25E-16	1.95E-16	1.51E-16	1.54E-16	1.34E-16	1.13E-16
		Female	2.26E-16	2.03E-16	1.01E-16	1.47E-16	1.25E-16	6.85E-17	1.50E-16	1.34E-16	9.97E-17	1.71E-16	1.46E-16	9.66E-17
	0.3	Male	2.92E-16	2.62E-16	2.12E-16	2.01E-16	1.71E-16	1.21E-16	1.96E-16	1.65E-16	1.36E-16	2.32E-16	2.01E-16	1.57E-16
		Female	2.71E-16	2.52E-16	1.75E-16	1.49E-16	1.36E-16	9.49E-17	1.67E-16	1.48E-16	1.17E-16	1.47E-16	1.33E-16	9.76E-17

Table J.16. Effective dose per source disintegration ($\text{Sv s}^{-1} \text{Bq}^{-1}$) of ^{192}Ir , $^{137}\text{Cs}/^{137\text{m}}\text{Ba}$ and ^{60}Co .

Level	Distance (m)	Direction											
		Anterior			Right lateral			Posterior			Left lateral		
		^{192}Ir	$^{137}\text{Cs}/^{137\text{m}}\text{Ba}$	^{60}Co									
Ground	0.005	1.08E-17	7.95E-18	3.64E-17	8.32E-18	5.88E-18	2.64E-17	8.04E-18	5.65E-18	2.49E-17	7.81E-18	5.49E-18	2.45E-17
	0.1	1.12E-17	8.33E-18	3.89E-17	3.99E-18	3.03E-18	1.53E-17	6.90E-18	5.16E-18	2.48E-17	4.26E-18	3.31E-18	1.66E-17
	0.3	1.33E-17	9.64E-18	4.32E-17	4.24E-18	3.40E-18	1.80E-17	8.46E-18	6.44E-18	3.02E-17	4.66E-18	3.77E-18	1.99E-17
Middle thigh	0.005	1.89E-16	1.30E-16	5.39E-16	4.85E-17	3.77E-17	1.87E-16	1.31E-16	9.14E-17	3.88E-16	5.21E-17	4.05E-17	2.00E-16
	0.1	1.37E-16	9.52E-17	4.00E-16	3.85E-17	3.06E-17	1.52E-16	8.89E-17	6.30E-17	2.71E-16	4.23E-17	3.34E-17	1.65E-16
	0.3	7.86E-17	5.45E-17	2.24E-16	2.96E-17	2.29E-17	1.09E-16	5.27E-17	3.77E-17	1.62E-16	3.38E-17	2.61E-17	1.24E-16
Lower torso	0.005	6.04E-16	4.27E-16	1.84E-15	3.28E-16	2.38E-16	1.06E-15	4.67E-16	3.30E-16	1.43E-15	3.70E-16	2.68E-16	1.19E-15
	0.1	3.63E-16	2.52E-16	1.04E-15	1.82E-16	1.31E-16	5.73E-16	2.68E-16	1.88E-16	8.04E-16	2.20E-16	1.58E-16	6.77E-16
	0.3	1.49E-16	1.01E-16	4.13E-16	7.15E-17	5.28E-17	2.33E-16	1.09E-16	7.62E-17	3.22E-16	8.31E-17	5.99E-17	2.62E-16
	1	2.50E-17	1.72E-17	6.74E-17	1.26E-17	9.49E-18	4.21E-17	1.93E-17	1.34E-17	5.64E-17	1.46E-17	1.06E-17	4.66E-17
	1.5	1.22E-17	8.13E-18	3.26E-17	6.28E-18	4.67E-18	2.09E-17	9.41E-18	6.54E-18	2.77E-17	7.15E-18	5.22E-18	2.27E-17
	3	3.29E-18	2.16E-18	8.72E-18	1.72E-18	1.29E-18	5.74E-18	2.51E-18	1.77E-18	7.43E-18	1.94E-18	1.40E-18	6.23E-18
Middle torso	0.005	1.12E-15	7.79E-16	3.28E-15	6.59E-16	4.60E-16	1.95E-15	7.33E-16	5.12E-16	2.17E-15	9.21E-16	6.37E-16	2.67E-15
	0.1	5.47E-16	3.77E-16	1.52E-15	2.53E-16	1.82E-16	7.85E-16	3.19E-16	2.24E-16	9.46E-16	3.31E-16	2.33E-16	9.86E-16
	0.3	1.71E-16	1.16E-16	4.64E-16	8.10E-17	5.97E-17	2.62E-16	1.14E-16	7.94E-17	3.34E-16	9.45E-17	6.84E-17	2.96E-16
Upper torso	0.005	1.46E-15	1.00E-15	4.09E-15	3.96E-16	2.82E-16	1.21E-15	4.70E-16	3.35E-16	1.45E-15	3.62E-16	2.59E-16	1.13E-15
	0.1	4.78E-16	3.26E-16	1.32E-15	1.58E-16	1.18E-16	5.41E-16	2.35E-16	1.67E-16	7.25E-16	1.49E-16	1.13E-16	5.22E-16
	0.3	1.64E-16	1.12E-16	4.50E-16	6.68E-17	4.98E-17	2.24E-16	9.63E-17	6.85E-17	2.92E-16	7.01E-17	5.22E-17	2.32E-16

Table J.17. Source self-shielding factors

Radioactive material thickness (diameter/height)	Capsule-wall thickness					
	1 mm			2 mm		
	¹⁹² Ir	¹³⁷ Cs/ ^{137m} Ba	⁶⁰ Co	¹⁹² Ir	¹³⁷ Cs/ ^{137m} Ba	⁶⁰ Co
1 mm	0.840	0.963	0.972	0.803	0.941	0.953
2 mm	0.717	0.961	0.965	0.694	0.935	0.947
3 mm	0.627	0.957	0.958	0.606	0.931	0.938
4 mm	0.556	0.952	0.949	0.536	0.927	0.929

ANNEX K. DESCRIPTION OF ELECTRONIC FILES

(K1) The compressed package of electronic files containing the detailed data on the adult mesh-type reference computational phantoms (MRCPs) can be found in the supplementary CD that accompanies the printed publication. The package is organised in 7 folders: (1) *PM-version Adult MRCP*, (2) *TM-version Adult MRCP*, (3) *Material Information*, (4) *Spongiosa Information*, (5) *Blood Information*, (6) *MC Input Examples* and (7) *Phantom Visualisation*. This annex briefly explains the files in these folders and their features.

K.1. Data files in *PM-version Adult MRCP*

(K2) This folder contains the following two data files:

MRCP_AM.obj
MRCP_AF.obj

The data files in the OBJ format contain the polygon mesh (PM) version of the adult mesh-type reference computational phantoms. These OBJ files can be imported in various 3D commercial programs such as *3ds MaxTM* (Autodesk, USA), *MAYATM* (Autodesk, USA), *RapidformTM* (INUS Technology Inc., Korea) and *Rhinoceros* (Robert McNeel, USA).

K.2. Data files in *TM-version Adult MRCP*

(K3) This folder contains the following four data files:

MRCP_AM.node
MRCP_AF.node
MRCP_AM.ele
MRCP_AF.ele

The data files in the NODE and ELE formats contain the tetrahedral mesh (TM) version of the adult mesh-type reference computational phantoms. The NODE-format files contain a list of node coordinates composing the TM-version phantoms. The ELE-format files contain a list of tetrahedrons composing the TM-version phantoms and each tetrahedron is represented as four node IDs listed in the corresponding NODE-format files and an organ ID number with respect to the tetrahedron.

K.3. Data files in *Material Information*

(K4) This folder contains the following two data files:

MRCP_AM_media.dat
MRCP_AF_media.dat

The data files contain lists of the media, elemental compositions and densities (Annex B).

K.4. Data files in Spongiosa Information

(K5) This folder contains the following two data files:

MRCP_AM_spongiosa.dat
MRCP_AF_spongiosa.dat

The data files contain the mass fractions of bone components (i.e. mineral bone, active marrow, inactive marrow, blood and skeletal miscellaneous) in the spongiosa region.

K.5. Data files in *Blood Information*

(K6) This folder contains the following two data files:

MRCP_AM_blood.dat
MRCP_AF_blood.dat

The data files contain the mass fractions of blood in the organs and tissues of the phantoms.

K.6. Data files in *MC Input Examples*

(K7) This folder contains the following three compressed files:

MRCP_GEANT4.tar.gz
MRCP_MCNP6.tar.gz
MRCP_PHITS.tar.gz

The data files contain input examples for implementation of the TM-version phantoms in the three Monte Carlo codes, i.e. Geant4 (Agostinelli et al., 2003), MCNP6 (Goorley et al., 2013) and PHITS (Sato et al., 2013). In these examples, a point source emitting 662-keV photons is located at 1 m in front of the phantom. Detailed information on the implementation is described in the ‘readme’ text file included in each compressed file.

K.7. Data files in Phantom Visualisation

(K8) This folder contains the following three PDF files:

MRCP_AM.pdf
MRCP_AF.pdf
How_to_use_3DPDF.pdf

The two PDF files (i.e. ‘MRCP_AM.pdf’ and ‘MRCP_AF.pdf’) visualise the mesh-type adult reference computational phantoms in a 3D view, as shown in Fig. M.1. The PDF files are read in the Acrobat program (Adobe Systems, San Jose, CA, USA) where one can navigate the phantoms in detail, e.g. by rotating or enlarging each of the organ/tissue models. Detailed instruction on these PDF files can be found in ‘How_to_use_3DPDF.pdf’.

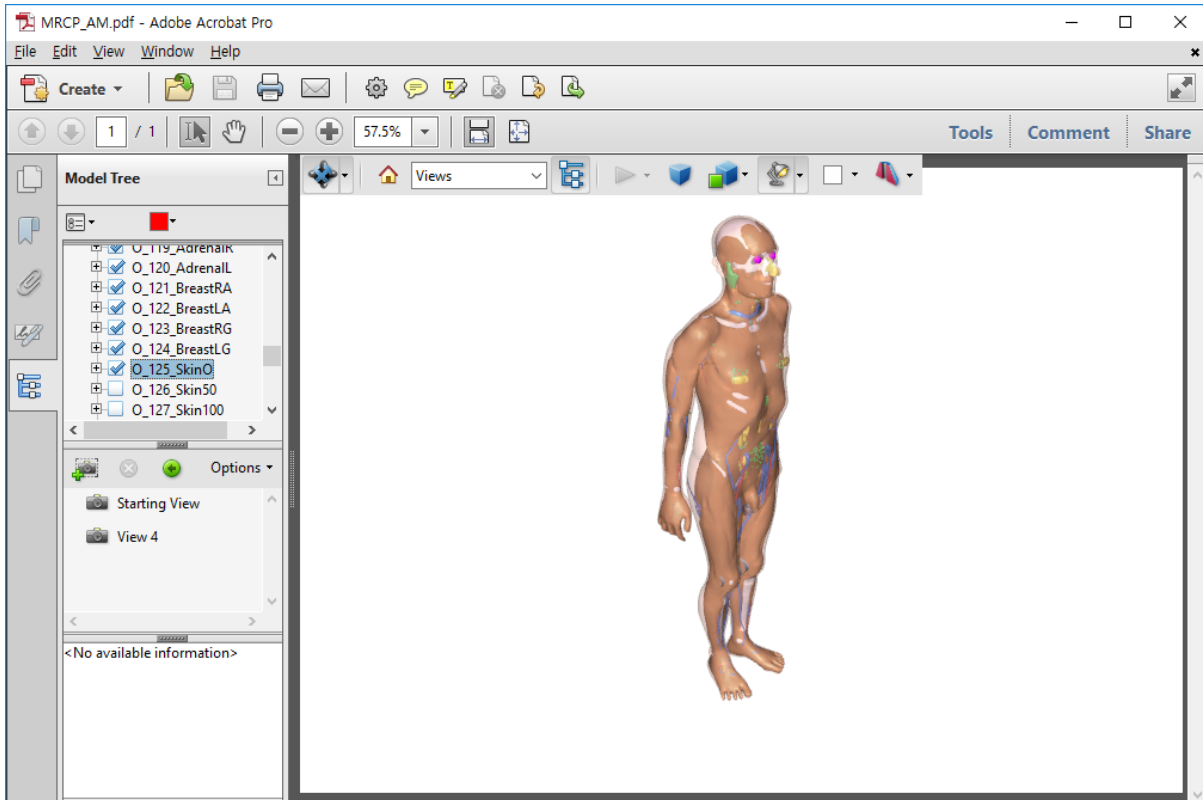


Fig. K.1. 3D view of the adult mesh-type reference phantom for the male visualised in the Adobe Acrobat program importing the MRCP_AM.pdf file.